論文 / 著書情報
Article / Book Information

題目(和文)	柔軟旋回クレーンの動力学解析モデルと振動制御法の開発
Title(English)	Development of Dynamic Model and Vibration Control of Flexible Rotary Cranes
著者(和文)	CHALERMPONGKolawach
Author(English)	Kolawach Chalermpong
出典(和文)	学位:博士(工学), 学位授与機関:東京工業大学, 報告番号:甲第12352号, 授与年月日:2023年3月26日, 学位の種別:課程博士, 審査員:山浦 弘,古谷 寛,坂本 啓,中野 寛,菅原 雄介
Citation(English)	Degree:Doctor (Engineering), Conferring organization: Tokyo Institute of Technology, Report number:甲第12352号, Conferred date:2023/3/26, Degree Type:Course doctor, Examiner:,,,,
学位種別(和文)	博士論文
Type(English)	Doctoral Thesis

Doctoral Dissertation of 2022

Development of Dynamic Model and Vibration Control of Flexible Rotary Cranes

CHALERMPONG Kolawach

Deparment of Mechanical Engineering
Graduate Major in Mechanical Engineering
School of Engineering
Tokyo Institute of Technology

Abstract

Vibration of the carrying object is a major problem in crane operation. The causes of this vibration are the rotational motion in crane's operation, and the flexibility within the crane's structure. This dissertation approaches this problem by developing the dynamic model and the vibration control strategy for a flexible rotary crane. The dynamic model was employed to simulate the motion of the crane to illustrate and study the crane's behavior. The vibration control strategy was employed to reduce the residual vibration of the crane caused by the carrying operation.

The development of the dynamic model of the flexible rotary crane aimed to address the problem of a long calculation time. First, the modeling of the hoisted rope was focused. The inertia included rope model was developed, and its bending deformation during the crane's motion was studied. From the numerical simulation, the dynamic model with the inertia included rope model was used to simulate the bending vibration of the rope during the crane operation. The magnitude of this bending vibration was increased with the length of the rope. This vibration was the result of the excitation from the boom's bending frequency when the natural frequency of the rope's bending was lower than the bending vibration frequency of the boom. When comparing the modeling of the rope as the rigid component, massless flexible component, and inertia included rope model, the trajectory of the rope model with inertia deviated from the other two rope's model as the length of the rope was increased. However, this deviation decreased as the mass of the hoisted load increased. With the example specification in this research, the motion of all rope models showed a similar trajectory overall.

Then, effcient dynamic model of the flexible crane was developed by applying the system-level model reduction of the adaptive modal integration (AMI). This development aimed to solve the problem of the numerical stiffness in the dynamic model of the flexible structure and the calculation cost of the time-variant inverse of the inertia matrix. The relative coordinate system was chosen as the primary formulation of the nonlinear equation of motion. Because the boom was modeled as a flexible body and the hoisted load was modeled as a point mass, there were not enough coordinates to map between the two bodies via a constrained joint. Therefore, the modeling of the flexible boom and the point mass hoisted load by considering the hoisted load as an additional particle of the boom was proposed.

The AMI crane model was developed such that an arbitrary motion can be employed. This was achieved by forming the modal reduction matrix from the mode shapes under the static conditions of the crane model. When the modal matrix was formed with the static mode shapes, it became the function of the configuration of the crane and became independent of the velocity and acceleration. Therefore, the arbitrary driving velocity and acceleration can be used. Then, the calculation cost of the inverse inertia matrix was reduced by precalculating this matrix before the simulation and interpolating it during the simulation. In this thesis, the piecewise bilinear interpolation and the radial basis function were used for comparison. The efficiency of this reduced model was shown by comparing it with the nonlinear model via numerical simulation. The comparison demonstrated that the reduced model could give an accurately simulated motion with a shorter calculation time

than the nonlinear model. Additionally, the reduced model with the piecewise bilinear interpolation used the shortest simulation time.

The vibration control strategy for the rotary crane with the flexible boom was developed. This research proposed a vibration control model that explicitly considered the flexibility of the boom. The vibration control model was developed by modeling the vibration of the boom tip as a simple mass-spring model. The vibrationless trajectory was designed by applying the optimal control theory to the proposed control model, where the optimal condition was determined via the trial calculation using the previously developed dynamic model. In this designed trajectory, the motion was divided into three periods: the acceleration period, constant velocity period, and deceleration period. In this trajectory, only the trajectory during the acceleration and deceleration periods had to be calculated. The crane was driven with a constant slewing velocity during the constant velocity period. Therefore, the target angle of the slewing operation was adjustable by simply adjusting the duration of the constant velocity period without redesigning the acceleration. This was the advantage of this trajectory.

The performance of the proposed vibration control model was confirmed by conducting a numerical simulation on the crane model with a specification that mimics the real-size crane. Then, the numerical simulation and experiment were conducted on a laboratory-size flexible crane. The effectiveness of the vibration reduction was demonstrated by comparing the proposed control model with the reference boom control model that did not consider the flexibility of the boom. The numerical simulation and the experiment demonstrated that the effectiveness between the flexible control model and the rigid control model was similar when the crane was driven at a low acceleration. The amplitude of the residual vibration from the vibration control model with boom's flexibility was similar to the vibration model without boom's flexibility. When the driving acceleration was increased, the proposed vibration control model with boom's flexibility showed a smaller residual vibration amplitude of both the boom tip and the hoisted load. These results showed that the proposed vibration control model was effective over the rigid boom control model since the proposed control model gave the crane potential to operate at a higher acceleration, which could enhance the work efficiency.

Acknowledgement

Firstly, I would like to express my gratitude to my supervisor Prof. Yamaura Hiroshi for his constant encouragement, guidance and support throughout my years of study from master's degree until doctoral degree.

I would like to express my sincere thanks to the Ministry of Education, Culture, Sport and Technology (MEXT) of Japan for the Japanese Government scholarship which gave me this great opportunity to achieved my goal here in Japan.

I would like to thank my beloved friends Dr. Tuchjuta, Dr. Promsen and Mr. Natdanai for all the encouragement, support and goodtime here in Japan. In my years in Japan, I faced many problems and difficulties, both in study and in daily life. However, I was able to get through those problems because of them. I also would like to thank all of my friend in the Thai community here in Japan. Although their names might have not been mentioned here, their precious supports were one of the reason that help me achieved this journey.

I also would like to thank all the members of the Yamaura laboratory for the friendship, generosity and support in my study and research here in Tokyo Institute of Technology. In addition, I would like to express my gratitude to Tadano ltd. for funding this research as well as supporting the information and knowledge regarding the crane technology.

Finally, I would like to thank my beloved family from the bottom of my heart. Because of their support, I was able to achieve this journey. The most important person who I have owed my achievement to is my father. He is the man who has been working very hard for the family. In my entire life, all of my happiness and success came from his sacrifice. My gratitude to him is beyond my ability to express in words.

Contents

Chapter 1

Introduction

1.1 Background

Crane is one of the lifting equipment. It is vastly employed in the industrial field for transporting cargo, and in the construction field for aiding the operation or carrying materials and equipment. A rotary crane consists of an operating arm called a "boom". An example of the rotary crane is shown in Fig. 1.1. The operation is performed by rotating the boom in slewing and lifting directions to carry the object (in this dissertation, the object was referred as the hoisted load), as shown in Fig. 1.2. A major problem in crane operation is the vibration of the hoisted load. At the end of the hoisted load transportation, the hoisted load vibrates with residual vibration after the crane stop. This creates an unsafe work environment. For safety aspect, the operators have to wait until the load stop vibrating before continuing the work. This vibration of the hoisted load is caused by the sway of the hoisted load from the rotational motion of the crane, and the flexibility of the structure.

Fig. 1.1: Tadano all-terrain crane AR-7000N
ref: Tadano Global news, Tadano Launches the AR-7000N, the Highest Lifting Capacity All-Terrain Crane from a Japanese Manufacturer

When the crane is operated with a slewing motion, the hoisted load sways because of the

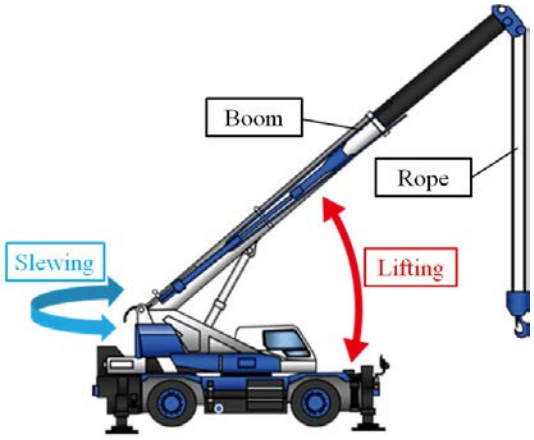

Fig. 1.2: Operation of the rotary crane

centrifugal force. When the crane stops, the hoisted is swung back from a swayed angle and keeps on vibrating with a pendulum motion. During the operation, the structure of the crane deforms and changes the equilibrium point of the hoisted load. This increases the amplitude of the hoisted load's residual vibration. In the rotary crane, the component that suffer the large deformation due to the flexibility is the boom.

The vibration of the hoisted load from the crane operation could be reduced by simply rotating the crane at a low speed. However, this increases the operation time and leads to an inefficient working process. Experience operators could operate the crane at medium to optimum speed to increase the work efficiency. However, this makes the crane operation rely too much on the experience and skill of the operators. The problem occurs because these skillful operators are aging every day. Thus, their numbers are reduced daily. Moreover, training new operators take time and resources. For the crane industry, it is crucial to develop a technical solution to control the vibration of the hoisted load in the crane operation that reduce the human input. One of the solutions is the implementation of the automatic driving system. Thus, it has become one of the agenda in the crane research to develop the automatic operation system of the crane that could carry the object to the designated location under a shortest time possible and creates a smallest residual vibration.

The development of the dynamic model and the vibration control can contribute to the development of the automatic crane operation. The dynamic model is used to simulate the motion and behavior of the crane. Then, it is used to assist in designing the vibration control approach. Thus, this dissertation focused on these topics.

1.2 Literature review

1.2.1 Dynamic model of the flexible crane

1.2.1.1 Crane's model assumption

The development of the dynamic model for the rotary crane has been studied for many years. The equation of motion of the rotary crane with a rigid body assumption was one of the earliest models[1]. The model may consider a flexibility supporting structure, such as the outrigger, as the external force[2]. Recently, the development of a dynamic model of the rotary crane that included

the flexibility of the structures has been presented in many papers.

The slewing drive or the slewing platform is the part that consists of the cockpit and the actuator systems of the crane. Many researchers have modeled this structure as a rigid body[3, 4, 5]. However, no study has shown the significance of including the flexibility of the slewing drive.

The boom is one of the components that flexibility is being focused on when modeling the rotary crane. The studies in [3] and [4] showed that the inclusion of the flexibility of the boom in a dynamic model of a rotary crane achieved better accuracy compared to the experiment results. The deformable beam was one of the modeling assumptions for the boom model. Maczyski and Wojciech[5] modeled the telescopic boom as a flexible beam with a variable cross-section using the finite element model and mode reduction. The flexible multibody dynamics with the floating frame of reference formulation (FFRF)[6] of the boom model was employed in the mobile crane model by [7], and in the floating crane by [8, 9]. In [10], the telescopic boom was modeled as multiple flexible beams connected via the flexible sliding plates.

In the rotary crane with a flexible boom, the tip of the boom is pulled by the weight of the hoisted load. Thus, the boom is deformed, and the working radius of the crane is changed, as shown in Fig. 1.3. When the boom tip deforms, the initial condition of the rotary crane changes.

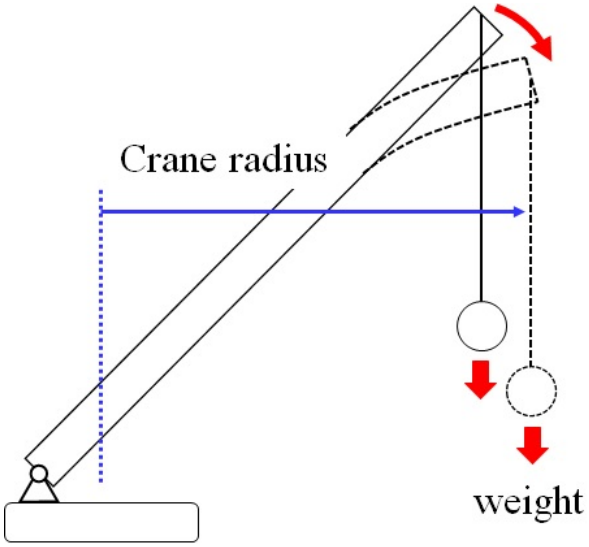

Fig. 1.3: Deformed boom tip at a static equilibrium condition

To demonstrate the influence of the boom's flexibility on the dynamic model, the rotary crane in Fig. 1.4 is used as an example. Its equation of motion is modeled in Appendix C. The natural frequencies of this structure are written in Table 1.1.

Table 1.1: The natural frequencies of the example rotary crane in Fig. 1.4

Boom criteria	Pendulum mode	Lowest boom bending mode
Rigid body	0.158 [Hz]	-
Flexible body	0.157 [Hz]	0.782 [Hz]

Table 1.1 shows the natural frequencies of the example crane model when the boom was a rigid body and a flexible body. From this table, the natural frequency of the pendulum mode (the lowest

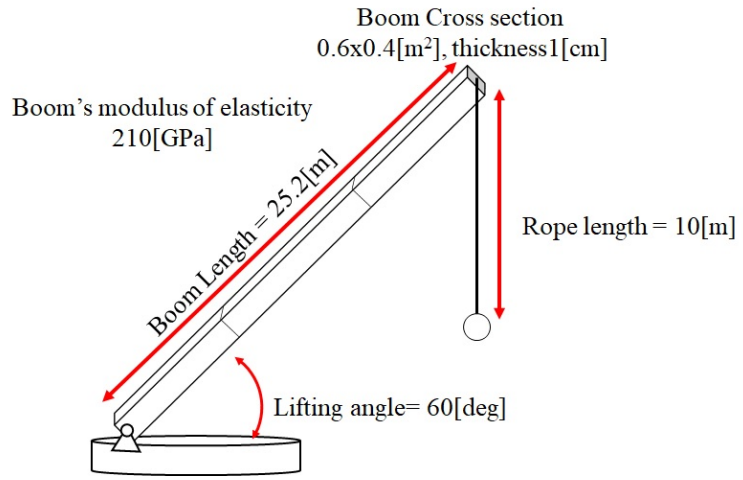

Fig. 1.4: Example of a rotary crane with flexible boom

frequency that related to the hoisted load's vibration) from a rigid boom model and a flexible boom model was similar. The difference between their frequency was around 2.5%. However, if the boom was made with softer material, this difference could be larger.

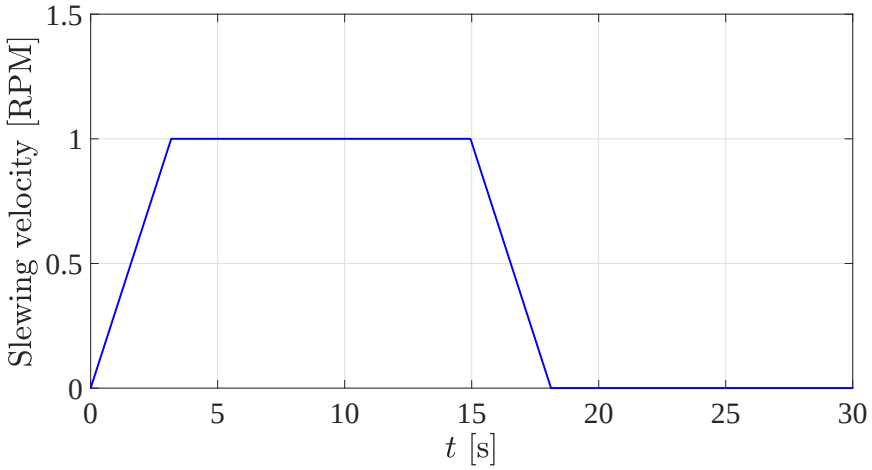

Fig. 1.5: Trapezoidal slewing velocity at 1[RPM]

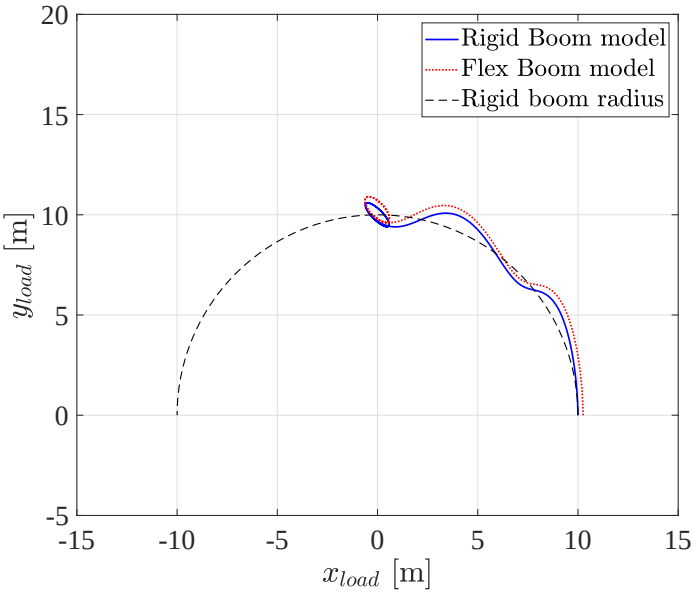

Fig. 1.6: Hoisted load trajectory with trapezoidal slewing velocity at 1[RPM] without vibration control

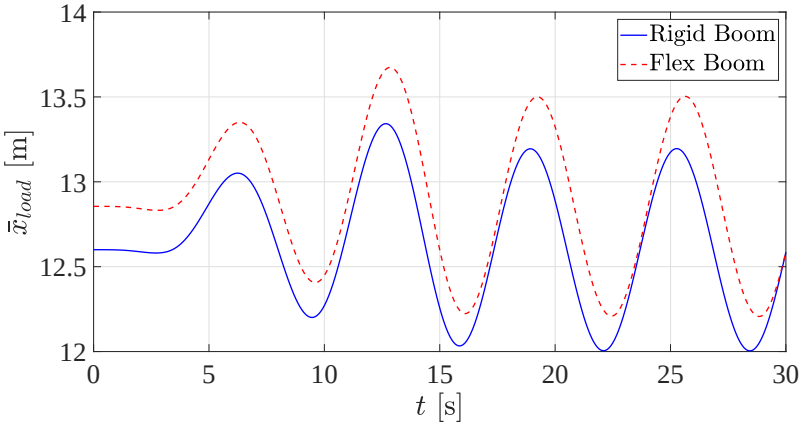

Fig. 1.7: Time-history of the hoisted load motion in x-direction with trapezoidal slewing velocity at 1[RPM] without vibration control

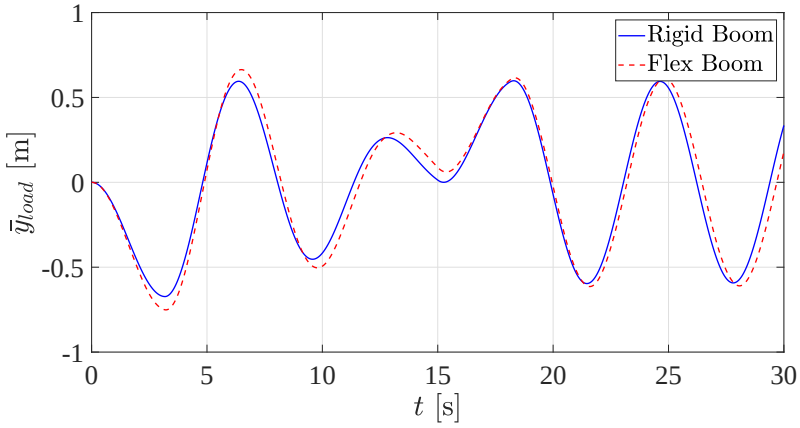

Fig. 1.8: Time-history of the hoisted load motion in y-direction with trapezoidal slewing velocity at 1[RPM] without vibration control

If the example model was driven with the trapezoidal slewing velocity in Fig. 1.5 without any vibration control strategy, the trajectory of the hoisted load on the xy-plane under this motion can be shown in Fig. 1.6. Furthermore, the time-history of the hoisted load motion in the x and y-directions on the boom's coordinate system are shown in Figs. 1.7 and 1.8. From Fig. 1.6, the radius of the hoisted load of the flexible boom model was larger than the rigid boom. This was because the boom tip was pulled by the hoisted load and deformed at the initial condition. The time-history of the hoisted load motion in x-direction, Fig. 1.7, shows that the amplitude of the hoisted load from the model with a flexible boom was larger than motion from a rigid boom. These results demonstrated the effect of the boom's flexibility on the dynamic model of the crane.

The hoisted rope is also a flexible component. Several assumptions could be employed to model the hoisted rope. Several models considered the hoisted rope by ignoring its inertia and modeled it as the massless spring[5, 8, 9, 11]. The works in [3, 4] developed the full finite element analysis model that also considered the inertia of the rope. However, it was unclear whether the inertia of the hoisted rope was compulsory for the dynamic model of the crane.

The hoisted load has been modeled as the point mass assumption by many researchers[1, 3, 4, 5, 7, 11]. By modeling the hoisted load as the point mass, the motion of the hoisted load was presented with the spherical pendulum dynamics. In [8, 9], the rectangular prism shape of the hoisted load was used to model the container lifting in a floating crane. In contrast to the point mass, this model could simulate the rotation dynamics of the hoisted load. However, it also limited the use of the model to a specific shape of the carrying object. On the other hand, the hoisted load with a point mass assumption could simulate an arbitrary cargo.

In summary, the assumption for the dynamic model of the flexible rotary crane that has been shared among many researchers are the rigid slewing drive, the flexible boom, the flexible rope, and the point mass hoisted load, as shown in Fig. 1.9.

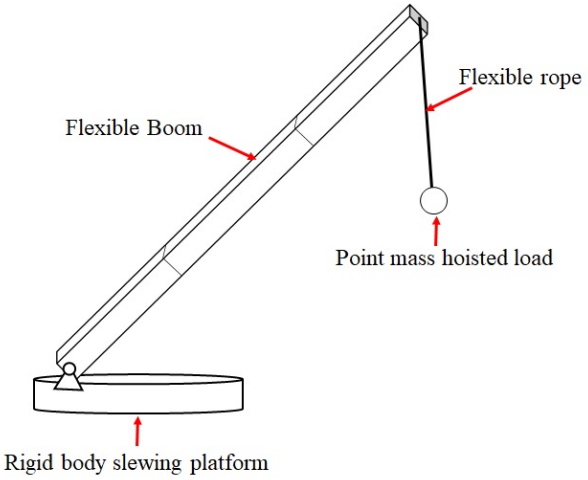

Fig. 1.9: The assumption of the flexible rotary crane model from literature reviews

1.2.1.2 Multibody dynamics model with relative coordinate system

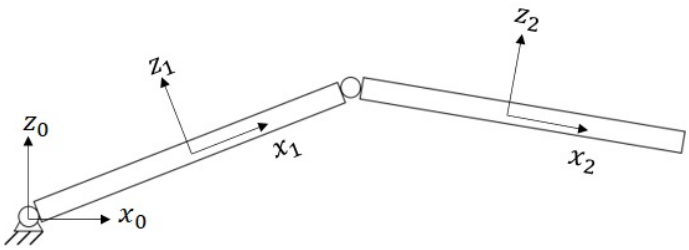

Fig. 1.10: Example of the two-links manipulator system in planar coordinates

Recently, the formulation of the multibody dynamic has been used in many modeling[12, 13, 14]. The differential algebraic equation (DAE) is a form of the equation of motion, which is widely employed in the multibody dynamics analysis. This formulation was used in modeling the rotary crane model in [7, 8, 9]. An advantage of the DAE equation of motion is the simplicity in the formulation of the equation of motion. To illustrate this advantage, the two linkages manipulator, as shown in Fig. 1.10, is used as an example. In this mechanism, the first link (body 1) is pinned to the ground with the revolute joint. Simultaneously, it connects to the second link (body 2) with the revolute joint as well. The typical equation of motion for each body can be written as

$$\mathbf{M}_i\ddot{\mathbf{q}}_i = \mathbf{Q}_{ext,i} + \mathbf{Q}_{const,i} \ (i = 1, 2), \tag{1.1}$$

where $\mathbf{M}_i$ is the matrix of mass-inertia of body-i, $\mathbf{q}_i = \begin{bmatrix} x_i & y_i & \theta_i \end{bmatrix}^T$ is the body-i's vector of the generalized coordinates. θ_i is the rotation of the body-i coordinate system with respect to the

global coordinate system. $\mathbf{Q}_{ext,i}$ and $\mathbf{Q}_{const,i}$ are the vector of generalized external forces and the constraint forces, respectively.

The common strategy in deriving the system equation of motion is connecting each body's equation of motion through the constraint forces. However, this process could be done easier by using the DAE formulation. First, the constraint equation must be set up. Here, the constraint equations are

$$\mathbf{C} = \begin{bmatrix} \mathbf{R}_1 - \mathbf{A}_1\bar{\mathbf{u}}_{1,c1} \\ \mathbf{R}_2 - \mathbf{A}_2\bar{\mathbf{u}}_{2,c2} - \mathbf{R}_1 - \mathbf{A}_1\bar{\mathbf{u}}_{1,c2} \end{bmatrix} = \mathbf{0}, \tag{1.2}$$

where $\bar{\mathbf{u}}_{i,cj}$ is the position vector of the constraint-j on the body-i, and the vector is viewed on the body-i's coordinate system. $\mathbf{A}_i$ is the rotation matrix of body-i. The systems equation of motion is rewritten as

$$\mathbf{M}\ddot{\mathbf{q}} = \mathbf{Q}_{ext} - \mathbf{C}_{\mathbf{q}}^T\boldsymbol{\lambda}, \tag{1.3}$$

where $\mathbf{C}_\mathbf{q}$ is the Jacobian matrix of the constraint equation $\mathbf{C}$ and $\boldsymbol{\lambda}$ is the vector of Lagrange's multipliers. The constraint forces are now presented with $\mathbf{C}_q^T\boldsymbol{\lambda}$. However, Eq. (1.3) has two unknown which are $\mathbf{q}$ and $\boldsymbol{\lambda}$. Thus, Eq. (1.3) alone is not enough to solve the motion. To calculate the motion, Eqs. (1.2) and (1.3) must be solved together, thus, the system become DAE.

From the above example, the formulation of the equation of motion was done by simply forming the equation of motion of each individual body then connect them via the constraint equations. Although the setup of the equation of motion was simple, its calculation is usually complex and expensive. One of the simplest ways to solve this system is transforming the equation of motion from the DAE form into the ordinary differential equation (ODE) form by mapping the vector of Lagrange's multipliers. This can be performed by calculating the second order derivative of Eq. (1.2) with time as

$$\mathbf{C}_\mathbf{q}\ddot{\mathbf{q}} = \mathbf{Q}_c. \tag{1.4}$$

where $\mathbf{Q}_c$ is the residual term as the result of the differentiation. Then the system equation becomes

$$\begin{bmatrix} \mathbf{M} & \mathbf{C}_\mathbf{q}^T \\ \mathbf{C}_\mathbf{q} & \end{bmatrix} \begin{bmatrix} \ddot{\mathbf{q}} \\ \boldsymbol{\lambda} \end{bmatrix} = \begin{bmatrix} \mathbf{Q}_{ext} \\ \mathbf{Q}_c \end{bmatrix}. \tag{1.5}$$

By solving Eq. (1.5), we will have $\ddot{\mathbf{q}}$ in the ODE form, which can be integrated with conventional integration method. However, this method also leads to an inefficient problem since the size of the problem is the total number of the degree of freedoms from each body as an individual plus the number of the constraint equations. Furthermore, this calculation suffer the instability problem when mapping DAE into ODE. Although this could be compensated by using the Baumgrate's stabilization[15], this even increases the calculation time because it requires additional calculation of the inverse Jacobian matrix of the constraint.

The relative coordinate system describes the motion of the mechanisms or the structures by using the relative motion between each body[16]. Once again, the two links manipulator system in

Fig. 1.10 is used as an example. The constraint equation in Eq. (1.2) can be rewritten to show the relation between each body as

$$\begin{aligned}
\begin{bmatrix}\dot{\mathbf{R}}_1\\ \dot{\theta}_1\end{bmatrix} &= \begin{bmatrix}\mathbf{A}_{1,\theta}\bar{\mathbf{u}}_{1,c1}\\ 1\end{bmatrix}\dot{\theta}_{10},\\
\dot{\mathbf{q}}_1 &= \begin{bmatrix}\bar{\mathbf{P}}_{10} & \mathbf{0}_{3\times 1}\end{bmatrix}\begin{bmatrix}\dot{\theta}_{10}\\ \dot{\theta}_{21}\end{bmatrix},\\
&= \mathbf{P}_{10}\dot{\mathbf{q}}_r,
\end{aligned} \tag{1.6}$$

$$\begin{aligned}
\begin{bmatrix}\dot{\mathbf{R}}_2\\ \dot{\theta}_2\end{bmatrix} &= \begin{bmatrix}\mathbf{I}_{3\times 3} & \mathbf{A}_{1,\theta}\bar{\mathbf{u}}_{1,c2} - \mathbf{A}_{1,\theta}\mathbf{A}_{21}\bar{\mathbf{u}}_{2,c2}\\ \mathbf{0}_{1\times 3} & 1\end{bmatrix}\begin{bmatrix}\dot{\mathbf{R}}_1\\ \dot{\theta}_1\end{bmatrix} + \begin{bmatrix}-\mathbf{A}_1\mathbf{A}_{21,\theta}\bar{\mathbf{u}}_{2,c2}\\ 1\end{bmatrix}\dot{\theta}_{21},\\
\dot{\mathbf{q}}_2 &= \bar{\mathbf{P}}_{21}\dot{\mathbf{q}}_1 + \bar{\mathbf{N}}_{21}\dot{\theta}_{21},\\
&= \bar{\mathbf{P}}_{21}\bar{\mathbf{P}}_{10}\dot{\theta}_{10} + \bar{\mathbf{N}}_{21}\dot{\theta}_{21},\\
&= \begin{bmatrix}\bar{\mathbf{P}}_{21}\bar{\mathbf{P}}_{10} & \bar{\mathbf{N}}_{21}\end{bmatrix}\begin{bmatrix}\dot{\theta}_{10}\\ \dot{\theta}_{21}\end{bmatrix},\\
&= \mathbf{P}_{20}\dot{\mathbf{q}}_r,
\end{aligned} \tag{1.7}$$

The rotation angle $\theta_{ij} = \theta_i - \theta_j$ is the relative angle between body-i and j. $\mathbf{A}_{ij}$ is the rotation matrix of the body-j's coordinate system on the body-i's coordinate system, and

$$\mathbf{A}_{1,\theta} = \frac{\partial \mathbf{A}_1}{\partial \theta_{10}}, \tag{1.8}$$

$$\mathbf{A}_{21,\theta} = \frac{\partial \mathbf{A}_2 1}{\partial \theta_{21}}. \tag{1.9}$$

The constraint is rewritten such that the motion of each body is now described with two relative angles. A concept from modeling with the relative coordinate system is the motion of the adjacent body is described with the motion from the previous joint. The velocity $\dot{\mathbf{q}}_2$ was calculated with the velocity of the body 1, $\dot{\mathbf{q}}_1$, and their relative angular velocity $\dot{\theta}_{21}$. Similarly, the velocity of the body 1 was calculated with the relative rotation between itself and the ground (body 0), θ_{10}. For each consecution body, the motion of the adjacent body can be expressed with its previous body via the mapping of $\mathbf{P}_{ij}$. The modeling of the motion with the relative coordinates system is also called the recursive method for this reason[16].

The equation of motion could be formulated by differentiating Eqs. (1.6) and (1.7) with time, and substituting them into Eq. (1.1) while multiplying the mapping matrix $\mathbf{P}_{10}^T$ and $\mathbf{P}_{20}^T$ to the left-side of each equation as shown in Eqs. (1.10) and (1.11).

$$\mathbf{P}_{10}^T\mathbf{M}_1(\mathbf{P}_{10}\ddot{\mathbf{q}}_r + \dot{\mathbf{P}}_{10}\dot{\mathbf{q}}_r) = \mathbf{P}_{10}^T\mathbf{Q}_{ext,1} + \mathbf{P}_{10}^T\mathbf{Q}_{const,1}, \tag{1.10}$$

$$\mathbf{P}_{20}^T\mathbf{M}_2(\mathbf{P}_{20}\ddot{\mathbf{q}}_r + \dot{\mathbf{P}}_{20}\dot{\mathbf{q}}_r) = \mathbf{P}_{20}^T\mathbf{Q}_{ext,2} + \mathbf{P}_{20}^T\mathbf{Q}_{const,2}. \tag{1.11}$$

The dimension of the equation of motion is reduced to 2×2 as the result of the mapping. Both equations are connected by using the relation between the joint reaction forces since $\mathbf{P}_{10}^T\mathbf{Q}_{const,1} =$

$-\mathbf{P}_{20}^{T}\mathbf{Q}_{const,2}$. By using this relation, Eq. (1.10) can be added to (1.11). Then, the equation of motion becomes

$$\mathbf{M}_r\ddot{\mathbf{q}}_r = \mathbf{Q}_{ext,r} + \mathbf{\Gamma}_r, \tag{1.12}$$

where $\mathbf{\Gamma}_r$ is the residual vector from the differentiation of the constraint equations.

Equation (1.12) has a dimension equal to the number of degrees of freedom. Furthermore, the equation is written in the ODE which is simpler to calculate compared to DAE. For the model with open-chain such as in Fig. 1.9, the ODE form can be considerably more efficient in simulation than the DAE.

The rotary crane was the open-chain mechanism. The constraints in this system were the revolute joint between the slewing drive and ground or the chassis in the case of the mobile crane, the revolute joint between and the boom, the spherical joint at the boom tip and rope [1, 2, 5, 7, 8, 9, 11].

1.2.1.3 The system level model reduction

The flexible component can be modeled with the finite element formulation. The finite element model has a large size due to many coordinates. In the flexible model, the inertia matrix varied with the configuration of the structure; thus, the inertia matrix varied with time during the motion[6, 12]. To solve the equation of motion, the inverse of the inertia matrix is required. However, its calculation cost is expensive. Since the inertia matrix varied with time, its inverse matrix was also time-variant. When the numerical integration was used, the inverse of the inertia matrix had to be calculated at every time step. Thus, the dynamic model requires a long calculation time to solve the equation. Another cause of the long calculation time of the flexible dynamic model was the numerical stiffness. For the structure with high natural frequency modes, its numerical integration requires a small integration step to avoid the instability of the calculation. Therefore, the calculation time was increased. The numerical stiffness and the calculation of the time-variant inverse inertia matrix were considered the major cause of the efficiency of the calculation of the flexible dynamic model of the rotary crane.

The model reduction was one of the techniques for enhancing the calculation performance of the dynamic model. The purpose of this scheme was to reduce the size of the problem. The modal reduction is one of the model reduction methods, which reduced the size of the problem by using the modal bases of the structure. Guyan[17] and Craig-Bampton[18] proposed a model reduction based on matrix partitioning. Guyan's method eliminated the coordinates that were not subjected to forces, while Craig-Bampton's method eliminated the coordinates such that only the dominant coordinates (the mode shapes at the boundary between two substructures) remained. In their methods, the coordinates truncation was calculated such that the nondominant modes were approximated with the dominant modes. The model reduction in [19] reduced the size of the problem by approximating the physical coordinates with a few modal coordinates. However, the nondominant modes were completely omitted. These methods have inspired several studies on the development of the model reduction technique[20, 21, 22, 23].

The system-level model reduction was the model reduction that considered the entire structure, then reduced the size of the problem with the modal bases from the modal analysis of the entire structure instead of an individual component. The system-level model reduction for the DAE-flexible multibody dynamics was studied in [24, 25, 26, 27, 28]. The system-level model reduction for the ODE-flexible multibody dynamics was studied in [29, 30, 31]. One of which was the adaptive modal integration (AMI) method by Aarts and Jonker [29]. The primary concept of the AMI was the consideration of the time-derivative of the mode shapes as the mechanism was moving. In

conventional modal reduction[19], the mode shapes of low natural frequency were used to form the modal reduction matrix. This matrix was multiplied to the physical coordinates to reduce the size of the system and change the system into modal coordinate system. However, this modal matrix remained constant matrix throughout the dynamic analysis. The mode shapes of the flexible mechanism changed during the motion since these mode shapes were a function of the structure's configuration. The AMI method compensated for this change by considering the time-variation of the mode shapes during the simulation. The mode shapes along the specific motion path were precalculated, then, the time-variant interpolation function was formed. The time-derivative of the mode shapes was calculated by differentiate these interpolations.

Among these techniques, the system-level model reduction was considerably suitable for the flexible dynamic model of the crane since the flexible motion of the crane exists at several parts. The AMI method was also considered the simplest implementation but with a powerful performance that was attractive. However, the disadvantage of this method was the limitation of the model to a specific driving motion.

1.2.2 Vibration control of cranes

The vibration control of the rotary crane has been studied for many years. Most research focused solely on the hoisted load while ignoring the flexibility in the structures. This was in contrast to the studies on the dynamic model development, where the flexibility in the structures, particularly the boom, was compulsory.

Maczyski and Wojciech presented a dynamic model of a flexible mobile-rotary crane and the trajectory design via optimization approach in [5]. Although their research developed a model that included the flexibility of the structure, the optimization of the motion did not consider this flexibility. In their optimal control, all components were considered a rigid body. The influence of flexibility was controlled with the feedback system. Furthermore, they only presented the draft idea of the feedback system without the design detail.

Uchiyama et al.[32] proposed the vibration control of the hoisted load using the open-loop system to design the vibrationless trajectory in S-curve while fixing the working radius of the crane. Kuo and Kang[33] proposed the design of the piecewise acceleration for the optimal control of the rotary crane using only slewing motion. The acceleration was designed based on the size of the sway. However, the flexibility in this structure was not considered. Aba and Okabe [34] also developed a feed-forward input for controlling the vibration of the rotary crane employing the polynomial and cycloid functions. Still, the flexibility of the system was not included.

In my research group, the feed-forward controller for a rotary crane was studied in [35, 36]. In these models, the vibrationless trajectory was designed using both slewing and lifting angles. The access control strategy was employed to design the optimal trajectory[37, 38, 39]. An advantage of this trajectory was the arbitrary duration of the acceleration period. In their models, the acceleration function was not restricted by the conventional trapezoidal velocity such as [33], or the famous input shaping method[40] which needed half of the natural period to reach the vibrationless point. However, the flexibility of the structure was not included in these studies.

Takagi and Nishimura presented the vibration control of the tower-type rotary crane which included the flexibility of the tower[41]. The tower was considered as the flexible beam, and its first vibration mode was used to design the control model. In their research, the boom was considered as a rigid body. The study by He et al. in [42] proposed the vibration control of a tower crane that considered the vibration of a rope. The vibration control of the tower crane that considered the flexibility of the rope with adjustable length was developed in [43].

Urbaś et al. studied the influence of flexible structures on the effectiveness of a proportional-

integral-derivative (PID) controller in [44]. A number of simulations were performed to compare the vibration of the structure from the dynamic model that considered the boom as a rigid body and flexible body. From their results, the PID control performed well on the crane with the rigid boom model while it was unable to suppress the vibration when the flexible boom was considered in the simulation.

Although the research on the vibration control of a crane has been studied by many researchers, the consideration of the flexibility of the boom in the controller design has not been developed yet. To demonstrate a significant of the boom's flexibility in the controller design, once again, an example rotary crane in Fig. 1.4 is used. The example model was driven with the vibrationless trajectory with the acceleration as shown in Fig. 1.11. This trajectory was designed with the vibration control model in [35] for a rotary crane with a rigid boom.

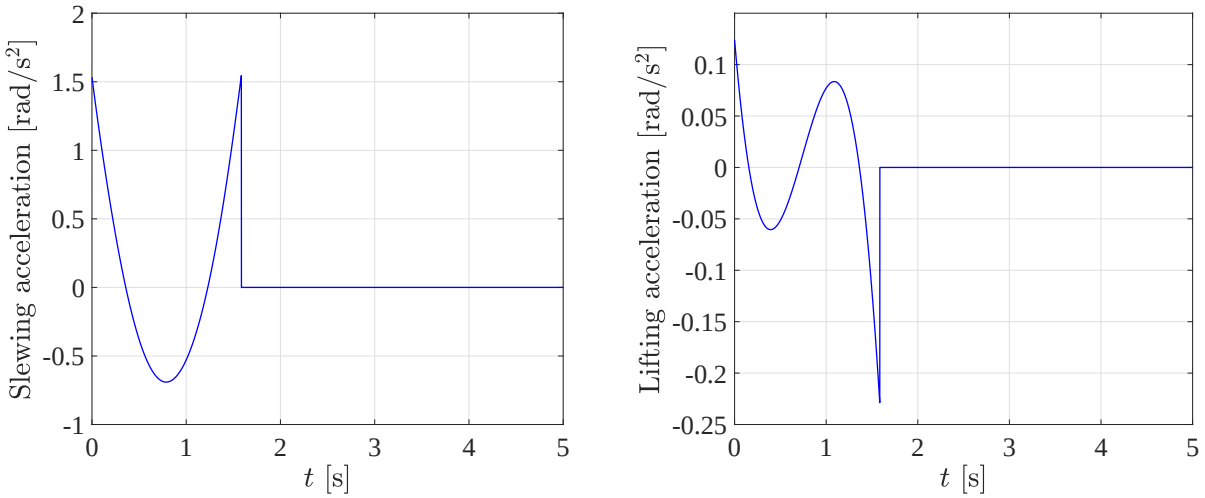

(a) Slewing control (b) Lifting control

Fig. 1.11: Example acceleration of the vibration control trajectory for a rigid boom crane

The trajectories of the hoisted load on the xy-plane from both a rigid boom and a flexible boom models are shown in Fig. 1.12. The time-history of the hoisted load motion in teh x and y directions are shown in Figs. 1.13 and 1.14.

In Figs. 1.12 to 1.14, both trajectory and time-history data of the hoisted load show that the vibration control model with the rigid boom became less effective when the flexibility of the boom was included in the dynamic model. In these figures, the motion of the hoisted load when the boom was a rigid body was stable and had small residual vibration. However, the same controlled trajectory could not suppress the vibration of the hoisted load when the boom was a flexible body. In Table 1.1, the natural frequency of the pendulum mode from the crane with a rigid boom and a flexible boom was close. However, the simulation results in Figs. 1.12 to 1.14 show that the flexibility of the boom could not be neglected even though the difference in the natural frequency is small.

From the above literature reviews, the vibration control of the rotary crane leans toward to the feed-forward control system[32, 33, 34, 35, 36, 41, 42, 43] more than the feedback system[44]. In the literature review on the vibration control of the overhead crane, a similar argument can be found. Sakawa and Shindo[45] calculated the optimized trajectory by minimizing the velocity of the trolley. Lee in [46] proposed the dynamic model of the overhead crane in spatial coordinates and the vibration control with feedback system. Jaafar, et al. in [47] proposed the design of the

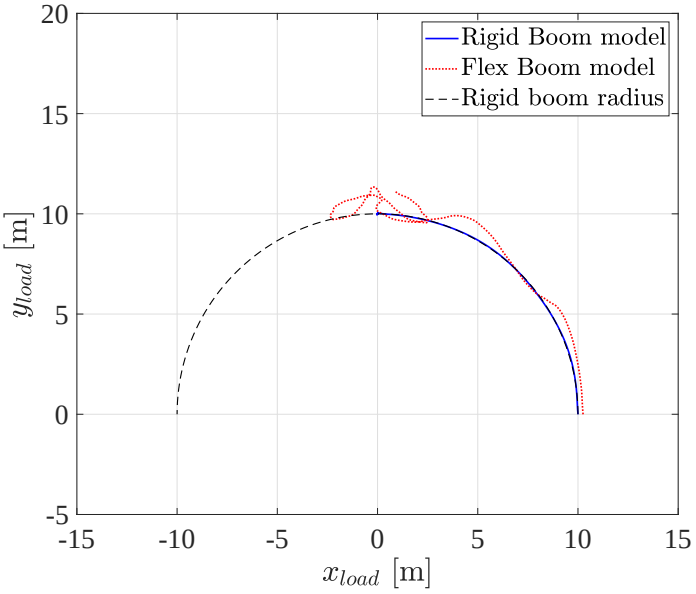

Fig. 1.12: Hoisted load trajectory with the rigid boom vibration controlled trajectory

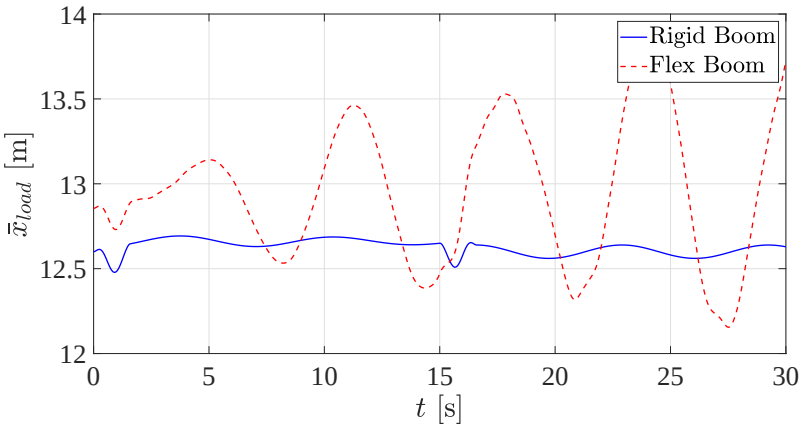

Fig. 1.13: Time-history of the hoisted load motion in x-direction with the rigid boom vibration controlled trajectory

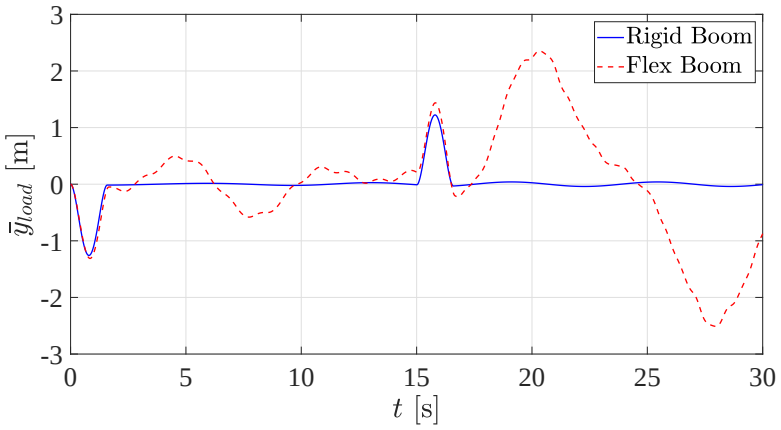

Fig. 1.14: Time-history of the hoisted load motion in y-direction with the rigid boom vibration controlled trajectory

input shaping that designed the shaper by using the zeros and poles for the damped-vibration problem in overhead crane. [48] designed the embedding calculation to derive the closed form of the vibrationless trajectory for a bang-bang acceleration and the input shaping trajectory.

From these literature review, the feed-forward controller is widely employed among the crane system in designing the vibration control strategy. It is understandable since the feed-forward system does not require the implementation of the sensors. Thus, the feed-forward system has implementation cost cheaper than the feedback system. However, the feedback control can be used to enhance the feed-forward control system by compensating an unpredicted influence that the feed-forward control could not consider. Additionally, there were several approaches in designing the feed-forward input that was shared among the work in vibration control of cranes: the trajectory design by setup the cost function to the interested vibration problem and calculate the minimization[5, 34, 35, 36, 45], designing of the bang-off-bang acceleration based on the size of the sway angle[33, 48], and employing the famous input shaping method[47, 48].

1.3 Motivation and objective

To develop a solution for the vibration problem in the rotary crane, two things are required: a dynamics model and a vibration control strategy. For the rotary crane, the flexibility of the boom is compulsory. The flexibility of the boom shifts the equilibrium position of the hoisted load; thus, the radius of the hoisted load's trajectory is changed, and its amplitude during the residual vibration increase. Furthermore, the vibration control of the crane with the rigid boom model could become less effective when the flexibility of the boom is included.

In modeling the dynamic model of the flexible crane, the model requires a long calculation time because of the numerical stiffness problem and the calculation cost of the inverse of the inertia matrix. The dynamic model that requires a long simulation time becomes inefficient when a large number of the motion are wanted to be calculated. This also limits the application of the model. If the dynamic model can simulate the motion under a short calculation time, the model become more useful in studying the crane motion in various cases. Such model could better assist in studying

the behavior of the flexible crane to find the solution to the vibration problem. Moreover, it could extend its usefulness to other application such as real-time simulation for training purpose.

From the literature review, the vibration control of the rotary crane that considered the flexibility of the boom has not been studied. However, the flexibility increases the amplitude of the hoisted load vibration due to the shifting of the equilibrium point. This became the motivation of this dissertation to develop a control strategy of the rotary crane that included the flexibility of the boom in the controller design.

Therefore, the objectives of this research were: 1) develop the efficient dynamic model of the rotary crane with a flexible boom that could simulate the motion of the crane under a short calculation time, and 2) develop the vibration control approach for the rotary crane that include the flexibility of the boom in the controller design.

Furthermore, the developed dynamic model and the vibration control approach can be applied to an arbitrary rotary crane in order to contributing to the development of the automatic crane operation. Thus, the general knowledge that was proposed by this dissertation is the procedure in modeling the efficient dynamic model and the vibration control model for a flexible rotary crane.

In this dissertation, the examples that were used in this research are based on the mobile crane with the boom length within 9[m] to 30[m]. These lengths were long enough to demonstrate the deformation of the boom, which is crucial to this study. Furthermore, this size covers the cargo crane and the rough terrain crane. The cargo crane is employed in the logistic operation, while the rough terrain crane is used in construction operation. Thus, the crane between these sizes could represent the overall application of the rotary crane. Therefore, the examples in this research were made by referring to these sizes.

Chapter 2

Dynamic model of flexible rotary crane

In this chapter, the details of the study on the dynamic model are discussed. The modeling condition, the formulation, and the modeling technique is researched and developed to achieve an efficient dynamic model of the flexible rotary crane.

The part of this chapter has been presented in

1. Chalermpong, K., Yamaura, H. and Hara, K., Investigation of the influence of the inertia of hoisting rope on mobile crane using flexible multibody model, the Japan Society of Mechanical Engineer, Transaction of the JSME (in Japanese), Vol.84, No.861 (2018), 17-00512.

2. Chalermpong, K., Hara, K. and Yamaura, H., Development of an efficient flexible dynamics model of a mobile crane with adaptive modal integration, Proceedings of the 15th International Conference on Motion and Vibration Control (MoViC 2020) (2020), 10039.

2.1 Study of the hoisted rope model

The hoisted rope is a flexible component. However, there was no study on whether it should be included in the dynamic model, or what was its appropriate modeling assumption. In this section, the optimal choice for the hoisted rope model assumption was studied. The inertia included hoisted rope model for the multibody dynamic formulation was developed. Then, the assumptions of the rope's model between the rigid rope, the massless spring, and the inertia included rope were compared.

2.1.1 Inertia included hoisted rope model

First, the modeling of the inertia included hoisted rope is discussed. The hoisted rope was modeled as a very thin circular beam. The FFRF[6] was chosen as the main formulation for modeling the flexible body in this study. The rope model was modeled, as shown in Fig. 2.1.

In Fig. 2.1, the rope was modeled with five beam elements. The position vector $\mathbf{r}_p$ from the origin of the global coordinates system to any arbitrary point on the rope was calculated as follows;

$$\mathbf{r}_p = \mathbf{R}_i + \mathbf{A}_i \left(\bar{\mathbf{u}}_{o,i} + \bar{\mathbf{u}}_{f,i} \right) = \mathbf{R}_i + \mathbf{A}_i \bar{\mathbf{u}}_i, \tag{2.1}$$

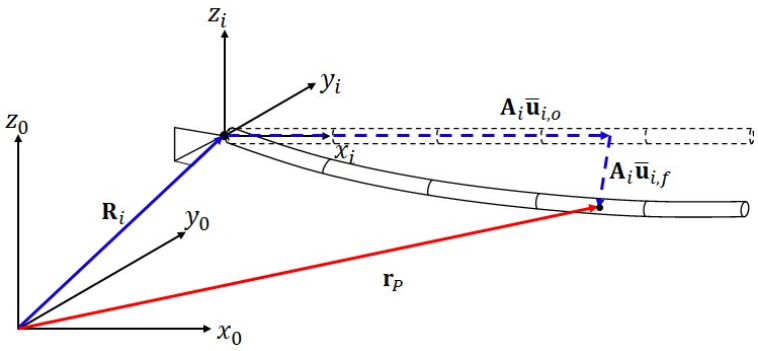

Fig. 2.1: The schematic of the inertia included flexible hoisted rope model

$$\bar{\mathbf{u}}_{f,i} = \mathbf{S}_i \bar{\mathbf{q}}_{f,i}, \tag{2.2}$$

$$\mathbf{S}^k_{beam} = \begin{bmatrix} 1-\frac{\bar{x}_i^k}{l_i^k} & 0 & 0 \\ 6\bar{y}_i^k\left(\frac{\bar{x}_i^k}{l_i^k}-\frac{\left(\bar{x}_i^k\right)^2}{\left(l_i^k\right)^3}\right) & 2\left(\frac{\bar{x}_i^k}{l_i^k}\right)^3-3\left(\frac{\bar{x}_i^k}{l_i^k}\right)^2+1 & 0 \\ 6\bar{z}_i^k\left(\frac{\bar{x}_i^k}{l_i^k}-\frac{\left(\bar{x}_i^k\right)^2}{\left(l_i^k\right)^3}\right) & 0 & 2\left(\frac{\bar{x}_i^k}{l_i^k}\right)^3-3\left(\frac{\bar{x}_i^k}{l_i^k}\right)^2+1 \\ 0 & \bar{z}_i^k\left(\frac{\bar{x}_i^k}{l_i^k}-1\right) & \bar{y}_i^k\left(1-\frac{\bar{x}_i^k}{l_i^k}\right) \\ \bar{z}_i^k\left(1+3\left(\frac{\bar{x}_i^k}{l_i^k}\right)^2-\frac{4\bar{x}_i^k}{l_i^k}\right) & 0 & \frac{2\left(\bar{x}_i^k\right)^2}{l_i^k}-\bar{x}_i^k-\frac{\left(\bar{x}_i^k\right)^3}{\left(l_i^k\right)^2} \\ \bar{y}_i^k\left(\frac{4\bar{x}_i^k}{l_i^k}-3\left(\frac{\bar{x}_i^k}{l_i^k}\right)^2-1\right) & \bar{x}_i^k-\frac{2\left(\bar{x}_i^k\right)^2}{l_i^k}+\frac{\left(\bar{x}_i^k\right)^3}{\left(l_i^k\right)^2} & 0 \\ \frac{\bar{x}_i^k}{l_i^k} & 0 & 0 \\ 6\bar{y}_i^k\left(\frac{\left(\bar{x}_i^k\right)^2}{\left(l_i^k\right)^3}-\frac{\bar{x}_i^k}{l_i^k}\right) & 3\left(\frac{\bar{x}_i^k}{l_i^k}\right)^2-2\left(\frac{\bar{x}_i^k}{l_i^k}\right)^3 & 0 \\ 6\bar{z}_i^k\left(\frac{\left(\bar{x}_i^k\right)^2}{\left(l_i^k\right)^3}-\frac{\bar{x}_i^k}{l_i^k}\right) & 0 & 3\left(\frac{\bar{x}_i^k}{l_i^k}\right)^2-2\left(\frac{\bar{x}_i^k}{l_i^k}\right)^3 \\ 0 & -\frac{\bar{x}_i^k\bar{z}_i^k}{l_i^k} & \frac{\bar{x}_i^k\bar{y}_i^k}{l_i^k} \\ \bar{z}_i^k\left(3\left(\frac{\bar{x}_i^k}{l_i^k}\right)^2-\frac{2\bar{x}_i^k}{l_i^k}\right) & 0 & \left(\frac{\bar{x}_i^k}{l_i^k}\right)^2-\left(\frac{\bar{x}_i^k}{l_i^k}\right)^3 \\ \bar{y}_i^k\left(\frac{2\bar{x}_i^k}{l_i^k}-3\left(\frac{\bar{x}_i^k}{l_i^k}\right)^2\right) & \left(\frac{\bar{x}_i^k}{l_i^k}\right)^3-\left(\frac{\bar{x}_i^k}{l_i^k}\right)^2 & 0 \end{bmatrix}^{\mathrm{T}}. \tag{2.3}$$

In Eq. (2.1), $\mathbf{A}_i$ is the rotation matrix, $\bar{\mathbf{u}}_{o,i}$ is the position vector from the origin of the i-th body coordinate system to an arbitrary point P on the body-i before undergoing deformation. $\bar{\mathbf{u}}_{f,i}$ is the displacement vector of the deformation at point P. $\bar{\mathbf{u}}_{o,i}$ and $\bar{\mathbf{u}}_{f,i}$ are the vectors on the body-i coordinate system. $\mathbf{S}_i$ is the matrix of shape functions, and $\bar{\mathbf{q}}_{f,i}$ is the vector of the generalized flexible coordinates. In this model, Euler-Bernoulli's beam was used to model the beam element. Its matrix of shape functions was calculated using Eq. (2.3). In Eq. (2.3), l_i^k is the length of the beam element, $(\bar{x}_i^k, \bar{y}_i^k, \bar{z}_i^k)$ are the position of the point on element k-th from the origin of the element's

coordinate system. The boundary condition of each element was applied via the Boolean matrices described as follows;

$$\mathbf{B}_i^1 = \begin{bmatrix} \mathbf{0}_{6\times6} & \mathbf{0}_{6\times24} \\ \mathbf{I}_{6\times6} & \mathbf{0}_{6\times24} \end{bmatrix} \tag{2.4}$$

$$\mathbf{B}_i^2 = \begin{bmatrix} \mathbf{I}_{12\times12} & \mathbf{0}_{12\times18} \end{bmatrix} \tag{2.5}$$

$$\mathbf{B}_i^3 = \begin{bmatrix} \mathbf{0}_{12\times6} & \mathbf{I}_{12\times12} & \mathbf{0}_{12\times12} \end{bmatrix} \tag{2.6}$$

$$\mathbf{B}_i^4 = \begin{bmatrix} \mathbf{0}_{12\times12} & \mathbf{I}_{12\times12} & \mathbf{0}_{12\times6} \end{bmatrix} \tag{2.7}$$

$$\mathbf{B}_i^5 = \begin{bmatrix} \mathbf{0}_{12\times18} & \mathbf{I}_{12\times12} \end{bmatrix} \tag{2.8}$$

The matrix of the shape functions of each element was calculated as

$$\mathbf{S}_i^k = \mathbf{S}_{beam}\mathbf{B}_i^k. \tag{2.9}$$

The mass-inertia matrix of the body was derived through the kinetic energy of the hoisted rope model. The mass-inertia matrix of each element was calculated as

$$\mathbf{M}_i^k = \int_{V_i^k} \rho_i \begin{bmatrix} \mathbf{I}_{3\times3} \\ -(\mathbf{A}_i\tilde{\tilde{\mathbf{u}}}_i^k)^T \\ (\mathbf{A}_i\mathbf{S}_i^k)^T \end{bmatrix} \begin{bmatrix} \mathbf{I}_{3\times3} & -\mathbf{A}_i\tilde{\tilde{\mathbf{u}}}_i^k & \mathbf{A}_i\mathbf{S}_i^k \end{bmatrix} d\mathbb{V}^k, \tag{2.10}$$

where $\mathbb{V}^k$ is the volume of the k-th element. The stiffness matrix of each element was calculated using

$$\mathbf{K}_{ff,i}^k = \int_{V_i^k} (\mathbf{D}_i^k\mathbf{S}_i^k)^T\mathbf{E}_i^k\mathbf{D}_i^k\mathbf{S}_i^k d\mathbb{V}^k, \tag{2.11}$$

where $\mathbf{E}_i^k$ is the elastic matrix, and $\mathbf{D}_i^k$ is the derivative matrix. Both matrices were calculated as

$$\mathbf{E}_i^k = \begin{bmatrix} E_{rope} & 0 & 0 \\ 0 & G_{rope} & 0 \\ 0 & 0 & G_{rope} \end{bmatrix}, \tag{2.12}$$

$$\mathbf{D}_i^k = \begin{bmatrix} \dfrac{\partial}{\partial x_i^k} & 0 & 0 \\ \dfrac{\partial}{\partial y_i^k} & \dfrac{\partial}{\partial x_i^k} & 0 \\ \dfrac{\partial}{\partial z_i^k} & 0 & \dfrac{\partial}{\partial x_i^k} \end{bmatrix}, \tag{2.13}$$

where E_{rope} is the elastic tension modulus and G_{rope} is the elastic torsional modulus of the rope model. Then, the total mass-inertia matrix and the stiffness matrix of the body-i were

$$\mathbf{M}_i = \sum_{k=1}^{5} \mathbf{M}_i^k, \tag{2.14}$$

$$\mathbf{K}_{ff,i} = \sum_{k=1}^{5} \mathbf{K}_{ff,i}^k. \tag{2.15}$$

2.1.2 The comparison of the rope's model assumption

Table 2.1: The specification of the crane model for observing the rope's model assumption

Specification	values
Chassis mass	20 000 [kg]
Chassis size	5, 2.5, 0.4 [m]
Outriggers' stiffness	1000, 1000, 7500 [kN/m]
Outriggers' damping	20, 20, 16 [kN.s/m]
Slewing platform mass	800 [kg]
Slewing platform radius and height	4, 1 [m]
Boom length	20 [m] (8[m]-6[m]-6[m])
Boom cross-section	0.5×0.3, 0.45×0.25, 0.4×0.2 [m^2]
Boom thickness	0.01 [m]
Booms' density	7800 [kg/m^2]
Booms' Young's modulus	210 [GPa]
Rope length	5, 10, 15 [m]
Rope diameter	30 [mm]
Rope material density	7800 [kg/m^2]
Rope Young's modulus	196 [GPa]
Rope Poisson's ratio	0.3
Mass of load	100, 500, 1000 [kg]

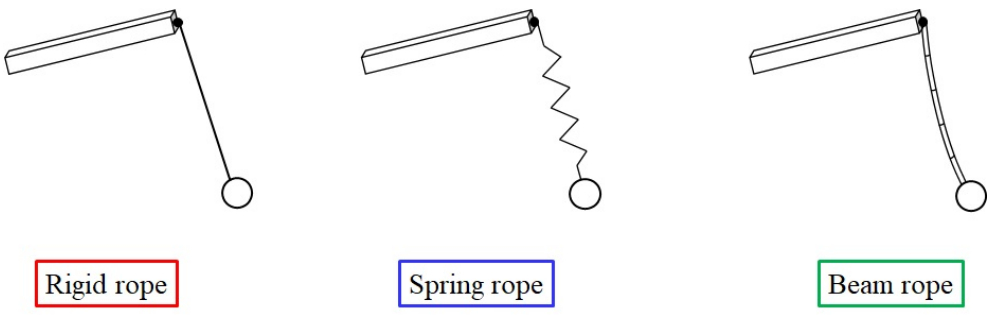

Fig. 2.2: The hoisted rope model for comparison

The assumptions of the hoisted rope model were compared. The assumptions were 1) a rigid rope, 2) a massless flexible rope (spring rope), and 3) an inertia included rope (beam rope). The comparison was conducted by performing a numerical simulation on the flexible mobile crane in Appendix A. The specifications of the crane in this study are given in Table 2.1. In this simulation, the boom's lifting angle was fixed at 60[deg] while the crane was slewed for 180[deg] with the velocity as shown in Fig. 2.3.

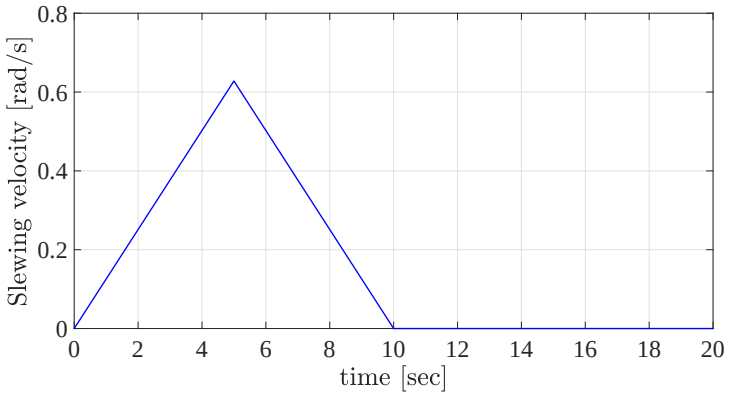

Fig. 2.3: The input slewing velocity for the model in Appendix A for comparing the rope's models

Firstly, the deformation of the inertia included rope model, during the crane motion was observed. From the simulation, the shape of the rope during the crane's motion is shown in Figs. 2.4 to 2.6.

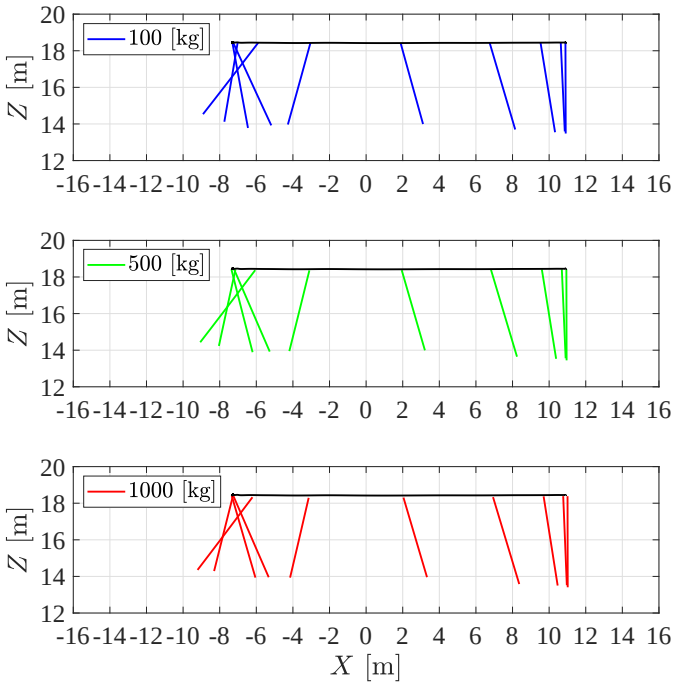

Fig. 2.4: Visual of the 5[m]-hoisted rope during the slewing motion in xz-plane

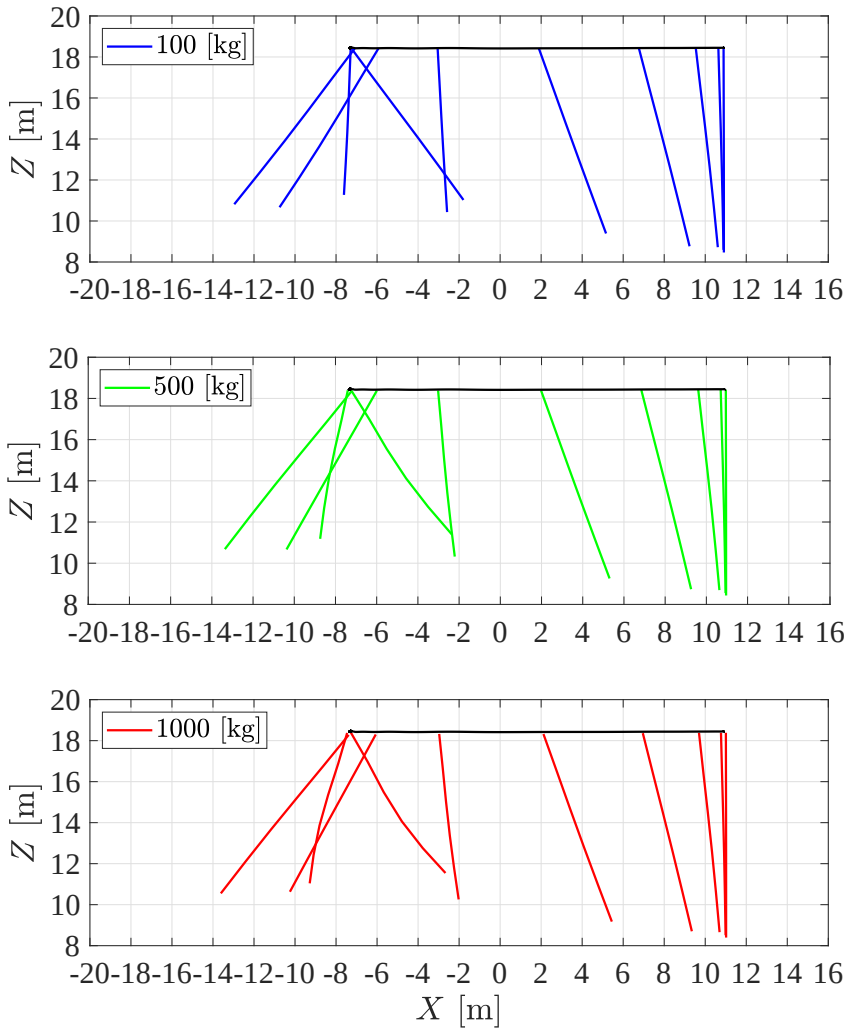

Fig. 2.5: Visual of the 10[m]-hoisted rope during the slewing motion in xz-plane

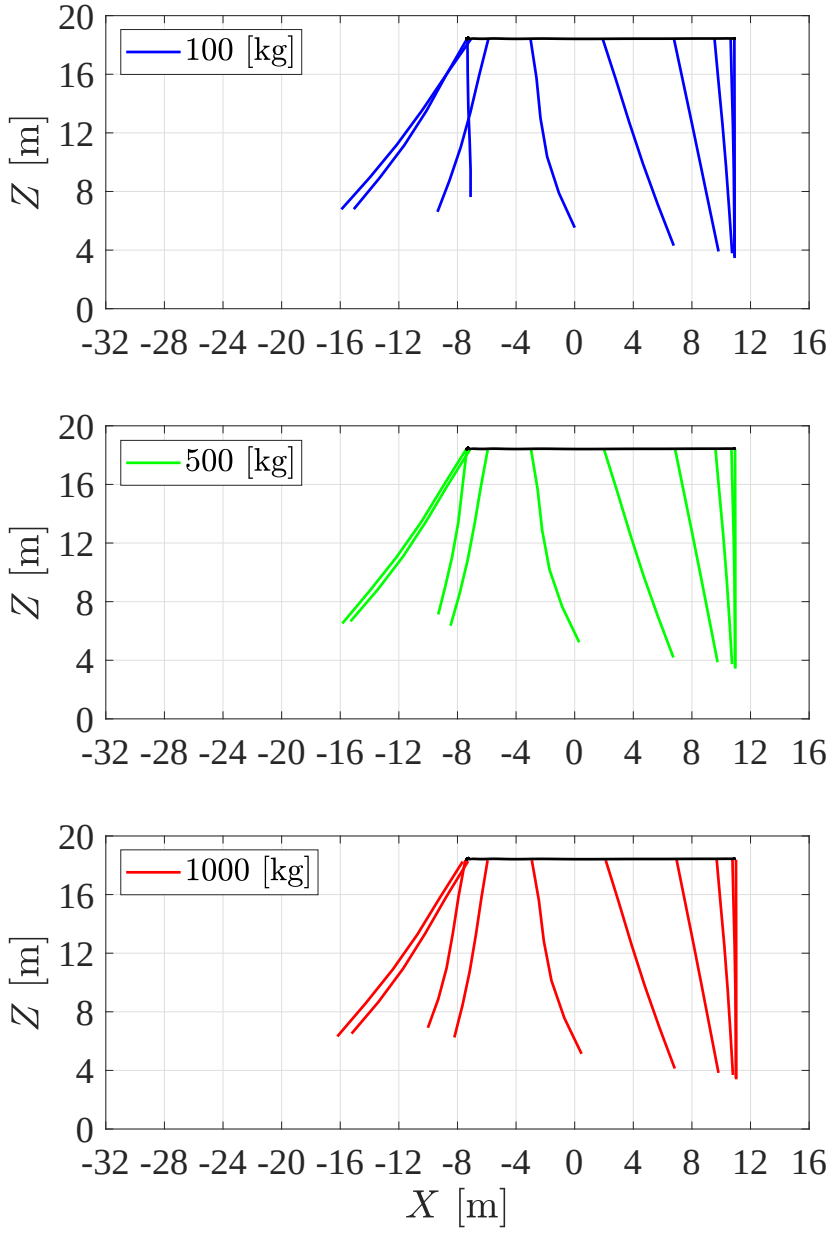

Fig. 2.6: Visual of the 15[m]-hoisted rope during the slewing motion in xz-plane

At 5[m]-rope model, the rope stayed in an almost straight line throughout the crane motion. The bending deformation of the rope was small to be observed in Fig. 2.4. When the rope length was increased to 10[m], a small bending deformation of the rope was observed during the crane motion. Then, a larger bending deformation was observed in the 15[m] rope. The deformation shape of the rope during the residual motion is shown in Figs. 2.7 to 2.9.

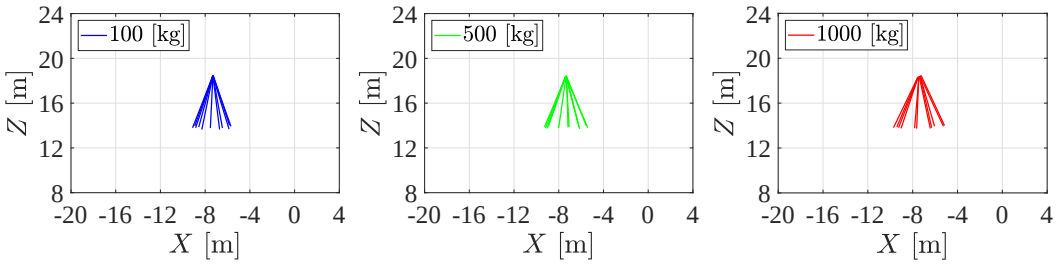

Fig. 2.7: Visual of the 5[m]-hoisted rope during the residual motion in xz-plane

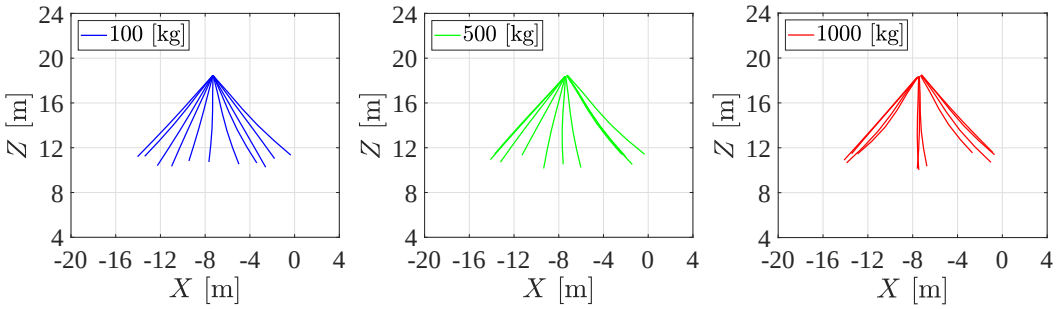

Fig. 2.8: Visual of the 10[m]-hoisted rope during the residual motion in xz-plane

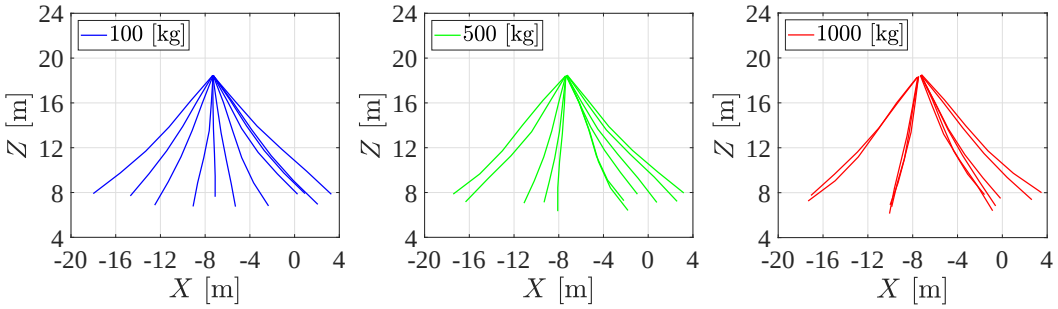

Fig. 2.9: Visual of the 15[m]-hoisted rope during the residual motion in xz-plane

From Fig. 2.7, the 5[m]-rope model showed a very small bending deformation during the residual period of the crane. In Figs. 2.8 and 2.9, the length of the rope was increased to 10[m] and 15[m], respectively. The size of the bending deformation increased and became more visible in these two cases. These deformations can be simpler shown by the time-history data.

As shown in Appendix A, the boundary condition that constrains the end of the hoisted rope and the load created a fixed-both ends cantilever beam condition for the rope model. Thus, the largest bending portion of the body was at the third node of the hoisted rope. Figures 2.10 to 2.12

show the magnitude of the deformation displacement of the third node on the hoisted rope body coordinates system while Table 2.2 summarize the average bending deformation during the entire crane motion. The results show that the bending of the rope was highest at about 0.01[m], with an average of 0.7[mm] to 0.8[mm] per 1[m] of the rope during the entire motion. At 10[m]-rope, the maximum deformation did reach 0.56[m] while the average was 19[mm] to 22[mm] per 1[m] of rope. Finally, the 15[m]-rope showed the largest deformation at 0.91[m], while the average deformation was around 30.6[mm] to 32.6[mm] per 1[m] of rope.

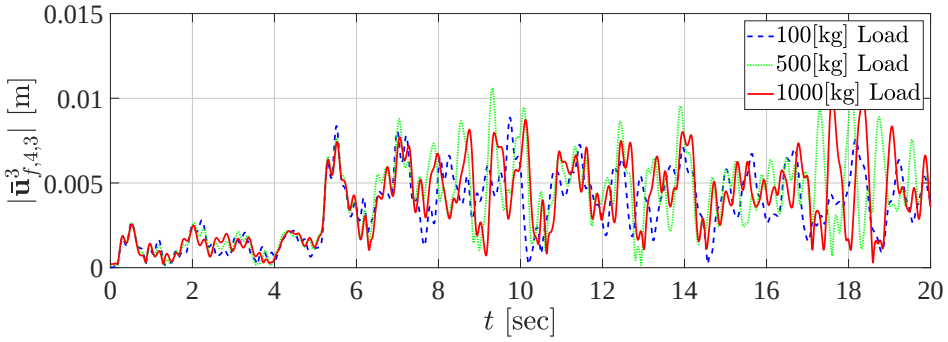

Fig. 2.10: The magnitude of the bending of the rope at 5[m] length

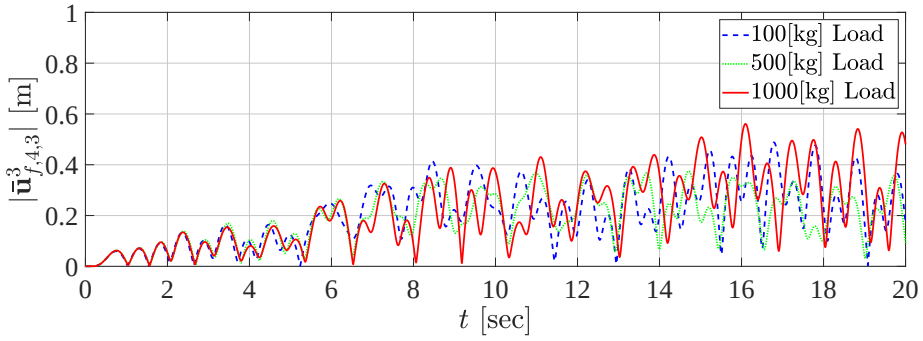

Fig. 2.11: The magnitude of the bending of the rope at 10[m] length

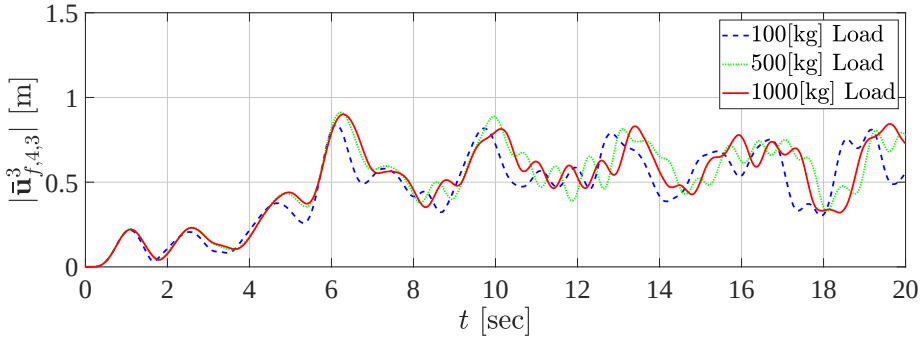

Fig. 2.12: The magnitude of the bending of the rope at 15[m] length

Table 2.2: Average bending displacement of inertia included hoisted rope model [mm] per 1[m] length of rope

Rope length	100[kg] load	500[kg] load	1000[kg] load
5[m]	0.7	0.8	0.76
10[m]	21	19	22
15[m]	30.6	32.6	32.6

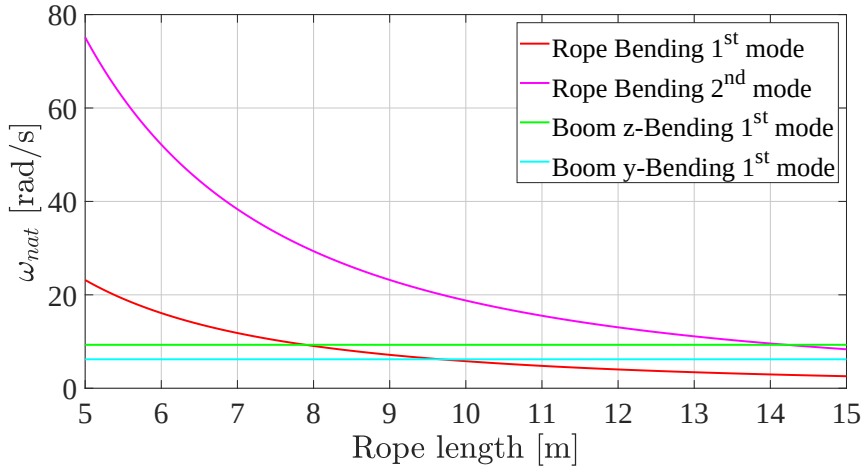

Fig. 2.13: Natural frequency of model in Appendix A

From these simulations, the size of the bending deformation increased with the length of the rope. This relation could be explained by the natural frequency of this crane structure. The natural frequency of the bending of the rope model and the flexible boom are shown in Fig. 2.13. In Fig. 2.13, the first and second modes of the bending frequency of the rope reduced as the length of the rope increased. The natural frequency of the first mode of bending deformation of the hoisted rope crossed the first bending mode of the flexible boom at a rope length of 7.8[m], while the second mode of the rope bending frequency cross the first mode of the flexible boom at 14.2[m]. Based on this observation, the boom's vibration was not strong enough to excite the bending vibration of the hoisted rope because the natural frequency of the first bending mode of 5[m] rope was 23.1[rad/s], while the boom's bending frequency was 6.2[rad/s] in the y-direction and 9.3[rad/s] in the z-direction. When the rope length was extended to 10[m], the first bending mode of the hoisted rope was decreased below the bending vibration of the flexible boom; thus, the boom could excite the bending of the hoisted rope and increased the magnitude of the bending deformation by more than approximately 20 times when the rope length was only increased twice by size. At the rope length of 15[m], the second mode of the hoisted rope's bending was lower than the bending of the boom in the z-direction. At this length, the excitation from the boom on the rope became even stronger. Thus, the average magnitude of the bending deformation was increased even further.

From the above results, it was confirmed that the inertia included rope underwent bending deformation during the crane motion. Next, this inertia included rope model was compared with the other rope's model under the same crane motion. The simulation of the flexible crane in Appendix A was conducted using the inertia included rope model, the massless flexible rope model, and the rigid rope model.

The comparison of the time-history of the hoisted load motion in x, y, and z directions are shown in Figs. 2.14 to 2.22. The rigid rope meant the rope was modeled as a massless component without flexibility, the spring rope meant the rope was modeled as a massless spring, and the beam rope meant the inertia included rope model. At 5[m] rope length, the motion of the hoisted load from all rope models showed a similar response, although the motion from the beam rope model slightly deviated from the motion of the other two models at 100[kg] load. The difference between the motion from the inertia included rope and the massless rope model was increased when the length of the rope was extended to 10[m] and 15[m] under the same mass of the hoisted load. At each length of the rope, the motion of the load from the beam rope model became closer to the motion from the other two rope models as the mass of the hoisted load was increased.

Figures 2.23 to 2.25 illustrate the trajectory of the hoisted load on the xy plane. The difference between the trajectory that was simulated with the beam rope model and the other two rope models was small at a rope length of 5[m]. It became larger as the length of the rope was increased to 10[m] and 15[m], respectively, under the 100[kg] of hoisted load. The size of this difference became smaller as the mass of the load was increased.

In addition to the different between the inertia included rope model and the massless rope model, when comparing the rigid rope and the spring rope, the motion and the trajectory of the hoisted load in all directions from both models were similar in every case from this example. It is crucial to note that these were the results under one rope's specification.

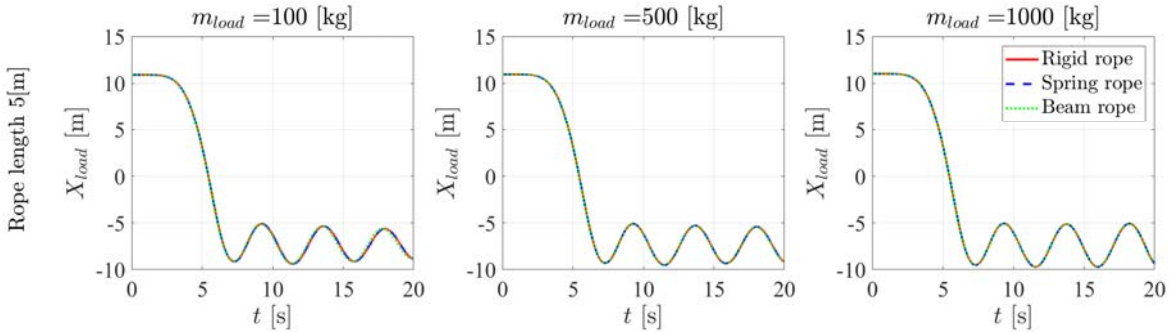

Fig. 2.14: Comparison of the time-history of the load motion in x-direction of the rope model at 5[m]

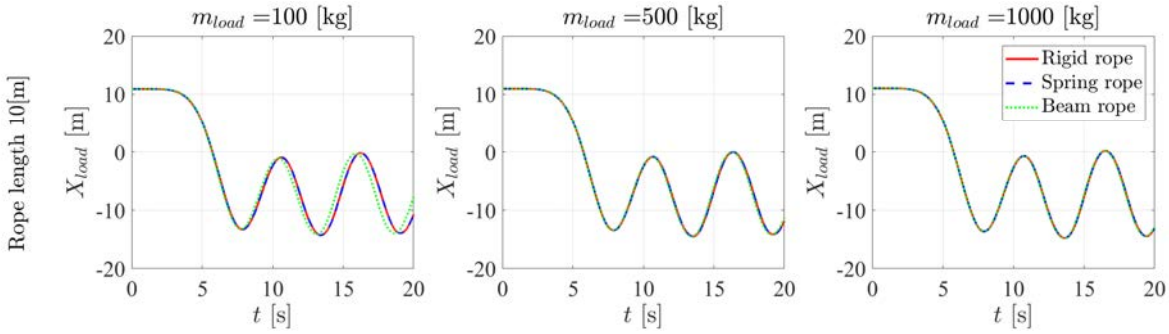

Fig. 2.15: Comparison of the time-history of the load motion in x-direction of the rope model at 10[m]

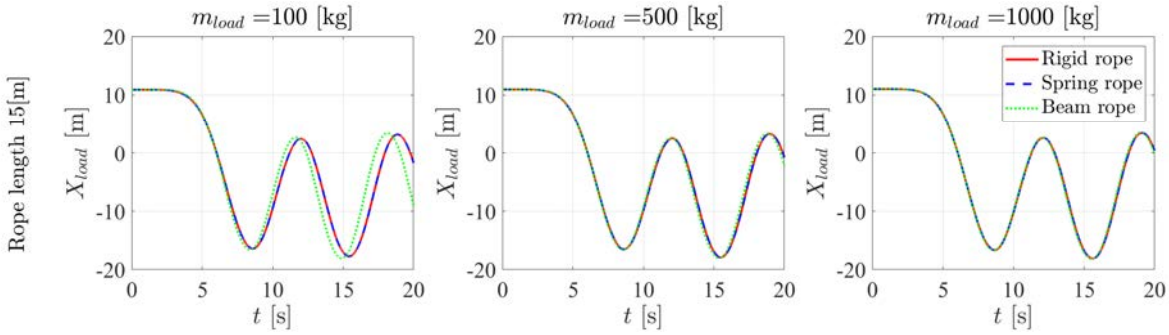

Fig. 2.16: Comparison of the time-history of the load motion in x-direction of the rope model at 15[m]

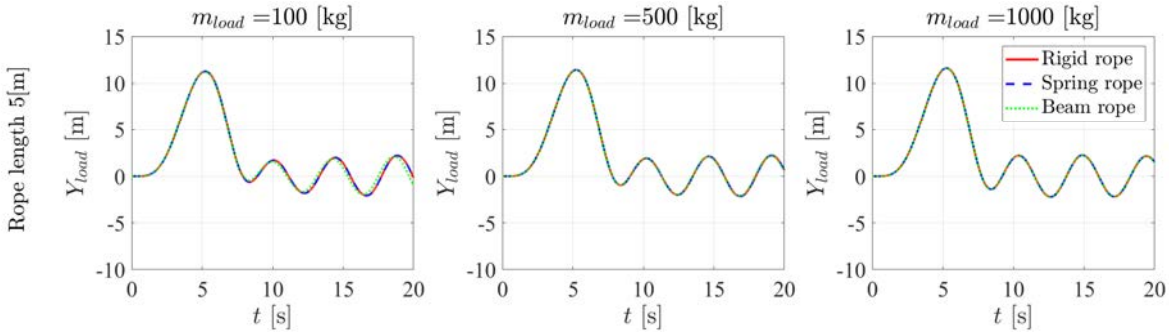

Fig. 2.17: Comparison of the time-history of the load motion in y-direction of the rope model at 5[m]

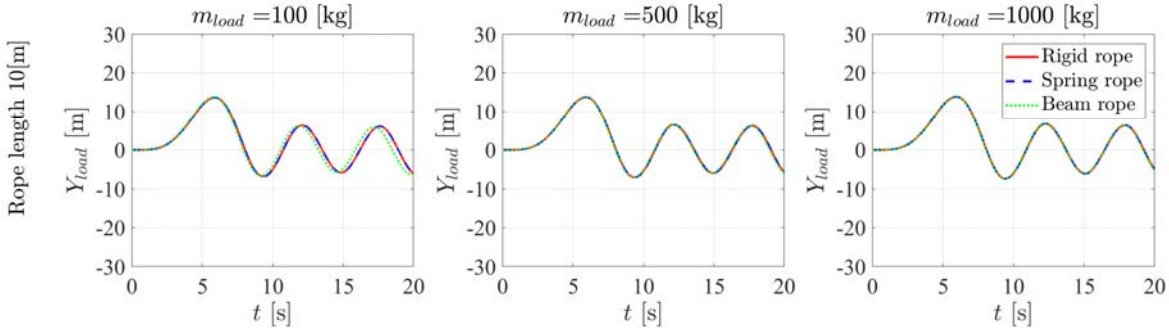

Fig. 2.18: Comparison of the time-history of the load motion in y-direction of the rope model at 10[m]

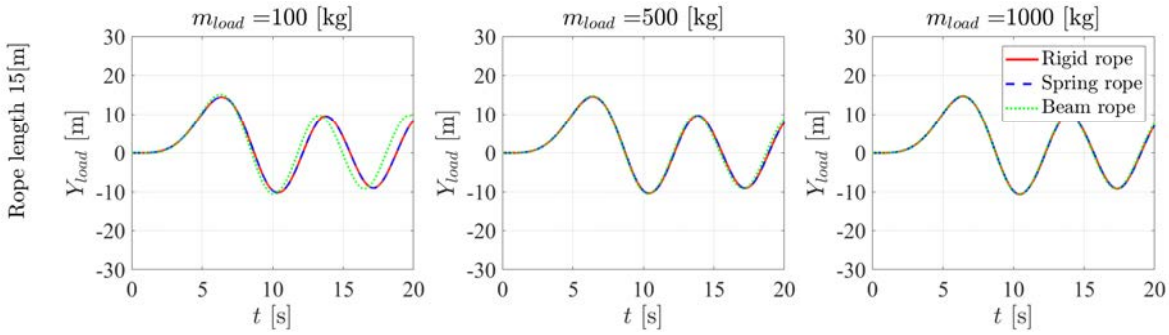

Fig. 2.19: Comparison of the time-history of the load motion in y-direction of the rope model at 15[m]

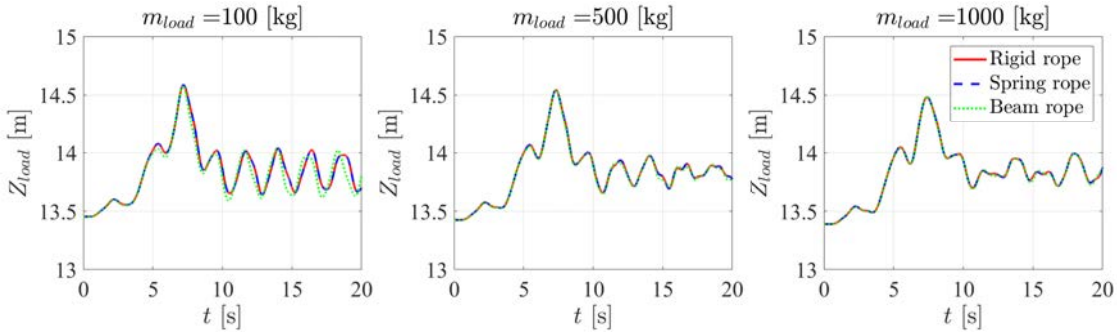

Fig. 2.20: Comparison of the time-history of the load motion in z-direction of the rope model at 5[m]

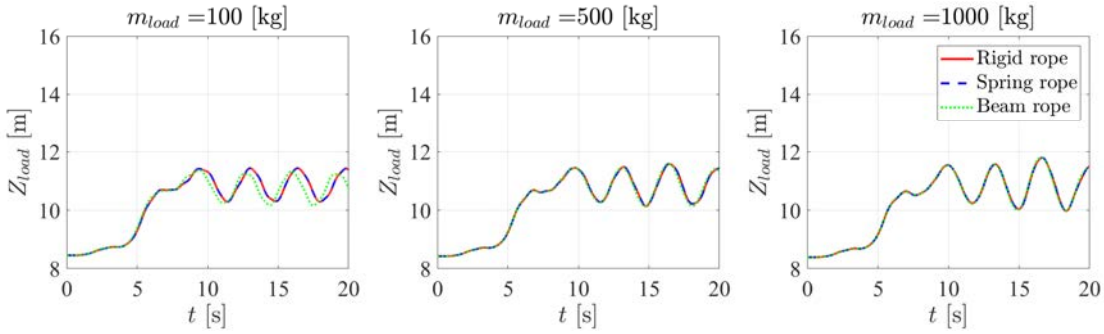

Fig. 2.21: Comparison of the time-history of the load motion in z-direction of the rope model at 10[m]

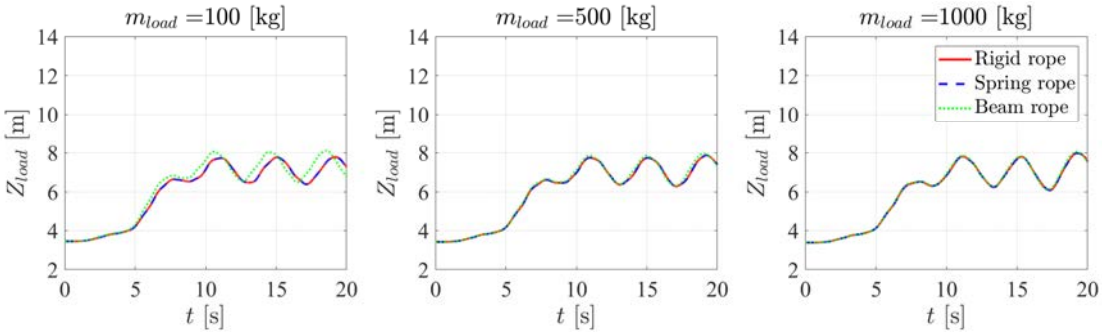

Fig. 2.22: Comparison of the time-history of the load motion in z-direction of the rope model at 15[m]

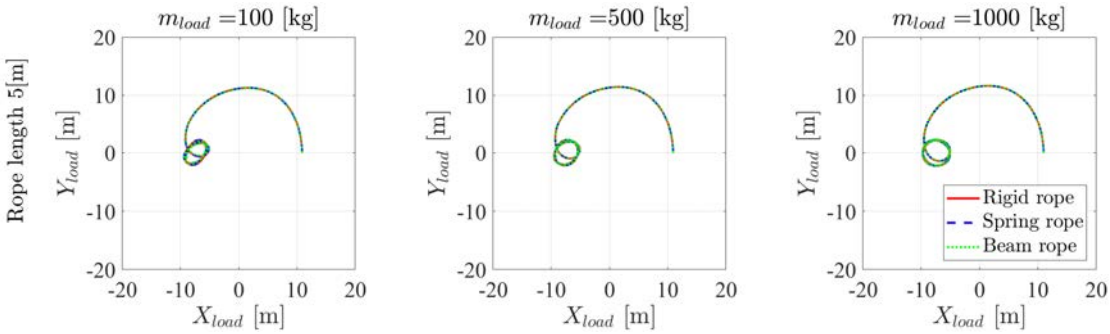

Fig. 2.23: Comparison the load trajectory on xy-plane of the rope model at 5[m]

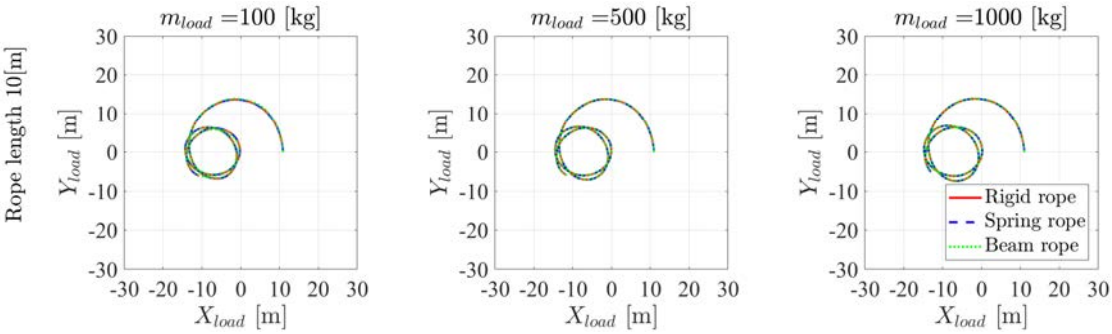

Fig. 2.24: Comparison the load trajectory on xy-plane of the rope model at 10[m]

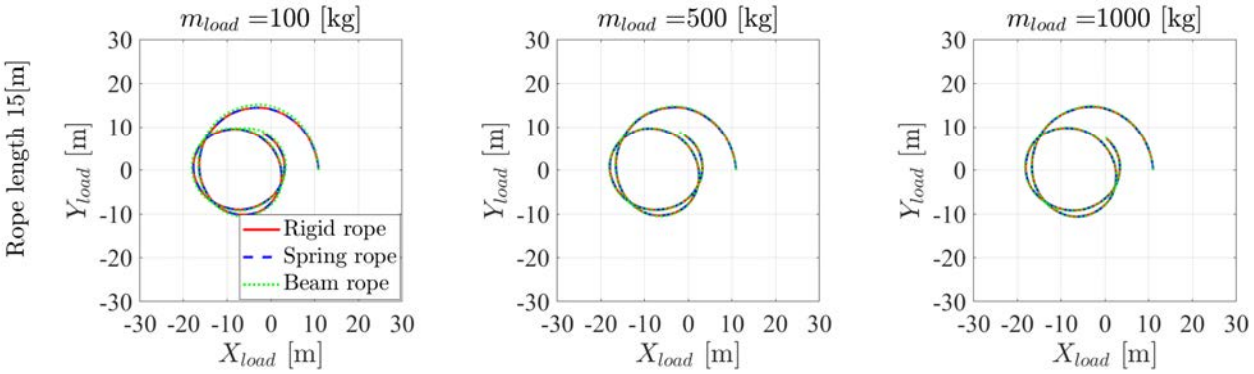

Fig. 2.25: Comparison the load trajectory on xy-plane of the rope model at 15[m]

Discussion

From these observations, the inertia included rope model presented a different motion and trajectory from the massless rope model when the light load was used. This difference increased as the length increased, while the mass of the load still stayed at a lightweight. When the mass of the load was increased, these differences became smaller. The inertia included rope model showed the different trajectory and motion of the hoisted load from the massless rope model as the length of the rope was increased due to the bending deformation and the different natural frequency of the hoisted load. When the inertia included rope was used, the natural frequency of the hoisted load changed due to the shifting of the center of gravity. Furthermore, the bending vibration of the rope increased with the rope length due to the excitation from the flexible boom. This bending vibration of the rope deviated the trajectory of the hoisted load. Therefore, the inertia included rope model calculated the different trajectory and the motion of the hoisted load when compared with the massless rope model. When the mass of the load was increased, the center of gravity was shifted toward the hoisted load, and the natural frequency of the load with the inertia included rope model became closer to the massless rope models. Although the bending vibration of the rope still existed, its impact on the load trajectory was small compared with the heavier load.

When comparing the motion of the hoisted load from the spring rope and a rigid rope, both models gave similar results. The simulations that were performed in this section were computed using the static equilibrium of the crane as the initial condition. The spring rope was already extended. Under the slewing motion, the vibration in the lateral direction of the rope was very small and did not impact the motion of the hoisted load. However, this was due to the material properties of the rope model in this example. Moreover, only slewing motion was simulated.

2.2 Flexible boom and hoisted load modeling

The formulation of the dynamic model with the relative coordinate system uses the mapping of the motion from one body to an adjacent body via the constraint equation such as joints. However, a difficulty existed at the connection between the boom and the hoisted load. The modeling assumption for the flexible crane was the flexible boom and the point mass hoisted load. The problem occurred because the point mass had only 2 DOF when it was modeled as the spherical pendulum. However, the boom had at least 6 DOF. This created a difficulty in modeling the equation of motion with the relative coordinate system because there was not enough DOF to map the coordinates. Therefore, the modeling procedure for the flexible boom and the point mass hoisted load was proposed.

2.2.1 Flexible boom model

Firstly, the flexible boom model is discussed. The flexible boom was modeled with the finite element Euler-Bernoulli's beam model. The FFRF was the main formulation for modeling the flexible dynamic model of the boom. The schematic of the flexible boom is shown in Fig. 2.26. An arbitrary point P on this body was specified from the global coordinate system by the position vector $\mathbf{r}_P$, where $\mathbf{u}_{i,P}$ is the position vector from the origin of the body-i's coordinates system to point P. The vector is viewed on the global coordinate system.

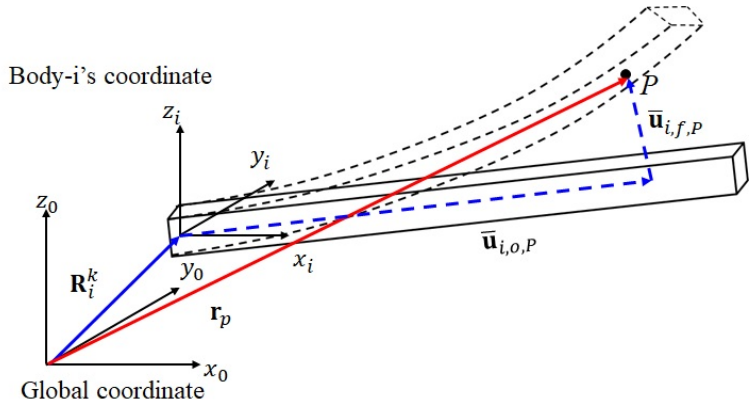

Fig. 2.26: The flexible beam model

$$\mathbf{r}_P = \mathbf{R}_i + \mathbf{u}_{i,P} \tag{2.16}$$

$$\mathbf{u}_{i,P} = \mathbf{u}_{i,o,P} + \mathbf{u}_{i,f,P} = \mathbf{A}_i\bar{\mathbf{u}}_{i,o,P} + \mathbf{A}_i\bar{\mathbf{u}}_{i,f,P} \tag{2.17}$$

In Fig. 2.26, $\mathbf{u}_{i,o,P}$ is the position vector from the origin of the body-i's coordinate system to point P before undergoing deformation, and $\mathbf{u}_{i,f,P}$ is the deformation displacement vector at point P. These vectors were lied on the global coordinate system. Its definition is same as in Section 2.1.1; thus, the displacement vector $\bar{\mathbf{u}}_{i,f,P}$ was calculated using Eqs. (2.2) and (2.3).

2.2.2 Hoisted load model

Next, the modeling of the hoisted load is discussed. As explained earlier, the formulation of the equation of motion with the relative coordinate system was performed by mapping the constraint equation between two adjacent bodies. As the results, the motion of each body was expressed in form of the motion from the adjacent body. However, the boom and the hoisted load had different DOF. The main difference that contributed to the problem was the rotation. In the case of rigid body boom, it had 3 DOF from rotational motion. In the case of the flexible boom, additional rotational DOF appeared from the bending and torsional deformation. These deformations were considered as the successive rotation of the body coordinate system. However, the point-mass hoisted load had only translational motion. When it was modeled into the spherical pendulum, the DOF was 2. It became a difficulty in derivation to map the two rotations with three rotations. Thus, in this research, the hoisted load was modeled as an additional particle of the boom, as shown in Fig. 2.27. The hoisted load was extended from the tip of the boom with the rope vector $\mathbf{d}_{rope}$.

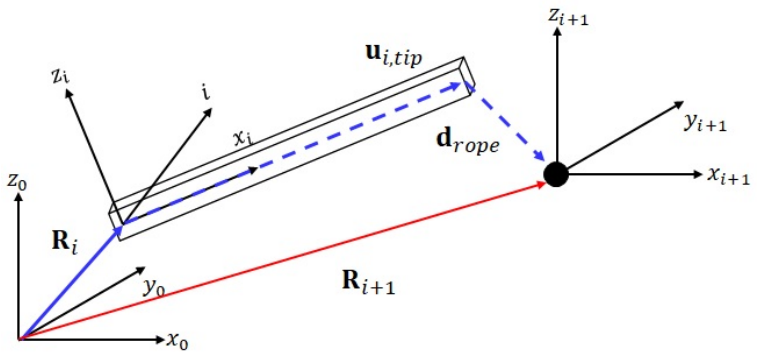

Fig. 2.27: The hoisted load on the boom model

The position vector of the hoisted load (body-(i+1)) was calculated from the flexible boom model (body-i) as

$$\mathbf{R}_{i+1} = \mathbf{R}_i + \mathbf{u}_{i,tip} + \mathbf{d}_{rope}, \tag{2.18}$$

where

$$\mathbf{d}_{rope} = \mathbf{A}_2 \bar{\mathbf{d}}_{rope}. \tag{2.19}$$

$\bar{\mathbf{d}}_{rope}$ is the rope vector on the boom's coordinate systems. The equation of motion of the flexible boom and the hoisted load was calculated via the virtual work theory as

$$\delta W = \int_{\mathbb{V}_i} \delta \mathbf{r}_i^T \left(\rho_i \ddot{\mathbf{r}}_i - \mathbf{f}_i\right) \mathrm{d}\mathbb{V} + \delta \mathbf{R}_{i+1}^T \left(m_{i+1} \ddot{\mathbf{R}}_{i+1} - \mathbf{f}_{i+1}\right) = \delta \mathbf{q}_{(i)-(i+1)}^T \left(\mathbf{M}_{(i)-(i+1)} \dot{\mathbf{V}}_{(i)-(i+1)} - \mathbf{Q}_{(i)-(i+1)}\right), \tag{2.20}$$

where

$$\mathbf{M}_{(i)-(i+1)} \dot{\mathbf{V}}_{(i)-(i+1)} = \mathbf{Q}_{(i)-(i+1)}, \tag{2.21}$$

is the equation of motion from the flexible boom to the hoisted load. The subscription $i-j$ referred to as the vectors or matrices were already considered body-i to j (i and j did not have to be adjacent bodies). $\mathbf{M}_{(i)-(i+1)} = \mathbf{M}_i + \mathbf{M}_{i+1}$ is the total mass-inertia matrix of the flexible boom, $\mathbf{M}_i$, and the hoisted load, $\mathbf{M}_{i+1}$.

$$\mathbf{M}_i = \rho_i \int_{\mathbb{V}_i} \begin{bmatrix} \mathbf{I}_{3\times3} & -\tilde{\mathbf{u}}_i & \mathbf{A}_i\mathbf{S}_i & \mathbf{0} \\ -\tilde{\mathbf{u}}_i^T & \tilde{\mathbf{u}}_i^T\tilde{\mathbf{u}}_i & -\mathbf{A}_i\tilde{\tilde{\mathbf{u}}}_i^T\mathbf{S}_i & \mathbf{0} \\ \mathbf{S}_i^T\mathbf{A}_i^T & -\mathbf{S}_i^T\tilde{\mathbf{u}}_i\mathbf{A}_i^T & \mathbf{S}_i^T\mathbf{S}_i & \mathbf{0} \\ \mathbf{0} & \mathbf{0} & \mathbf{0} & \mathbf{0} \end{bmatrix} \mathrm{d}\mathbb{V}, \tag{2.22}$$

$$\mathbf{M}_{i+1} = m_{i+1}\mathbf{D}_{(i+1)(i)}^T\mathbf{D}_{(i+1)(i)}, \tag{2.23}$$

where

$$\mathbf{D}_{(i+1)(i)} = \begin{bmatrix} \mathbf{I} & -\tilde{\mathbf{u}}_{i,tip} & \mathbf{A}_i\mathbf{S}_{i,tip} & \mathbf{A}_i\mathbf{L}_{(i+1)(i)} \end{bmatrix}, \tag{2.24}$$

in which $\mathbf{L}_{(i+1)(i)} = \dfrac{\partial\bar{\mathbf{d}}_{rope}}{\partial\bar{\mathbf{q}}_{(i+1)(i)}}$, and $\bar{\mathbf{q}}_{(i+1)(i)}$ is the vector of the generalized coordinates of the hoisted load. m_{i+1} is the mass of the hoisted load.

It is important to choose the appropriate rotation angles to express the rotation of the hoisted load. The spherical pendulum could be modeled as in Fig. 2.28. These angles were used in the model by [35, 36]. However, the rotation $\bar{\phi}$ only existed when the angle from the z-axis $\bar{\theta}$ was not zero. Therefore, these rotations were valid only after the motion had begun. If the crane stayed at rest position, and the hoisted load was hung down vertically, the equation of motion would reach the singularity point of the motion. Therefore, the equation of motion of the crane could not calculate the motion from the rested position unless an additional assumption was applied. Thus, these rotation angles were unsuitable for the rotary crane model.

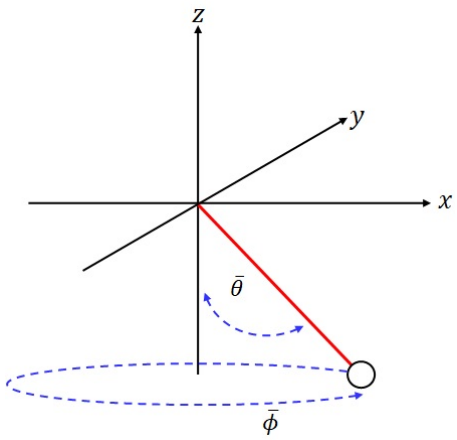

Fig. 2.28: The rotation of the point-mass load in spherical pendulum motion

To avoid this problem, the modeling of the hoisted load on the crane model by employing the rotation angles around the x and y axes of the boom, as shown in Fig. 2.29, was proposed. In

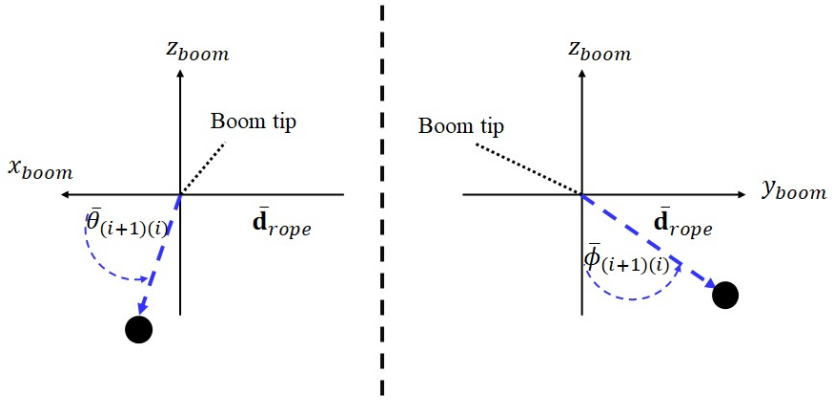

Fig. 2.29: The model of the rope vector

Fig. 2.29, $\bar{\phi}_{(i+1)(i)}$ and $\bar{\theta}_{(i+1)(i)}$ were the rotation angles around x_i and y_i axes, respectively. These angles were the relative angles to the boom's coordinate system. These rotation angles were able to avoid the singularity problem in the model when the crane was at a rested position and the hoisted load was hung down vertically from the boom tip because both rotation angles were independent of each other. The rope vector on body-i coordinate system, $\bar{\mathbf{d}}_{rope}$, was calculated as,

$$\bar{\mathbf{d}}_{rope} = \begin{bmatrix} -\ell \cos\left(\bar{\phi}_{(i+1)(i)}\right) \sin\left(\bar{\theta}_{(i+1)(i)}\right) \\ \ell \sin\left(\bar{\phi}_{(i+1)(i)}\right) \\ -\ell \cos\left(\bar{\phi}_{(i+1)(i)}\right) \cos\left(\bar{\theta}_{(i+1)(i)}\right) \end{bmatrix}, \tag{2.25}$$

where ℓ is the rope's length.

By using the boom and hoisted load model that was derived in this section, the equation of motion of the rotary crane in the relative coordinate system formulation could be derived. This modeling was not valid for only the flexible boom but also the rigid boom as well. In the case of the rigid boom, the flexible term was omitted and the modeled was formulated by following the same procedure.

2.3 AMI model reduction on the flexible rotary crane

In this section, the development of the efficient dynamics model of the flexible crane is discussed. This research developed a dynamic model of a flexible rotary crane that could calculate the motion in a short time. In this development, the model reduction method of the Adaptive Modal Integration (AMI)[29] was applied. The primary concept of the AMI was the accounting of the time derivative of the mode shape during the simulation, as shown in Eqs. (2.26) to (2.28).

$$\Delta \mathbf{q} \approx \mathbf{\Phi} \boldsymbol{\eta}, \tag{2.26}$$

$$\Delta \dot{\mathbf{q}} \approx \mathbf{\Phi} \dot{\boldsymbol{\eta}} + \dot{\mathbf{\Phi}} \boldsymbol{\eta}, \tag{2.27}$$

$$\Delta\ddot{\mathbf{q}} \approx \boldsymbol{\Phi}\ddot{\boldsymbol{\eta}} + 2\dot{\boldsymbol{\Phi}}\dot{\boldsymbol{\eta}} + \ddot{\boldsymbol{\Phi}}\boldsymbol{\eta}, \tag{2.28}$$

where the matrix of mode shapes, $\boldsymbol{\Phi}$, was formed via interpolation.

To form the interpolation, the mode shapes along the interesting configuration were precalculated. In the work by Aarts and Jonker[29], the trajectory was selected, and the motion was specified. The precalculated mode shapes were calculated along this trajectory. The velocity and acceleration were included in the modal analysis. This limited the use of the model to a specific motion because the mode shapes were the function of the configuration, velocity, and acceleration. Although it could calculate more mode shapes at different velocities and accelerations, the interpolation would become more complex because it increased the dimension of the interpolated data. This research modified the procedure in the derivation of the reduced dynamic model with the AMI method so that the model was usable for an arbitrary driving motion.

2.3.1 Configuration discretization and linearization

First, the discretization and linearization of the motion were performed. For the rotary crane model with the equation of motion that was written as in Eq. (2.29), the movable configuration was determined by the slewing angle ψ_{in} and the lifting angle θ_{in}.

$$\mathbf{F} = \mathbf{M}\dot{\mathbf{v}} - \mathbf{Q} + \mathbf{M}_r\ddot{\mathbf{q}}_r + \boldsymbol{\Gamma}_r = \mathbf{0}. \tag{2.29}$$

where $\bar{\mathbf{q}}_r = \begin{bmatrix}\psi_{in} & \theta_{in}\end{bmatrix}^T$. Suppose that Fig. 2.30 represents the configuration plane of the rotary crane model.

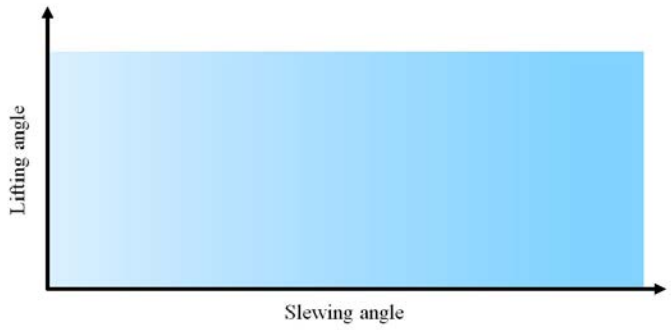

Fig. 2.30: The configuration plane of the rotary crane

Every point on this plane was a movable configuration of the crane. Within this movable configuration of the crane, the slewing and lifting angles were discretized into M and N points, respectively, as shown in Fig. 2.31. Then, the linearization was performed at each configuration.

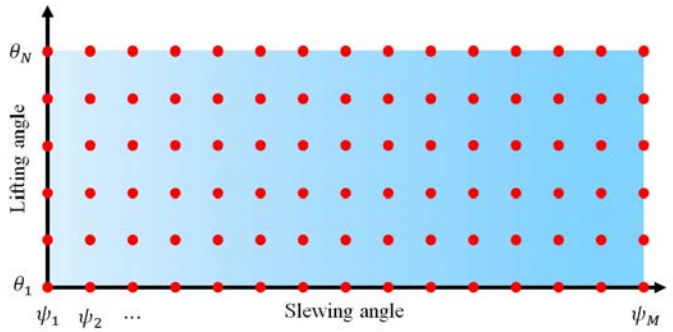

Fig. 2.31: The configuration plane of the rotary crane with the discretization

In the linearization, the approximation for the vector of the generalized coordinates, $\mathbf{q}$, was

$$\mathbf{q} = \mathbf{q}_0 + \Delta\mathbf{q}, \tag{2.30}$$

where $\mathbf{q}_0$ is the vector of the generalized coordinates at the rigid body state or nonvibrational state, and $\Delta\mathbf{q}$ is the vector of the small deformation or the vibration around that rigid body state. $\mathbf{X} = \begin{bmatrix}\mathbf{q}^T & \dot{\mathbf{q}}^T & \ddot{\mathbf{q}}^T\end{bmatrix}^T$ was defined as the state-vector of the equation of motion. At each configuration $m = 1, 2, ...M$ and $n = 1, 2, ...N$, the equation of motion was linearized around the rigid body state $\mathbf{X}_0^{m,n} = \begin{bmatrix}(\mathbf{q}_0^{m,n})^T & \mathbf{0} & \mathbf{0}\end{bmatrix}^T$. The result of the linearization can be written as

$$\begin{aligned}\mathbf{F}^{m,n} \approx & \mathbf{F}_0^{m,n} + \left.\frac{\partial \mathbf{F}}{\partial \mathbf{X}}\right|(\mathbf{X} - \mathbf{X}_0^{m,n}), \\ \approx & \mathbf{M}_0^{m,n}\Delta\ddot{\mathbf{q}} + \mathbf{D}_0^{m,n}\Delta\dot{\mathbf{q}} + \mathbf{K}_0^{m,n}\Delta\mathbf{q} - \mathbf{Q}_0^{m,n} + \mathbf{M}_{r,0}^{m,n}\Delta\ddot{\mathbf{q}}_r + \mathbf{\Gamma}_{r,0}^{m,n}.\end{aligned} \tag{2.31}$$

In Eq. (2.31), the matrices and vectors with subscription "0" mean the properties were calculated at rigid body state. It is important to note that the driving velocity, $\dot{\mathbf{q}}_r$, and acceleration, $\ddot{\mathbf{q}}_r$, were not substituted in this step. Only the configuration $\mathbf{q}_r$ was substituted in the linearization. As the results, the linearized damping matrix $\mathbf{D}_0^{m,n}$, stiffness matrix $\mathbf{K}_0^{m,n}$, the constraint inertia matrix $\mathbf{M}_{r,0}^{m,n}$ and the residual of the constraint inertia $\mathbf{\Gamma}_{r,0}^{m,n}$ at any configuration (m,n) became the explicit function of the $\dot{\mathbf{q}}_r$ and $\ddot{\mathbf{q}}_r$. This helped the reduced model to be able to calculate with an arbitrary motion later.

2.3.2 Forming of the modal reduction matrix

After the linearization, the mode shape at each configuration was calculated through the modal analysis. In this model reduction, the unwanted mode shapes were omitted, and the motion was approximated by using only a few numbers of the selected modes. Conventionally, the modes with high frequency are omitted. For the flexible mechanism, the velocity stiffens the structure; thus, the natural frequencies change with the velocity of the motion. Therefore, it is understandable to calculate the mode shapes by including this effect. In the original work[29], the specific motion and path was selected. Then, the discretization and modal analysis were performed along this path. This included the motion's velocity and acceleration. Thus, the interpolation of the mode shapes was the multivariable function of the configuration, the driving velocity and the driving

acceleration. To form the interpolation, the information of all configurations at many sets different of driving velocity and acceleration was required. Otherwise, the interpolation was restricted to a specific motion. This limited the use of the model. If the velocity and acceleration are considered in the interpolation, the function becomes more complex and requires more precalculated data. Thus, the modeling criteria, which extended the use of the reduced model to an arbitrary motion by calculating the mode shapes at the static condition, as described in Eq. (2.32), was proposed.

$$\left(\mathbf{K}_{0,static}^{m,n} - (\omega_{nat,k}^{m,n})^2 \mathbf{M}_0^{m,n}\right) \hat{\boldsymbol{\phi}}_k^{m,n} = 0 \tag{2.32}$$

In Eq. (2.32), the stiffness matrix $\mathbf{K}_{0,static}^{m,n}$ was calculated by substituting $\dot{\mathbf{q}}_r = \ddot{\mathbf{q}}_r = \mathbf{0}$ into $\mathbf{K}_0^{m,n}$ from Eq. (2.31). By using the mode shapes at static condition, the effect of the geometric stiffening from the mechanism's velocity was neglected. Although the reduced model lost the dynamics from the geometric stiffening, the reduced model was no longer restricted to the specific velocity or acceleration.

After calculating the mode shapes at each configuration, the modal reduction matrix was formed by selecting low frequency modes such that

$$\boldsymbol{\Phi}^{m,n} = \begin{bmatrix} \hat{\boldsymbol{\phi}}_1^{m,n} & \hat{\boldsymbol{\phi}}_2^{m,n} & \dots & \hat{\boldsymbol{\phi}}_p^{m,n} \end{bmatrix}, \tag{2.33}$$

where p is the number of the modes that were selected from the total P DOF ($p < P$). In the rotary crane model, the number of the selected modes was considered from the possible movable directions of the crane. These directions were two rotation angles of the hoisted load, three translational deformations of the boom tip, two bending deformations of the boom tip, and one torsional deformation of the boom tip. In the case of the mobile crane that had the chassis with the flexible outriggers, an additional 6 DOF were included.

The model reduction was performed by substituting Eqs. (2.26) to (2.28) into the linearized equation (2.31) and multiply the modal matrix $\boldsymbol{\Phi}^T$ to the left side of the equation. The reduced equation of motion at each configuration can be written as follows;

$$\mathbf{M}_\eta^{m,n}\ddot{\boldsymbol{\eta}} + \mathbf{D}_\eta^{m,n}\dot{\boldsymbol{\eta}} + \mathbf{K}_\eta^{m,n}\boldsymbol{\eta} + \mathbf{M}_{\eta,r}^{m,n}\ddot{\mathbf{q}}_r + \boldsymbol{\Gamma}_{\eta,r}^{m,n} - \mathbf{Q}_\eta^{m,n} = \mathbf{0} \tag{2.34}$$

Where

$$\mathbf{M}_\eta^{m,n} = (\boldsymbol{\Phi}^{m,n})^T \mathbf{M}_0^{m,n} \boldsymbol{\Phi}^{m,n}, \tag{2.35}$$

$$\mathbf{D}_\eta^{m,n} = (\boldsymbol{\Phi}^{m,n})^T \mathbf{D}_0^{m,n} \boldsymbol{\Phi}^{m,n} + 2(\boldsymbol{\Phi}^{m,n})^T \mathbf{M}_0^{m,n} \dot{\boldsymbol{\Phi}}^{m,n}, \tag{2.36}$$

$$\mathbf{K}_\eta^{m,n} = (\boldsymbol{\Phi}^{m,n})^T \mathbf{K}_0^{m,n} \boldsymbol{\Phi}^{m,n} + (\boldsymbol{\Phi}^{m,n})^T \mathbf{D}_0^{m,n} \dot{\boldsymbol{\Phi}}^{m,n} + (\boldsymbol{\Phi}^{m,n})^T \mathbf{M}_0^{m,n} \ddot{\boldsymbol{\Phi}}^{m,n}, \tag{2.37}$$

$$\mathbf{Q}_\eta^{m,n} = (\boldsymbol{\Phi}^{m,n})^T \mathbf{Q}_0^{m,n}, \tag{2.38}$$

$$\mathbf{M}_{\eta,r}^{m,n} = (\boldsymbol{\Phi}^{m,n})^T \mathbf{M}_{r,0}^{m,n}, \tag{2.39}$$

$$\mathbf{\Gamma}_{\eta,r}^{m,n} = (\mathbf{\Phi}^{m,n})^T \mathbf{\Gamma}_{r,0}^{m,n}. \tag{2.40}$$

The motion was calculated by solving Eq. (2.34) for the vector of the generalized modal coordinates, $\boldsymbol{\eta}$. To transform the modal coordinates motion back to physical coordinate motion, the mode-acceleration method[49] in Eq. (2.41) was used.

$$\Delta\mathbf{q} \approx \mathbf{K}_0^{-1} \left(\mathbf{Q}_0 - \mathbf{M}_0 \Delta\ddot{\mathbf{q}} - \mathbf{D}_0 \Delta\dot{\mathbf{q}} - \mathbf{M}_{r,0} \ddot{\bar{\mathbf{q}}}_r - \mathbf{\Gamma}_{r,0} \right) \tag{2.41}$$

When solving Eqs. (2.34) and (2.41), the matrices $\mathbf{M}_0$, $\mathbf{\Phi}$ and $\mathbf{M}_\eta^{-1}$ could be precalculated since they were only function of the configuration ($\bar{\mathbf{q}}_r$). These matrices were precalculated before the simulation, and were interpolated during the simulation. This shows the reason of using the mode shape at static conditions. If the mode shapes were calculated at dynamics condition as in the original work, the interpolation must also perform with variated velocity and acceleration which complicate the calculation.

2.3.3 Interpolation

In this research, two interpolation functions were used for comparison: 1) the piecewise bilinear function, and 2) the radial basis function (RBF).

2.3.3.1 Piecewise Bilinear Interpolation

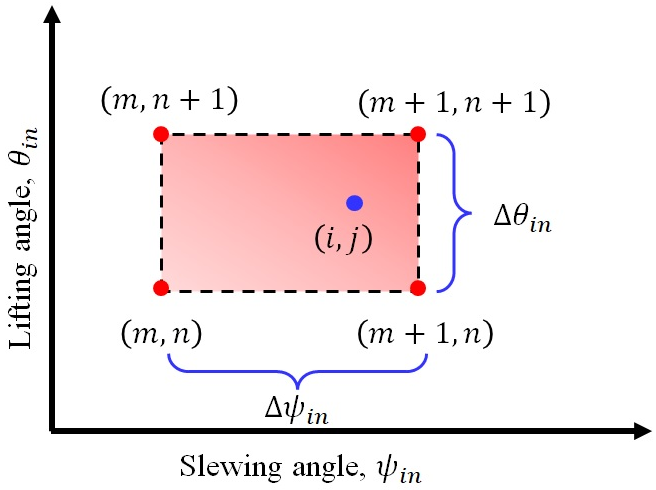

Fig. 2.32: Piecewise bilinear interpolation

The piecewise bilinear function interpolated the matrices between four points as shown in Fig. 2.32. Any matrix $\mathbf{U}$ at any configuration (i, j) was calculated using

$$\begin{aligned} \mathbf{U}(\psi_{in}^i, \theta_{in}^j) =& \mathbf{U}^{m,n} + (\mathbf{U}^{m+1,n} - \mathbf{U}^{m,n}) \frac{\psi_{in}^i - \psi_{in}^m}{\Delta\psi_{in}} + (\mathbf{U}^{m,n+1} - \mathbf{U}^{m,n}) \frac{\theta_{in}^i - \theta_{in}^m}{\Delta\theta_{in}} \\ &+ (\mathbf{U}^{m+1,n+1} - \mathbf{U}^{m+1,n} - \mathbf{U}^{m,n+1} + \mathbf{U}^{m,n}) \frac{(\psi_{in}^i - \psi_{in}^m)(\theta_{in}^i - \theta_{in}^m)}{\Delta\psi_{in}\Delta\theta_{in}} \end{aligned}. \tag{2.42}$$

The time-derivative of the modal matrices under the piecewise bilinear interpolation was calculated as follows;

$$\begin{aligned}\dot{\mathbf{\Phi}} &= (\mathbf{\Phi}^{m+1,n}-\mathbf{\Phi}^{m,n})\frac{\dot{\psi}_{21}}{\Delta\psi_{21}}+(\mathbf{\Phi}^{m,n+1}-\mathbf{\Phi}^{m,n})\frac{\dot{\theta}_{32}}{\Delta\theta_{32}} \\ &\quad +\left(\mathbf{\Phi}^{m+1,n+1}-\mathbf{\Phi}^{m+1,n}-\mathbf{\Phi}^{m,n+1}+\mathbf{\Phi}^{m,n}\right)\frac{\dot{\psi}_{21}(\theta_{32}-\theta_{32}^{n})+\dot{\theta}_{32}(\psi_{21}-\psi_{21}^{m})}{\Delta\psi_{21}\Delta\theta_{32}}\end{aligned} \tag{2.43}$$

$$\begin{aligned}\ddot{\mathbf{\Phi}} &= (\mathbf{\Phi}^{m+1,n}-\mathbf{\Phi}^{m,n})\frac{\ddot{\psi}_{21}}{\Delta\psi_{21}}+(\mathbf{\Phi}^{m,n+1}-\mathbf{\Phi}^{m,n})\frac{\ddot{\theta}_{32}}{\Delta\theta_{32}} \\ &\quad +\left(\mathbf{\Phi}^{m+1,n+1}-\mathbf{\Phi}^{m+1,n}-\mathbf{\Phi}^{m,n+1}+\mathbf{\Phi}^{m,n}\right)\left\{\frac{\ddot{\psi}_{21}(\theta_{32}-\theta_{32}^{n})+\ddot{\theta}_{32}(\psi_{21}-\psi_{21}^{m})}{\Delta\psi_{21}\Delta\theta_{32}}\right. \\ &\quad \left.+2\frac{\dot{\psi}_{21}\dot{\theta}_{32}}{\Delta\psi_{21}\Delta\theta_{32}}\right\}\end{aligned} \tag{2.44}$$

2.3.3.2 Radial basis function

In contrast to the Piecewise bilinear function, the RBF interpolation used the entire existing data to form the one interpolating function. The matrix $\mathbf{U}$ at configuration (i,j) was calculated using

$$\mathbf{U}(\psi_{in}^{i},\theta_{in}^{j})=\mathbf{U}(\bar{\mathbf{q}}_r^{k})=\sum_{k=1}^{M\times N}\mathbf{W}_k\beta_k(\bar{\mathbf{q}}_r^{k}), \tag{2.45}$$

where

$$\beta_k(\bar{\mathbf{q}}_r)=exp\left(-\frac{\left\|\bar{\mathbf{q}}_r-\bar{\mathbf{q}}_r^{k}\right\|}{2\sigma}\right) \tag{2.46}$$

is the Gaussian's basis function, and $\mathbf{W}$ is the weighted matrix. The weighted matrix was calculated through the least square error estimation [50] as follows;

$$\mathbf{W}_k=\sum_{l=1}^{M\times N}[\mathbf{H}]_{k,l}\,\mathbf{U}_k \tag{2.47}$$

$$\mathbf{H}=(\mathbf{B}^T\mathbf{B}+\lambda\mathbf{I})^{-1}\mathbf{B}^T \tag{2.48}$$

$$\mathbf{B}=\begin{bmatrix}\beta_1(\mathbf{q}_r^1) & \beta_2(\mathbf{q}_r^1) & \cdots & \beta_{M\times N}(\mathbf{q}_r^1)\\ \beta_1(\mathbf{q}_r^2) & \beta_2(\mathbf{q}_r^2) & \cdots & \beta_{M\times N}(\mathbf{q}_r^2)\\ \vdots & \vdots & \ddots & \vdots\\ \beta_1(\mathbf{q}_r^{M\times N}) & \beta_2(\mathbf{q}_r^{M\times N}) & \cdots & \beta_{M\times N}(\mathbf{q}_r^{M\times N})\end{bmatrix} \tag{2.49}$$

where λ is the regularization parameter.

Since the weighted matrices were the constant matrices, the time-derivative of the modal matrices with the RBF interpolation were calculated as follows;

$$\dot{\mathbf{\Phi}}\left(\mathbf{q}_r, \dot{\mathbf{q}}_r\right) = \sum_{i=1}^{M\times N} \mathbf{W}_i \frac{\partial}{\partial t}\beta_i(\mathbf{q}_r) \tag{2.50}$$

$$\dot{\mathbf{\Phi}}\left(\mathbf{q}_r, \dot{\mathbf{q}}_r, \ddot{\mathbf{q}}_r\right) = \sum_{i=1}^{M\times N} \mathbf{W}_i \frac{\partial^2}{\partial t^2}\beta_i(\mathbf{q}_r) \tag{2.51}$$

2.3.4 Numerical simulation on the reduced model

To validate the efficiency of the developed model reduction, the numerical analysis on the mobile-type rotary crane model in Appendix B was performed. The physical specification of this mobile crane model is shown in Table 2.3. The simulations were conducted using several input acceleration patterns. The calculation time between the reference model (nonreduction) and the reduced models was compared.

Table 2.3: Specification of the AMI testing mobile crane model

Specification	values
Chassis mass	20 000 [kg]
Chassis size	5, 2.5, 0.4 [m]
Outriggers' stiffness	1000, 1000, 7500 [kN/m]
Outriggers' damping	20, 20, 16 [kN.s/m]
Slewing platform mass	800 [kg]
Slewing platform radius and height	4, 1 [m]
Boom length	10 [m]
Boom cross-section	40, 20 [cm]
Boom thickness	2 [cm]
Booms' density	7800 [kg/m^2]
Booms' Young's modulus	210 [GPa]
Rope length	5 [m]

The correctness of the reduced model was measured by the root mean square of the deviation from the reference model calculated using Eqs. (2.52) and (2.53) where T is the number of steps from $t = 0$ to $t = t_{end}$. The calculation was performed on *MATLAB* with Intel Core i5 2.40GHz CPU and 8.00G RAM. The fourth order Runge-Kutta was used to integrate the dynamic model. In order to demonstrate the advanatge of the reduced model, the integration step-size for the reference model

was set at 0.5[ms] while the reduced model was set at 5[ms].

$$\begin{aligned} \delta x_i &= \sqrt{\sum_{t=0}^{t_{end}} (x_{i,red}(t) - x_{i,ref}(t))^2 / T} \\ \delta y_i &= \sqrt{\sum_{t=0}^{t_{end}} (y_{i,red}(t) - y_{i,ref}(t))^2 / T} \\ \delta z_i &= \sqrt{\sum_{t=0}^{t_{end}} (z_{i,red}(t) - z_{i,ref}(t))^2 / T} \end{aligned} \tag{2.52}$$

$$\mathrm{dev}_i = \sqrt{\delta x_i^2 + \delta y_i^2 + \delta z_i^2},\ i = \{tip, load\} \tag{2.53}$$

In this dissertation, the results from the reduced model with the nonreduced model were compared at several motion patterns. The motion patterns in this dissertation are shown in Table 2.4.

Table 2.4: The motion patterns for observing the reduced models

Motion	Pattern number
180[deg] slewing and 60[deg] lifting	No. 1
180[deg] slewing at fixed 60[deg] lifting angle	No. 2
180[deg] slewing at fixed 45[deg] lifting	No. 3

The motion from the nonreduced model was used as a reference; thus, it was named reference model or "Ref". The reduced model with the piecewise bilinear interpolation was named "Linear" model, and the reduced model with the RBF interpolation was named "RBF" model. The total mode shapes of the model in Appendix B before the reduction were 26 modes. The number of mode shapes after the model reduction was 14 modes.

2.3.4.1 Comparing the input acceleration pattern

Firstly, the crane model was simulated under several acceleration patterns. The motion of the boom tip and the hoisted load from the reduced models were compared to the Ref. model. Three patterns of the driving acceleration functions were used in this dissertation. In this test, the slewing angle was discretized from 0[deg] to 360[deg] with step size of 18[deg], while the lifting angle was discretized from 0[deg] to 60[deg] with step size of 12[deg].

Bang-Bang acceleration

The bang-bang input accelerations in Figs. 2.33 were considered. Firstly, the motion of the crane with pattern No. 1 was calculated. The trajectory of the boom tip and the hoisted load in time history of this motion are shown in Figs. 2.34 and 2.35. Their respective deviation and the calculation time of the model are summarized in Tables 2.5 to 2.8.

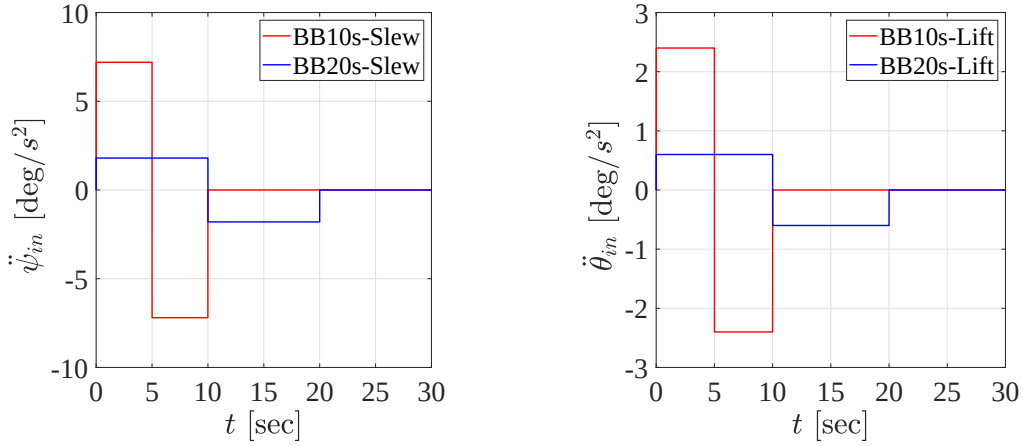

(a) Slewing acceleration (b) Lifting acceleration

Fig. 2.33: Bang-Bang input acceleration pattern

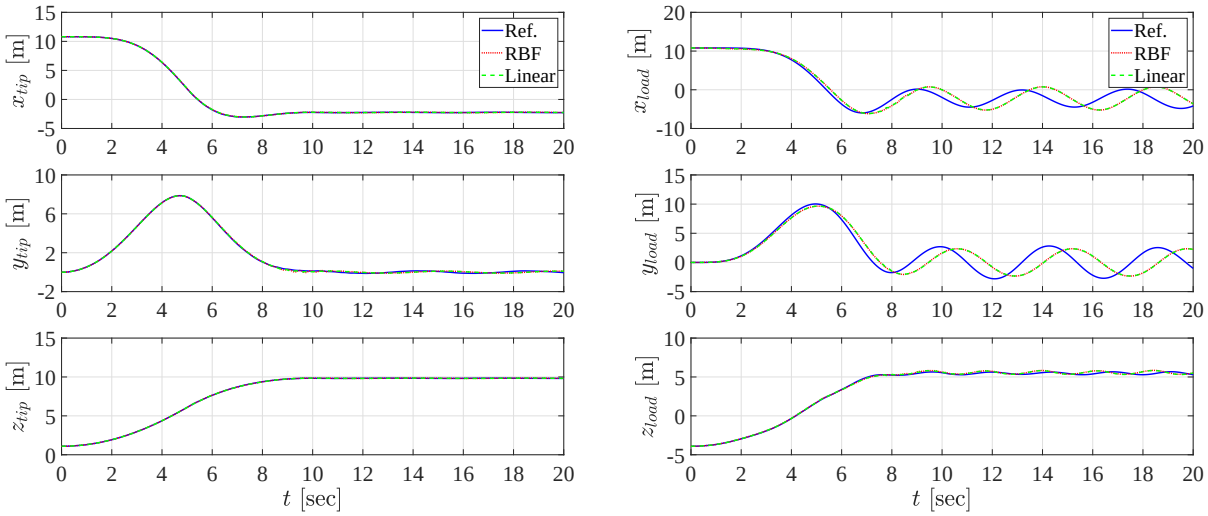

(a) Boom tip (b) Hoisted load

Fig. 2.34: Time-history of the boom tip and the hoisted load motion under BB10s with motion pattern No. 1

Table 2.5: Deviation of the reduced models' results of pattern No. 1 under BB10s

Interpolation model	Boom tip	Hoisted load
RBF	1.29	38.5 [mm]
Linear	1.27	38.6 [mm]

Table 2.6: Calculation time of pattern No. 1 under BB10s

Model	Time[s]
Ref	80.9
RBF	21.8
Linear	8.73

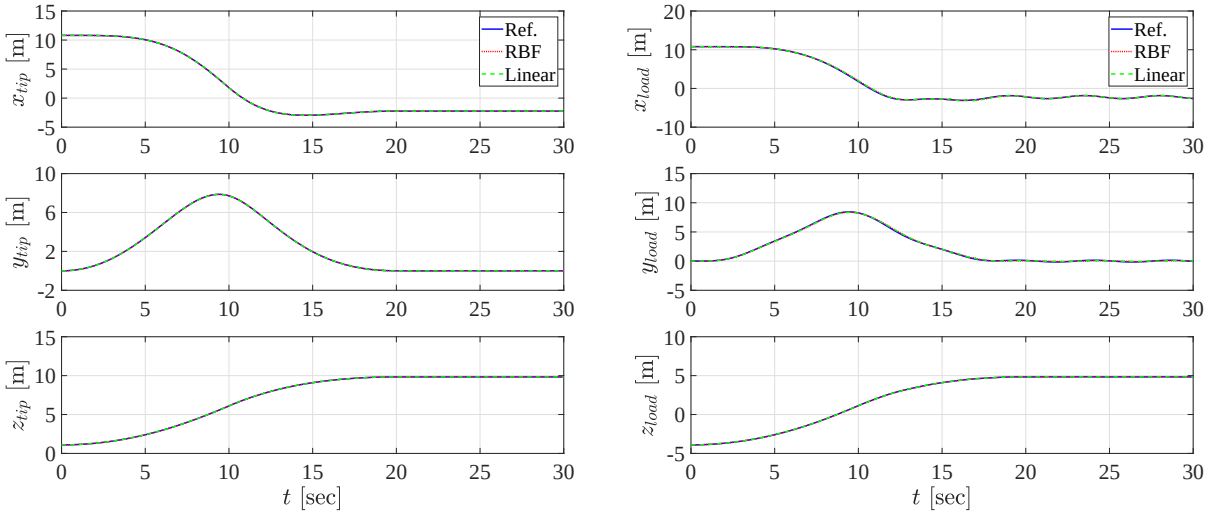

(a) Boom tip

(b) Hoisted load

Fig. 2.35: Time-history of the boom tip and the hoisted load motion under BB20s with motion pattern No. 1

Table 2.7: Deviation of the reduced models' results of pattern No. 1 under BB20s

Interpolation model	Boom tip	Hoisted load
RBF	0.09	1.28 [mm]
Linear	0.13	1.32 [mm]

Table 2.8: Calculation time of pattern No. 1 under BB20s

Model	Time[s]
Ref	98.0
RBF	32.1
Linear	12.6

The results showed that the motion from the reduced model had a large deviation of the hoisted load from the reference model under the BB10s acceleration. When the BB20s was used, the deviations became smaller. Next, the motion pattern No. 2 and No. 3 under the BB10s acceleration were simulated. The results are shown from Figs. 2.36 to 2.39, and Tables 2.9 to 2.16.

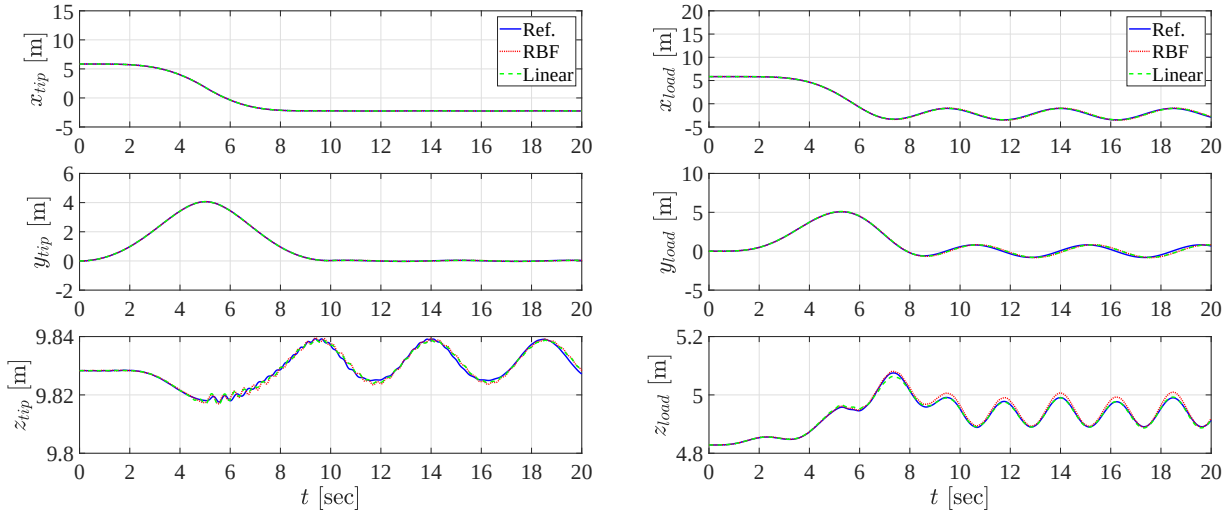

(a) Boom tip (b) Hoisted load

Fig. 2.36: Time-history of the boom tip and the hoisted load motion under BB10s with motion pattern No. 2

Table 2.9: Deviation of the reduced models' results of pattern No. 2 under BB10s

Interpolation model	Boom tip	Hoisted load
RBF	0.09	2.33 [mm]
Linear	0.8	2.14 [mm]

Table 2.10: Calculation time of pattern No. 2 under BB10s

Model	Time[s]
Ref	64.4
RBF	22.2
Linear	4.94

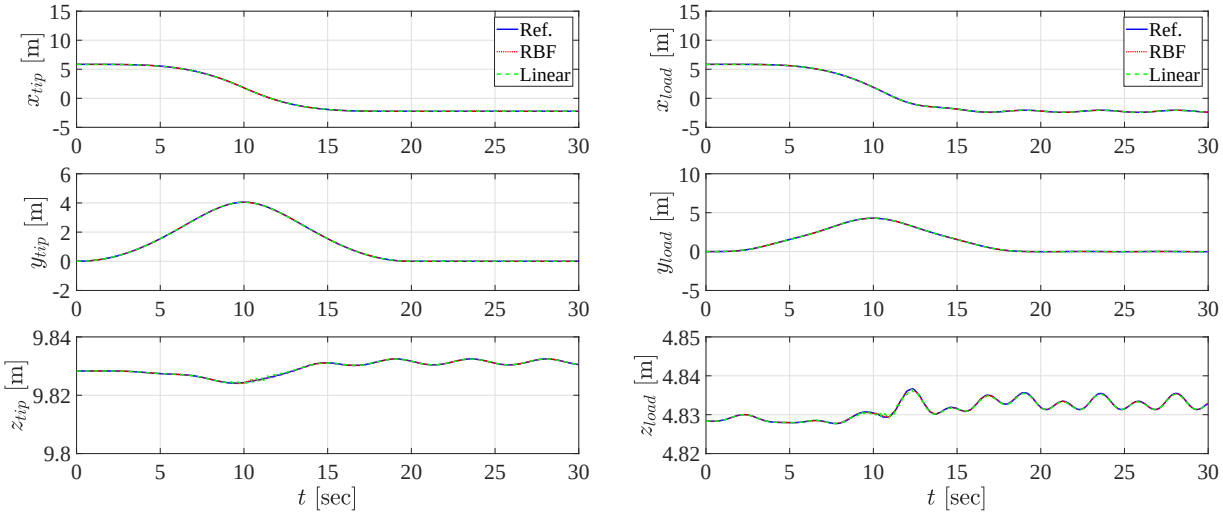

(a) Boom tip

(b) Hoisted load

Fig. 2.37: Time-history of the boom tip and the hoisted load motion under BB20s with motion pattern No. 2

Table 2.11: Deviation of the reduced models' results of pattern No. 2 under BB10s

Interpolation model	Boom tip	Hoisted load
RBF	0.002	0.032 [mm]
Linear	0.007	0.054 [mm]

Table 2.12: Calculation time of pattern No. 2 under BB20s

Model	Time[s]
Ref	98.0
RBF	53.2
Linear	12.3

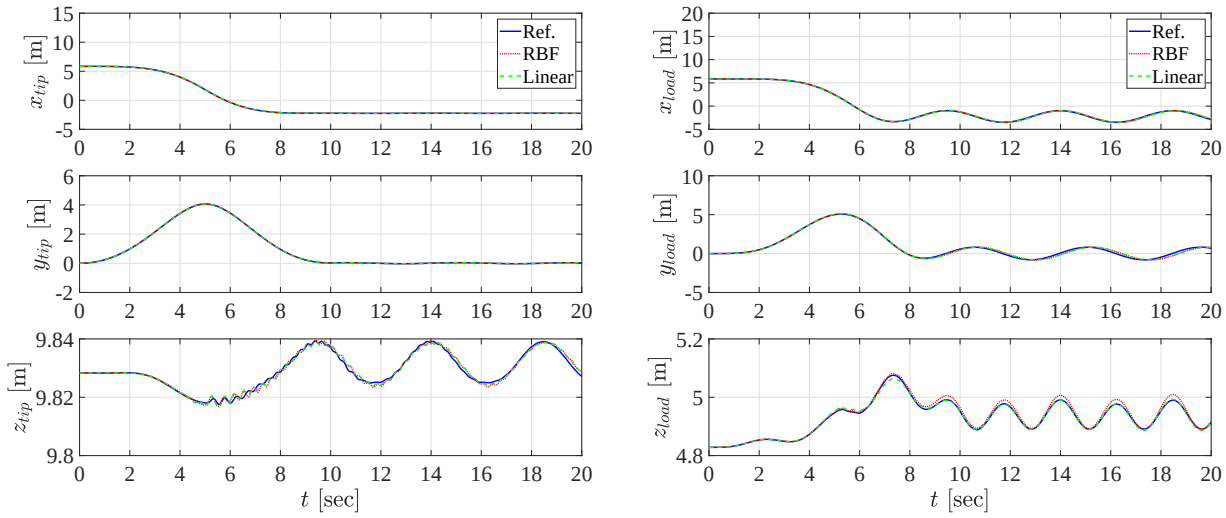

(a) Boom tip (b) Hoisted load

Fig. 2.38: Time-history of the boom tip and the hoisted load motion under BB10s with motion pattern No. 3

Table 2.13: Deviation of the reduced models' results of pattern No. 3 under BB10s

Interpolation model	Boom tip	Hoisted load
RBF	0.26	7.51 [mm]
Linear	0.26	7.17 [mm]

Table 2.14: Calculation time of pattern No. 3 under BB10s

Model	Time[s]
Ref	111
RBF	20.84
Linear	8.43

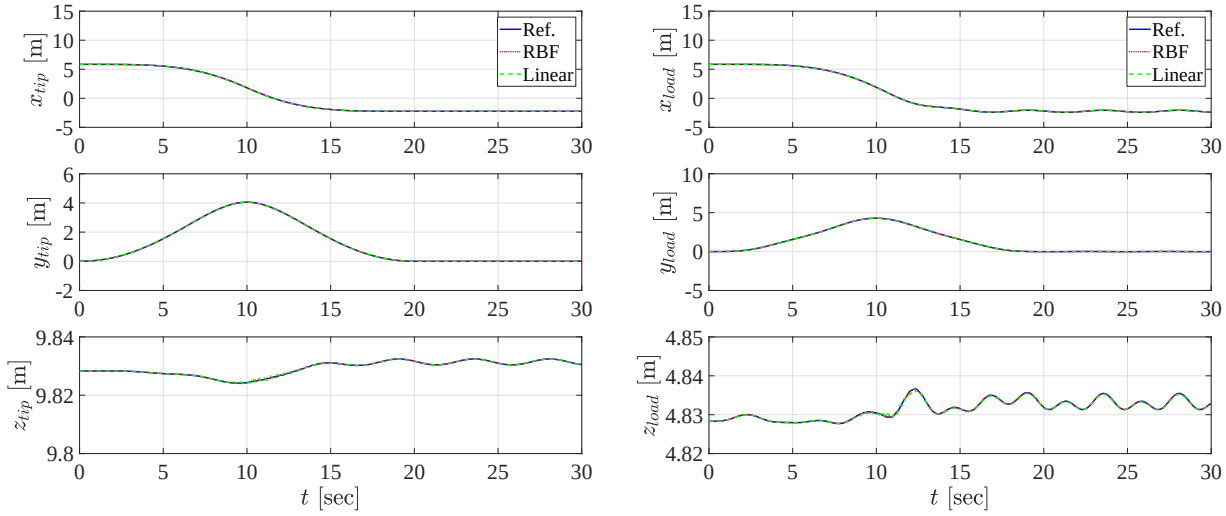

(a) Boom tip (b) Hoisted load

Fig. 2.39: Time-history of the boom tip and the hoisted load motion under BB20s with motion pattern No. 3

Table 2.15: Deviation of the reduced models' results of pattern No. 3 under BB20s

Interpolation model	Boom tip	Hoisted load
RBF	0.003	0.042 [mm]
Linear	0.005	0.034 [mm]

Table 2.16: Calculation time of pattern No. 3 under BB20s

Model	Time[s]
Ref	116
RBF	49.6
Linear	12.1

From these results, the motion under the BB10s acceleration had a larger inaccuracy than the BB20s even when the lifting angle was fixed. In addition, when comparing the motion at fixed 60[deg] and 45[deg] with BB10s, the deviation of the hoisted load and the boom tip at 45[deg] condition was slightly larger than at 60[deg].

Palabolic acceleration

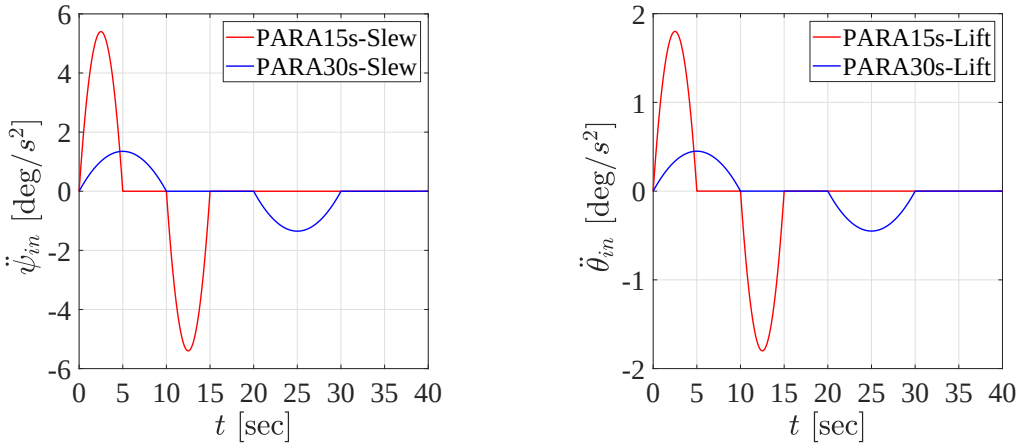

(a) Slewing acceleration (b) Lifting acceleration

Fig. 2.40: Parabolic input acceleration pattern

The Parabolic acceleration in Fig. 2.40 was employed. First, the crane motion with motion pattern No. 1 was simulated. The results of the boom tip and hoisted load's trajectory in time history are shown in Figs. 2.41 and 2.42 while their respective model's correctness and calculation time are summarized in Tables 2.17 to 2.20.

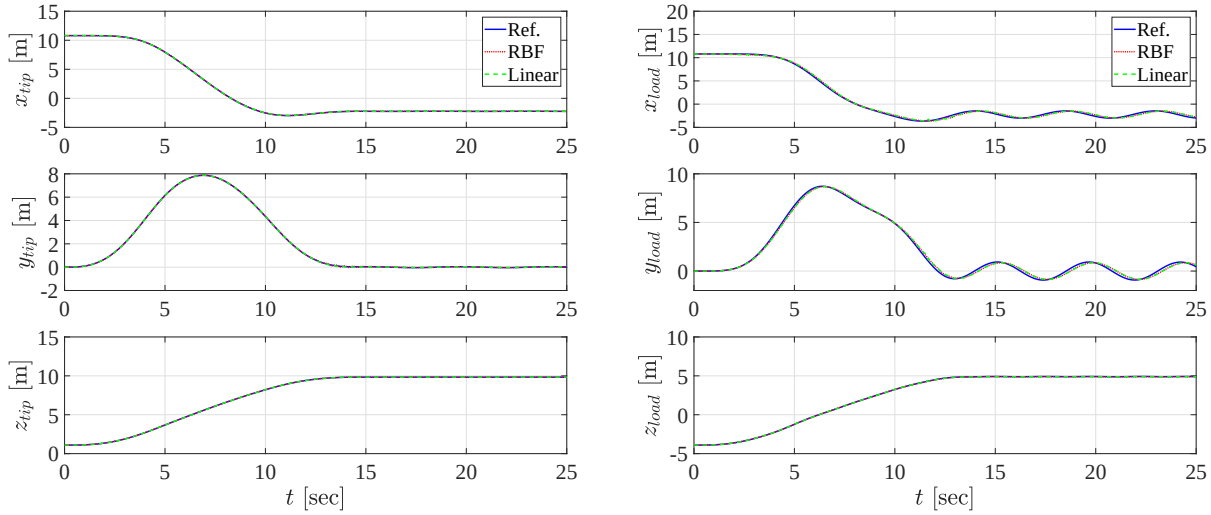

(a) Boom tip (b) Hoisted load

Fig. 2.41: Time-history of the boom tip and the hoisted load motion under PARA15s with motion pattern No. 1

Table 2.17: Deviation of the reduced models' results of pattern No. 1 under PARA15s

Interpolation model	Boom tip	Hoisted load
RBF	0.22	3.56 [mm]
Linear	0.17	3.74 [mm]

Table 2.18: Calculation time of pattern No. 1 under PARA15s

Model	Time[s]
Ref	85.3
RBF	43.1
Linear	10.8

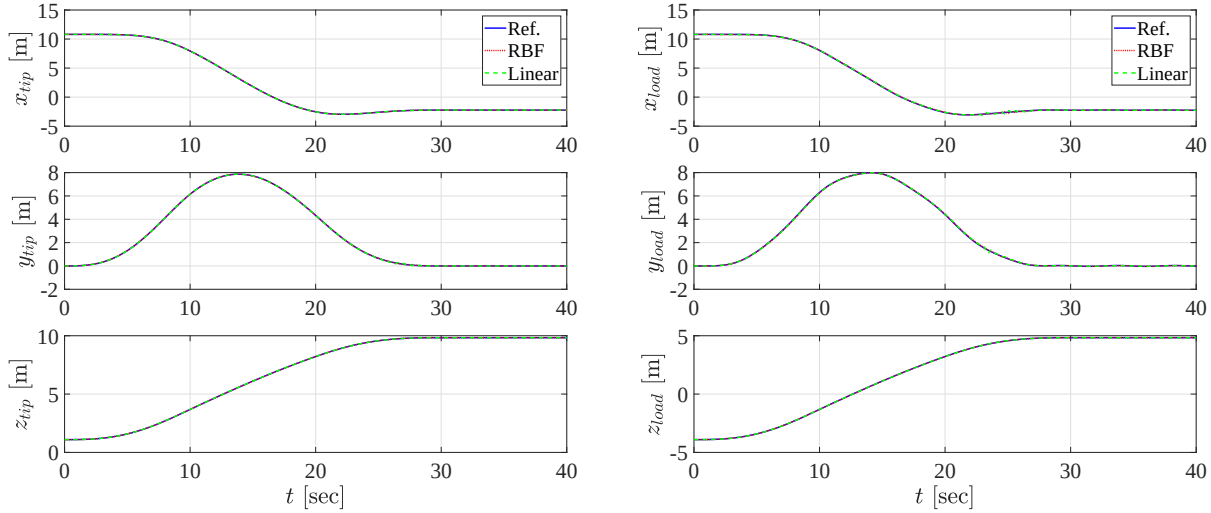

(a) Boom tip

(b) Hoisted load

Fig. 2.42: Time-history of the boom tip and the hoisted load motion under PARA30s with motion pattern No. 1

Table 2.19: Deviation of the reduced models' results of pattern No. 1 under PARA30s

Interpolation model	Boom tip	Hoisted load
RBF	0.04	0.403 [mm]
Linear	0.143	0.653 [mm]

Table 2.20: Calculation time of pattern No. 1 under PARA30s

Model	Time[s]
Ref	120
RBF	42.8
Linear	16.6

The comparison of the PARA15s and PARA30s acceleration on motion pattern No. 1 showed that the former acceleration had a slightly larger deviation of the hoisted load than the other one. The behavior was similar to the results from the Bang-Bang acceleration cases. Next, motion pattern No. 2 and 3 were considered. Figures 2.45 to 2.46 and Tables 2.21 to 2.24 show the results from pattern No. 2, while Figs. 2.47 to 2.48 and Tables 2.25 to 2.28 show the results from pattern No. 3.

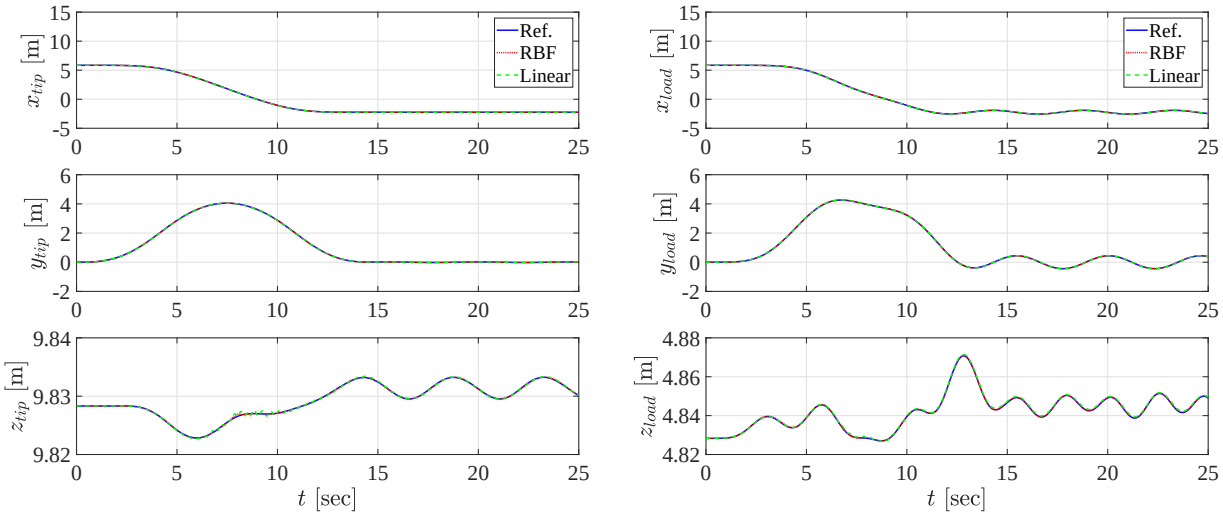

(a) Boom tip (b) Hoisted load

Fig. 2.43: Time-history of the boom tip and the hoisted load motion under PARA15s with motion pattern No. 2

Table 2.21: Deviation of the reduced models' results of pattern No. 2 under PARA15s

Interpolation model	Boom tip	Hoisted load
RBF	0.0031	0.089 [mm]
Linear	0.009	0.144 [mm]

Table 2.22: Calculation time of pattern No. 2 under PARA15s

Model	Time[s]
Ref	87.3
RBF	45.7
Linear	10.4

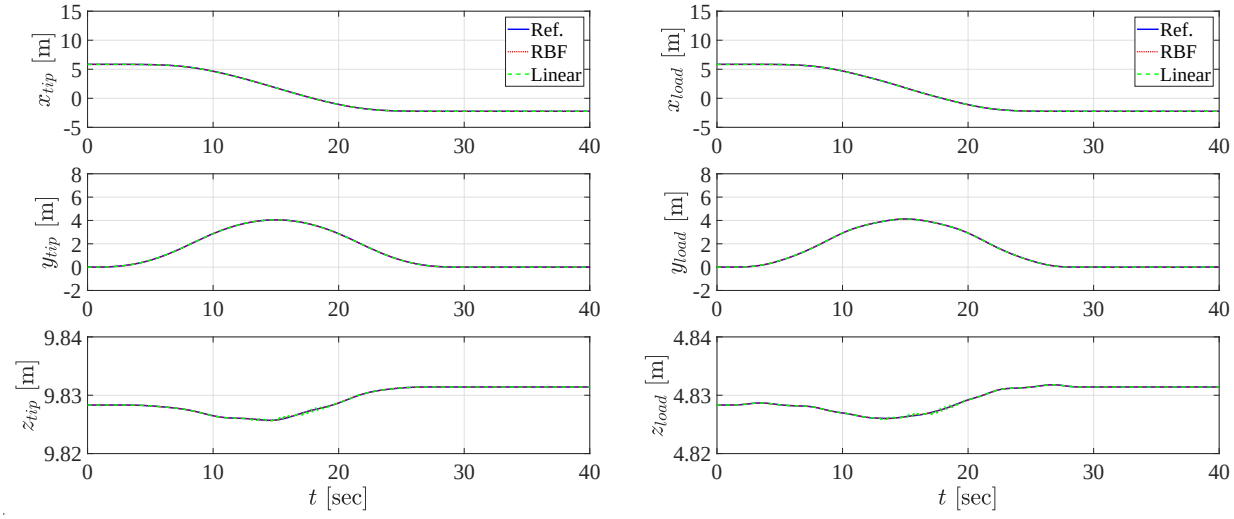

(a) Boom tip (b) Hoisted load

Fig. 2.44: Time-history of the boom tip and the hoisted load motion under PARA30s with motion pattern No. 2

Table 2.23: Deviation of the reduced models' results of pattern No. 2 under PARA30s

Interpolation model	Boom tip	Hoisted load
RBF	0.0006	0.0199 [mm]
Linear	0.0034	0.0039 [mm]

Table 2.24: Calculation time of pattern No. 2 under PARA30s

Model	Time[s]
Ref	200.5
RBF	43.7
Linear	9.48

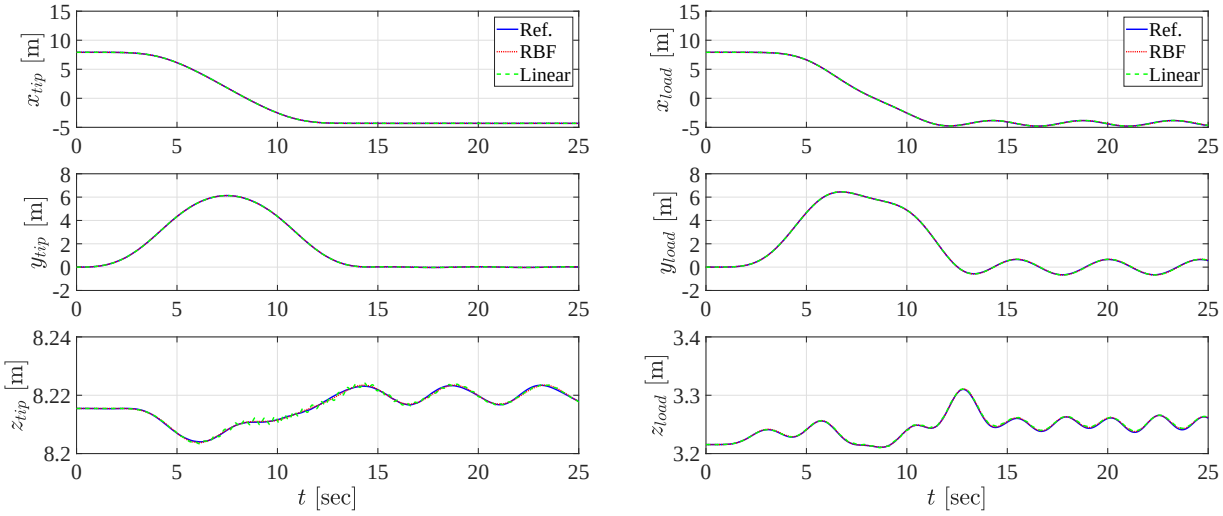

(a) Boom tip (b) Hoisted load

Fig. 2.45: Time-history of the boom tip and the hoisted load motion under PARA15s with motion pattern No. 3

Table 2.25: Deviation of the reduced models' results of pattern No. 3 under PARA15s

Interpolation model	Boom tip	Hoisted load
RBF	0.01	0.362 [mm]
Linear	0.0153	0.367 [mm]

Table 2.26: Calculation time of pattern No. 3 under PARA15s

Model	Time[s]
Ref	90.2
RBF	44.3
Linear	6.1

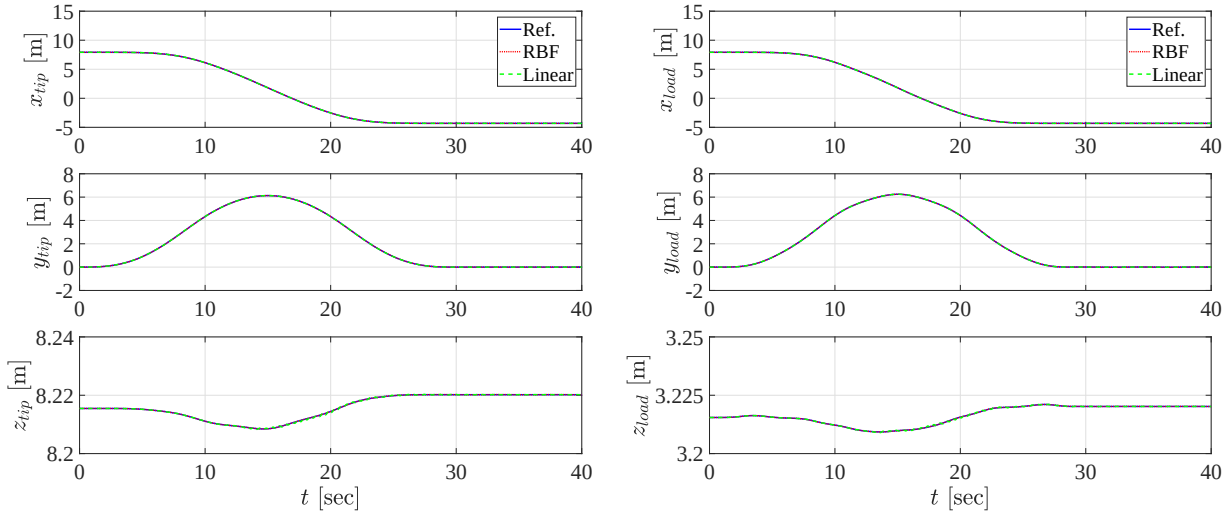

(a) Boom tip (b) Hoisted load

Fig. 2.46: Time-history of the boom tip and the hoisted load motion under PARA30s with motion pattern No. 3

Table 2.27: Deviation of the reduced models' results of pattern No. 3 under PARA30s

Interpolation model	Boom tip	Hoisted load
RBF	0.0008	0.03 [mm]
Linear	0.0026	0.0035 [mm]

Table 2.28: Calculation time of pattern No. 3 under PARA30s

Model	Time[s]
Ref	202
RBF	41.7
Linear	9.35

When comparing the PARA15s and PARA30s at a fixed lifting angle, the PARA15s had a larger deviation than the motion with the PARA30s. The motion from the reduced models at a fixed 45[deg] lifting angle was also larger than at a fixed 60[deg] lifting angle.

Triangular acceleration

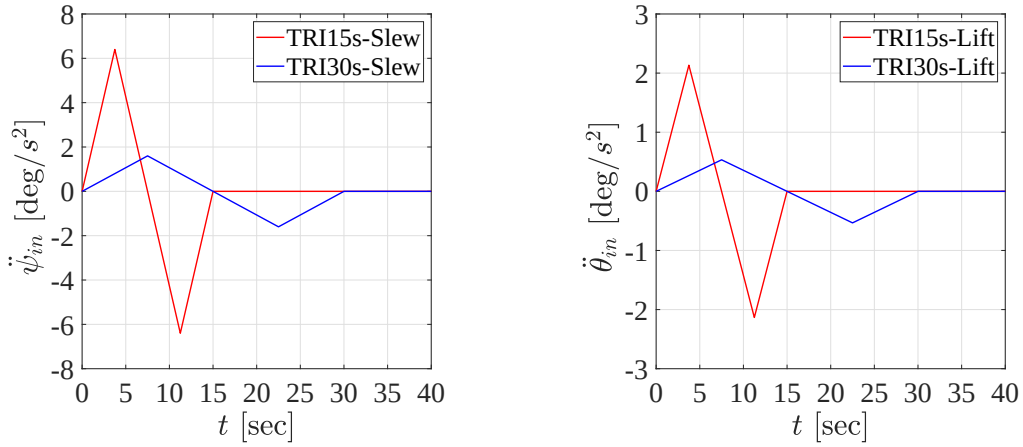

(a) Slewing acceleration (b) Lifting acceleration

Fig. 2.47: Triangular input acceleration pattern

Next, the triangular acceleration patterns in Fig. 2.47 were used. Firstly, the motion pattern No. 1 was considered, and the results are shown in Figs. 2.48 and 2.49, and Tables 2.29 to 2.32.

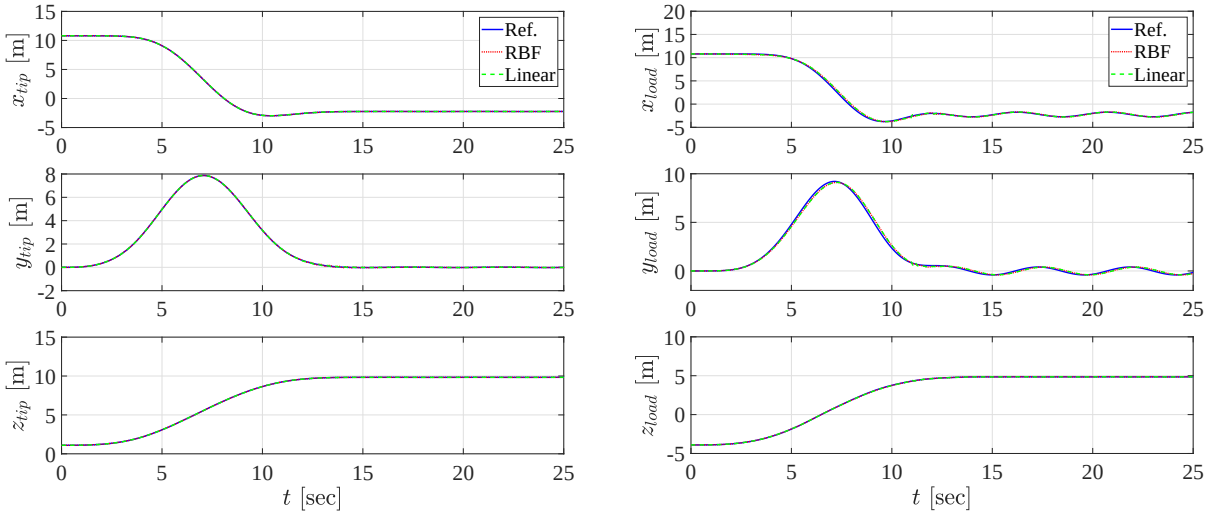

(a) Boom tip (b) Hoisted load

Fig. 2.48: Time-history of the boom tip and the hoisted load motion under triangularTRI15s with motion pattern No. 1

Table 2.29: Deviation of the reduced models' results of pattern No. 1 under TRI15s

Interpolation model	Boom tip	Hoisted load
RBF	0.2	2.88 [mm]
Linear	0.163	2.93 [mm]

Table 2.30: Calculation time of pattern No. 1 under TRI15s

Model	Time[s]
Ref	74.9
RBF	28.3
Linear	10.8

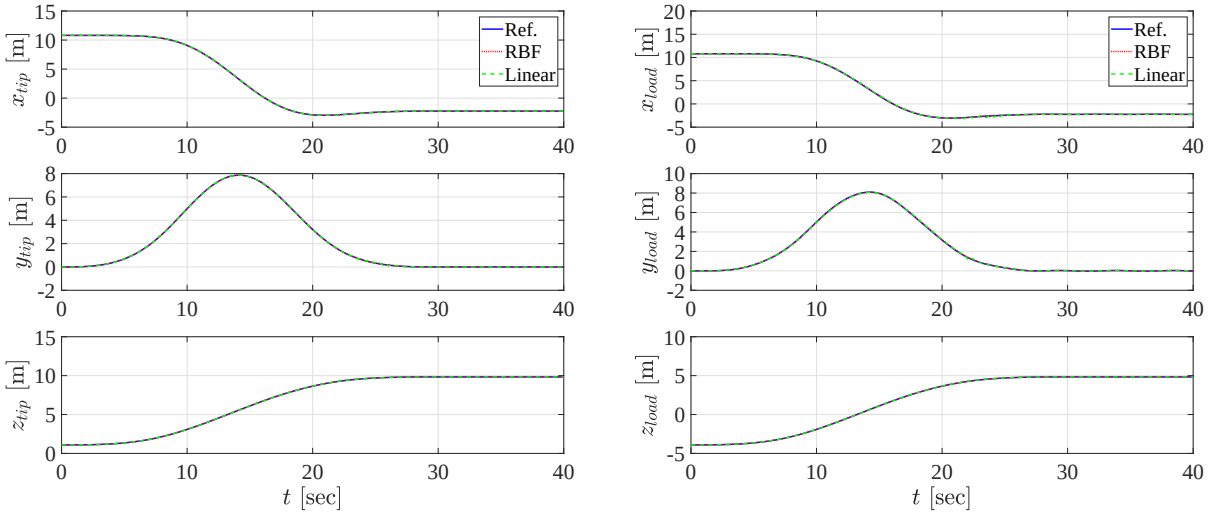

(a) Boom tip

(b) Hoisted load

Fig. 2.49: Time-history of the boom tip and the hoisted load motion under triangularTRI30s with motion pattern No. 1

Table 2.31: Deviation of the reduced models' results of pattern No. 1 under TRI30s

Interpolation model	Boom tip	Hoisted load
RBF	0.0373	0.493 [mm]
Linear	0.142	0.712 [mm]

Table 2.32: Calculation time of pattern No. 1 under TRI30s

Model	Time[s]
Ref	191
RBF	42.5
Linear	16.6

Similar to the motion from the Parabolic acceleration patterns, the deviation of the boom tip and the hoisted load from TRI15s was larger than in TRI30s with motion pattern No. 1. On the same hand, the motion at a fixed lifting angle in patterns No. 2 and 3 also showed that the motion from the reduced models under the acceleration TRI15s had larger deviation than the motion under TRI30s acceleration.

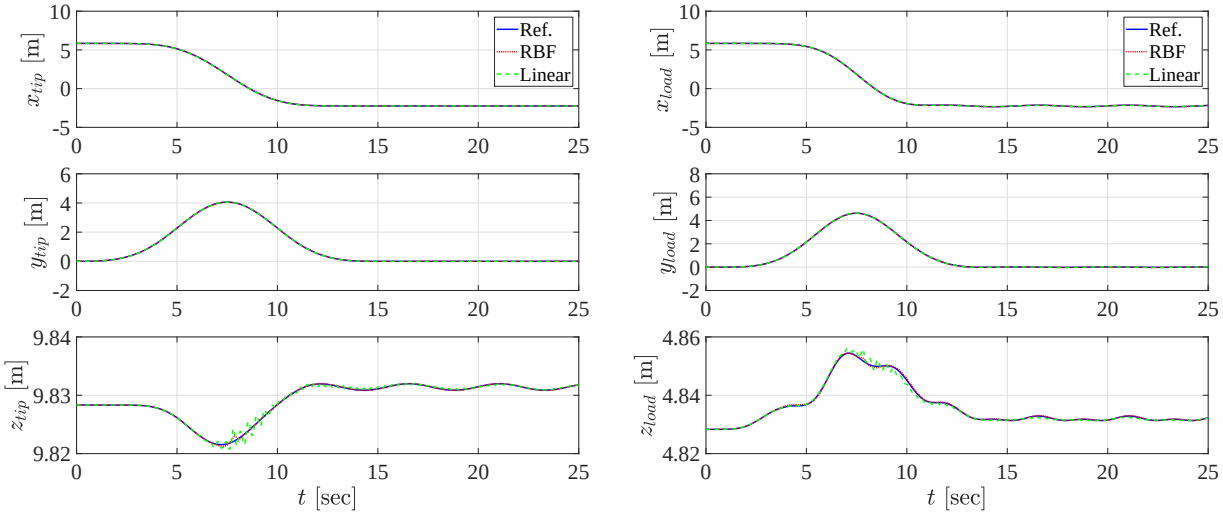

(a) Boom tip (b) Hoisted load

Fig. 2.50: Time-history of the boom tip and the hoisted load motion under triangularTRI15s with motion pattern No. 2

Table 2.33: Deviation of the reduced models' results of pattern No. 2 under TRI15s

Interpolation model	Boom tip	Hoisted load
RBF	0.0037	0.0723 [mm]
Linear	0.0175	0.1959 [mm]

Table 2.34: Calculation time of pattern No. 2 under TRI15s

Model	Time[s]
Ref	74.3
RBF	26.8
Linear	10.4

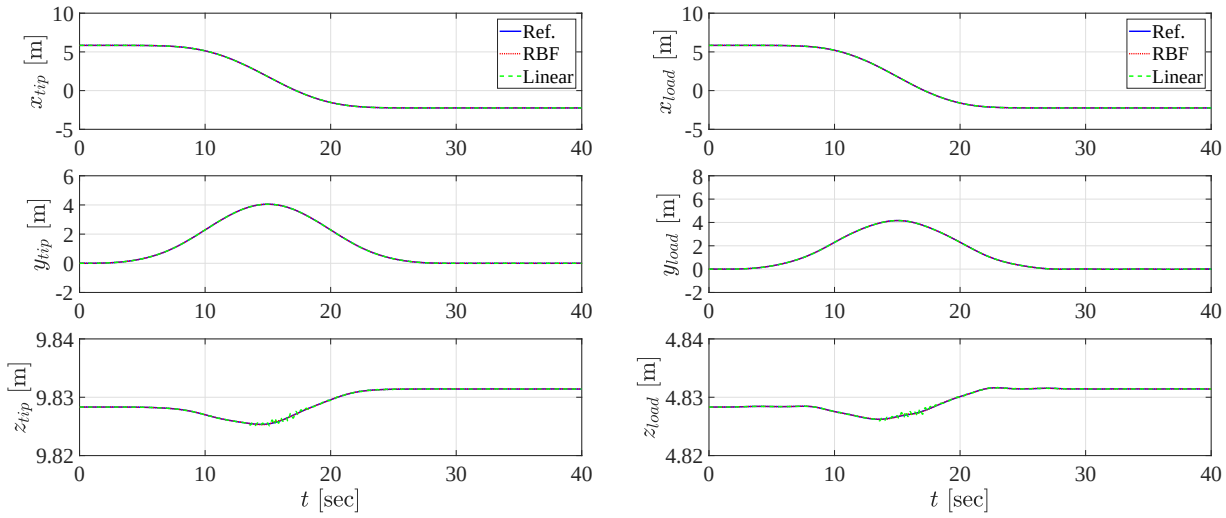

(a) Boom tip (b) Hoisted load

Fig. 2.51: Time-history of the boom tip and the hoisted load motion under triangularTRI30s with motion pattern No. 2

Table 2.35: Deviation of the reduced models' results of pattern No. 2 under TRI30s

Interpolation model	Boom tip	Hoisted load
RBF	0.0007	0.0205 [mm]
Linear	0.0045	0.0043 [mm]

Table 2.36: Calculation time of pattern No. 2 under TRI30s

Model	Time[s]
Ref	118
RBF	42.5
Linear	16.3

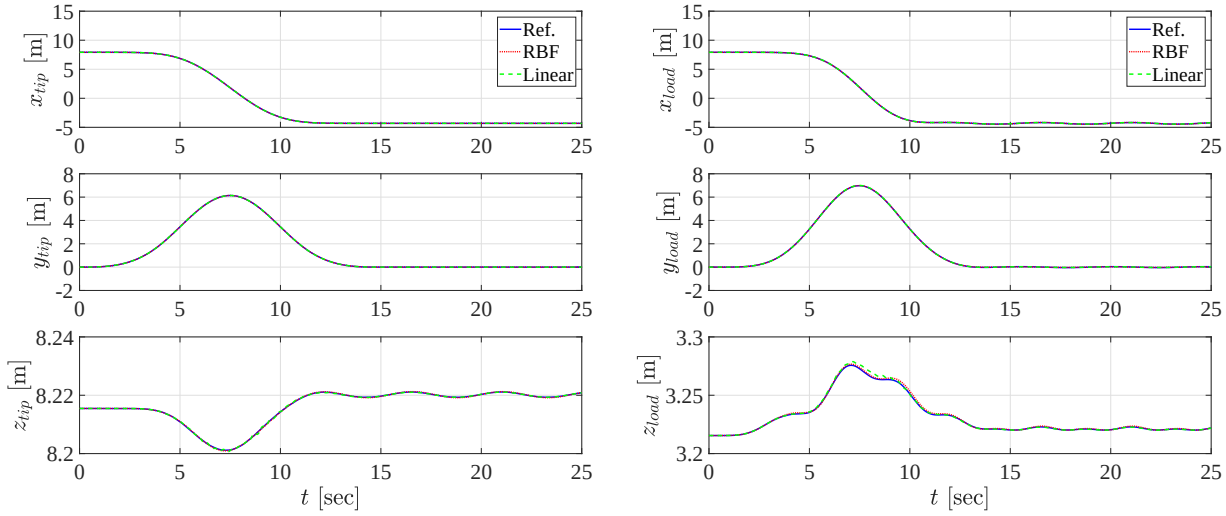

(a) Boom tip (b) Hoisted load

Fig. 2.52: Time-history of the boom tip and the hoisted load motion under triangularTRI15s with motion pattern No. 3

Table 2.37: Deviation of the reduced models' results of pattern No. 3 under TRI15s

Interpolation model	Boom tip	Hoisted load
RBF	0.0052	0.21 [mm]
Linear	0.007	0.12 [mm]

Table 2.38: Calculation time of pattern No. 3 under TRI15s

Model	Time[s]
Ref	75
RBF	26.7
Linear	6.05

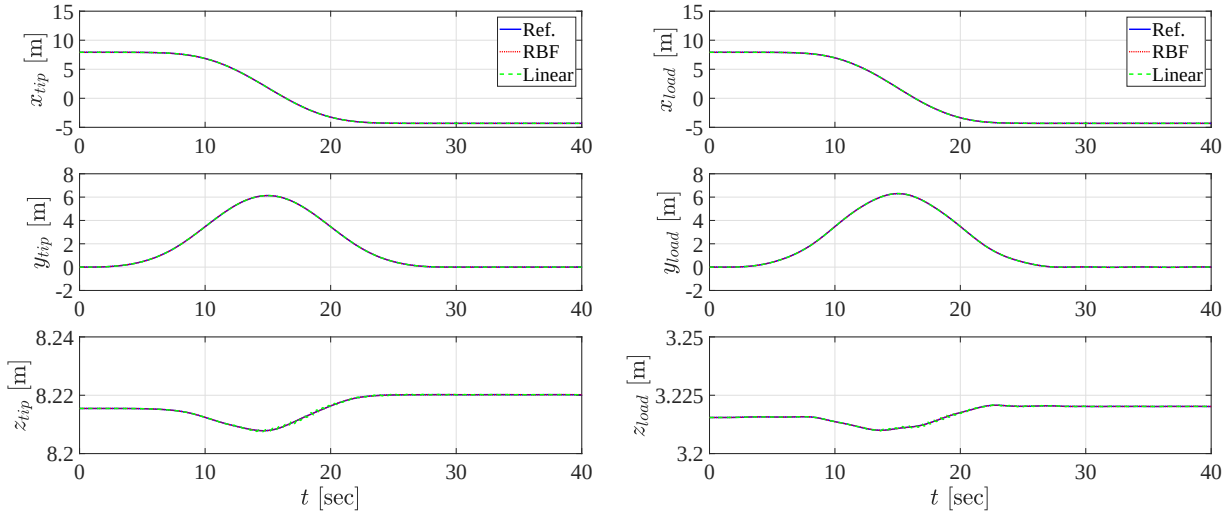

(a) Boom tip (b) Hoisted load

Fig. 2.53: Time-history of the boom tip and the hoisted load motion under triangularTRI30s with motion pattern No. 3

Table 2.39: Deviation of the reduced models' results of pattern No. 3 under TRI30s

Interpolation model	Boom tip	Hoisted load
RBF	0.0007	0.03 [mm]
Linear	0.003	0.008 [mm]

Table 2.40: Calculation time of pattern No. 3 under TRI30s

Model	Time[s]
Ref	122
RBF	41.7
Linear	9.39

Discussion

The above simulation showed that when the acceleration was large, the deviation became larger. This might be the consequence of the linearization. The geometric stiffening was a function of the velocity. When the acceleration was large, the velocity became faster, and the linearized geometric stiffening showed a larger diversion from the nonlinear results[27]. The results from BB20s, PARA30s, and TRI30s did not show distinguished accuracy. All motion from these acceleration patterns showed a good degree of small deviation. Furthermore, the reduced model under the BB20s had a smaller deviation of the boom tip and the hoisted load motion, from the nonlinear model, than the PARA15s and TRI15s. This also showed that the swift change of the acceleration such as in the Bang-Bang function did not worsen the results. On the same hand, the smooth change of the acceleration function such as the parabolic function or triangular function did not give better

accuracy as well. The accuracy of the reduced models depended on only the magnitude of the acceleration that was used to drive the crane model.

At a fast motion from each acceleration pattern, the motion at a fixed 60[deg] lifting angle was better than in the fixed 45[deg]. In this calculation, the lifting angle of 60[deg] was a raw data point. However, the 45[deg] lifting angle was not and had to be interpolated. Thus, the motion at a 60[deg] lifting angle from the reduced model was better because it required less interpolation.

When comparing the reduced model that used the piecewise bilinear interpolation and the RBF interpolation, neither model showed better accuracy than the other. This demonstrated that the smoothness of the derivative of the mode shapes did not enhance the accuracy of the reduced model. When considering the calculation time of the model, both reduced models used shorter integration time than the nonlinear model (reference model). This was because the reduced models were able to be integrated with larger time step than the nonlinear model. The reduced model with the piecewise bilinear interpolation was the fastest model. It was faster than the RBF model because it used a piecewise strategy. Another contribution to the shorter calculation time was the interpolation of the inverse of the inertia matrix. However, only the integration time was shown in the above results. If the preparation time was included (modal analysis and inverse inertia matrix calculation), the reduced models would have a longer calculation time in one simulated motion. In this example, the time for modal analysis and inverse inertia matrix calculation was 247[s]. If the model was used only once, the reduced models required longer simulation time than the nonlinear model. However, the precalculation data only needed to be calculated one time. Therefore, as the reduced model is used, the more efficient the reduced model could become.

2.3.4.2 Comparing the sizes of discretizations

Next, the relation between the accuracy of the reduced model and the number of discretization was observed. The observation was performed by trialing the size of the discretization on the slewing angle. The discretization sizes of $\Delta\psi_{in} = \{90, 36, 18, 3.6\}$ [deg] were observed. This gave us a total of 5, 11, 21 and 101 discretized points, respectively. The simulation with acceleration pattern No. 1 with PARA15s was used as an example.

Figures 2.54 and 2.55 show the results from the reduced model with piecewise bilinear interpolation. In these figures, the interpolation with 5 points deviated from the reference results with the largest amount. The model with 5 and 11 points interpolation also showed the instability of the results between the 10th and 15th second. These instabilities were not observable when the 21 points interpolation was used. The results with the 101 points interpolation did not improve the accuracy.

Then, the same observation was performed with the model under the RBF interpolation, and the results are shown in Figs. 2.56 and 2.57. The results from the interpolation with 5 and 11 points were unobservable since the instability was large such that the diverged results were obtained. At the same time, the interpolation with the 101 points did not improve the reduced model either.

However, a sufficient number of the discretization was required. When the piecewise bilinear interpolation was used, the results showed instability when the number of data points was small. However, the model was computable. The piecewise bilinear interpolation used only at least four data points. Therefore, as long as this number was matched, the model was usable. The instability occurred from the lack of data. The missing information on the dynamics properties might result in an error from the interpolation. Still, the accuracy of the data is bounded by the 4 points. This was opposite to the RBF model. The RBF model interpolated the result using all data points. When the data points too few to connect the information, the dynamics model was unable to be integrated.

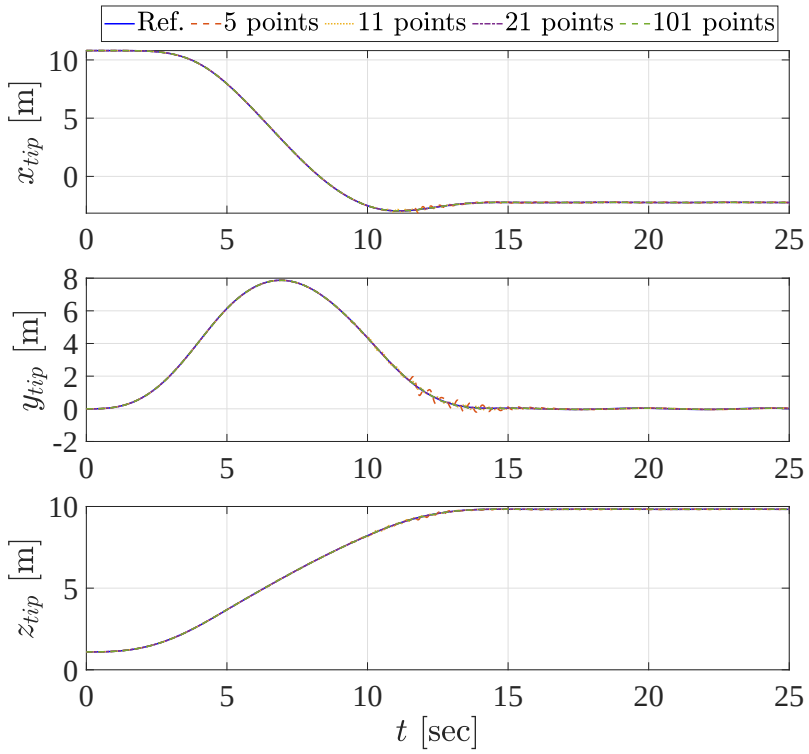

Fig. 2.54: The boom tip motion at different number of points with Bilinear interpolation

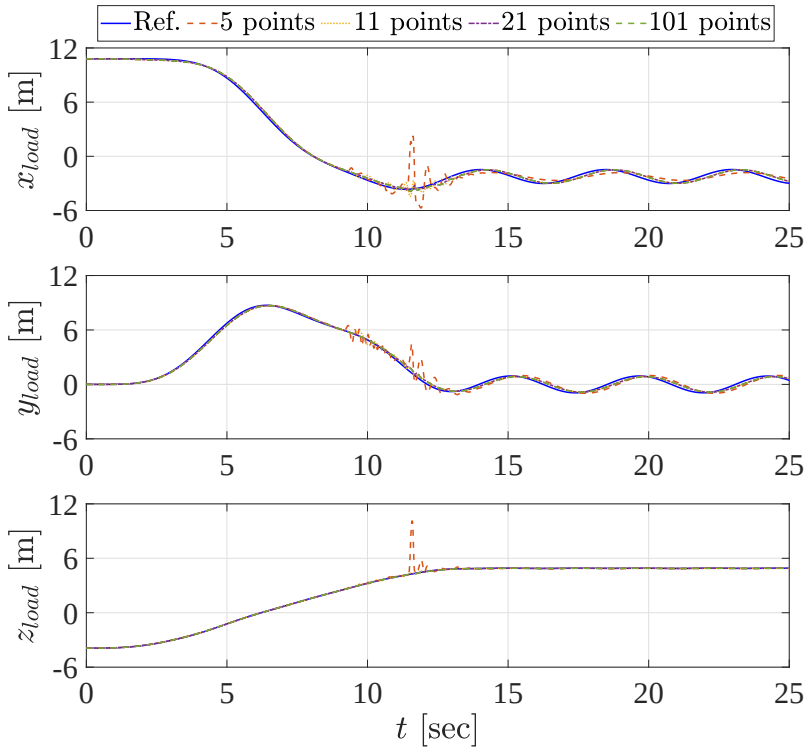

Fig. 2.55: The hoisted load motion at different number of points with Bilinear interpolation

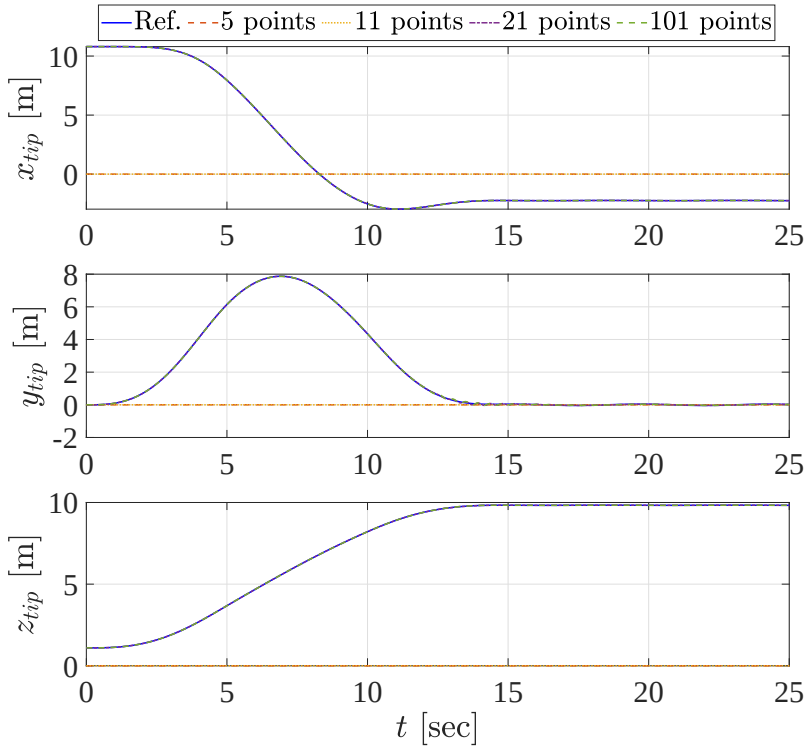

Fig. 2.56: The boom tip motion at different number of points with RBF interpolation

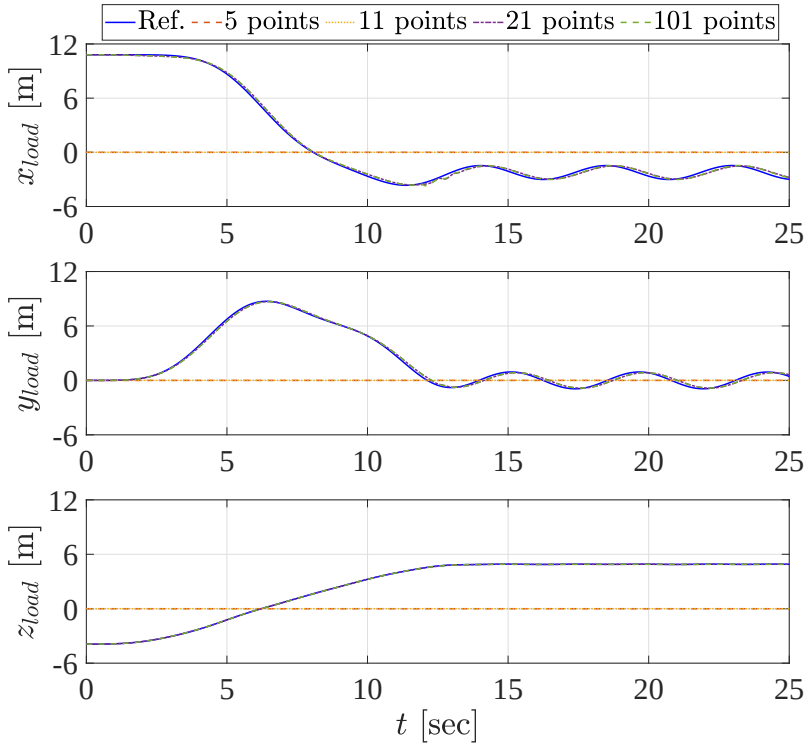

Fig. 2.57: The hoisted load motion at different number of points with RBF interpolation

Chapter 3

Vibration control of flexible crane

In this chapter, the development of the vibration control strategy for the rotary crane with flexible boom is discussed. The vibration control model for designing the vibrationless trajectory of the rotary crane with flexible boom was developed. Then, the optimal control trajectory was designed.

The part of this chapter has been presented in

1. Chalermpong, K., Hirata, S. and Yamaura, H., Vibration reduction of the rotary crane with flexible boom, The Bullettin of JSME, Mechanical Engineering Journal, Vol. 9, No. 5 (2022), 22-00231.

3.1 Proposing control model

In this research, the control model of the crane that explicitly included the flexibility of the boom was developed. The proposed control model for the flexible rotary crane was developed based on the vibration control model from [35] that was developed for the rotary crane with rigid boom. The control model was the simplified crane's equation of the motion that was used to design the vibrationless trajectory. The boom was considered as the flexible beam. The concept of the equivalent model between the flexible cantilever beam and the simple mass-spring model was used. The vibration of the boom tip was considered as the mass-spring model as shown in Fig 3.1. This concept was applied to develop the vibration control model for the rotary crane with the flexible boom. The vibration control model was separated into two directions: the slewing direction and the lifting direction.

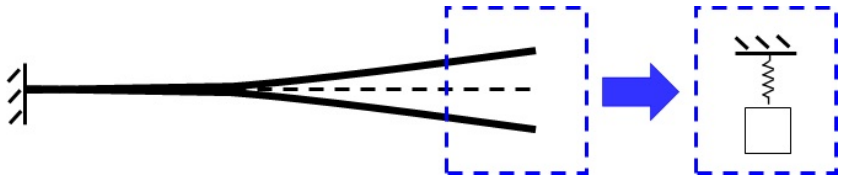

Fig. 3.1: Equivalent model between the cantilever beam and simple mass-spring model

3.1.1 Slewing control model

The proposed vibration control model of the crane in slewing direction is shown in Fig 3.2. This model assumed that the boom tip translated with a linear motion. In Fig 3.2, $u(t)$ is the displacement of the boom tip before undergoing deformation. The vibration of the boom tip was modeled with the simple mass-spring system where $m_{e,y}$ and $k_{e,y}$ are equivalent mass and stiffness coefficient, respectively. $q_y(t)$ is the deformation of the boom tip in $\bar{y}_{slew}$ direction, and it is the relative displacement to $u(t)$. The hoisted load swings around $\bar{x}_{slew}$ axis with angle $\phi_x(t)$. The equation of motion of the vibration control model in slewing direction is written in Eq. (3.1), where ℓ is the rope length, m_ℓ is the mass of load ,and g is the acceleration due to gravity.

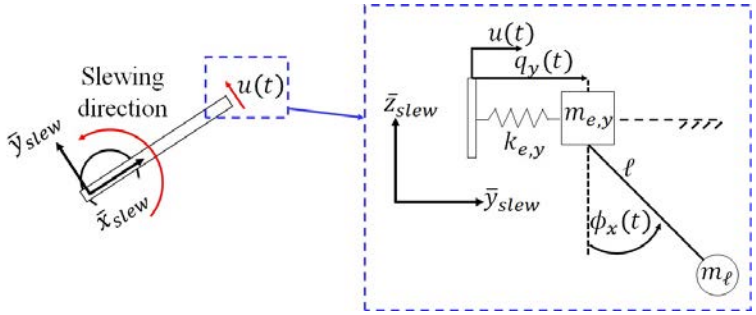

Fig. 3.2: Proposed vibration control model for the slewing direction

$$\begin{bmatrix} m_{e,y}+m_\ell & m_\ell\ell \\ m_\ell\ell & m_\ell\ell^2 \end{bmatrix} \begin{bmatrix} \ddot{q}_y \\ \ddot{\phi}_x \end{bmatrix} + \begin{bmatrix} k_{e,y} & 0 \\ 0 & m_\ell g\ell \end{bmatrix} \begin{bmatrix} q_y \\ \phi_x \end{bmatrix} = \begin{bmatrix} -(m_{e,y}+m_\ell) \\ -m_\ell\ell \end{bmatrix} \ddot{u}, \tag{3.1}$$
$$\mathbf{M}_s\ddot{\bar{\mathbf{q}}}_s + \mathbf{K}_s\bar{\mathbf{q}}_s = \mathbf{b}_s\ddot{u}.$$

3.1.2 Lifting control model

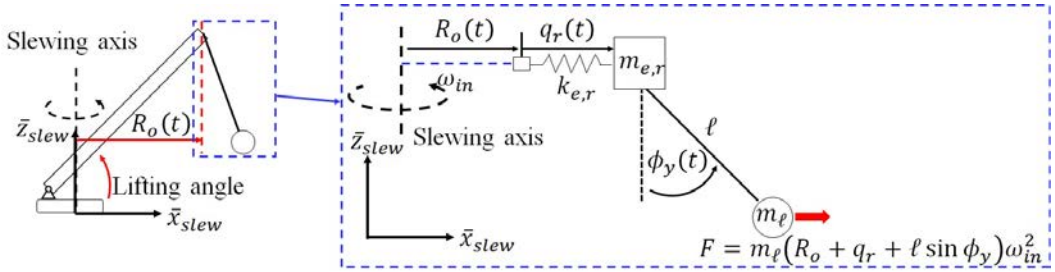

Fig. 3.3: Proposed vibration control model for the lifting direction

During the slewing motion, the hoisted load sways in the radial direction due to the centrifugal force. This sway can be controlled using the lifting motion. Therefore, the lifting control model was designed to control the vibration in the radial direction of the crane, as shown in Fig 3.3.

The position of the boom tip was determined by the crane's radius $R_o(t)$. This radius was the radius of the crane before the boom tip deformed in radial direction. In this model, it was assumed that the lifting angle changed at small amount such that it can assume that there is no change in height of the boom tip, and the boom tip translates in horizontal direction. The vibration of the boom tip was modeled as the mass-spring system with the equivalent mass, $m_{e,r}$ and stiffness, $k_{e,r}$. These coefficients were calculated from the boom's mechanical properties with respected to the radius direction. The deformation of the tip is $q_r(t)$, and it is the relative displacement to $R_o(t)$. The lifting model was separated from the slewing model. Therefore, the slewing velocity, ω_{in}, was assumed constant, which contribute the centrifuge force F.

When the lifting angle changes, the tip of boom and the hoisted load's relative inertia in the vertical and radial directions change. Thus, the equation of motion of the lifting control model was taken account of this change and can be written as in Eq. (3.2). As mentioned, the lifting control model assumed that the motion occurred at a constant slewing velocity. However, the crane is not always driven with constant velocity. In this model, the regulated constant slewing velocity Ω was used to compensate this uncertainty. It was calculated using Eq. (3.3), where regulated constant, a_c, was decided through trial and errors [35].

$$\begin{bmatrix} m_{e,r}+m_\ell(1+\cos^2\bar{\theta}_{in}) & m_\ell\ell \\ m_\ell\ell & m_\ell\ell^2 \end{bmatrix}\begin{bmatrix}\ddot{q}_r \\ \ddot{\phi}_y\end{bmatrix}+\begin{bmatrix} k_{e,r}-m_\ell\Omega^2 & -m_\ell\ell\Omega^2 \\ -m_\ell\ell\Omega^2 & m_\ell g\ell - m_\ell\ell^2\Omega^2\end{bmatrix}\begin{bmatrix}q_r \\ \phi_y\end{bmatrix} = \begin{bmatrix}-(m_{e,r}+m_\ell(1+\cos^2\bar{\theta}_{in}))\\ -m_\ell\ell\end{bmatrix}\ddot{R}_o+\begin{bmatrix}m_\ell\Omega^2 \\ m_\ell\ell\Omega^2\end{bmatrix}R_o \tag{3.2}$$

$$\mathbf{M}_l\ddot{\bar{\mathbf{q}}}_l+\mathbf{K}_l\bar{\mathbf{q}}_l=\mathbf{b}_l\ddot{R}_o+\mathbf{d}_lR_o.$$

$$\Omega=\frac{\omega_{in}}{a_c} \tag{3.3}$$

3.2 Optimized vibration control

In this research, the access control method by Yamaura and Ono [37, 38, 39] was used to designed the optimized vibrationless trajectory.

3.2.1 Three periods trajectory design

The trajectory was designed into three periods: the acceleration period, the constant velocity period, and the deceleration period. The trajectory can be illustrated as in Figs. 3.4 and 3.5.

During the acceleration period, the slewing motion was accelerated from a rest condition to the desired velocity or called "the control velocity". At the same time, the boom was lifted to counter this hoisted load's sway due to the centrifugal force. During the constant velocity period, the crane kept slewing at constant velocity. The lifting angle was fixed during this period. During the deceleration period, the slewing motion was decelerated from the desired velocity to stop while the boom angle was lowered back to initial position. The angular deceleration of the slewing direction was equal to the minus of the acceleration period. These trajectories were written as the function

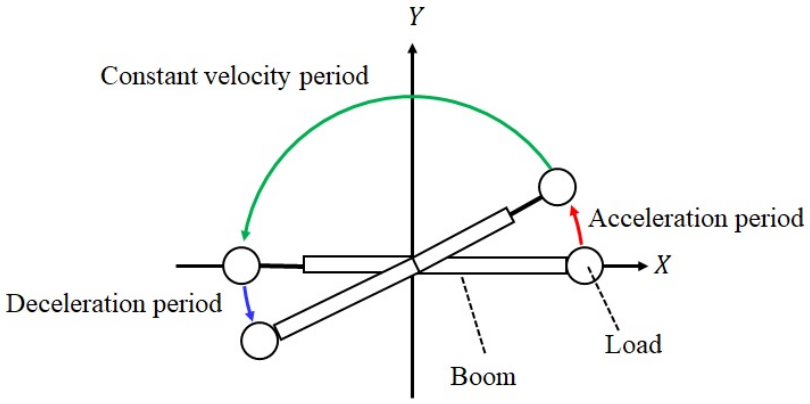

Fig. 3.4: The position of boom tip in the optimized trajectory in slewing direction

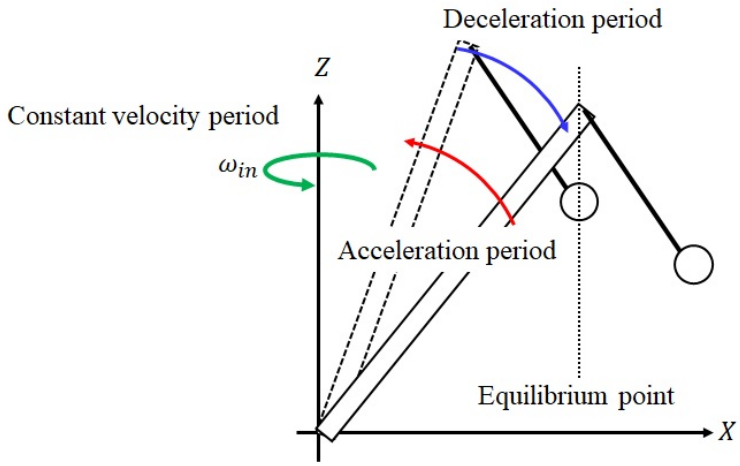

Fig. 3.5: The position of boom tip in the optimized trajectory in lifting direction

of time as

$$\ddot{u}(t) = \begin{cases} \ddot{u}_{in} & ;0 < t < T_c \\ 0 & ;T_c < t < T_c + T_{const} \\ -\ddot{u}_{in} & ;T_c + T_{const} < t < 2T_c + T_{const} \end{cases}, \tag{3.4}$$

$$\dot{R}_o(t) = \begin{cases} \dot{R}_{up} & ;0 < t < T_c \\ 0 & ;T_c < t < T_c + T_{const} \\ \dot{R}_{down} & ;T_c + T_{const} < t < 2T_c + T_{const} \end{cases}. \tag{3.5}$$

where T_c is the control period. The control period is the designed duration of the acceleration and the deceleration periods. In this trajectory, the total rotation of the slewing motion was arbitrarily designated by adjusting the duration of the constant velocity period, T_{const}. This was the advantage of this trajectory design.

3.2.2 Design of the vibrationless trajectory

This section discusses the designing of the optimal driving trajectory of the flexible rotary crane which resulted in zero vibration.

3.2.2.1 Modal coordinates transformation

In order to perform the optimization, it was convenient to express the equation of motion with independent coordinates and natural frequencies. However, the equation of motion in Eqs. (3.1) and (3.2) had the coupling motion between the tip and the hoisted load. Therefore, these coordinates were uncoupled by transforming the equation of motion into modal coordinates systems.

The modal analysis was performed on Eqs. (3.1) and (3.2), and the modal matrix $\boldsymbol{\Phi}_i = \begin{bmatrix}\boldsymbol{\phi}_{i,1} & \boldsymbol{\phi}_{i,2}\end{bmatrix}$ was calculated where i is either s for slewing direction or l for lifting motion. It was assumed that the physical coordinates $\mathbf{q}_i$ had the relationship to the modal coordinates vector as

$$\mathbf{q}_i = \boldsymbol{\Phi}_i \boldsymbol{\eta}_i. \tag{3.6}$$

Equation 3.6 was substituted into Eqs. (3.1) and (3.2), and $\boldsymbol{\Phi}_i^T$ was multiplied to the equation the from the left side. The equation of motion of the proposed control models were rewritten as follows;

$$\begin{aligned}
\boldsymbol{\Phi}_s^T \mathbf{M}_s \boldsymbol{\Phi}_s \ddot{\boldsymbol{\eta}}_s + \boldsymbol{\Phi}_s^T \mathbf{K}_s \boldsymbol{\Phi}_i \boldsymbol{\eta}_s &= \boldsymbol{\Phi}_s^T \mathbf{b}_s \ddot{u}, \\
\ddot{\boldsymbol{\eta}}_s + \boldsymbol{\Lambda}_s \boldsymbol{\eta}_s &= \mathbf{b}_s \ddot{u}, \\
\begin{bmatrix}\ddot{\eta}_{s,1} \\ \ddot{\eta}_{s,2}\end{bmatrix} + \begin{bmatrix}\omega_{s,1}^2 & 0 \\ 0 & \omega_{s,2}^2\end{bmatrix} \begin{bmatrix}\eta_{s,1} \\ \eta_{s,2}\end{bmatrix} &= \begin{bmatrix}b_{s,1} \\ b_{s,2}\end{bmatrix} \ddot{u},
\end{aligned} \tag{3.7}$$

$$\begin{aligned}
\boldsymbol{\Phi}_l^T \mathbf{M}_l \boldsymbol{\Phi}_l \ddot{\boldsymbol{\eta}}_l + \boldsymbol{\Phi}_l^T \mathbf{K}_l \boldsymbol{\Phi}_l \boldsymbol{\eta}_l &= \boldsymbol{\Phi}_l^T \mathbf{b}_l \ddot{R}_o + \boldsymbol{\Phi}_l^T \mathbf{d}_l R_o, \\
\ddot{\boldsymbol{\eta}}_l + \boldsymbol{\Lambda}_l \boldsymbol{\eta}_l &= \mathbf{b}_l \ddot{R}_o + \mathbf{d}_l R_o, \\
\begin{bmatrix}\ddot{\eta}_{l,1} \\ \ddot{\eta}_{l,2}\end{bmatrix} + \begin{bmatrix}\omega_{l,1}^2 & 0 \\ 0 & \omega_{l,2}^2\end{bmatrix} \begin{bmatrix}\eta_{l,1} \\ \eta_{l,2}\end{bmatrix} &= \begin{bmatrix}b_{l,1} \\ b_{l,2}\end{bmatrix} \ddot{R}_o + \begin{bmatrix}d_{l,1} \\ d_{l,2}\end{bmatrix} R_o.
\end{aligned} \tag{3.8}$$

3.2.2.2 Acceleration minimization

To calculate the vibrationless trajectory, the minimization problem was chosen. In the machinery such as a crane, the mechanism is driven with force or acceleration. Therefore, the vibrationless trajectory was derived from the minimization of the input acceleration. The cost functions are written in Eq. (3.9) for slewing motion, and Eq. (3.10) for the lifting motion.

$$J_s = \int_{-\infty}^{\infty} \frac{1}{2} \ddot{u}_{in}^2 \, \mathrm{d}t, \tag{3.9}$$

$$J_l = \int_{-\infty}^{\infty} \frac{1}{2} \ddot{R}_o^2 \, \mathrm{d}t, \tag{3.10}$$

However, both $\ddot{u}_{in}$ and $\ddot{R}_o$ were constrained by the control models. To account these constraints, the modal equation of motion from Eqs. (3.7) and (3.8) were considered. Then the cost functions of the crane systems become

$$J_i = \int_0^{T_c} L_i \, \mathrm{d}t, \tag{3.11}$$

where

$$L_s = \frac{1}{2}\ddot{u}_{in}^2 + p_{1,s}(\ddot{\eta}_{1,s} + \omega_{1,s}^2\eta_{1,s} - b_{1,s}\ddot{u}_{in}) + p_{2,s}(\ddot{\eta}_{2,s} + \omega_{2,s}^2\eta_{2,s} - b_{2,s}\ddot{u}_{in}), \tag{3.12}$$

$$L_l = \frac{1}{2}\ddot{R}_o^2 + p_{1,l}(\ddot{\eta}_{1,l} + \omega_{1,l}^2\eta_{1,l} - b_{1,l}\ddot{R}_o - d_{1,l}R_o) + p_{2,l}(\ddot{\eta}_{2,l} + \omega_{2,l}^2\eta_{2,l} - b_{2,l}\ddot{R}_o - d_{2,l}R_o). \tag{3.13}$$

$p_{m,n}$ is the Lagrange's multiplier.

The Euler's minimization, Eq. (3.14), was used on Eqs. (3.12) and (3.13), where $w = \{u_{in}, \eta_{1,s}, \eta_{2,s}, p_{1,s}, p_{2,s}\}$ for slewing direction and $w = \{R_o, \eta_{1,l}, \eta_{2,l}, p_{1,l}, p_{2,l}\}$ for lifting direction.

$$\frac{\partial L_i}{\partial w} - \frac{\mathrm{d}}{\mathrm{d}t}\frac{\partial L_i}{\partial \dot{w}} + \frac{\mathrm{d}^2}{\mathrm{d}t^2}\frac{\partial L_i}{\partial \ddot{w}} = 0 \tag{3.14}$$

The trajectory was derived by solving the system of equations that was obtained from Eq. (3.14).

Slewing control

The minimization on the slewing control model with Eq. (3.14) resulted in

$$u_{in}^{(4)} - \ddot{\mathbf{p}}_s^T\mathbf{b}_s = 0 \tag{3.15}$$

$$\ddot{\mathbf{p}} + \mathbf{\Lambda}_s\mathbf{p} = 0 \tag{3.16}$$

$$\ddot{\boldsymbol{\eta}}_s + \mathbf{\Lambda}_s\boldsymbol{\eta}_s = \mathbf{b}_s\ddot{u}. \tag{3.17}$$

As shown above, the calculation would result in Eq. (3.17) which repeating Eq. (3.7). The vector $\mathbf{p}$ is the vector of Lagrange's multiplier. The input trajectory u_{in} was obtained by solving Eqs. (3.15) to (3.17). To solve this system of equations, the boundary conditions were required. As shown in Section 3.2.1, only trajectory during the acceleration period was required for the slewing control. In the slewing control, the slewing motion was accelerated from zero velocity at $t = 0$ to the designated control velocity $\dot{u}_{in,c,e}$ at $t = T_c$ without vibration at either point. Under this criterion, the boundary conditions were designed as

$$\eta_{1,s}(T_c) = 0, \tag{3.18}$$

$$\dot{\eta}_{1,s}(T_c) = 0, \tag{3.19}$$

$$\eta_{2,s}(T_c) = 0, \tag{3.20}$$

$$\dot{\eta}_{2,s}(T_c) = 0, \tag{3.21}$$

$$u_{in}(0) = 0, \tag{3.22}$$

$$\dot{u}_{in}(0) = 0, \tag{3.23}$$

$$\dot{u}_{in}(T_c) = \dot{u}_{in,c,e}, \tag{3.24}$$

$$\left[\frac{\partial L}{\partial \dot{u}_{in}} - \frac{\mathrm{d}}{\mathrm{d}t}\frac{\partial L}{\partial \ddot{u}_{in}}\right]_{t=T_c} = 0, \tag{3.25}$$

$$\eta_{1,s}(0) = 0, \tag{3.26}$$

$$\dot{\eta}_{1,s}(0) = 0, \tag{3.27}$$

$$\eta_{2,s}(0) = 0, \tag{3.28}$$

$$\dot{\eta}_{2,s}(0) = 0. \tag{3.29}$$

These conditions were called “Constant-velocity control”.

Lifting control

The lifting trajectory was derived in the similar fashion. The results from the minimization on the lifting control model were

$$R_o^{(4)} - \ddot{\mathbf{p}}_l^T \mathbf{b}_l - \mathbf{p}^T \mathbf{d}_l = 0 \tag{3.30}$$

$$\ddot{\mathbf{p}} + \mathbf{\Lambda}_l \mathbf{p} = 0 \tag{3.31}$$

$$\ddot{\boldsymbol{\eta}}_l + \mathbf{\Lambda}_l \boldsymbol{\eta}_l = \mathbf{b}_l \ddot{R}_o + \mathbf{d}_l R_o. \tag{3.32}$$

Then, the lifting trajectory was derived by solving the systems equations of Eqs. (3.30) to (3.32). The lifting trajectory was designed to move the boom tip from initial radius $R_{c,s,0}$ at $t = 0$ to $R_{c,s,e}$ at $t = T_c$ without causing the vibration. This condition was called the “Point-to-Point (PTP) control”. These conditions are written in mathematical form as

$$\eta_{1,l}(T_c) = \eta_{1,l,e}, \tag{3.33}$$

$$\dot{\eta}_{1,l}(T_c) = 0, \tag{3.34}$$

$$\eta_{2,l}(T_c) = \eta_{2,l,e}, \tag{3.35}$$

$$\dot{\eta}_{2,l}(T_c) = 0, \tag{3.36}$$

$$R_o(0) = R_{c,s,0}, \tag{3.37}$$

$$\dot{R}_o(0) = 0, \tag{3.38}$$

$$R_o(T_c) = R_{c,s,e}, \tag{3.39}$$

$$\dot{R}_o(T_c) = 0, \tag{3.40}$$

$$\eta_{1,l}(0) = \eta_{1,l,0}, \tag{3.41}$$

$$\dot{\eta}_{1,l}(0) = 0, \tag{3.42}$$

$$\eta_{2,l}(0) = \eta_{2,l,0}, \tag{3.43}$$

$$\dot{\eta}_{2,l}(0) = 0. \tag{3.44}$$

where $\eta_{i,l,n}$ is the modal amplitude of the system at equilibrium condition, and $i = \{1, 2\}$ and $e = \{0, e\}$ means the amplitude are calculated at $t = 0$ and T_c respectively. The equilibrium amplitudes were calculated from the centrifugal force that was acting on the hoisted load. The equilibrium displacement in physical coordinates were calculated with

$$q_{r,c} = \frac{m_\ell R_c}{k_{r,e}} \omega_{in}^2, \tag{3.45}$$

$$\phi_{y,c} = \tan\left(\frac{R_c \omega_{in}^2}{g}\right), \tag{3.46}$$

where R_c is the radius at initial lifting angle. The physical coordinates were transformed to modal coordinates as

$$\begin{bmatrix} \eta_{1,l,c} \\ \eta_{2,l,c} \end{bmatrix} = \mathbf{\Phi}_l^{-1} \begin{bmatrix} q_{r,e} \\ \phi_{y,e} \end{bmatrix}. \tag{3.47}$$

During the acceleration period, the boom was lifted up from the initial state. The equilibrium amplitudes were

$$\begin{bmatrix} \eta_{1,l,0} \\ \eta_{2,l,0} \end{bmatrix} = \begin{bmatrix} 0 \\ 0 \end{bmatrix}, \tag{3.48}$$

$$\begin{bmatrix}\eta_{1,l,e}\\ \eta_{2,l,e}\end{bmatrix} = \begin{bmatrix}\eta_{1,l,c}\\ \eta_{2,l,c}\end{bmatrix}. \tag{3.49}$$

During the deceleration period, the boom angle was lowered back to initial angle. The process started from the state which the centrifugal force was already applied, and all motion stop at the end. Therefore, the equilibrium amplitudes were

$$\begin{bmatrix}\eta_{1,l,0}\\ \eta_{2,l,0}\end{bmatrix} = \begin{bmatrix}\eta_{1,l,c}\\ \eta_{2,l,c}\end{bmatrix}, \tag{3.50}$$

$$\begin{bmatrix}\eta_{1,l,e}\\ \eta_{2,l,e}\end{bmatrix} = \begin{bmatrix}0\\ 0\end{bmatrix}. \tag{3.51}$$

3.2.2.3 Jerk minimization

The trajectory under the acceleration minimization gave the trajectory with $\ddot{u}_{in}(0) \neq 0$. When applying this to the actuators, the high frequency bandwidth is required to accelerate the mechanism with this function. This is difficult for the crane because the working bandwidth of the crane is around 2[Hz], which is considerably in low bandwidth. The actuator might not work properly with the designed trajectory. Therefore, the first order filter frequency weighting function[38, 39] was applied to solve this issue. This function added additional constraint to the cost function. This new cost function allowed the minimization of the initial jerk of the trajectory through additional boundary conditions. Thus, this trajectory was called "Jerk minimization". To explain this function, let $U_{in}(s)$ be the Laplace transform of $u_{in}(t)$, the relation between input signal and its weighted function, $v_{in}(t) = \mathcal{L}^{-1}\{V_{in}(s)\}$, is described in Eq. (3.52).

$$s^2 V_{in}(s) = W(s) s^2 U_{in}(s), \tag{3.52}$$

where, j is a imaginary number, $s = \omega j$, and $W(s)$ is the frequency weighting function. The first-order frequency function, W_1, is designed with Eqs. (3.53) to (3.55), where γ is weighting coefficient, and $\omega_{cut} = 2\pi f_{cut}$ is the cut-off frequencies.

$$W_1(s) = \frac{1+\beta s}{1+\alpha s} \tag{3.53}$$

$$\alpha = \frac{1}{\omega_{cut}}\sqrt{\frac{3+\gamma}{1+3\gamma}} \tag{3.54}$$

$$\beta = \gamma\alpha \tag{3.55}$$

When $\gamma > 1$, the amplitude of the weighting function, $\|W_1(s)\|$, of the frequency components that higher than the cut-off frequency becomes large. Thus, after the optimization, these high frequency components become smaller. By substituting Eq. (3.53) into (3.52), then calculated its

inverse Laplace transform, the relation of the first-order filter input function in the time domain was obtained as follows:

$$\dot{z}_{in} = \frac{-z_{in} + v_{in}}{\beta}, \tag{3.56}$$

where

$$z_{in}(t) = \frac{\alpha v_{in}(t) - \beta u_{in}(t)}{\alpha - \beta}. \tag{3.57}$$

Then, the minimization problem, L was replaced with Eq. (3.58) when the first-order filter was used. μ is the additional Lagrange's multiplier.

$$L = \frac{1}{2}\ddot{v}_{in}^2 + \mathbf{p}^T(\ddot{\mathbf{x}} + \mathbf{\Lambda}\mathbf{x} - \mathbf{b}\ddot{u}_{in}) + \mu\left(\dot{z}_{in} + \frac{z_{in} - v_{in}}{\beta}\right) \tag{3.58}$$

The optimized input trajectory with the first order filter, v_{in}, was derived by substituting Eq. (3.58) into (3.11), where $w = \{v_{in}, \mathbf{x}, \mathbf{p}, \mu, z_{in}\}$. This yields Eqs. (3.6), (3.13), (3.56), (3.59) and (3.60). Then, v_{in} was obtained by solving these equations under designated boundary condition for the first order filter.

$$v_{in}^{(4)} - \frac{\alpha\ddot{\mathbf{p}}^T\mathbf{b}}{\beta} - \frac{\mu}{\beta} = 0 \tag{3.59}$$

$$\frac{\mu}{\beta} - \dot{\mu} + \frac{(\alpha - \beta)}{\beta}\ddot{\mathbf{p}}^T\mathbf{b} = 0 \tag{3.60}$$

When the first order filter was used on the slewing control model, the optimization problem was rewritten as

$$L_s = \frac{1}{2}\ddot{v}_{in}^2 + p_{1,s}(\ddot{\eta}_{1,s} + \omega_{1,s}^2\eta_{1,s} - b_{1,s}\ddot{u}_{in}) + p_{2,s}(\ddot{\eta}_{2,s} + \omega_{2,s}^2\eta_{2,s} - b_{2,s}\ddot{u}_{in}) + \mu_s\left(\dot{z}_{in} + \frac{z_{in} - v_{in}}{\beta}\right) \tag{3.61}$$

and the additional boundary conditions were

$$\ddot{\eta}_{1,s}(T_c) = 0, \tag{3.62}$$

$$\ddot{\eta}_{2,s}(T_c) = 0, \tag{3.63}$$

$$\ddot{\eta}_{1,s}(0) = 0, \tag{3.64}$$

$$\ddot{\eta}_{2,s}(0) = 0, \tag{3.65}$$

$$\ddot{u}_{in}(0) = 0, \tag{3.66}$$

$$\ddot{u}_{in}(T_c) = 0. \tag{3.67}$$

Similarly, the optimization problem of the lifting control model became

$$\begin{aligned} L_l =& \frac{1}{2}\ddot{v}_{in}^2 + p_{1,l}(\ddot{\eta}_{1,l} + \omega_{1,l}^2\eta_{1,l} - b_{1,l}\ddot{R}_o - d_{1,l}R_o) + p_{2,l}(\ddot{\eta}_{2,l} + \omega_{2,l}^2\eta_{2,l} - b_{2,l}\ddot{R}_o - d_{2,l}R_o) \\ &+ \mu_l\left(\dot{z}_{in} + \frac{z_{in} - v_{in}}{\beta}\right) \end{aligned}, \tag{3.68}$$

and the additional boundary conditions were

$$\ddot{\eta}_{1,l}(T_c) = 0, \tag{3.69}$$

$$\ddot{\eta}_{2,l}(T_c) = 0, \tag{3.70}$$

$$\ddot{\eta}_{1,l}(0) = 0, \tag{3.71}$$

$$\ddot{\eta}_{2,l}(0) = 0, \tag{3.72}$$

$$\ddot{R}_o(0) = 0, \tag{3.73}$$

$$\ddot{R}_o(T_c) = 0. \tag{3.74}$$

3.3 Testing of the proposed control model

In order to validate the performance of the proposed vibration control model with the flexible boom, the numerical simulation and the experiment were performed on the example crane models. In this dissertation, two example models were used: 1) the numerical simulation on the crane model that mimicked the real size crane, 2) the numerical simulation and experiment on the laboratory size crane model.

3.3.1 Numerical simulation on typical rotary crane model

Firstly, the proposed vibration control method was trial on the flexible crane model from Appendix C. This model used the specification of the physical properties that were mimicked the real-size rotary crane. The physical specification of this model is written in Table 3.1.

Table 3.1: The specification of the rotary crane model for validating the controller effectiveness

Specification	values
Slewing platform mass	800 [kg]
Slewing platform radius and height	4, 1 [m]
Boom length	10 [m]
Boom cross-section	40, 20 [cm]
Boom thickness	2 [cm]
Booms' density	7800 [kg/m^2]
Booms' Young's modulus	210 [GPa]
Rope length	10 [m]

3.3.1.1 Calculation of equivalent mass and stiffness of the boom

In order to calculate the vibrationless trajectory, the equivalent mass and stiffness of the boom must be extracted from the crane model. As presented in this dissertation, the flexible boom was considered as the Euler-Bernoulli's beam. In the case of the control model, the boom was considered as a one fixed-end cantilever beam. In the slewing direction, the equivalent mass and stiffness were

$$m_{e,v} = \frac{33 m_{boom}}{144}, \tag{3.75}$$

$$k_{e,v} = \frac{3 E_{boom} I_v}{L^3}, \tag{3.76}$$

where m_{boom} is the mass of boom, E is the Young's modulus, I_v is the second moment of inertia with respect to the slewing motion, and L_{boom} is the boom length. To calculate the equivalent parameter in a radial direction, firstly, the rotated fixed-end beam as shown in Fig. 3.6 was considered. In this figure, $\bar{w}_i$ and $\bar{F}_i$ are the function of the deflection of the beam and the forces in i axis on the boom's body coordinates system. Then, the z direction on the boom's body coordinates system was focused. In this direction, the deflection of the tip was calculated as

$$\bar{w}_z = \frac{\bar{F}_z}{k_{e,z}}, \tag{3.77}$$

where $k_{e,z}$ is the equivalent stiffness in z direction. If the force was added in the radial direction such as F_r in Fig. 3.6, its relation with the $\bar{F}_z$ became

$$\bar{F}_z = F_r \sin\theta_{lift,0}. \tag{3.78}$$

At the same time, the deflection of the boom tip in the radial direction was

$$w_r = \bar{w}_z \sin\theta_{lift,0} = \frac{\bar{F}_z}{k_{e,z}} \sin\theta_{lift,0}. \tag{3.79}$$

The relation between F_r and w_r was written in Hook's law as

$$w_r = \frac{F_r}{k_{e,r}} = \frac{\bar{F}_z}{k_{e,r} \sin\theta_{lift,0}}. \tag{3.80}$$

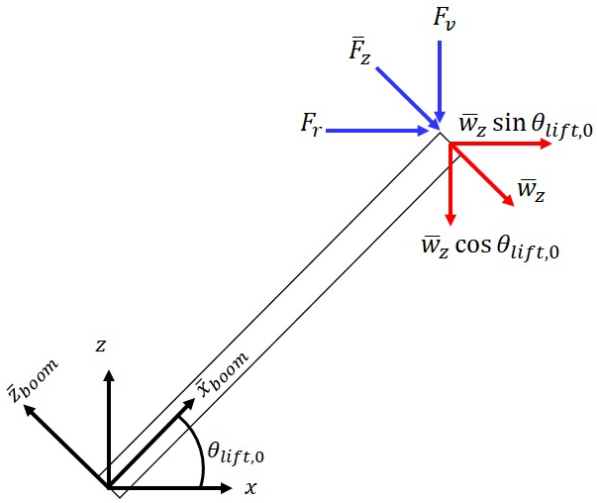

Fig. 3.6: The rotated flexible beam example

Since Eq. (3.79) was equal to Eq. (3.80), the equivalent stiffness in radial direction was calculated as

$$k_{e,r} = \frac{k_{e,z}}{\sin\theta_{lift,0}^2}, \tag{3.81}$$

where the equivalent stiffness $k_{e,z}$ was calculated the same way as Eq. (3.76).

To calculate the equivalent mass in radial direction, the natural angular velocity of the boom tip was focused. Since the simple beam theory was used, the natural vibration of the boom tip in vertical (z_{boom}) and radial direction were the same. Thus, their relation can be written as

$$\begin{aligned} \omega_{nat,z} &= \omega_{nat,r}, \\ \frac{k_{e,z}}{m_{e,z}} &= \frac{k_{e,r}}{m_{e,r}}. \end{aligned} \tag{3.82}$$

Thus,

$$m_{e,r} = \frac{m_{e,z}}{\sin\theta_{lift,0}^2}. \tag{3.83}$$

3.3.1.2 Simulation results with the minimum acceleration trajectory

The equivalent mass and stiffness coefficient for designing the control model were calculated by using the above calculations and the crane specification. The equivalent masses and stiffnesses of the example model in Appendix C were summarized in Table 3.2. Table 3.2 also specified the control slewing velocity for this simulation.

Firstly, the simulation was performed at variated T_c and a_c. These two parameters were independent to the model specification, thus, they were used to determine the optimized control condition.

Table 3.2: Equivalent control model parameter of the crane in Appendix C

Parameter	Value
$m_{e,y}$	934.6 [kg]
$k_{e,y}$	21 565 [N/m]
$m_{e,r}$	1241.59 [kg]
$k_{e,r}$	53 619[N/m]
m_ℓ	1000 [kg]
ω_{in}	1 [RPM]
T_n	6.4 [s]

In this simulation, the crane was driven from rested condition until the slewing velocity reached the designated value. Then, the motion kept at the constant velocity period.

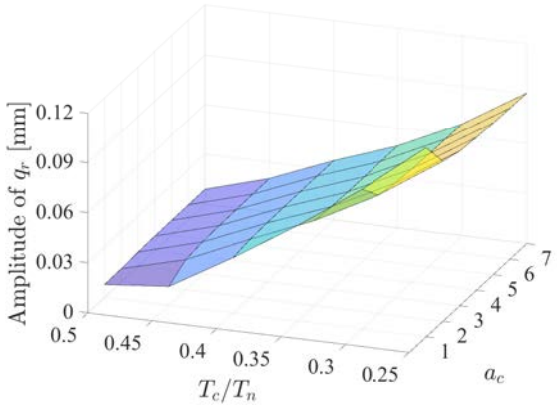

(a) Boom tip amplitude in radial direction

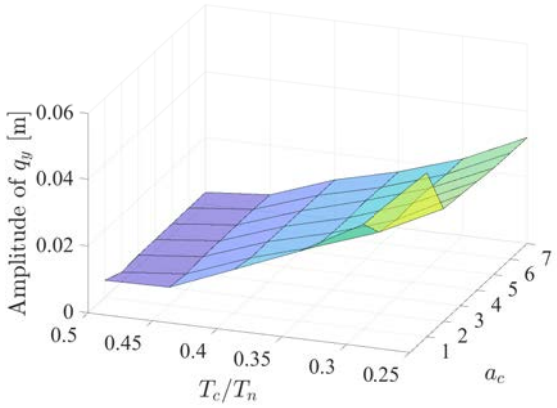

(b) Boom tip amplitude in slewing direction

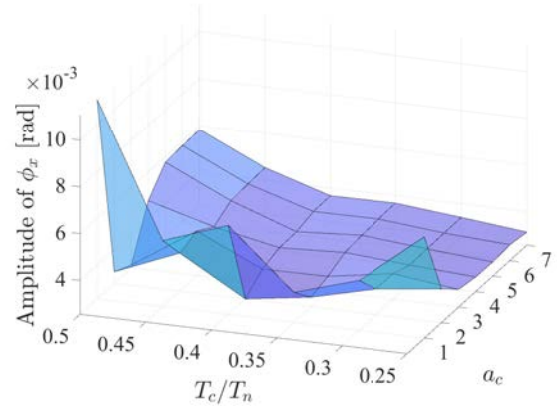

(c) Load sway amplitude in slewing direction

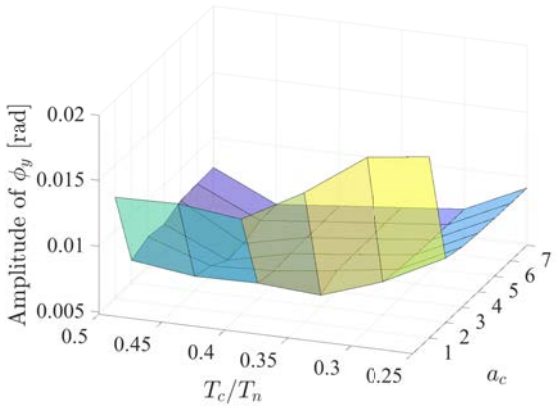

(d) Load sway amplitude in radial direction

Fig. 3.7: The sway of the boom tip and the hoisted load during the simulation on Appendix C model

The average amplitude during the constant velocity period were collected and presented in Fig. 3.7. From this figure, the amplitude of the boom tip increased as the control period decreased. However, around $T_c = 0.45T_n$, the amplitude of the boom tip revealed its minimum point. The amplitude of the hoisted load angle in radial direction also showed the similar results. However, the hoisted load angle in slewing direction showed the mixed relation. The sign of the convergence showed around $T_c = 0.45T_n$ and $a_c = 4$ which was similar to the other results, and $T_c = 0.25T_n$ and $a_c = 7$ which similar to the condition in [35].

In Fig. 3.7, after the control period was decreased beyond $T_c = 0.45T_n$, the amplitude of the boom tip in both directions kept on increasing. Since the longer control period also mean the low acceleration, it was understood that as the acceleration increased, the amplitude of these coordinates increased.

Next, the numerical simulation of the crane operation that carried the hoisted load for 90[deg] in slewing angle from the rested position was simulated. The trajectory of the crane was compared between the result from the proposed control model and the reference control model [35]. The reference method was the trajectory of the control model that did not included the flexibility of the boom. Firstly, the controlled trajectory with minimum acceleration was considered. The control condition of $T_c = 0.45T_n$ and $a_c = 4$, and $T_c = 0.25T_n$ and $a_c = 7$ were simulated.

The trajectory with the control condition of $T_c = 0.45T_n$ and $a_c = 4$ was simulated. Figure 3.8 shows the acceleration of this control condition from both models. The calculated trajectory of the boom tip and the hoisted load are shown in Figs. 3.9 to 3.12. At this control condition, the residual vibration of the boom tip from the flexible control was smaller. The amplitude of the residual vibration of the hoisted load from both models showed similar magnitude.

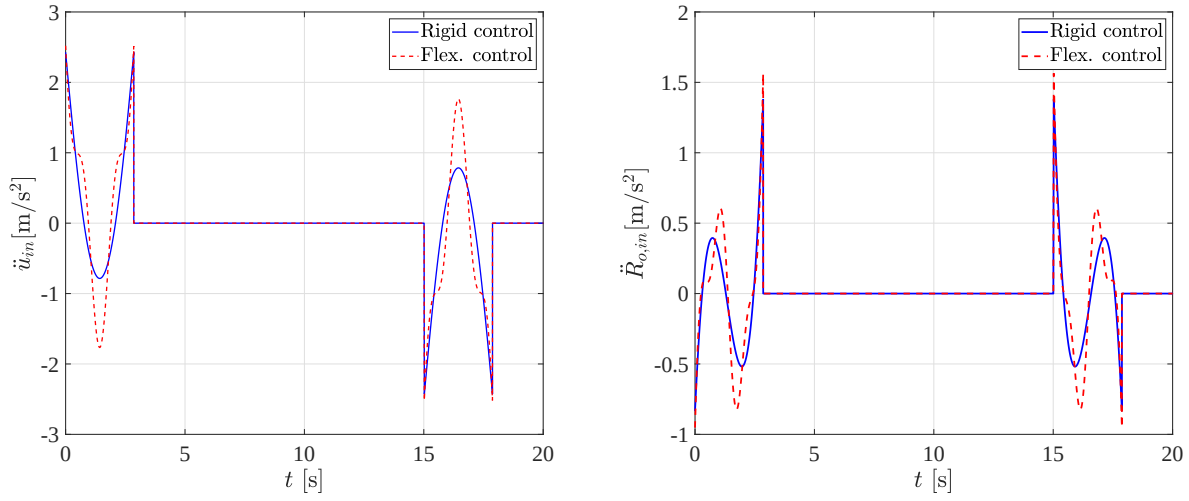

(a) Slewing control (b) Lifting control

Fig. 3.8: Control trajectory acceleration at control condition of $T_c = 0.45T_n$ and $a_c = 4$

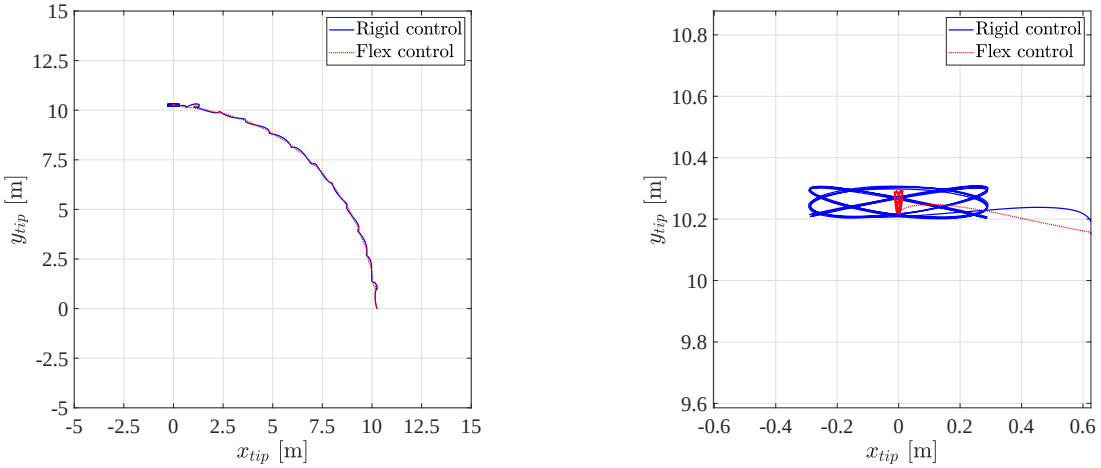

(a) Full trajectory (b) Residual motion

Fig. 3.9: The comparison of the boom tip's trajectory in xy-plane between the control method on Appendix C model at $T_c = 0.45T_n$ and $a_c = 4$ with minimum acceleration trajectory

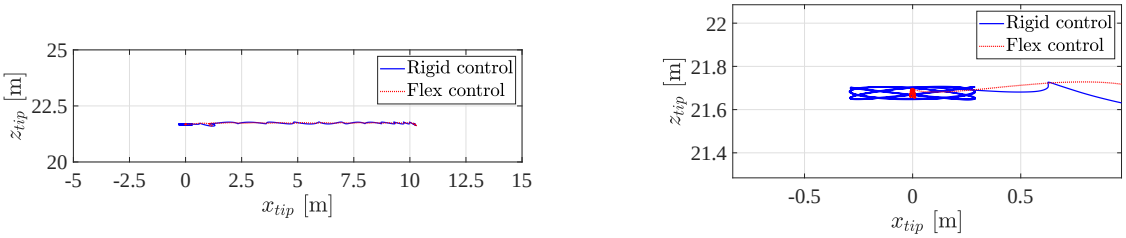

(a) Full trajectory (b) Residual motion

Fig. 3.10: The comparison of the boom tip's trajectory in xz-plane between the control method on Appendix C model at $T_c = 0.45T_n$ and $a_c = 4$ with minimum acceleration trajectory

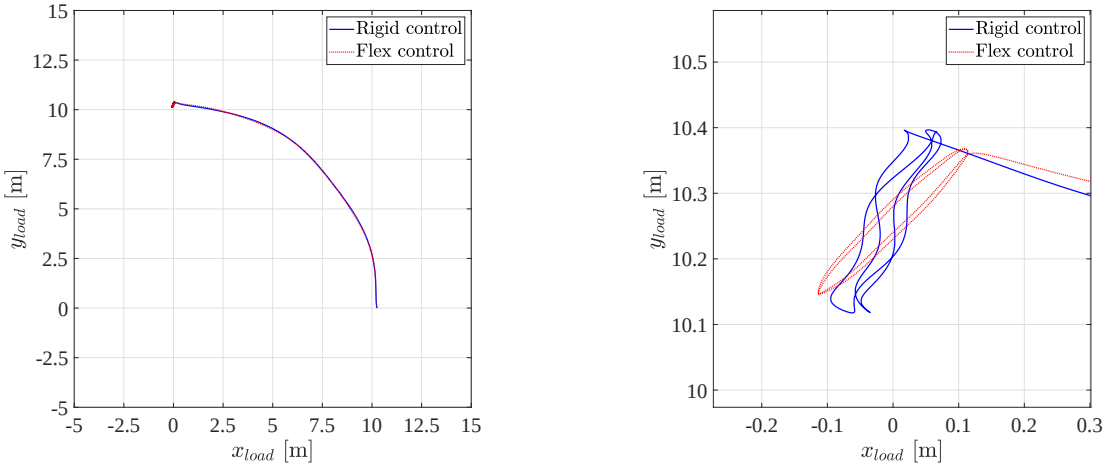

(a) Full trajectory (b) Residual motion

Fig. 3.11: The comparison of the hoisted load's trajectory in xy-plane between the control method on Appendix C model at $T_c = 0.45T_n$ and $a_c = 4$ with minimum acceleration trajectory

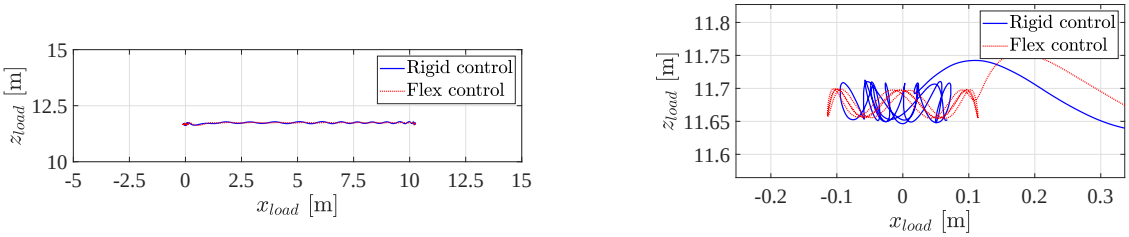

(a) Full trajectory (b) Residual motion

Fig. 3.12: The comparison of the hoisted load's trajectory in xz-plane between the control method on Appendix C model at $T_c = 0.45T_n$ and $a_c = 4$ with minimum acceleration trajectory

Next, the trajectory under the control condition of $T_c = 0.25T_n$ and $a_c = 7$ was simulated. The driving accelerations are shown in Fig. 3.13 and the simulated results are shown in Figs. 3.14 to 3.17.

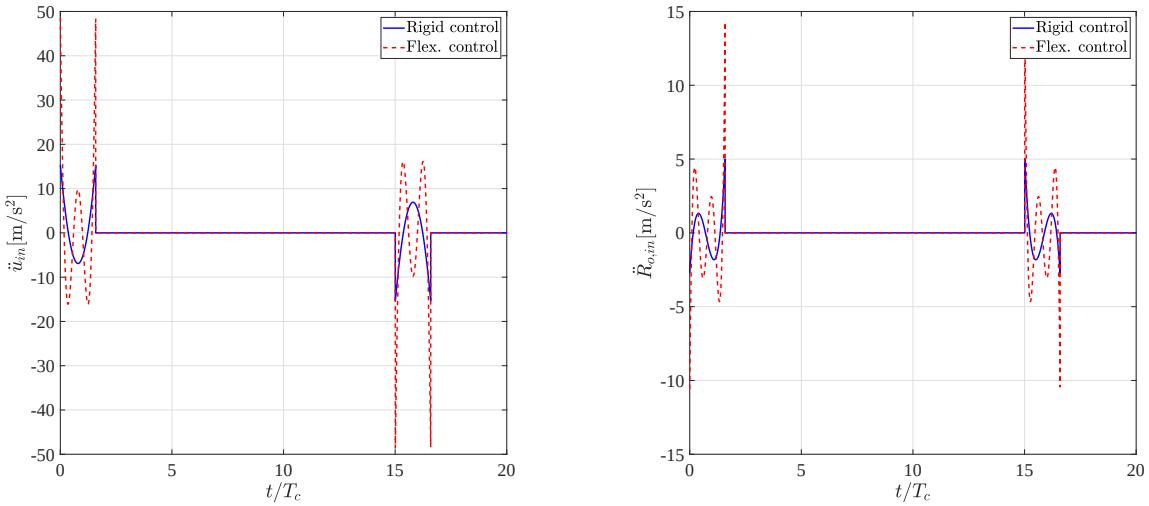

(a) Slewing control (b) Lifting control

Fig. 3.13: Control trajectory acceleration at control condition of $T_c = 0.25T_n$ and $a_c = 7$

Figures 3.14 to 3.17 show that the reference control model that did not consider the boom's flexibility was not able to suppress the vibration of both the boom tip and the load at this condition. On the other hand, the proposed control model was able to suppress the vibration of the boom tip and the hoisted load, as the results showed that the amplitude of the residual vibration of both boom tip and the hoisted load from the proposed control model for flexible boom were significantly smaller than control model for rigid boom.

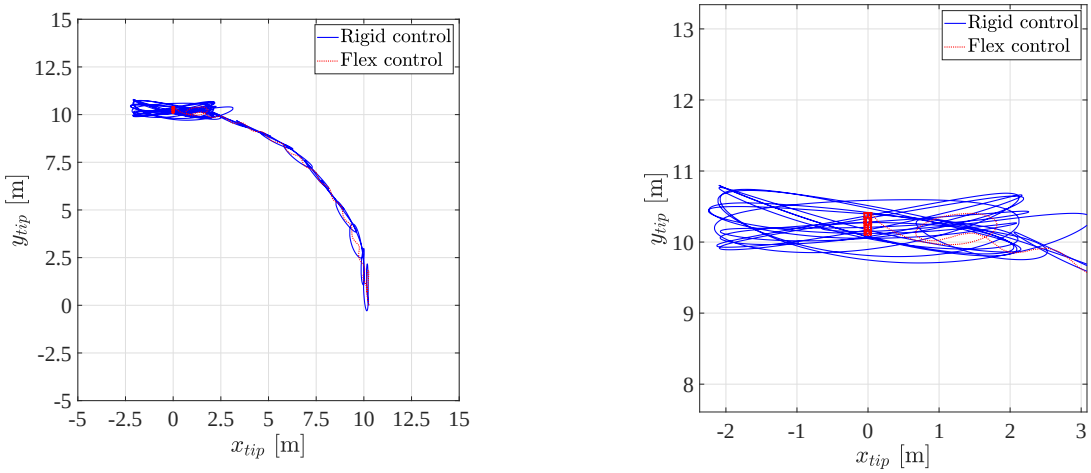

(a) Full trajectory (b) Residual motion

Fig. 3.14: The comparison of the boom tip's trajectory in xy-plane between the control method on Appendix C model at $T_c = 0.25T_n$ and $a_c = 7$ with minimum acceleration trajectory

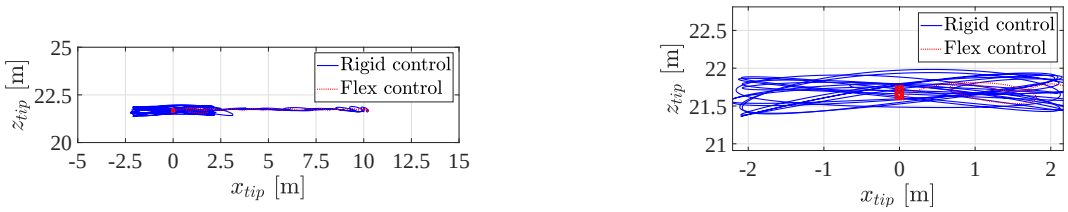

(a) Full trajectory (b) Residual motion

Fig. 3.15: The comparison of the boom tip's trajectory in xz-plane between the control method on Appendix C model at $T_c = 0.25T_n$ and $a_c = 7$ with minimum acceleration trajectory

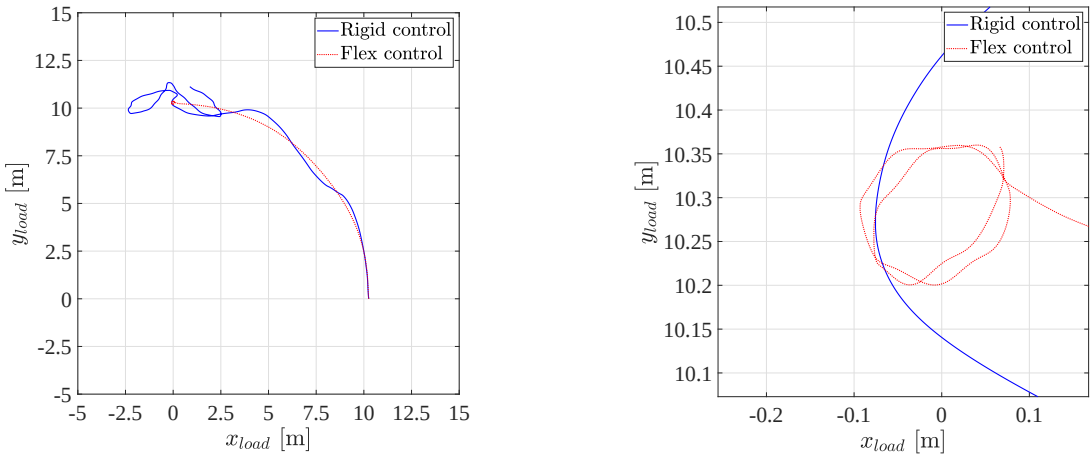

(a) Full trajectory (b) Residual motion

Fig. 3.16: The comparison of the hoisted load's trajectory in xy-plane between the control method on Appendix C model at $T_c = 0.25T_n$ and $a_c = 7$ with minimum acceleration trajectory

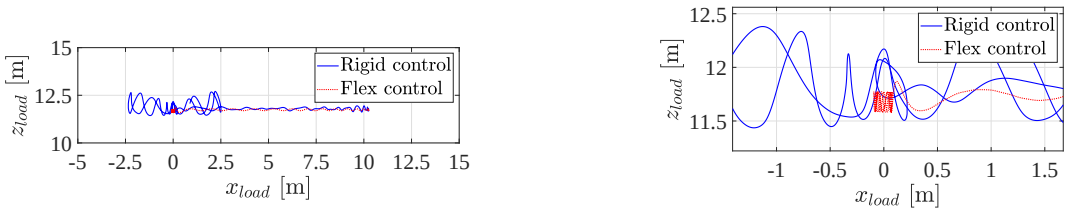

(a) Full trajectory (b) Residual motion

Fig. 3.17: The comparison of the hoisted load's trajectory in xz-plane between the control method on Appendix C model at $T_c = 0.25T_n$ and $a_c = 7$ with minimum acceleration trajectory

It is to mention that the boom was modeled with the Euler's beam theory. Therefore, the amplitude of the vibration under the reference control method might larger than the possible amplitude in the actual crane. Still, under the same dynamic model, the proposed control model was able to suppress the supposedly large amplitude of the vibration of this model.

3.3.1.3 Minimum acceleration trajectory and the minimum jerk trajectory

Next, the results of the trajectory with the minimum jerk were simulated. The same control conditions as in the previous cases were considered. The trajectory of the boom tip and the hoisted load between the minimum acceleration and the minimum jerk were compared.

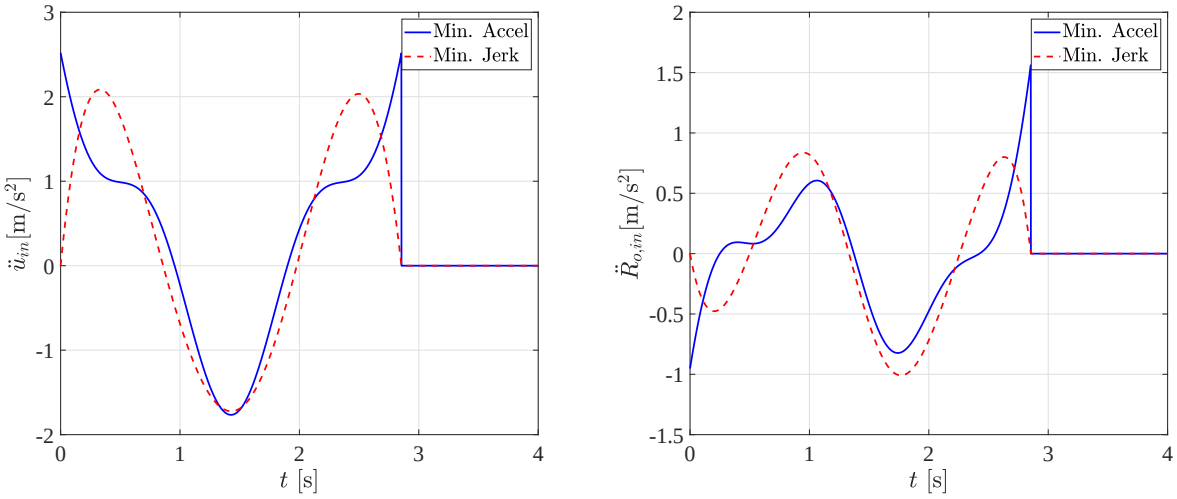

(a) Slewing control (b) Lifting control

Fig. 3.18: Control trajectory acceleration at control condition of $T_c = 0.45T_n$ and $a_c = 4$ of flexible crane

The results showed that the amplitude of the residual vibration from the trajectory with the minimum jerk was larger than the trajectory from the minimum acceleration. The amplitudes increased as the control period became shorter as in the minimum acceleration cases. It could be understood that because the high frequency component in the designed trajectory under minimized jerk was largely reduced, the vibration of the crane in respected to that component was not sufficiently suppress. Therefore, the amplitude of the residual vibration under the minimized jerk trajectory was larger. However, the results from the minimized jerk trajectory still showed an effective suppression of the rotary crane with the flexible boom.

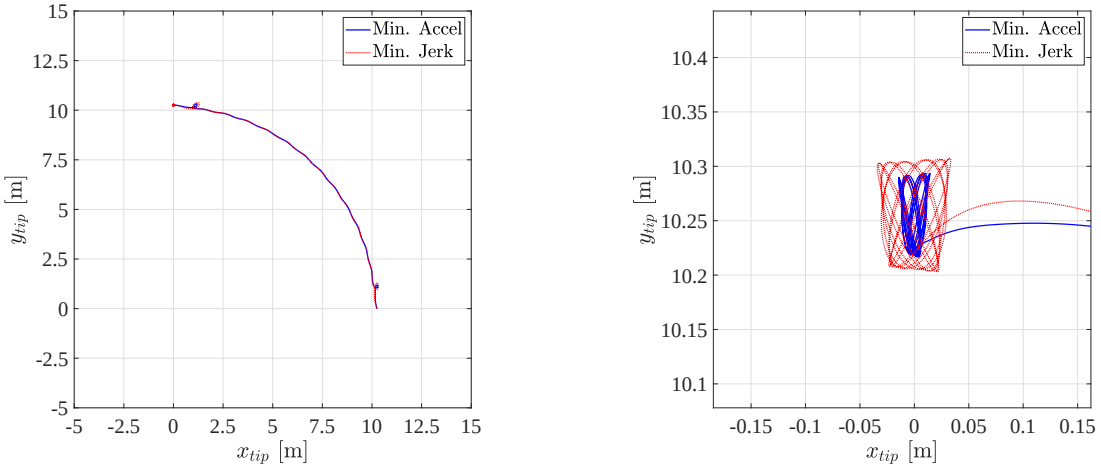

(a) Full trajectory (b) Residual motion

Fig. 3.19: The comparison of the boom tip's trajectory in xy-plane between the control method on Appendix C model at $T_c = 0.45T_n$ and $a_c = 4$ between minimum acceleration and jerk trajectories

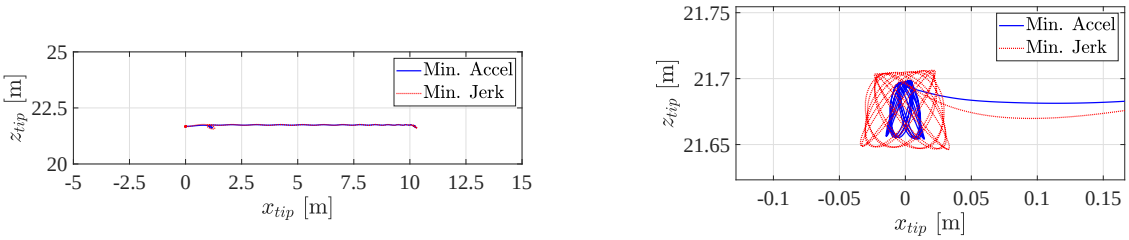

(a) Full trajectory (b) Residual motion

Fig. 3.20: The comparison of the boom tip's trajectory in xz-plane between the control method on Appendix C model at $T_c = 0.45T_n$ and $a_c = 4$ between minimum acceleration and jerk trajectories

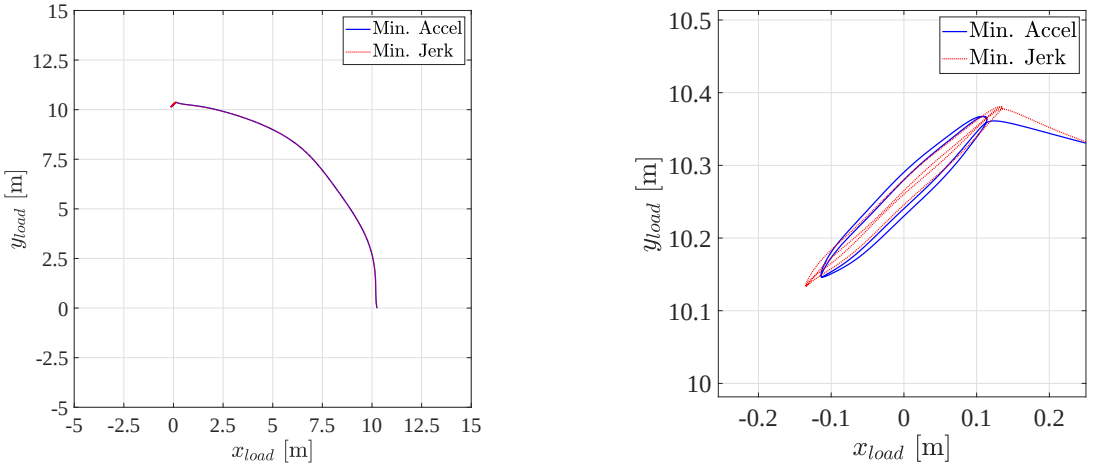

(a) Full trajectory (b) Residual motion

Fig. 3.21: The comparison of the hoisted load's trajectory in xy-plane between the control method on Appendix C model at $T_c = 0.45T_n$ and $a_c = 4$ between minimum acceleration and jerk trajectories

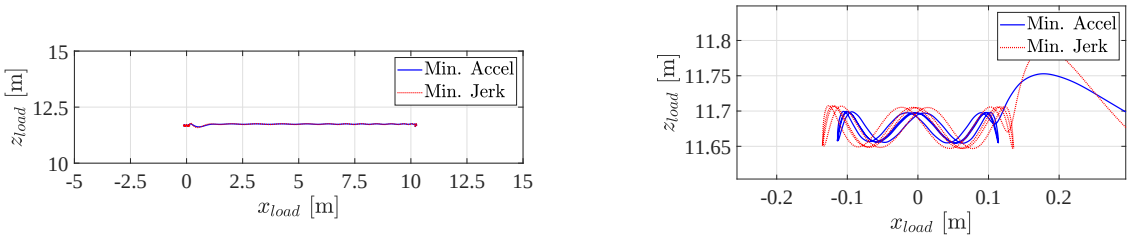

(a) Full trajectory (b) Residual motion

Fig. 3.22: The comparison of the hoisted load's trajectory in xz-plane between the control method on Appendix C model at $T_c = 0.45T_n$ and $a_c = 4$ between minimum acceleration and jerk trajectories

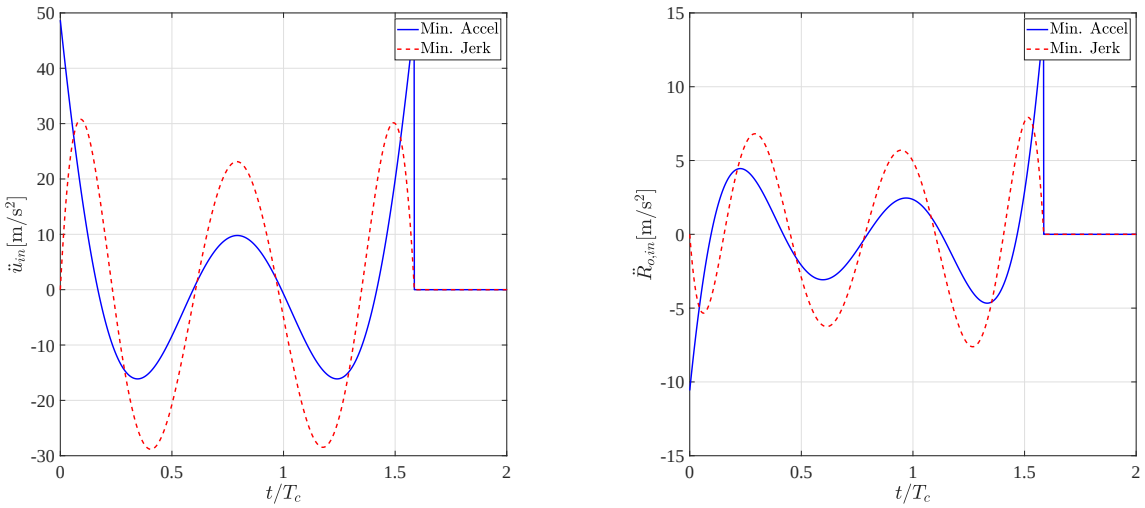

(a) Slewing control (b) Lifting control

Fig. 3.23: Control trajectory acceleration at control condition of $T_c = 0.25T_n$ and $a_c = 7$ of flexible crane

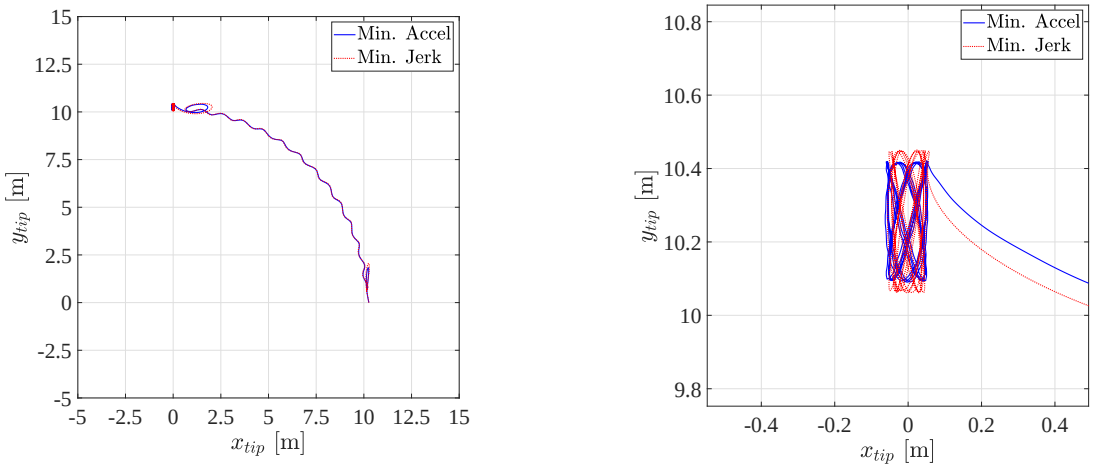

(a) Full trajectory (b) Residual motion

Fig. 3.24: The comparison of the boom tip's trajectory in xy-plane between the control method on Appendix C model at $T_c = 0.25T_n$ and $a_c = 6$ between minimum acceleration and jerk trajectories

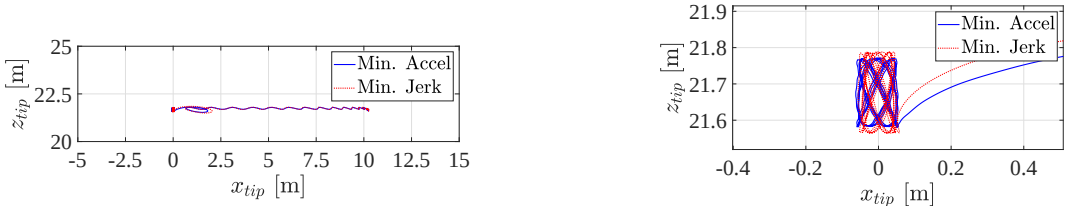

(a) Full trajectory (b) Residual motion

Fig. 3.25: The comparison of the boom tip's trajectory in xz-plane between the control method on Appendix C model at $T_c = 0.25T_n$ and $a_c = 6$ between minimum acceleration and jerk trajectories

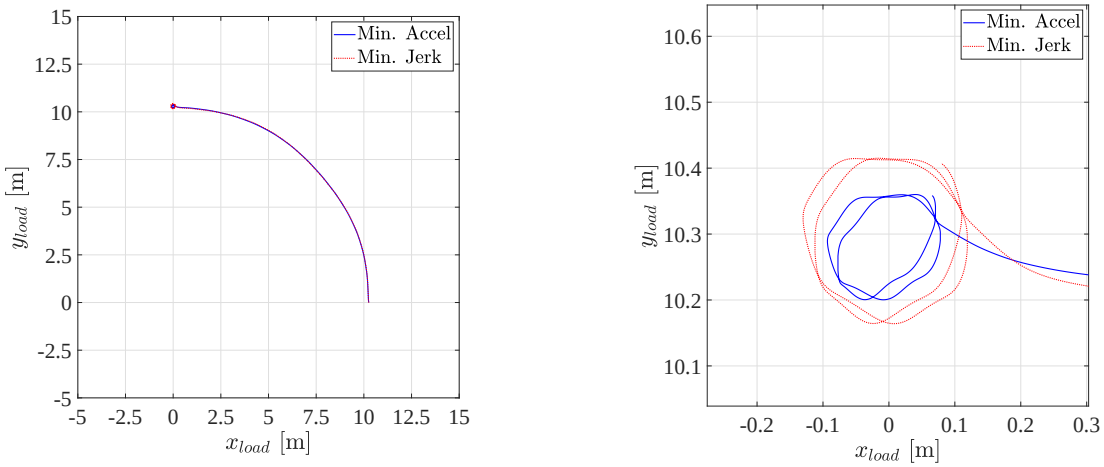

(a) Full trajectory (b) Residual motion

Fig. 3.26: The comparison of the hoisted load's trajectory in xy-plane between the control method on Appendix C model at $T_c = 0.25T_n$ and $a_c = 6$ between minimum acceleration and jerk trajectories

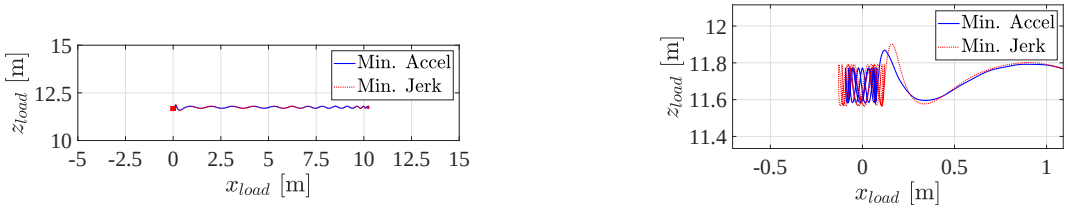

(a) Full trajectory (b) Residual motion

Fig. 3.27: The comparison of the hoisted load's trajectory in xz-plane between the control method on Appendix C model at $T_c = 0.25T_n$ and $a_c = 6$ between minimum acceleration and jerk trajectories

3.3.1.4 Increasing the slewing velocity

Next, the performance of the proposed control model was validated with the increased slewing velocity. The slewing velocity during the constant velocity period was increased from 1[RPM] to 1.5[RPM] or 50 percent, then the simulation was performed in order inspect its effectiveness at higher velocity. The amplitude during the constant velocity period as the relation to the control period T_c and the a_c at 1.5[RPM] are shown in Fig. 3.28.

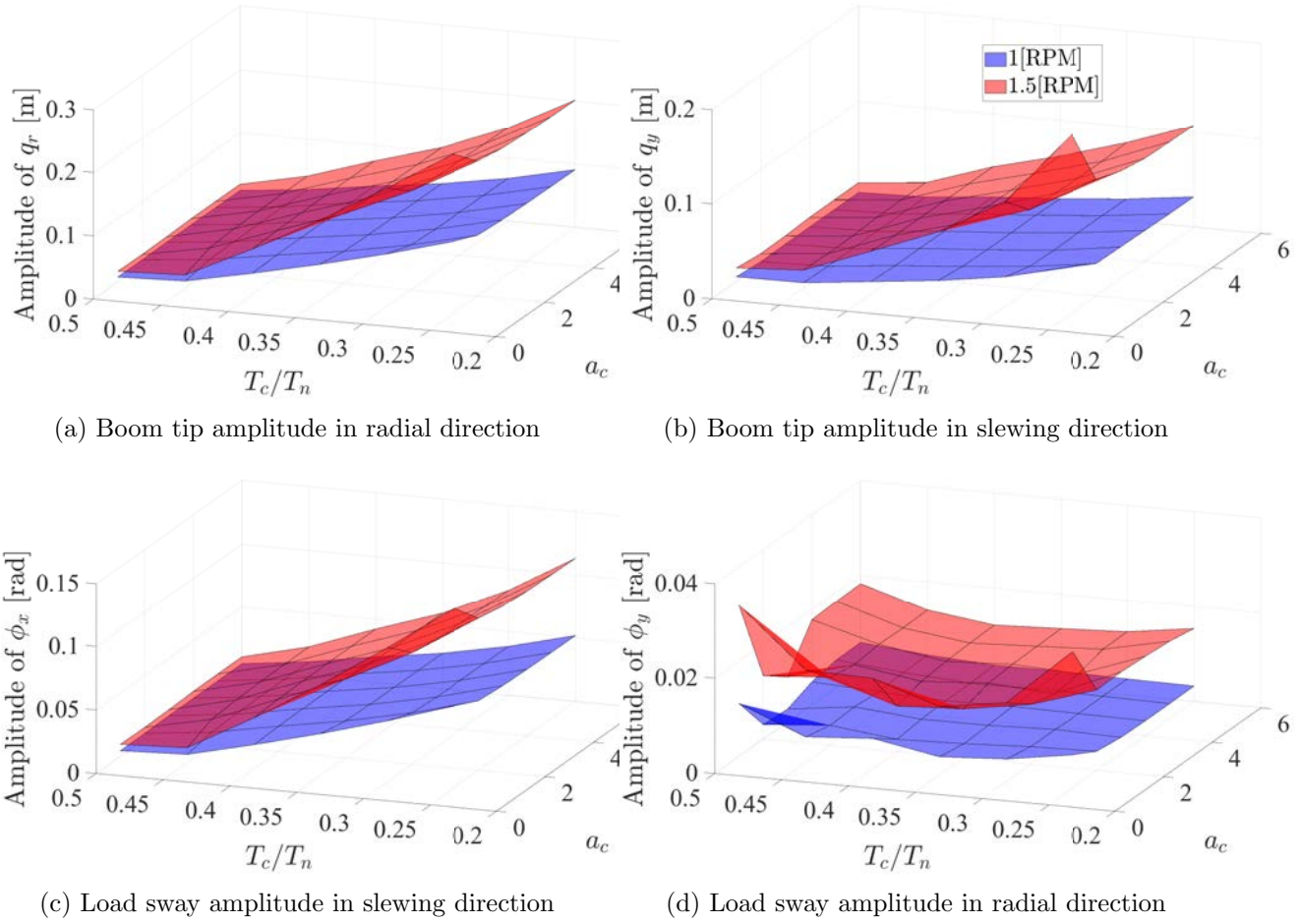

(a) Boom tip amplitude in radial direction

(b) Boom tip amplitude in slewing direction

(c) Load sway amplitude in slewing direction

(d) Load sway amplitude in radial direction

Fig. 3.28: The sway of the boom tip and the hoisted load during the simulation on Appendix C model at 1.5[RPM]

When observing Fig. 3.28, the average amplitude in all direction increased as the crane was driven with faster speed as expected. The relation of the amplitude to T_c and a_c was similar to the 1[RPM] case. Next, the control condition of $T_c = 0.45T_n$ and $a_c = 4$ were, once again, considered. Figures 3.29 to 3.33 show the input acceleration and the calculated trajectory of the boom tip and the hoisted load. The results from the reference and the proposed controller were compared. The simulation results showed that the rigid boom control became less effective in suppressing the residual vibration of the hoisted load when the control velocity was increased to 1.5[RPM]. On the other hand, the proposed control model still effective in reducing the residual vibration of the hoisted load and the boom tip, and showed smaller amplitude of the residual vibration than the reference controller.

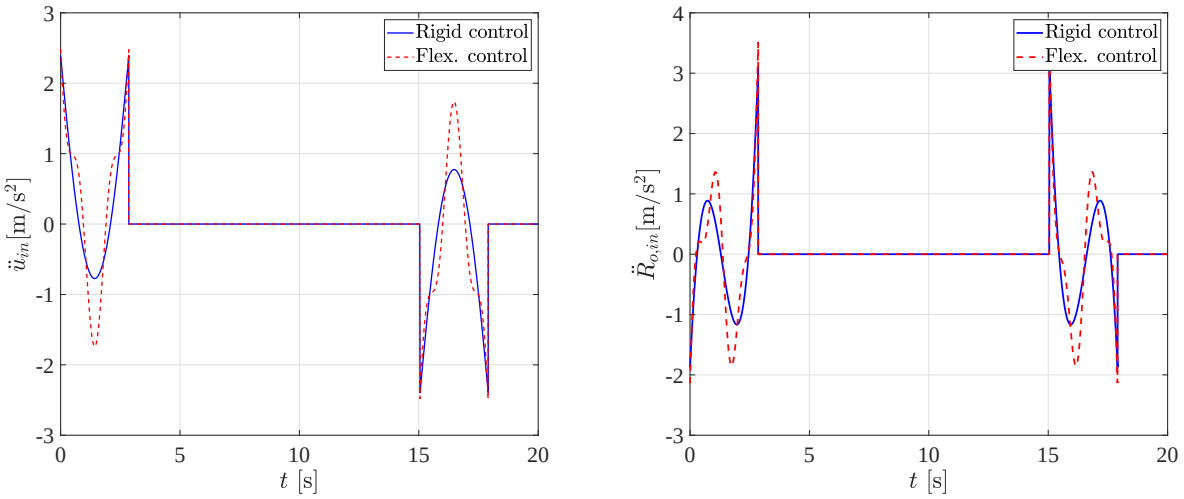

(a) Slewing control (b) Lifting control

Fig. 3.29: Control trajectory acceleration at control condition of $T_c = 0.45T_n$ and $a_c = 2$ at 1.5[RPM]

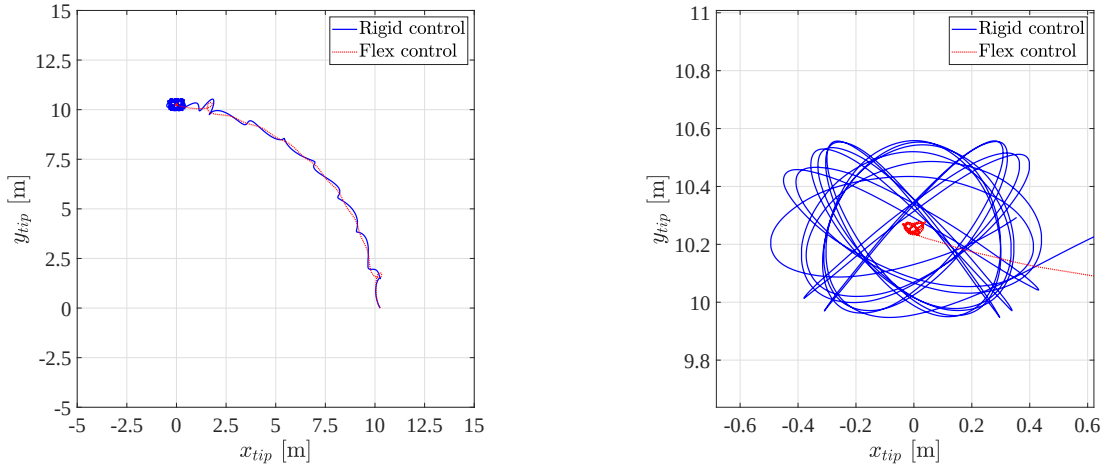

(a) Full trajectory (b) Residual motion

Fig. 3.30: The comparison of the boom tip's trajectory in xy-plane between the control method on Appendix C model at $T_c = 0.45T_n$ and $a_c = 4$ with minimum acceleration at 1.5[RPM]

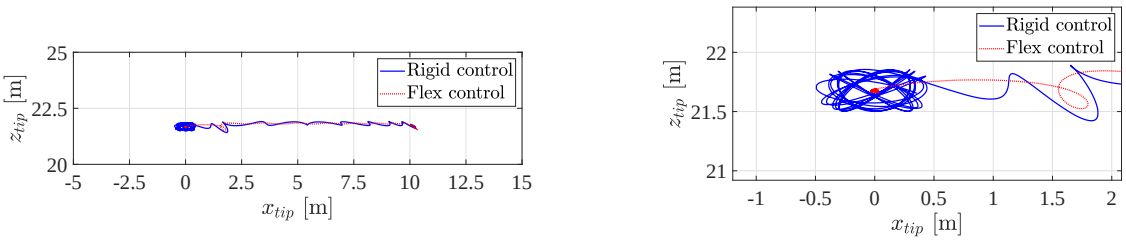

(a) Full trajectory (b) Residual motion

Fig. 3.31: The comparison of the boom tip's trajectory in xz-plane between the control method on Appendix C model at $T_c = 0.45T_n$ and $a_c = 4$ with minimum acceleration at 1.5[RPM]

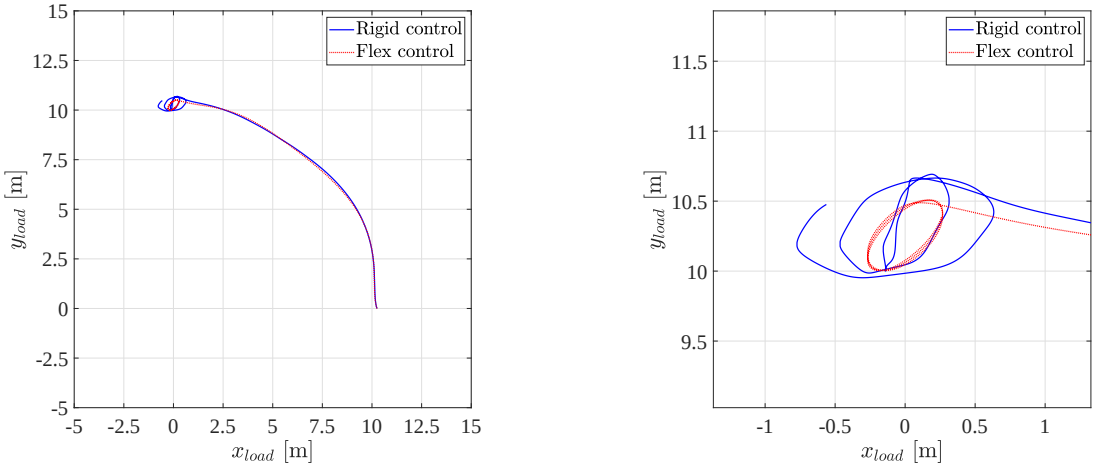

(a) Full trajectory (b) Residual motion

Fig. 3.32: The comparison of the hoisted load's trajectory in xy-plane between the control method on Appendix C model at $T_c = 0.45T_n$ and $a_c = 4$ with minimum acceleration at 1.5[RPM]

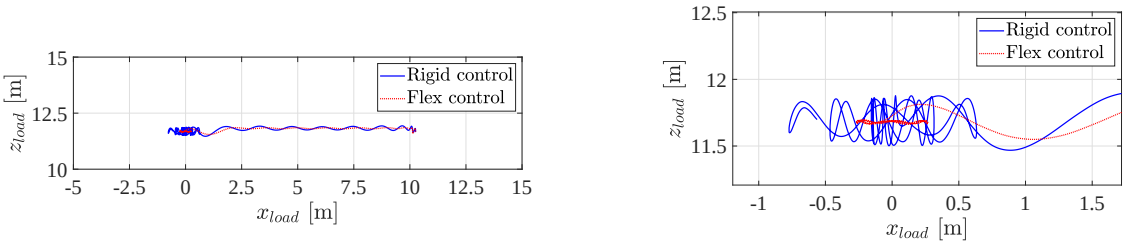

(a) Full trajectory (b) Residual motion

Fig. 3.33: The comparison of the hoisted load's trajectory in xz-plane between the control method on Appendix C model at $T_c = 0.45T_n$ and $a_c = 4$ with minimum acceleration at 1.5[RPM]

3.3.2 Numerical simulation and experiment on the laboratory-size crane

In this section, the effectiveness of the proposed control method was validated via the numerical simulation and the experiment on the laboratory-size crane model. Figure 3.34 shows the setting of the laboratory-size flexible rotary crane that was used in this study. The setting consisted of the flexible rotary crane and two cameras above the crane. The test crane was constructed with the slewing platform, the base boom, the top boom, and the hoisted load. The base boom and the top boom were connected with the flexible joint made from silicone rubber. Typically, the dominant vibration mode in the crane operation was the pendulum mode of the hoisted load. Therefore, the bending vibration of the flexible would not exceed the first lowest bending mode. Therefore, it was sufficient for the experimental setting to build the boom that vibrate only at the tip to represent the first bending mode.

The experiment was conducted by driving the crane with the designed trajectory from the previous Sections. The white ball was attached at the boom tip, while the hoisted load was a black spherical rubber ball. These objects were used to track the motion of the boom tip and hoisted load, respectively. The crane's motion was recorded by the video cameras. The motion of the boom tip and the hoisted load was extracted from the recorded video. The motion was recorded at 40[FPS]. The motion of the crane from the rest position until it stopped and entered the residual period was considered.

For numerical simulation, the dynamical model of this laboratory-size crane was described in Appendix D.

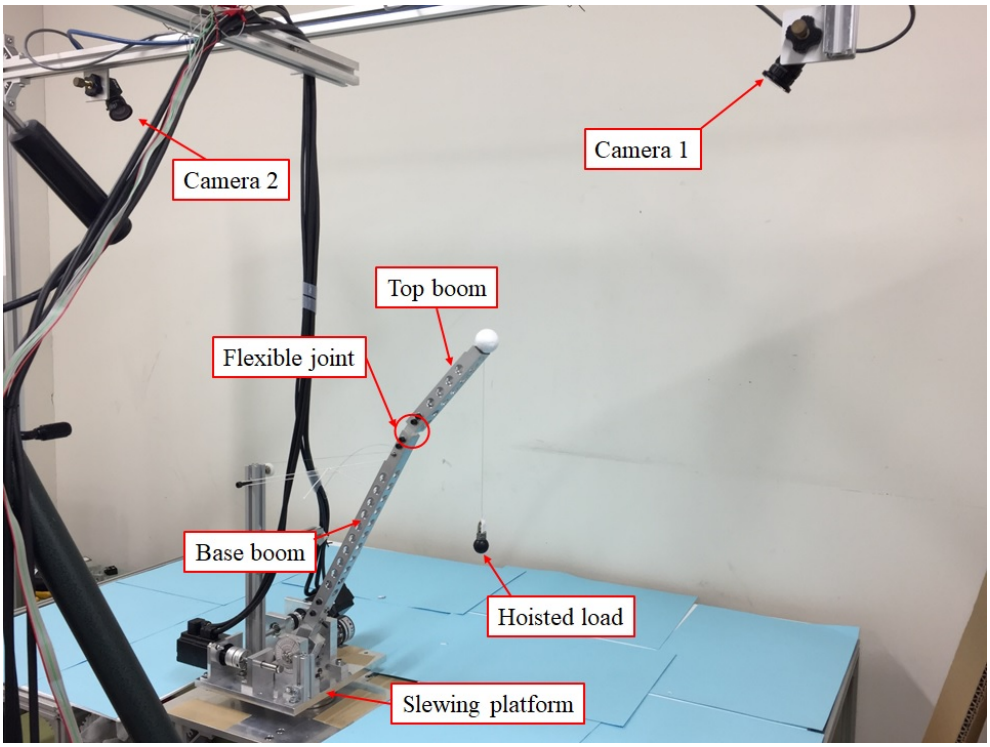

Fig. 3.34: The setting of the laboratory-scale flexible crane

3.3.2.1 Numerical simulation on the laboratory-size crane

Table 3.3: Specification of the laboratory-size crane

Parameter	Value
Base boom length, L_{base}	350 [mm]
Top boom length, L_{top}	150 [mm]
Top boom mass, m_3	40 [g]
Top boom moment of inertia, J_3	3×10^{-4} [kg.m^3]
Hoisted load mass, m_4	22 [g]
Rope length, ℓ_{rope}	235 [mm]
Hoisted load natural period, T_n	0.973 [s]
Rotational stiffness coefficient with respects to vertical direction, k_θ	0.35 [N.m/rad]
Rotational stiffness coefficient with respects to horizontal direction, k_ψ	1.12 [N.m/rad]
Rotational damping coefficient with respects to vertical direction, d_θ	0.011 [N.m.s/rad]
Rotational damping coefficient with respects to horizontal direction, d_ψ	0.005[N.m.s/rad]

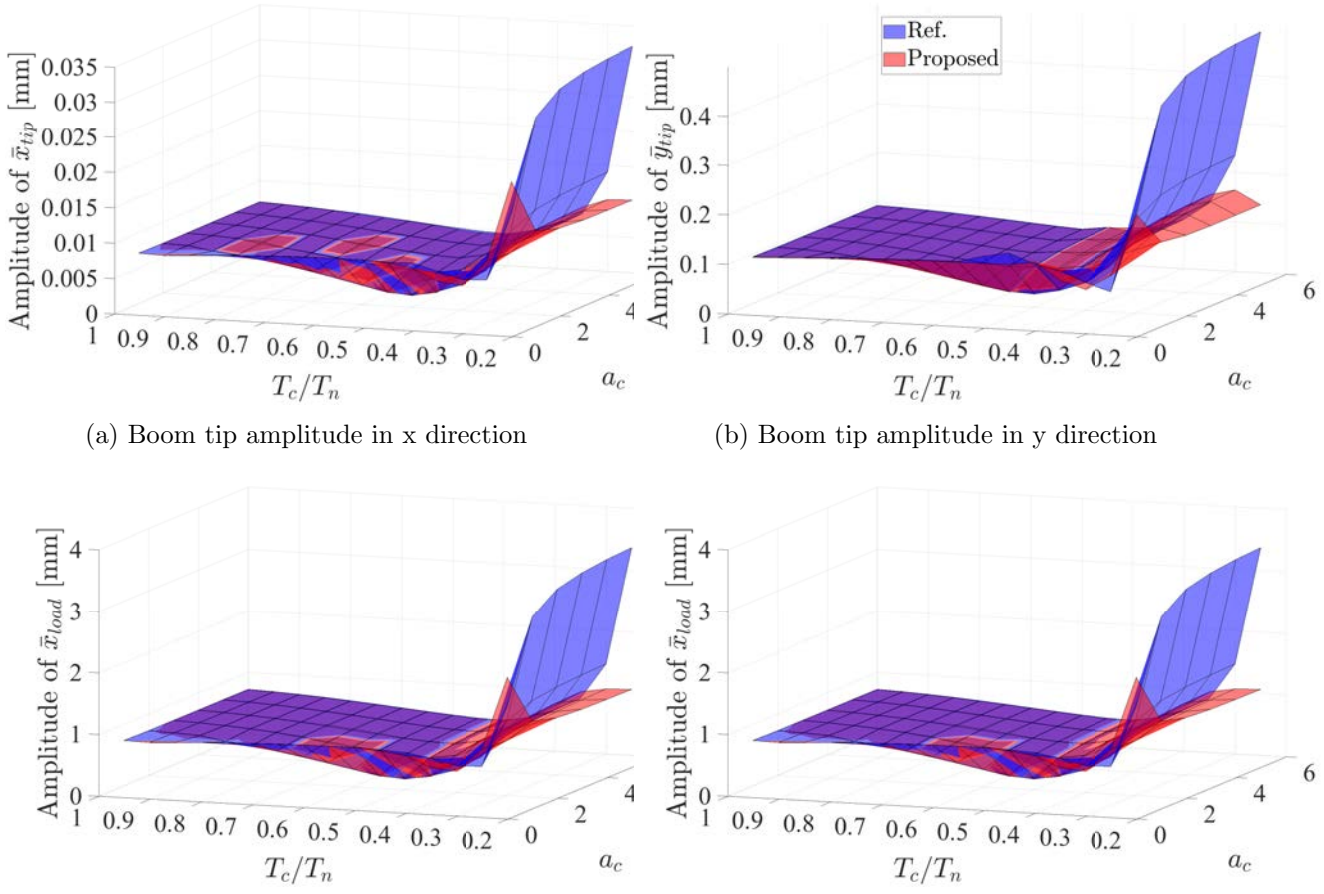

(a) Boom tip amplitude in x direction

(b) Boom tip amplitude in y direction

(c) Load sway amplitude in x direction

(d) Load sway amplitude in y direction

Fig. 3.35: The average amplitudes of the boom tip and the hoisted load during the constant velocity period from the simulation at variated control periods, T_c, and slewing velocity regulated constants a_c

Firstly, the numerical simulation on the dynamic model of the laboratory-size crane with variated T_c and a_c were calculated. The specification for the dynamic model of the laboratory-size model is written in Table 3.3. The minimized acceleration trajectory was used. The result from the reference control model was calculated for comparison as well. The control velocity at the boom tip was 0.19[m/s]. Figure 3.35 shows the amplitude of the boom tip and the hoisted load's vibration during the constant velocity period under variated T_c and a_c. The results in Fig. 3.35 were calculated on the x and y axes of the base boom coordinates systems.

From Fig. 3.35, the amplitude of the boom tip and the hoisted load during the constant velocity period from both controllers were similar during control period from $T_c = T_n$ to $0.45T_n$. However, as the control period kept decreasing, the amplitude of the boom tip and hoisted load under the reference controller showed a drastic increase, whereas the results under the proposed control approach was increased at a significantly smaller rate. The smallest amplitude of this model was found at condition of $T_c = 0.5T_n$ and $a_c = 2$.

Next, the trajectory of the full crane operation from the numerical simulation was observed. In this trajectory, the target slewing angle was 90[deg]. Based on the results in Fig. 3.35, the control conditions at 1) $T_c = 0.5T_n$, $a_c = 2$ and 2) $T_c = 0.25T_n$, $a_c = 6$ were chosen for this study. The first condition was the most minimized amplitude, while the second condition was the best condition at the highest acceleration, which was considered in this study. For each condition, four trajectories were calculated, and their results were compared. The detail of each trajectory was written in Table 3.4.

The acceleration during the acceleration period of each controller at both control conditions are shown in Figs. 3.36 and 3.37.

Table 3.4: Detail of the control model in laboratory scale crane exeperiment

Control approach	Minimization	Given name
Reference	Acceleration	Model 1
Proposed	Acceleration	Model 2
Reference	Jerk ($\omega_{cut} = 6.46$[rad/s])	Model 3
Proposed	Jerk ($\omega_{cut} = 52.08$[rad/s])	Model 4

Firstly, the simulation results at the condition of $T_c = 0.5T_n$ and $a_c = 2$ was observed. From Fig. 3.38, the overall trajectory of the boom tip and the hoisted load from all models were similar. However, the size of residual vibration of the boom tip and the hoisted load from Models 2 and 4 were slightly smaller than from Models 1 and 3. The amplitude during the residual vibration period was increased when the minimized jerk trajectory was used.

Next, the simulation results at the condition of $T_c = 0.25T_n$ and $a_c = 6$ was considered. From Fig. 3.39, the residual vibration of the boom tip and the hoisted load under Models 2 and 4 was smaller than the result under Models 1 and 3. The trajectory of the hoisted load from Models 2 and 4 was steadier than that in Models 1 and 3, even though the motion of the boom tip were not significantly different. Under the same control approach, the residual vibration of the trajectory with minimized acceleration (Models 1 and 2) was smaller than the minimized jerk (Models 3 and 4).

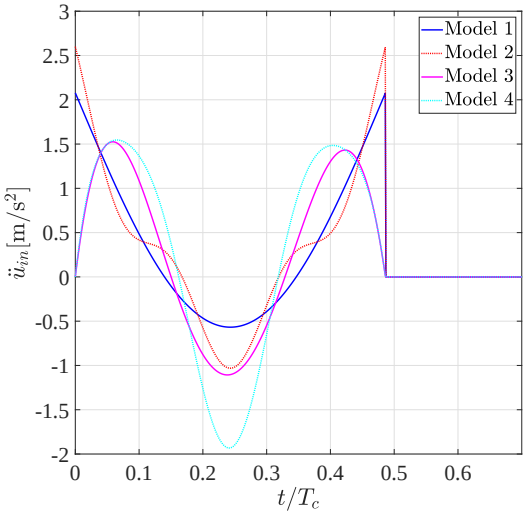

(a) Slewing control

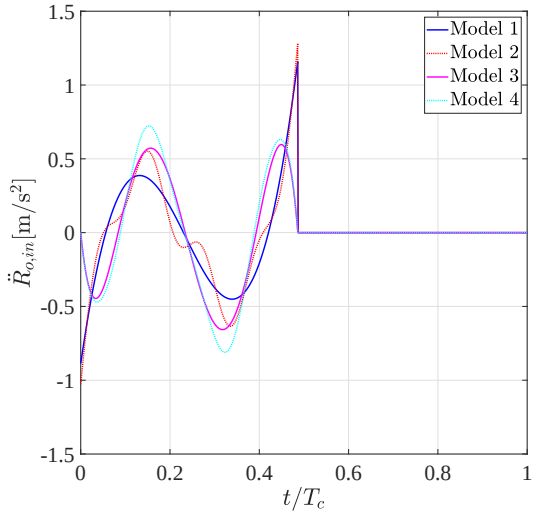

(b) Lifting control

Fig. 3.36: Control trajectory acceleration at control condition of $T_c = 0.5T_n$ and $a_c = 2$

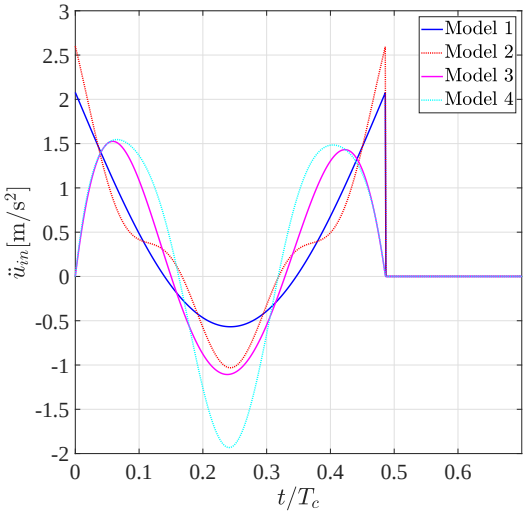

(a) Slewing control

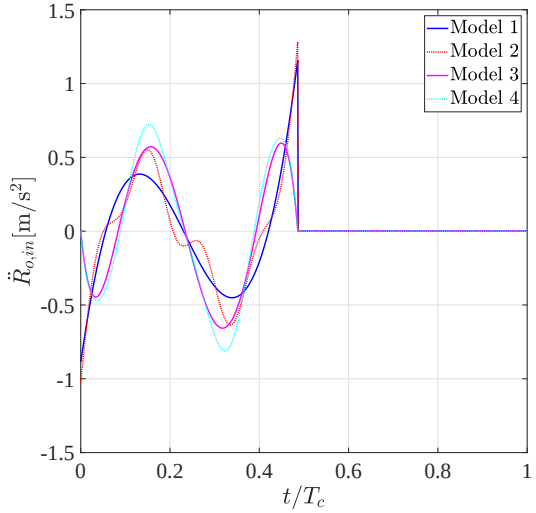

(b) Lifting control

Fig. 3.37: Control trajectory acceleration at control condition of $T_c = 0.25T_n$ and $a_c = 6$

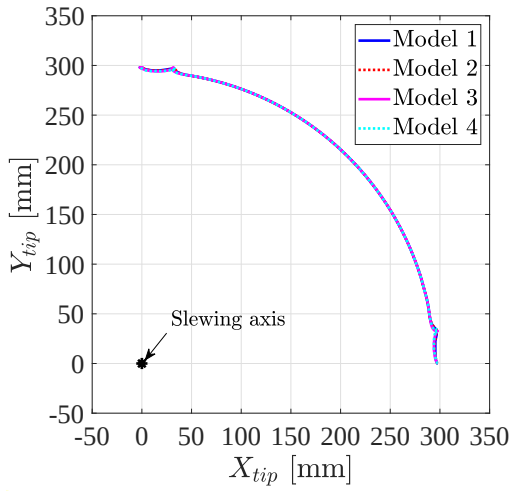

(a) Boom tip's full trajectory

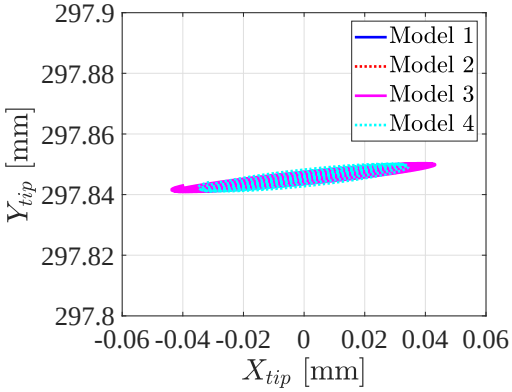

(b) Boom tip's residual vibration

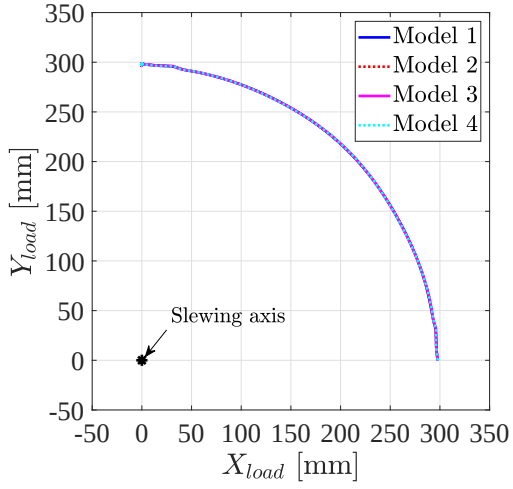

(c) Hoisted load's full trajectory

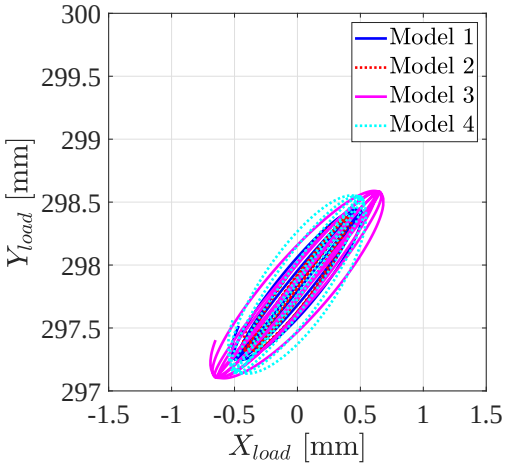

(d) Hoisted load's residual vibration

Fig. 3.38: The trajectory of the boom tip and the hoisted load on XY-plane from numerical simulation at control condition of $T_c = 0.5T_n$ and $a_c = 2$

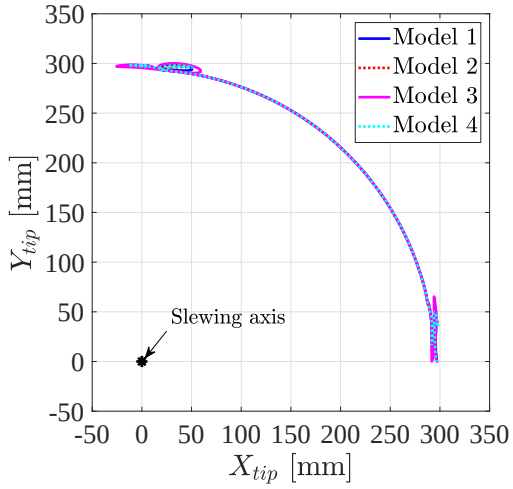

(a) Boom tip's full trajectory

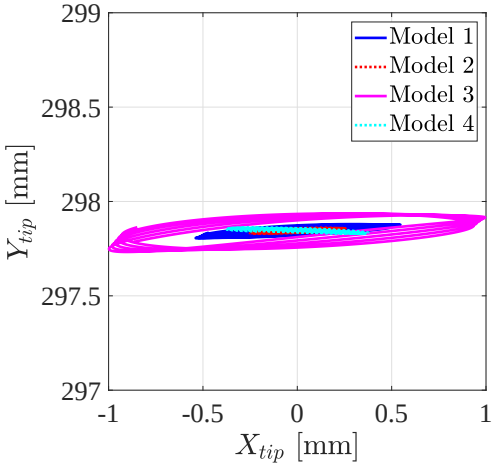

(b) Boom tip's residual vibration

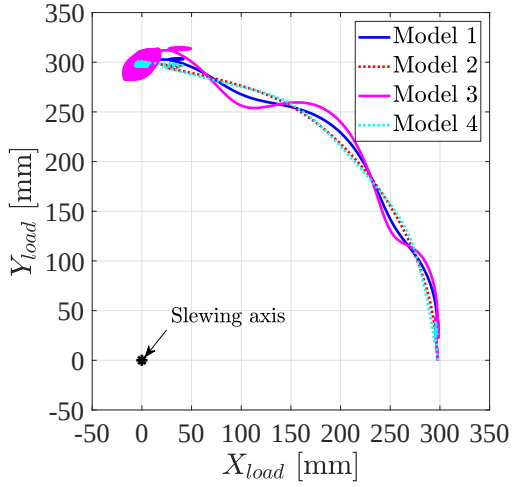

(c) Hoisted load's full trajectory

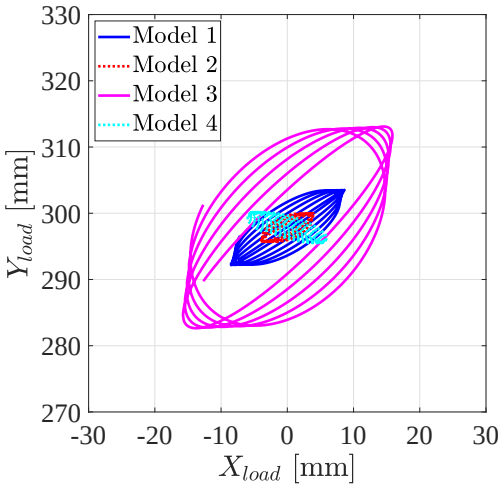

(d) Hoisted load's residual vibration

Fig. 3.39: The trajectory of the boom tip and the hoisted load on XY-plane from numerical simulation at control condition of $T_c = 0.5T_n$ and $a_c = 2$

3.3.2.2 Experiment on the laboratory-size crane

The experiment on the laboratory-size crane was conducted by using the same control condition as in the numerical simulation. Firstly, the experiment at the condition of $T_c = 0.5T_n$ and $a_c = 2$ was observed. In Fig. 3.40(a), the trajectory of the boom tip was almost the same in all models. In Fig. 3.40(b), all results also showed the same range of scattered points, which illustrated that the boom tip from all models vibrated with similar amplitude during the residual period. Figure 3.40(c) also shows that the trajectory of the hoisted load from all models were similar. However, from Fig. 3.40(d), Models 1 and 3 had a slightly smaller amplitude of vibration than Models 2 and 4.

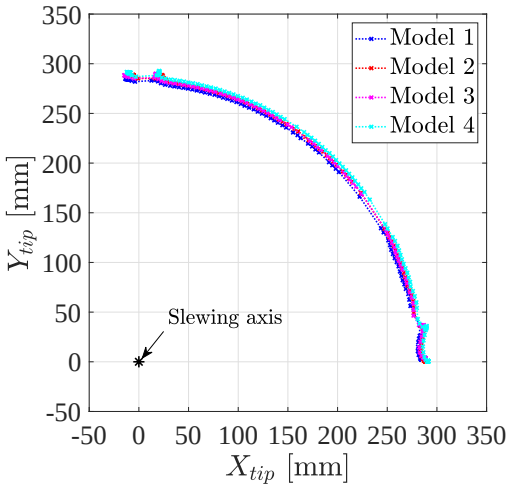

(a) Boom tip's full trajectory

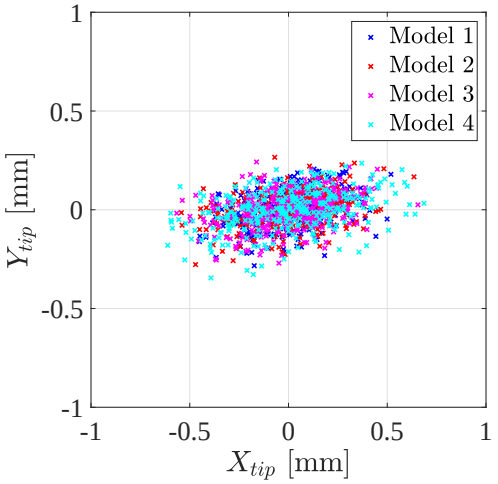

(b) Boom tip's residual vibration

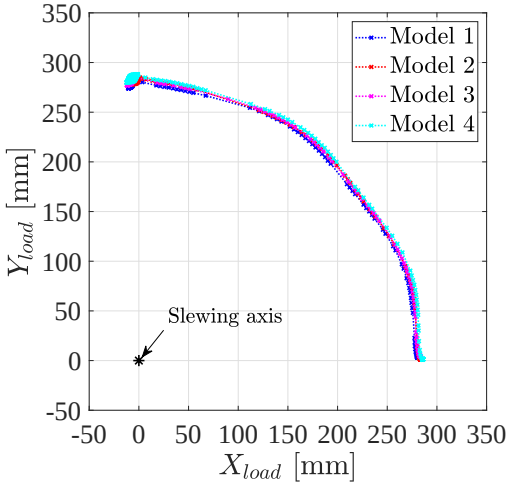

(c) Hoisted load's full trajectory

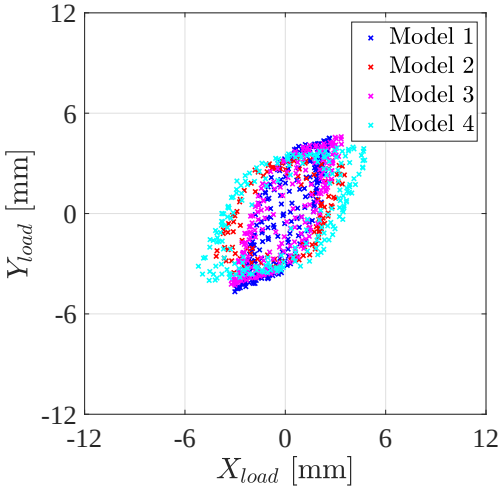

(d) Hoisted load's residual vibration

Fig. 3.40: The trajectory of the boom tip and the hoisted load on XY-plane from experiment at control condition of $T_c = 0.5T_n$ and $a_c = 2$

Next, the experiment at the condition of $T_c = 0.25T_n$ and $a_c = 6$ was observed. From Fig. 3.41(a), the trajectory of the boom tip from all models showed similar motion. However, Fig.

3.41(b) shows that the amplitudes of the residual vibration of the boom tip from Models 2 and 4 was smaller than in Models 1 and 3. Figure 3.41(c) shows a similar trajectory of the hoisted load from all models but the amplitude of the residual vibration was different. As shown in Fig. 3.41(d), the residual vibration of the hoisted load under the Models 2 and 4 had a smaller amplitude than Models 1 and 3.

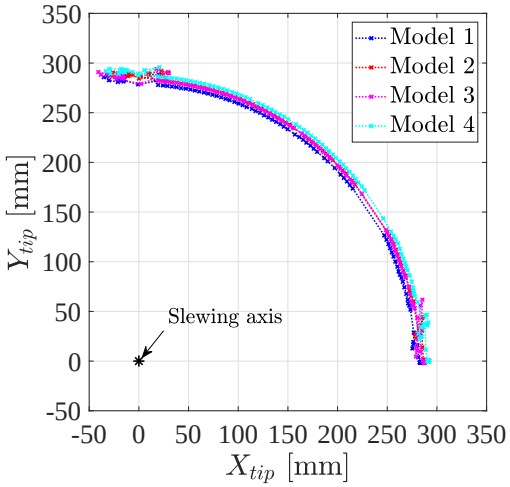

(a) Boom tip's full trajectory

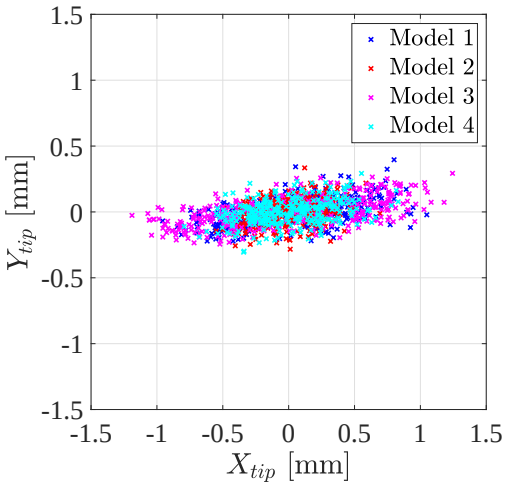

(b) Boom tip's residual vibration

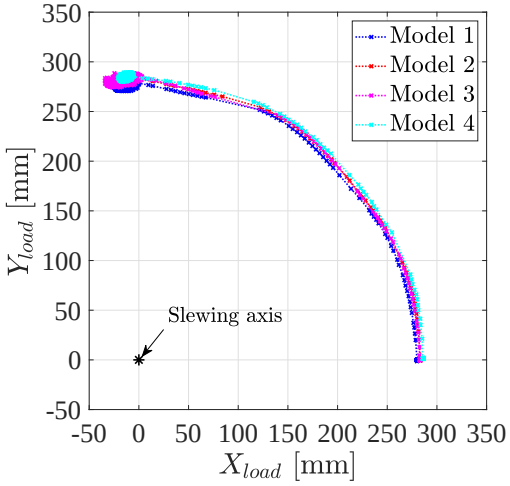

(c) Hoisted load's full trajectory

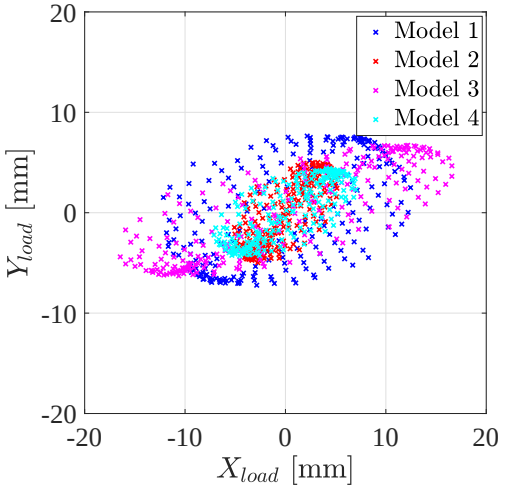

(d) Hoisted load's residual vibration

Fig. 3.41: The trajectory of the boom tip and the hoisted load on XY-plane from experiment at control condition of $T_c = 0.25T_n$ and $a_c = 6$

3.3.2.3 Experiment with increased velocity

The experiment on the laboratory-size crane was continued by increasing the control velocity. The control velocity was increased by 50 percent. Then, the experiment was carried out with the same control conditions. The same conditions from previous example were used. The driving acceleration at increased speed are shown in Figs. 3.42 and 3.43.

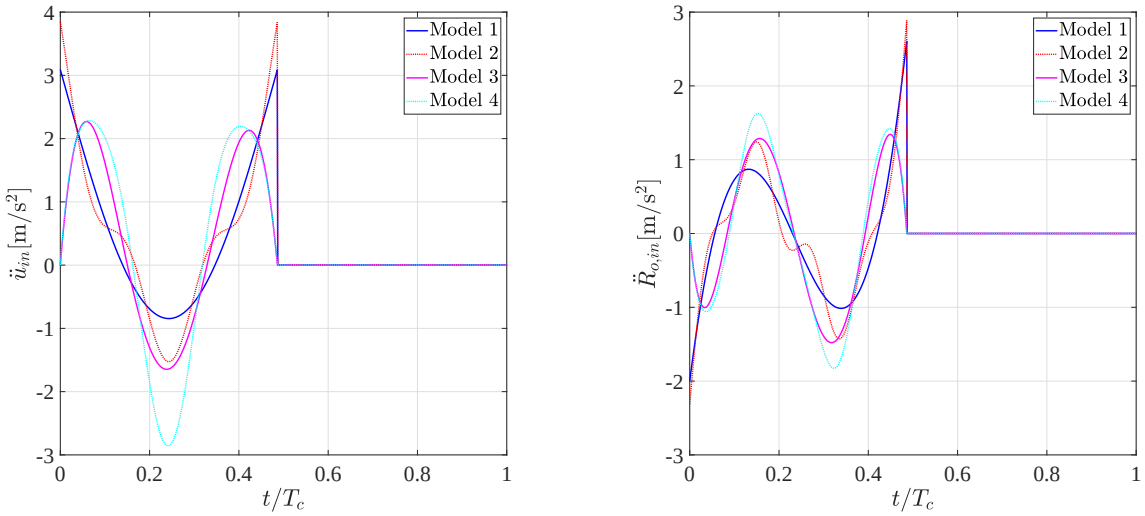

(a) Slewing control (b) Lifting control

Fig. 3.42: Control trajectory acceleration at control condition of $T_c = 0.5T_n$ and $a_c = 2$ at increased velocity

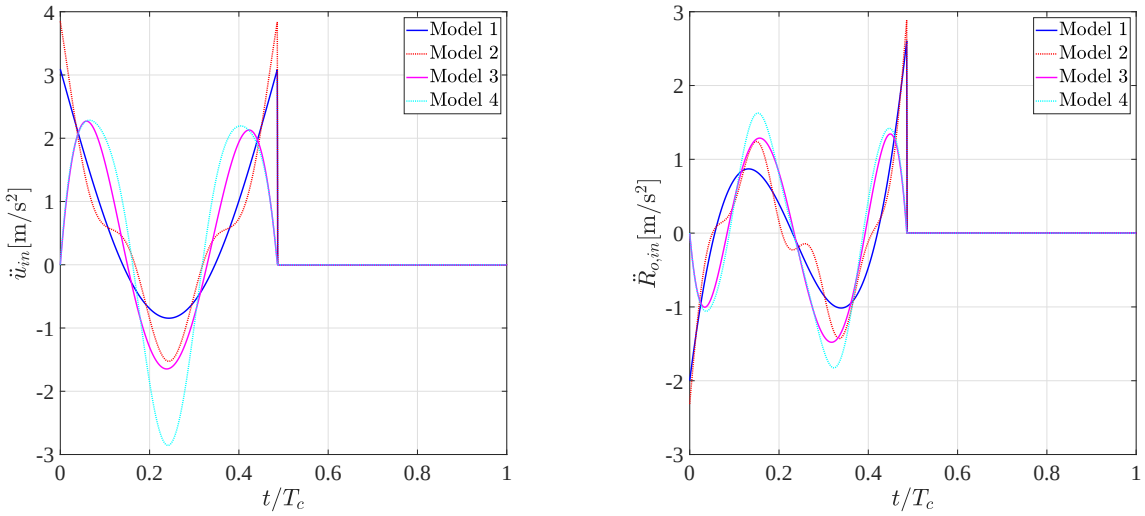

(a) Slewing control (b) Lifting control

Fig. 3.43: Control trajectory acceleration at control condition of $T_c = 0.25T_n$ and $a_c = 6$ at increased velocity

Firstly, the control condition of $T_c = 0.5T_n$ and $a_c = 2$ was observed. The trajectory of the

boom tip and the hoisted load are shown in Fig. 3.44.

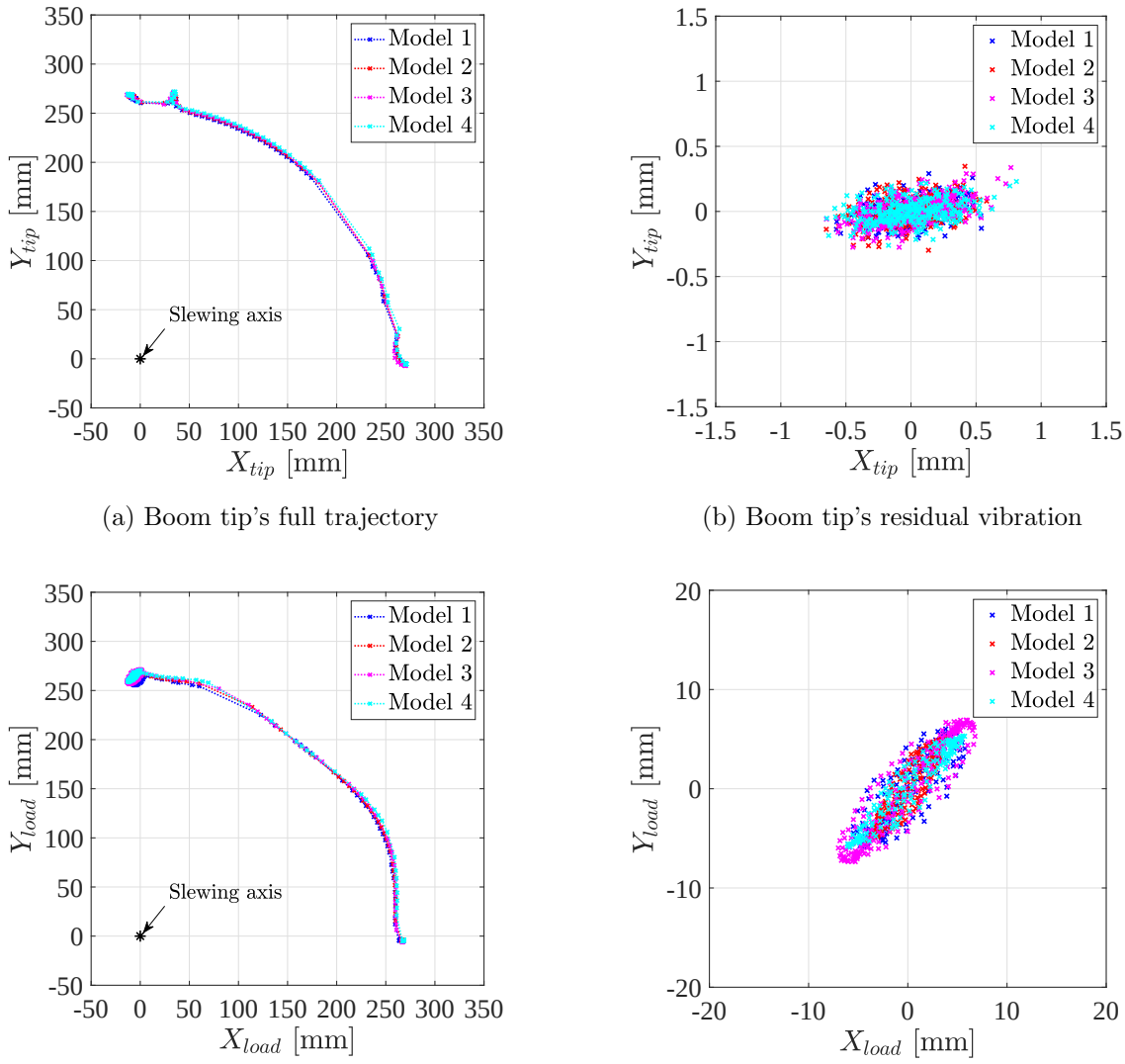

(a) Boom tip's full trajectory

(b) Boom tip's residual vibration

(c) Hoisted load's full trajectory

(d) Hoisted load's residual vibration

Fig. 3.44: The trajectory of the boom tip and the hoisted load on XY-plane from experiment at control condition of $T_c = 0.5T_n$ and $a_c = 2$ with increased velocity

Figure 3.44 shows that Models 1 and 3 had amplitude of the residual vibration of the boom tip and the hoisted load larger than Model 2 and 4. Next, the results from the experiment under control condition of $T_c = 0.25T_n$ and $a_c = 6$ are shown in Fig. 3.45. At this condition, the different between the proposed model and the reference model became more observable as the residual vibration of the proposed method (Models 2 and 4) was much smaller than the reference method (Models 1 and 3).

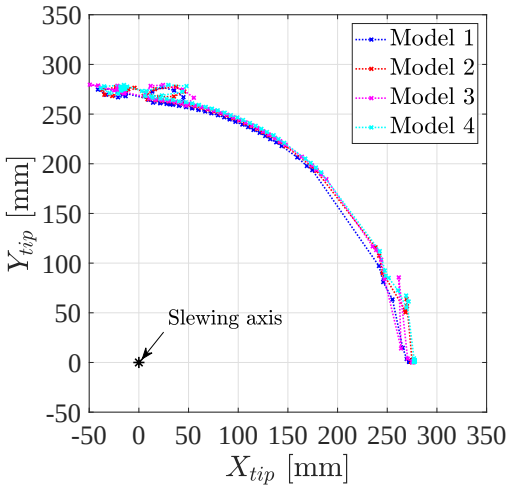

(a) Boom tip's full trajectory

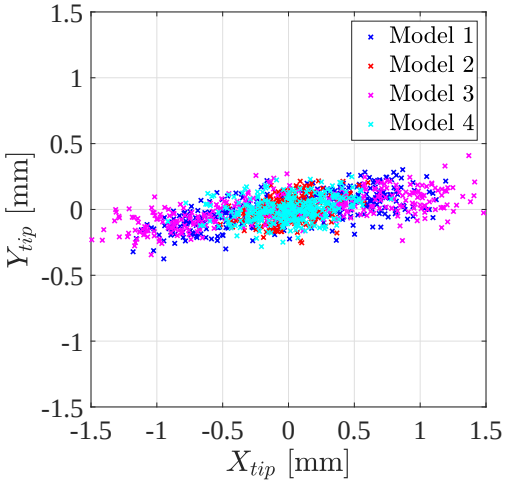

(b) Boom tip's residual vibration

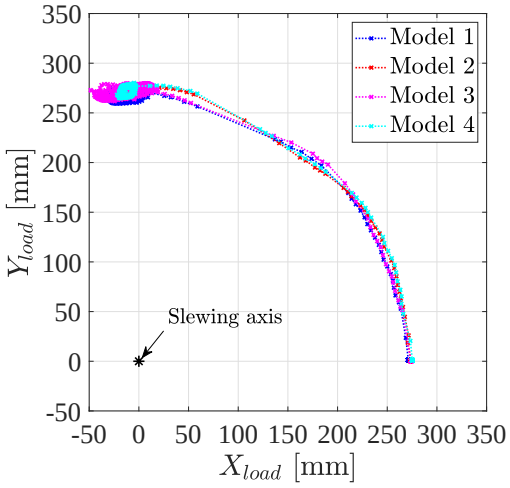

(c) Hoisted load's full trajectory

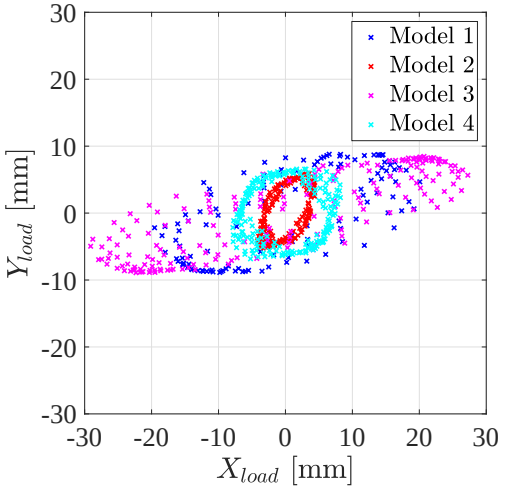

(d) Hoisted load's residual vibration

Fig. 3.45: The trajectory of the boom tip and the hoisted load on XY-plane from experiment at control condition of $T_c = 0.25T_n$ and $a_c = 6$ with increased velocity

The experiment results in Figs. 3.44 and 3.45 showed that the rigid control model became less effective when the control velocity became larger. When the control velocity was increased, the acceleration was increased as the consequence. This was similar to shortening of the control period T_c, as the acceleration also increased as well. The proposed flexible control method became better effectiveness in reducing the vibration of the flexible crane as the acceleration increased.

Chapter 4

Conclusions, discussion and future work

4.1 The development of flexible crane's dynamic model

The hoisted rope model

In the study of the modeling assumption for the hoisted rope, the inertia included flexible rope model was studied and trial in order investigate the influence of the inertia of the rope in dynamic model. The inertia included rope model was formulated with the flexible multibody dynamics. The hoisted rope was modeled as a very thin flexible beam. When the inertia included rope model was used in the simulation, the bending deformation during the crane's motion was observable. The magnitude of the bending was increased with the length of the rope. In the example that was used in Section 2.1, the length of the rope was 5[m] to 15[m]. The observation of the example showed that as the length of the rope increased, the bending natural frequency of the rope became smaller. When the lowest bending mode of the rope smaller than the natural frequency of the flexible boom, the bending vibration of the rope was excited by the vibration of the flexible boom. At rope length of 15[m], the first bending mode of the rope was lower than the first bending mode of the boom in both directions, and the second bending mode of the rope was lower than the first bending mode of the boom in vertical direction. Thus, the only the first mode of the rope's bending was excited during the slewing motion (horizontal direction). If the length of the rope was increased further, the higher bending mode of the rope was expected to be excited. For example, if the rope length was increased to 40[m] as in Fig. 4.1, the second bending mode of the rope became lower than the first bending mode of the boom in slewing direction. Thus, the slewing motion might exit the second bending vibration of the rope. Moreover, the first bending mode of the rope was matched the pendulum mode at 32.5[m]. At this length, the rope could be excited by both the vibration of the boo and the pendulum motion of the hoisted load and increase the magnitude of the bending vibration.

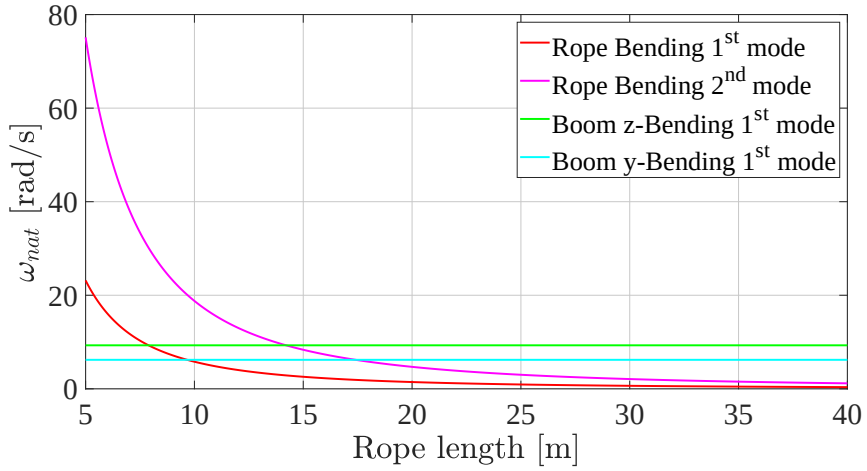

Fig. 4.1: Natural frequency of model in Appendix A with increased rope length

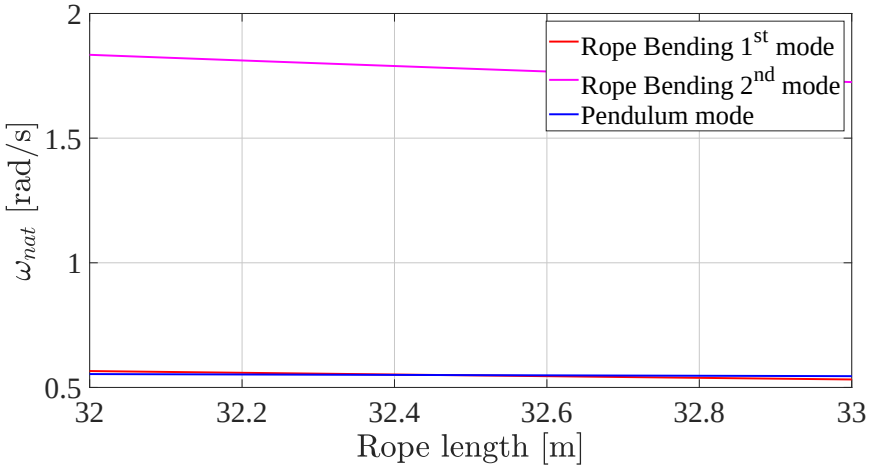

Fig. 4.2: Natural frequency of the rope's bending frequency of the pendulum mode

Then, the numerical simulation was carried out to compare three types of the rope models: the rigid rope, the massless flexible model rope, and the inertia included rope model. Although, the inertia included rope model showed the bending deformation of the rope during the crane's motion, the trajectory of the hoisted load under this model showed only the slightly different from the other rope's models. As explained above, only the first bending mode of the in the trial example was excited by the slewing motion of the crane from the vibration of the boom. This vibration was not enough to affect the trajectory of the hoisted load since the pendulum mode still the dominant motion. In this case, the inertia of the rope could be neglect. By using the rope model without the inertia, the calculation cost was drastically cheaper. If the length of the rope is sufficiently long such that the frequency of the lowest bending mode is the dominant motion, such as in Fig. 4.2. In this case, the bending vibration of the rope could result in different trajectory of the hoisted load. Thus, the inertia of the hoisted rope is essential for the dynamic model.

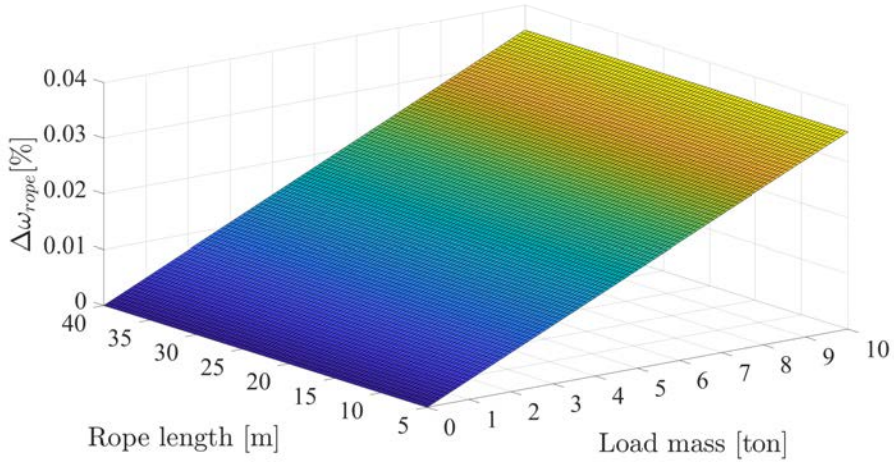

Fig. 4.3: Difference between the natural frequency of the hoisted load with flexible rope and rigid rope model

When comparing between the massless spring rope model and the rigid rope model, the trajectory that was calculated in Section 2.1 showed that both models had almost same motion. In the example. the hoisted load was already lifted up from the ground, and the crane operation began from the static equilibrium point. Thus, the flexible rope was already extended. It was shown that the stiffness of the rope was very high, thus, the amplitude of the vibration in lateral direction was small. Moreover, the extended length of the rope was small. Thus, the difference of the natural frequency of the hoisted load between the flexible rope and the rigid rope was small. The difference of the hoisted load natural frequency between these two rope models at different rope length and load mass could be shown with Fig. 4.3. This figure showed that even with the 10[ton] hoisted load, the largest difference of the natural frequency was not more than 0.004 percent. Thus, the rigid rope model and the flexible rope models showed very similar motion. Although this was depending on the mechanical property of the rope, the example used the steel wire which was the typical material for the hoisted rope in crane design. Therefore, if the length of the rope was not long enough such that its bending deformation had an effect on the hoisted load trajectory, then, the rope could be modeled as the rigid component.

The efficient dynamic model

The efficient dynamics model of the flexible crane was developed via the relative coordinates systems and the AMI model order reduction method. The dynamic model of the crane with the flexible boom via the relative coordinates systems was implemented. The modeling of the flexible boom and the hoisted load for this coordinates systems was introduced. The hoisted load was modeled as an additional particle of the flexible boom that was extended with the rope vector. The rotation angle around the x and y axes of the boom's body coordinates system were chosen to represent the motion of the hoisted load. These angles prevented the singularity problem of the dynamic model when the crane was at rested position.

The order-reduced dynamic model of the flexible crane was developed with the adaptive modal integration (AMI) method. This development was aimed to solve the problem of the numerical stiffness in the flexible dynamic model, and the calculation cost of the inverse inertia matrix. The developed AMI crane model was implemented in the way such that the model was independent to the input velocity and acceleration. This was done by, firstly, linearized the nonlinear equation around the rigid body condition and left the input velocity and acceleration unsubstituted. Then,

during the modal analysis, the mode shapes were calculated at static condition of the structures. These implementations gave the inertia matrices and the modal matrices as the function of the configuration. Because the inertia matrices and the modal matrices independent to the velocity and the accelerations, they were able to be interpolated only with the boom's angles.

The modal matrix was formulated with the few numbers of the lower frequency mode shapes. This provided the dynamic model a potential to increase the size of the integration step in numerical calculation. In this model, the inertia matrix and its inverse were precalculated prior to the simulation. The inertia matrix, the inverse matrix and the modal matrix were interpolated during the simulation. The interpolation of the inverse of the inertia matrix highly reduced the cost of the calculation due to the inverse matrices. These implementations contributed to the shorter calculation time in the dynamic model.

The effectiveness of the reduced dynamic model was validated through the numerical simulations. The simulated motion was compared to the motion from the nonreduced dynamic model. From the example model that was used in this dissertation, the reduced model was able to use the size of the integration step 10 times larger than the nonreduced model. In simulation, the reduced model calculated the motion faster than the nonreduced model due to larger integration step. The reduced model also showed good correctness when comparing to the nonlinear model even though the deviation of the results increase as the mechanism was driven with higher acceleration.

If the precalculation of the modal matrices, inertia matrices and the inverse matrix of inertia for the reduced model was included, the reduced model required longer calculation time than the nonreduced model. However, those data were needed to be calculated only one time. Therefore, the reduced model would have more cost effectiveness over the nonreduced model when a number of simulations were carried out.

In conclusion, the procedure of the formulation of the short-calculation time dynamic model with AMI model reduction and static mode shapes was developed. Although the rotary crane model with one single solid boom model was studied, this procedure also applicable to the multiple booms structure such as telescopic boom as well.

4.2 The development of the flexible crane's vibration control

The vibration control strategy for the rotary crane with a flexible boom was developed. The control model or the simplified equation of motion of the flexible crane was introduced. In this model, the flexibility of the boom was modeled with the equivalent mass-spring system. Then, the vibration control model in slewing and lifting directions of the crane were developed accordingly. The developed models were used to design the vibrationless trajectory via the optimal control method. The designed trajectory was separated into three periods: the acceleration period, the constant velocity period, and the deceleration period. The optimal control condition for the slewing motion was the constant-velocity control and the lifting motion was the point-to-point control. The mathematical expressions for the boundary conditions for the proposed control model with flexibility of the boom were introduced. Then, the effectiveness of the proposed control strategy was inspected through the numerical simulation and the experiment on two crane examples: 1) the numerical simulation on the dynamic model of the flexible crane with specification close real crane size, and 2) the numerical simulation and experiment on the laboratory-size crane.

The simulation results from the crane's model with the real-size parameter showed that the proposed vibraiton control method was able to suppress the vibration of both boom tip and the hoisted load of the crane. Its effectiveness could be seen from comparing with the reference model that did not include the boom's flexibility. In this simulation, the proposed control model was able to achieve small vibration of the boom tip and the hoisted load. When comparing to the reference

control model that did not include the boom's flexibility, the propsoed flexible crane control model showed better suppression as the driving acceleration increased. This was shown as the proposed control model showed smaller residual vibration of the boom tip and the hoisted load when the short acceleration period was used, or the designated control speed was increased.

The numerical simulation and experiment on the laboratory-size crane also showed the similar results. When the crane was driven at high acceleration, the proposed control model illustrated better vibration reduction than the control model without the flexibility of the boom.

It was understood that at high acceleration, the boom was subjected to higher inertia force and resulted in larger deformation. In this situation, the control strategy that considered the flexibility of the boom showed its advantage over the control model with rigid boom. The developed controller provided the crane a potential to operate at high acceleration which able to shorten the operation time since the crane required less time to reach the desired velocity. In addition, the equivalent stiffness and mass of the boom that are required for calculating the proposed control model are depending on the mechanical properties of the boom structure. Thus, the proposed control model could be used with any design of the rotary crane.

4.3 Future work

The developed efficient model with the AMI showed good accuracy when comparing to the nonlinear model. However, the model still has the problem of the instability from the mode veering and mode crossing. The accuracy could be more improved as the problem is solved.

As discussed above, the AMI flexible crane model was able to calculate the results with the calculation time shorter than the target motion time when the bilinear interpolation was used. This shows that the model has the potential of developing the real-time simulation.

The developed vibration control of the crane with flexible boom could be further validated by testing with the real crane.

The rope reeling also one of the operations in cranes. The current dynamic model and the vibration control model have not included this motion yet. The proposed method could be improved further by considering other degree of freedoms such as the change of rope length.

The wind disturbance is one of the sources of vibration of the crane. The dynamics model and the vibration control model could be improved by considering this external disturbance as well.

Bibliography

[1] Posiadala, B., Skalmierski, B., Tomski, L., Motion of the lifted load brought by a kinematic forcing of the crane telescopic boom, Pergamon Press, Mechanism and Mechine Theory, Vol.25, No.5 (1989), pp. 547-556.

[2] Posiadala, B., Influence of crane support system on motion of the lifted load, Pergamon Press, Mechanism and Mechine Theory, Vol.32, No.1 (1997), pp. 9-20.

[3] Trabka, A., Dynamics of telescopic cranes with flexible structural components, Elsevier, International Journal of Mechanical Sciences, Vol.88 (2014), pp. 162-174.

[4] Trabka, A., Influence of flexibilities of cranes structural components on load trajectory, Springer, Journal of Mechanical Science and Technology, Vol.30, No.1 (2016), pp. 1-14.

[5] Maczyski, A. and Wojciech, S., Dynamics of a mobile crane and optimisation of the slewing motion of its upper structure, Kluwer Academic, International Journal of Nonlinear Dynamics, Vol.32, No.3 (2003), pp. 259-290.

[6] De Veubeke, B. F., The dynamics of flexible bodies, Elsevier, International Journal for Engineering Science, Vol.14, No.10 (1976), pp. 895-913.

[7] Sun, G. and Kleeberger, M., Dynamics responses of hydraulic mobile crane with consideration of the drive system, Pergamon Press, Mechanism and Machine Theory, Vol.38, No.12 (2003), pp. 1489-1508.

[8] Park, K.-P., Cha, J.-H., Lee, K.-Y., Dynamics factor analysis considering elastic boom effects in heavy lifting operations, Elsevier, Ocean Engineering, Vol.38, No.10 (2011), pp. 1100-1113.

[9] Ham, S.-H., Roh, M.-I., Lee, H., Ha, S., Multibody dynamics analysis of a heavy load suspended of a floating crane with constraint-based wire rope, Elsevier, Ocean Engineering, Vol.109, No.15 (2015), pp. 145-160.

[10] Posiadala, B. and Cekus, D., Discrete model of vibration of truck crane telescopic boom with consideration of the hydraulic cylinder of crane radius change in the rotary crane, Elsevier, Automation in Construction, Vol. 17 (2008), pp. 245-250.

[11] Sun, G., Kleeberger, M., Liu, J., Complete dynamics calculation of lattice mobile crane during hoisting motion, Elsvier, Mechanism and Machine Theory, Vol.40, No.4 (2005), pp. 447-466.

[12] Shabana, A. A., Dynamics of multibody system 4th edition (2013), Cambridge University Press.

[13] The Japan Society of Mechanical Engineers ed., Multibody dynamics 1 fundamental theory (computer dynamics series 3), Corona Publishing (in Japanese).

[14] The Japan Society of Mechanical Engineers ed., Multibody dynamics 2 numerical analysis and problems (computer dynamics series 4), Corona Publishing (in Japanese).

[15] Baumgarte, J., Stabilization of constraints and integrals of motion in dynamics systems, Elsevier, Computer Method in Applied Mechanics and Engineering, Vol.1, No.1 (1972), pp. 1-16.

[16] Shabana, A. A., Computational dynamics 3rd edition (2010), John Wiley and Son Ltd.

[17] Guyan, R. J., Reduction of stiffness and mass matrices, AIAA Journal, Vol. 3, No. 2 (1965), p. 380.

[18] Craig, R. and Bampton, M., Coupling of substructures for dynamic analyses, AIAA Journal, Vol. 6, No. 7 (1968), pp.1313-1319.

[19] Cornwell, R. E., Craig, R.R. JR. and Johnson, C.P., On the application of the mode-acceleration method to structural engineering problems, John Wiley & Sons, Earthquake Engineering and Structural Dynamics, Vol. 11, No. 5 (1983), pp. 679-688.

[20] Jain, S., Tiso, P., Rutzamoser, J. B., and Rixen, D. J., A quadratic manifold for model order reduction of nonlinear structural dynamics, Elsevier, Computers and Stuctures, Vol. 188 (2017), pp.80-94.

[21] Rutzamoser, J. B., Rixen, D. J., Tiso, P. and Jain, S., Generalization of quadratic manifold for reduced order modeling of nonlinear structural dynamics, Elsevier, Computers and Stuctures, Vol. 192 (2017), pp. 196-209.

[22] Kim, J-G., Park, Y-J., Lee, G. H., Kim, D-N., A general model reduction with primal assembly in stuctural dynamics, Elsevier, Computer Methods in Applied Mechanics and Engineering, Vol. 324 (2017), pp. 1-28.

[23] Boo, S-H., Kim, J-H., and Lee, P-S., Towards improving the enchanced Craig-Bampton method, Elsevier, Computers and Stuctures, Vol. 196 (2018), pp. 63-75.

[24] Brls O., Integrated simulation and reduced-order modeling of controlled flexible multibody systems, Ph.D. Thesis (2005), Universit de Lige, Lige, Belgium.

[25] Brls O., Pierre, D., and Golinval, J-C., The global modal parameterization for non-linear model-order reduction in flexible multibody dynamics, John & Wiley, International Journal for Numerical Method in Engineering, Vol. 69 (2007), pp. 948-977.

[26] Heirman, G. H. K., Naets, F. and Desmet, W., A system-level model reduction technique for the efficient simulation of flexible multibody systems, John Wiley & Sons, International Journal for Numerical Methods in Engineering, Vol. 85, No. 3 (2011), pp. 330-354.

[27] Naets, F., Heirman, G. H. K., Vandepitte, D. and Desmet, W., Inertial force term approximations for the use of global modal parameterization for planar mechanisms, John Wiley & Sons, International Journal for Numerical Methods in Engineering, Vol. 85, No. 4 (2011), pp. 518-536.

[28] Naets, F., Heirman, G. H. K. and Desmet, W., Subsystem global modal parameterization for efficient simulation of flexible multibody systems, John Wiley & Sons, International Journal for Numerical Methods in Engineering, Vol. 89 (2012), pp. 1227-1248.

[29] Aarts, R.G.K.M. and Jonker, J.B., Dynamic simulation of planar flexible link manipulators using adaptive modal integration, Springer, Multibody System Dynamics, Vol. 6, No. 3 (2001), pp. 245-266.

[30] Boer, S.E., Hoopen, D., Aarts, R.G.K.M., Hakvoort, W.B.J. and Jonker, J.B., Model reduction for efficient time-integration of planar flexible multibody models, Elsevier, International Journal of Non-Linear Mechanics, Vol. 53 (2013), pp. 75-82.

[31] Boer, S.E., Aarts, R.G.K.M. and Hakvoort, W.B.J., Model reduction for efficient time-integration of spatial flexible multibody models, Springer, Multibody System Dynamics, Vol. 31 (2014), pp. 69-91.

[32] Uchiyama, N., Ouyang, H. and Sano, S., Simple rotary crane dynamics modeling and open-loop control for residual load sway suppression by only horizontal boom motion, Elsevier, Mechatronics, Vol. 23 (2013), pp. 1223-1236.

[33] Kuo, T.Y. and Kang, S.-C., Control of fast crane operation, Elsevier, Automation in Construction, Vol. 42 (2014), pp. 25-35.

[34] Abe, A. and Okabe, K., Anitisway control for a rotary crane by using evolutionary computation, Fuji Technology press, Journal of Robotics and Mechatronics, Vol. 28, No. 5 (2016), pp. 646-653.

[35] Fukuzawa, T., Vibration suppression control of rotary crane using frequency weighting function, Tokyo Institute of Technology Master's thesis (2018, in Japanese).

[36] Kinoshita, J., Vibration suppression control of rotary crane with disturbance consideration, Tokyo Institute of Technology Master's thesis (2021, in Japanese).

[37] Yamaura, H. and Ono K., Access control for a positioning mechanism with multi-degree-of-vibration-freedom, Transaction of the JSME series C (in Japanese), Vol. 57, No. 538 (1991).

[38] Yamaura, H. and Ono K., Vibrationless access control of a positioning mechanism for high-order natural modes of vibration, Transaction of the JSME series C (in Japanese), Vol. 54, No. 508 (1991).

[39] Yamaura, H. and Ono K., Vibrationless access control of a positioning mechanism for high-order natural modes of vibration (2nd report, vibrationless velocity control), Transaction of the JSME series C (in Japanese), Vol. 59, No. 568 (1993).

[40] Singer, N. C. and Seeing, W. P., Preshaping command inputs to reduce system vibration, Journal of Dynamic Systems, Measurement, and Control, Vol. 112 (1990), pp. 76-82.

[41] Takagi, K. and Nishimura, H., Control of a jib-type crane mounted on an flexible structure, IEEE Transactions on Control systems technology, Vol. 11, No. 1 (2003), pp. 32-42.

[42] He, W., Zhang, S. and Ge, S.S., Adaptive control of a flexible crane system with the boundary output constraint, IEEE Transactions on Industrial Electronics, Vol. 61, No. 8 (2014), pp. 4126-4133.

[43] He, X., He., W., Shi, J. and Sun, C., Boundary vibration control of variable length crane systems in two-dimensional space with output contraints, IEEE/ASME Transactions on Mechatronics, Vol. 22, No. 5 (2017), pp. 1952-1962.

[44] Urbaś, A., Kłosiński, J. and Augustynek, Z., The influence of the PID controller settings on the motion of a truck-mounted crane with a flexible boom and friction in joints, Elsevier, Control Engineering Practice, Vol. 103 (2020), 104610.

[45] Sakawa, Y. and Shindo Y., Optimal control of container cranes, Automatica, Vol. 18, No. 3 (1982), pp. 257-266.

[46] Lee, H.-H, Modeling and control of a three-dimensional overhead crane, ASME, Journal of Dynamic System, Measurement, and Control, Vol. 120, No. 4 (1998), pp.417-476.

[47] Jaafar, H.I., Mohamed, Z., Shamsudin, M.A., Subha, N.A.M., Ramli, L. and Abdullahi, A.M., Model reference command shaping for vibration control of multimode flexible systems with application to a double-pendulum overhead crane, Elsevier, Mechanical Systems and Signal Processing, Vol. 115 (2019), pp. 677-695.

[48] Tho, H.D., Kaneshige, A. and Terashima, K., Minimum-time S-curve commands for vibration-free transportation of an overhead crane with actuator limits, Elsevier, Control Engineering Practice, Vol. 90 (2020), 104390.

[49] Cornwell, R. E., Craig, R.R. JR. and Johnson, C.P., On the application of the mode-acceleration method to structural engineering problems, John Wiley & Sons, Earthquake Engineering and Structural Dynamics, Vol. 11, No. 5 (1983), pp. 679-688.

[50] Matsuda, T. and Yamaura, H., Frequency characteristics analysis and design method of FIR filter for velocity and acceleration estimation using radial basis function network, The Transaction of the JSME, Journal of System Design and Dynamics, Vol. 2, No. 5 (2008), pp. 1137-1147.

Appendix A

DAE-dynamic model of the flexible mobile crane

This appendix explains the equation of motion for the mobile-type rotary crane that was used in investigating the influence of the flexibility in rope and its inertia in Section 2.1. The equation of motion was formulated in form of the differential-algebraic equation. The model is shown in Fig. A.1. This model was used to investigate the influence of the flexibility in rope and its inertia in Section 2.1. This model was constructed with a rigid body chassis with the flexible outriggers (body-1), the rigid slewing drive (body-2), the flexible boom (body-3), the ropes (body-4) and the point mass hoisted load (body-5).

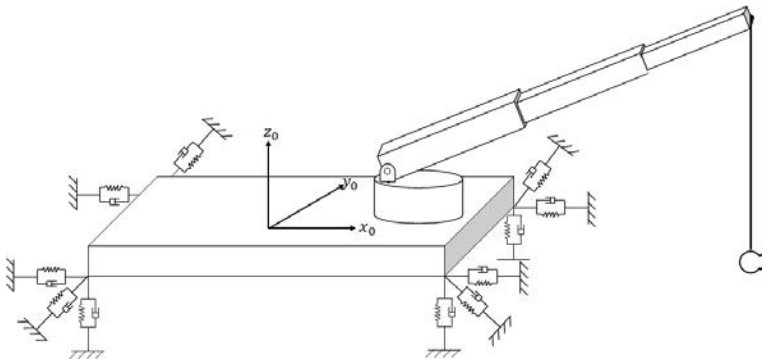

Fig. A.1: Mobile crane model with telescopic boom

The coordinates of the rigid body chassis were presented as shown in Fig. A.2. The mass-inertia matrix of this body was calculated as

$$\mathbf{M}_1 = \begin{bmatrix} \mathbf{m}_{RR,1} & \\ & \bar{\mathbf{J}}_{\theta\theta,1} \end{bmatrix}, \tag{A.1}$$

where $\mathbf{m}_{RR,1} = diag\{m_1, m_1, m_1\}$, and $\bar{\mathbf{J}}_{\theta\theta,1} = diag\left\{\bar{J}_{xx,1}, \bar{J}_{yy,1}, \bar{J}_{zz,1}\right\}$. m_1 is the mass of the chassis, and $\bar{J}_{ii,1}$ is the mass-moment of inertia around the i axis of the body-1 coordinate systems.

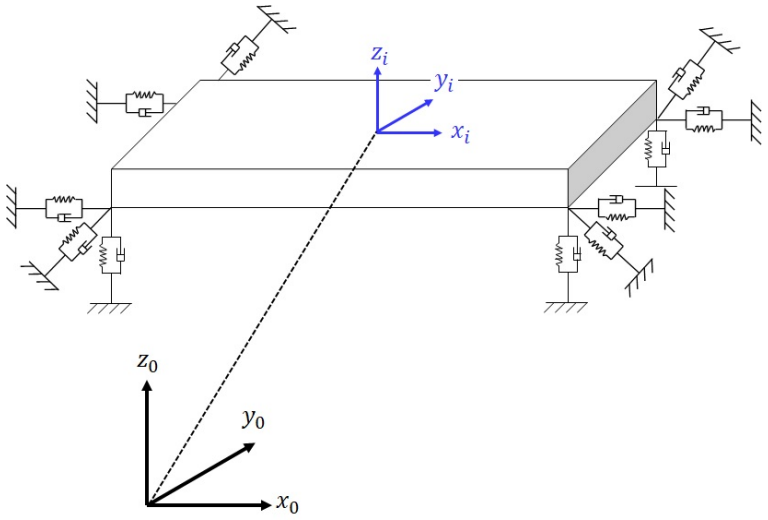

Fig. A.2: Rigid body chassis's coordinates systems

The rotation matrix of this body was the linearized Tait-Brayan rotation which was calculated as

$$\mathbf{A}_1 \approx \begin{bmatrix} 1 & -\psi_1 & \theta_1 \\ \psi_1 & 1 & -\phi_1 \\ -\theta_1 & \phi_1 & 1 \end{bmatrix}, \tag{A.2}$$

where $\mathbf{R}_i = \begin{bmatrix} x_i & y_i & z_i \end{bmatrix}^T$ is the position vector from the global origin to body-i's origin, and $\mathbf{\Theta}_i = \begin{bmatrix} \phi_i & \theta_i & \psi_i \end{bmatrix}^T$ is the vector of the Euler's angle where ϕ_i, θ_i and ψ_i are the rotation around x, y and z axes, respectively. The vector of the generalized coordinates of body-1 was

$$\mathbf{q}_1 = \begin{bmatrix} \mathbf{R}_1 \\ \mathbf{\Theta}_1 \end{bmatrix}. \tag{A.3}$$

Since the rotation was linearized, the vector of angular velocities can be approximated as $\bar{\boldsymbol{\omega}}_1 \approx \dot{\mathbf{\Theta}}_1$. Therefore, the vector of the generalized velocities could be approximated as $\mathbf{v}_1 \approx \dot{\mathbf{q}}_1$.

The chassis was subjected to the gravity force, damping-stiffness force from the outrigger, and the quadratic velocity of from the rotational velocity.

The mass-inertia matrix of the rigid body slewing drive, as shown in Fig. A.3, was calculated as

$$\mathbf{M}_2 = \begin{bmatrix} \mathbf{m}_{RR,2} & \\ & \bar{\mathbf{J}}_{\theta\theta,2} \end{bmatrix}, \tag{A.4}$$

where $\mathbf{m}_{RR,2} = diag\{m_2, m_2, m_2\}$, and $\bar{\mathbf{J}}_{\theta\theta,2} = diag\left\{\bar{J}_{xx,2}, \bar{J}_{yy,2}, \bar{J}_{zz,2}\right\}$. m_2 is the mass of the slewing body, and $\bar{J}_{ii,2}$ is the mass-moment of inertia around the i axis of the body-2 coordinates systems. The total force on the slewing drive, $\mathbf{Q}_2$, are the gravitational force and the quadratic velocity vector.

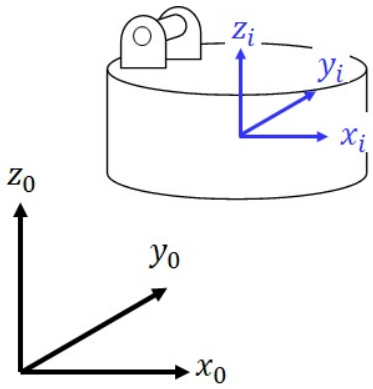

Fig. A.3: Rigid body slewing drive's coordinates systems

The flexible boom model was formulated with the FFRF, as explained in Chapter 2. The formulation was the same even this model was a telescopic boom, as shown in Fig. A.4. In this model, the boom was modeled with three beam elements. The Boolean's matrices for this boom model were

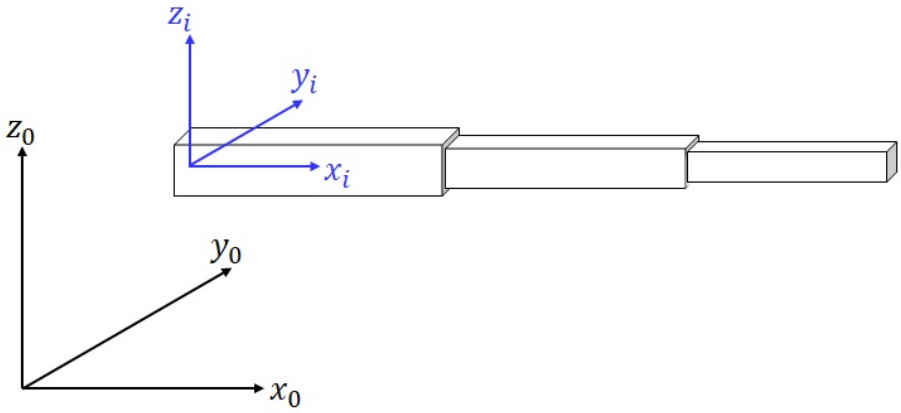

Fig. A.4: Telescopic boom's coordinates systems

$$\begin{aligned} \mathbf{B}_3^1 &= \begin{bmatrix} \mathbf{0}_{6\times6} & \mathbf{0}_{6\times12} \\ \mathbf{I}_{6\times6} & \mathbf{0}_{6\times6} \end{bmatrix}, \\ \mathbf{B}_3^2 &= \begin{bmatrix} \mathbf{I}_{12\times12} & \mathbf{0}_{12\times6} \end{bmatrix}, \\ \mathbf{B}_3^3 &= \begin{bmatrix} \mathbf{0}_{12\times6} & \mathbf{I}_{12\times12} \end{bmatrix}. \end{aligned} \tag{A.5}$$

Thus, the matrix of shape function of each k-element was

$$\mathbf{S}_3^k = \mathbf{S}_{beam}\mathbf{B}_3^k. \tag{A.6}$$

In total, the vector of the generalized flexible coordinates of the boom was

$$\bar{\mathbf{q}}_{f,3} = \begin{bmatrix} e_{3,1} & e_{3,2} & \dots & e_{3,18} \end{bmatrix}^T. \tag{A.7}$$

The inertia matrix, the stiffness matrix and the vector of the quadratic velocity of the flexible boom was calculated through the derivation as explained in Section 2.2.

The hoisted load was modeled as the point-mass (Fig. A.5), and its inertia matrix was $\mathbf{M}_4 = \mathbf{m}_{RR,4}$.

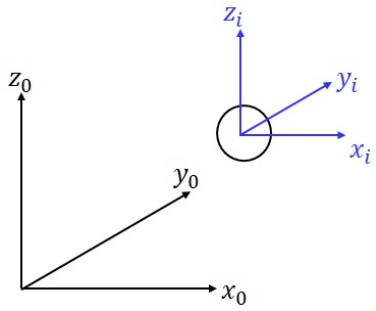

Fig. A.5: The hoisted load's coordinates systems

The constraint equations for this model were described as follows:

$$\mathbf{C}_1 = \mathbf{R}_1 + \mathbf{A}_1\bar{\mathbf{u}}_{1,C_1} - \mathbf{R}_2 - \mathbf{A}_2\bar{\mathbf{u}}_{2,C_1}, \tag{A.8}$$

$$\mathbf{C}_2 = \begin{bmatrix} \phi_1 \\ \theta_1 \end{bmatrix} - \begin{bmatrix} \phi_2 \\ \theta_2 \end{bmatrix}, \tag{A.9}$$

$$\mathbf{C}_3 = \mathbf{R}_2 + \mathbf{A}_2\bar{\mathbf{u}}_{2,C_3} - \mathbf{R}_3^1, \tag{A.10}$$

$$\mathbf{C}_4 = \begin{bmatrix} \phi_2 \\ \psi_2 \end{bmatrix} - \begin{bmatrix} \phi_3^1 \\ \psi_3^1 \end{bmatrix}, \tag{A.11}$$

$$\mathbf{C}_5 = \mathbf{R}_3 + \mathbf{A}_3\bar{\mathbf{u}}_{3,C_4} - \mathbf{R}_4, \tag{A.12}$$

$$\mathbf{C}_6 = \mathbf{R}_4 + \mathbf{A}_4\bar{\mathbf{u}}_{4,C_5} - \mathbf{R}_5, \tag{A.13}$$

$$\mathbf{C}_7 = \begin{bmatrix} e_{4,26} & e_{4,27} \end{bmatrix}^T. \tag{A.14}$$

$$C_8 = \mathbf{d}_{rope}^T \mathbf{d}_{rope} - \ell_{rope}^2. \tag{A.15}$$

In case of the model with the inertia included rope model, the total constraint equation was

$$\mathbf{C} = \begin{bmatrix} \mathbf{C}_1^T & \mathbf{C}_2^T & ... & \mathbf{C}_7^T \end{bmatrix}^T. \tag{A.16}$$

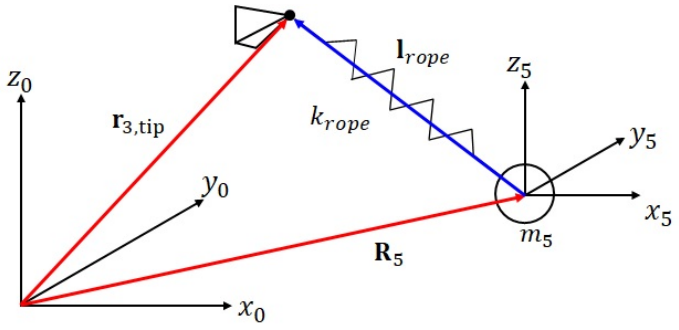

Fig. A.6: Spring rope model

The constraint equations when the spring rope was used was

$$\mathbf{C} = \begin{bmatrix} \mathbf{C}_1^T & \mathbf{C}_2^T & \mathbf{C}_3^T & \mathbf{C}_4^T \end{bmatrix}^T. \tag{A.17}$$

Instead of the constraint equations, the spring rope in Fig. A.6 used the flexible forces to connect the bodies. The generalized rope's spring force was calculated as follows;

$$\mathbf{l}_{rope} = \mathbf{R}_3 + \mathbf{A}_3 \bar{\mathbf{u}}_{3,tip} - \mathbf{R}_5, \tag{A.18}$$

$$\mathbf{F}_{rope} = -k_{rope}(\ell_{rope} - \ell_{rope,0})\hat{\mathbf{l}}_{rope}, \tag{A.19}$$

$$\ell_{rope} = \|\mathbf{l}_{rope}\|, \tag{A.20}$$

$$\hat{\mathbf{l}}_{rope} = \mathbf{l}_{rope} \frac{1}{\ell_{rope}}, \tag{A.21}$$

where k_{rope} is the stiffness of the rope in lateral direction, $\ell_{rope,0}$ is the initial rope length. The generalized force was written as

$$\mathbf{Q}_{rope} = \begin{bmatrix} \mathbf{0}_{12\times 1} \\ \mathbf{F}_{rope} \\ (\mathbf{F}_{rope}^T \mathbf{A}_3 \tilde{\mathbf{u}}_{tip})^T \\ (\mathbf{F}_{rope}^T \mathbf{A}_3 \mathbf{S}_{3,tip})^T \\ -\mathbf{F}_{rope} \end{bmatrix}. \tag{A.22}$$

When the was a rigid body, the constraint equations became

$$\mathbf{C} = \begin{bmatrix} \mathbf{C}_1^T & \mathbf{C}_2^T & \mathbf{C}_3^T & \mathbf{C}_4^T & C_8 \end{bmatrix}^T. \tag{A.23}$$

The equation of motion was formulated as

$$\mathbf{M}\dot{\mathbf{v}} + \mathbf{K}\mathbf{q} + \mathbf{C}_\mathbf{q}^{\mathrm{T}}\boldsymbol{\lambda} = \mathbf{Q}, \tag{A.24}$$

$$\mathbf{C}_\mathbf{q}\dot{\mathbf{v}} = \mathbf{Q}_\mathbf{c} - \alpha\dot{\mathbf{C}} - \beta^2\mathbf{C} = \boldsymbol{\gamma}. \tag{A.25}$$

where $\mathbf{C}_\mathbf{q}$ is the Jacobian matrix of the constraint equation. In this work, the Lagrange's multiplier was calculated as

$$\boldsymbol{\lambda} = (\mathbf{C}_\mathbf{q}\mathbf{M}^{-1}\mathbf{C}_\mathbf{q}^{\mathrm{T}})^{-1}(\mathbf{C}_\mathbf{q}\mathbf{M}^{-1}\mathbf{Q} - \boldsymbol{\gamma}), \tag{A.26}$$

where α and β are the constant for the Buamgarte's stabilization.

Appendix B

Dynamic model of flexible mobile crane with relative coordinates system

In this appendix, the dynamics model of the mobile crane for the Section 2.3 is explained. This dynamic model was formulated with the relative coordinate systems. The mobile crane model is shown in Fig. B.1.

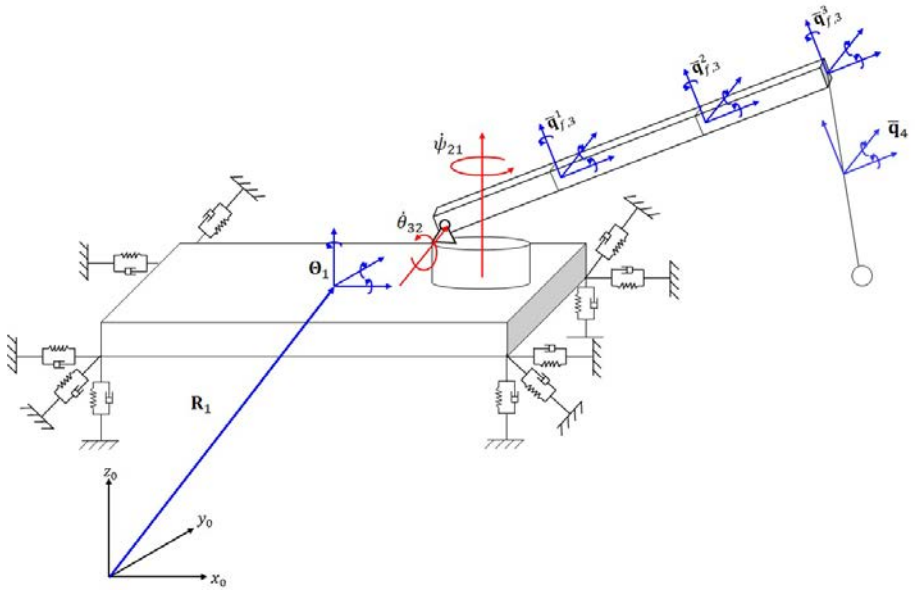

Fig. B.1: Mobile crane's coordinates system

The chassis and the slewing drive were constrained with the revolute joint with the relative motion as shown in Fig. B.2. Their relative motion was calculated as Eq. (B.1).

$$\begin{aligned} \mathbf{R}_2 &= \mathbf{R}_1 + \mathbf{u}_{1,c1} - \mathbf{u}_{2,c1}, \\ \boldsymbol{\omega}_2 &= \boldsymbol{\omega}_1 + \dot{\psi}_{21}\mathbf{e}_{1,c1}. \end{aligned} \tag{B.1}$$

where $\mathbf{e}_{i,cj}$ is the unit vector of the constraint axis j on body-i.

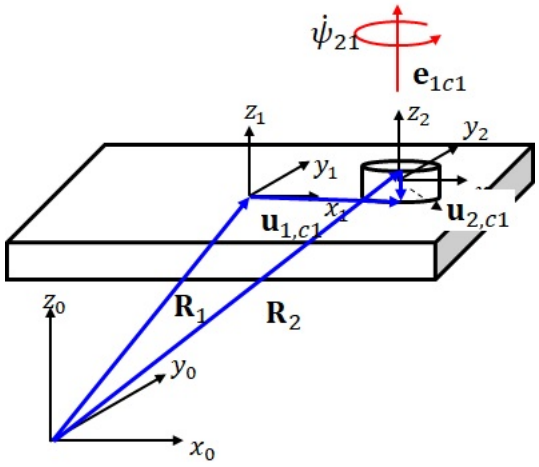

Fig. B.2: Chassis and slewing drive's relative motion

The slewing drive and the flexible boom were constraint with the revolute joint as shown in Fig. B.3. Their constraint relation was calculated as Eq. (B.2).

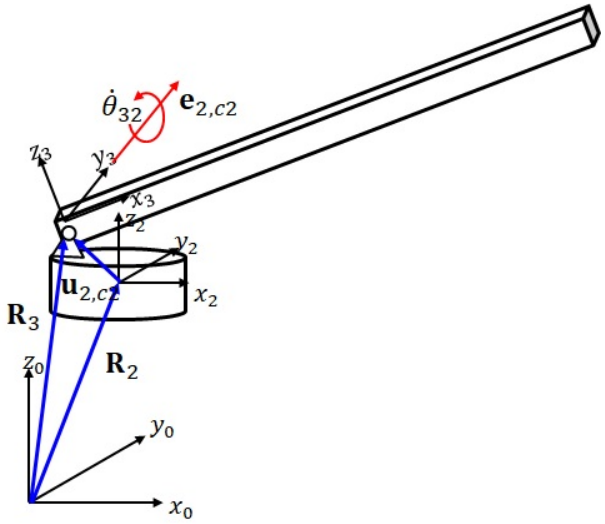

Fig. B.3: Slewing drive and bomm's relative motion

$$\begin{aligned} \mathbf{R}_3 &= \mathbf{R}_2 + \mathbf{u}_{2,c2} \\ \boldsymbol{\omega}_3 &= \boldsymbol{\omega}_2 + \dot{\theta}_{32}\mathbf{e}_{2,c2}. \end{aligned} \tag{B.2}$$

The formulation of the flexible boom and the hoisted load for the relative coordinate model was explained in Section 2.2.

From this constraint, the acceleration relation within this model were described as follows:

$$\begin{bmatrix} \ddot{\mathbf{R}}_2 \\ \dot{\boldsymbol{\omega}}_2 \\ \ddot{\tilde{\mathbf{q}}}_{f,3} \\ \ddot{\tilde{\mathbf{q}}}_4 \end{bmatrix} = \begin{bmatrix} \mathbf{I} & \tilde{\mathbf{u}}_{2,c2} - \tilde{\mathbf{u}}_{1,c1} & \mathbf{0} & \mathbf{0} \\ \mathbf{0} & \mathbf{I} & \mathbf{0} & \mathbf{0} \\ \mathbf{0} & \mathbf{0} & \mathbf{I} & \mathbf{0} \\ \mathbf{0} & \mathbf{0} & \mathbf{0} & \mathbf{I} \end{bmatrix} \begin{bmatrix} \ddot{\mathbf{R}}_1 \\ \dot{\boldsymbol{\omega}}_1 \\ \ddot{\tilde{\mathbf{q}}}_{f,3} \\ \ddot{\tilde{\mathbf{q}}}_4 \end{bmatrix} + \begin{bmatrix} \mathbf{0} \\ \mathbf{e}_{1,c1} \\ \mathbf{0} \\ \mathbf{0} \end{bmatrix} \ddot{\psi}_{21} + \begin{bmatrix} (\tilde{\boldsymbol{\omega}}_1)^2 \mathbf{u}_{1,c1} - (\tilde{\boldsymbol{\omega}}_2)^2 \mathbf{u}_{2,c1} \\ \dot{\psi}_{21} \tilde{\boldsymbol{\omega}}_1 \mathbf{e}_{1,c1} \\ \mathbf{0} \\ \mathbf{0} \end{bmatrix} \tag{B.3}$$

$$\dot{\mathbf{v}}_{2-4} = \mathbf{D}_2 \dot{\mathbf{v}}_{1-4} + \mathbf{N}_{21} \ddot{\psi}_{21} + \mathbf{H}_{21}$$

$$\begin{bmatrix} \ddot{\mathbf{R}}_3 \\ \dot{\boldsymbol{\omega}}_3 \\ \ddot{\tilde{\mathbf{q}}}_{f,3} \\ \ddot{\tilde{\mathbf{q}}}_4 \end{bmatrix} = \begin{bmatrix} \mathbf{I} & -\tilde{\mathbf{u}}_{2,c2} & \mathbf{0} & \mathbf{0} \\ \mathbf{0} & \mathbf{I} & \mathbf{0} & \mathbf{0} \\ \mathbf{0} & \mathbf{0} & \mathbf{I} & \mathbf{0} \\ \mathbf{0} & \mathbf{0} & \mathbf{0} & \mathbf{I} \end{bmatrix} \begin{bmatrix} \ddot{\mathbf{R}}_2 \\ \dot{\boldsymbol{\omega}}_2 \\ \ddot{\tilde{\mathbf{q}}}_{f,3} \\ \ddot{\tilde{\mathbf{q}}}_4 \end{bmatrix} + \begin{bmatrix} \mathbf{0} \\ \mathbf{e}_{2,c2} \\ \mathbf{0} \\ \mathbf{0} \end{bmatrix} \ddot{\theta}_{32} + \begin{bmatrix} (\tilde{\boldsymbol{\omega}}_2)^2 \mathbf{u}_{2,c2} \\ \dot{\theta}_{32} \tilde{\boldsymbol{\omega}}_2 \mathbf{e}_{2,c2} \\ \mathbf{0} \\ \mathbf{0} \end{bmatrix} \tag{B.4}$$

$$\dot{\mathbf{v}}_{3-4} = \mathbf{D}_3 \dot{\mathbf{v}}_{2-4} + \mathbf{N}_{32} \ddot{\theta}_{32} + \mathbf{H}_{32}$$

while the equation of motion of each body could be written as

$$\begin{aligned} \mathbf{M}_1 \dot{\mathbf{v}}_{1-4} &= \mathbf{Q}_1 + \mathbf{Q}_{1,c1} \\ \mathbf{M}_2 \dot{\mathbf{v}}_{2-4} &= \mathbf{Q}_2 + \mathbf{Q}_{2,c1} + \mathbf{Q}_{2,c2} \\ \mathbf{M}_3 \dot{\mathbf{v}}_{3-4} &= \mathbf{Q}_3 + \mathbf{Q}_{3,c2}. \end{aligned} \tag{B.5}$$

Each generalized forces vector $\mathbf{Q}_i$ consisted of the gravity force and the quadratic velocity vectors. In addition to these forces, the chassis was subjected to the flexible and damping forces from the outriggers, and the flexible boom was subjected to its own flexible forces. The constraint relations were substituted into these equations of motion which resulted in constraint forces cancelling each other and gave the final equation of motion as

$$\mathbf{M}\dot{\mathbf{v}} = \mathbf{Q} - \mathbf{M}_r \ddot{\tilde{\mathbf{q}}}_r - \boldsymbol{\Gamma}_r. \tag{B.6}$$

Appendix C

Dynamic model of flexible crane with relative coordinates system

This appendix explains the formulation of the dynamic model of the flexible rotary crane that fixed on the ground or steady platform. This model was similar to the Appendix B except there was no chassis as shown in Fig. C.1.

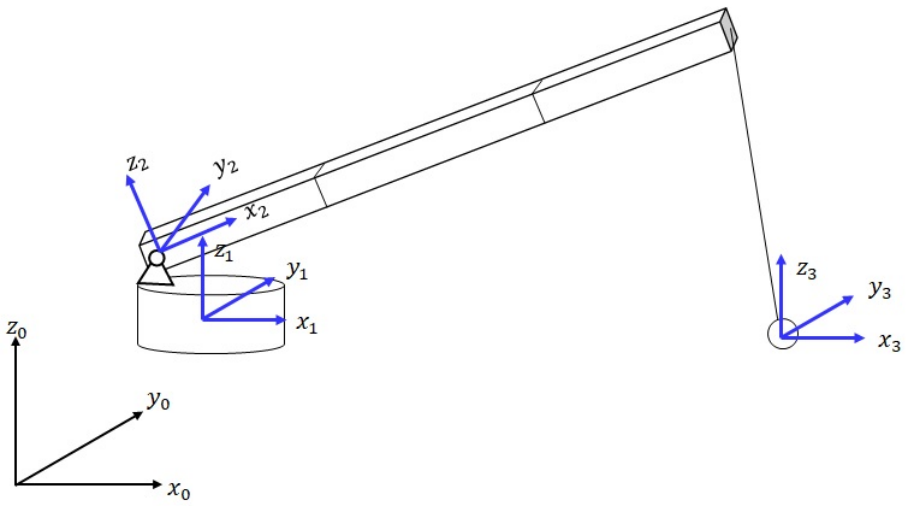

Fig. C.1: Flexible rotary crane coordinates

The slewing platform, described as body-1, is shown in Fig. C.2. The equation of motion was written as

$$\begin{bmatrix} \mathbf{m}_1 & \mathbf{0}_{3\times3} \\ \mathbf{0}_{3\times3} & \mathbf{J}_1 \end{bmatrix} \begin{bmatrix} \ddot{\mathbf{R}}_1 \\ \dot{\boldsymbol{\omega}}_1 \end{bmatrix} = \mathbf{Q}_{1,ext} + \mathbf{Q}_{1,c1} + \mathbf{Q}_{1,c2}, \tag{C.1}$$

where $\mathbf{Q}_{1,total}$ is the vector of the total generalized forces that exerting on the body-1, and the force vectors, $\mathbf{Q}_{1,ext}$, $\mathbf{Q}_{1,c1}$ and $\mathbf{Q}_{1,c2}$ are the external forces, the constraint force from first and second constraints on the body-1.

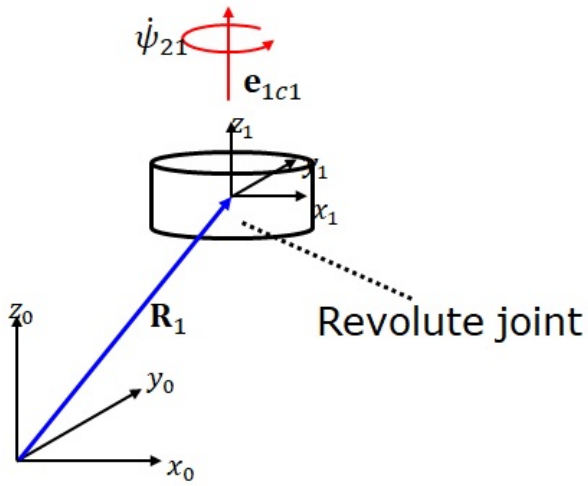

Fig. C.2: The slewing platform model

The slewing platform was constrained to on the ground with the revolute joint, and it rotated around z_1 axis where $\mathbf{e}_{1,c1}$. This constraint is described as constraint-1, $c1$. It was assumed that the origin of body-1's coordinates system was fixed on the origin of the global coordinates systems. Thus, the positional constraint equation was written as Eq. (C.2).

$$\mathbf{R}_1 = \mathbf{0}_{3\times 1}. \tag{C.2}$$

The angular velocity constraint of the revolute joint in $c1$ was written as

$$\boldsymbol{\omega}_1 = \mathbf{e}_{1,c1}\dot{\psi}_{10}. \tag{C.3}$$

The constraint force $\mathbf{Q}_{2,c2}$ was the connection between bodies 1 and 2. The boom was constrained on the slewing platform with the revolute joint as shown in Fig. C.3. The positional constraint equation of $c2$ was written as Eq. (C.4).

$$\mathbf{R}_2 = \mathbf{R}_1 + \mathbf{u}_{1,c2}, \tag{C.4}$$

where $\mathbf{u}_{1,c2} = \mathbf{A}_1\bar{\mathbf{u}}_{1,c2}$. The relation of the angular velocity of the revolute joint in $c2$ was

$$\boldsymbol{\omega}_2 = \boldsymbol{\omega}_1 + \mathbf{e}_{1,c2}\dot{\theta}_{21}, \tag{C.5}$$

where $\mathbf{e}_{1,c2} = \mathbf{A}_1\bar{\mathbf{e}}_y$. The acceleration constraint was calculated from Eqs. (C.4) and (C.5), and resulted as,

$$\ddot{\mathbf{R}}_2 = \ddot{\mathbf{R}}_1 - \tilde{\mathbf{u}}_{1,c2}\dot{\boldsymbol{\omega}}_1 + (\tilde{\boldsymbol{\omega}}_1)^2\mathbf{u}_{1,c2}, \tag{C.6}$$

$$\dot{\boldsymbol{\omega}}_2 = \dot{\boldsymbol{\omega}}_1 + \mathbf{e}_{1,c2}\ddot{\theta}_{21} + \dot{\theta}_{21}\tilde{\boldsymbol{\omega}}_1\mathbf{e}_{1,c2} \tag{C.7}$$

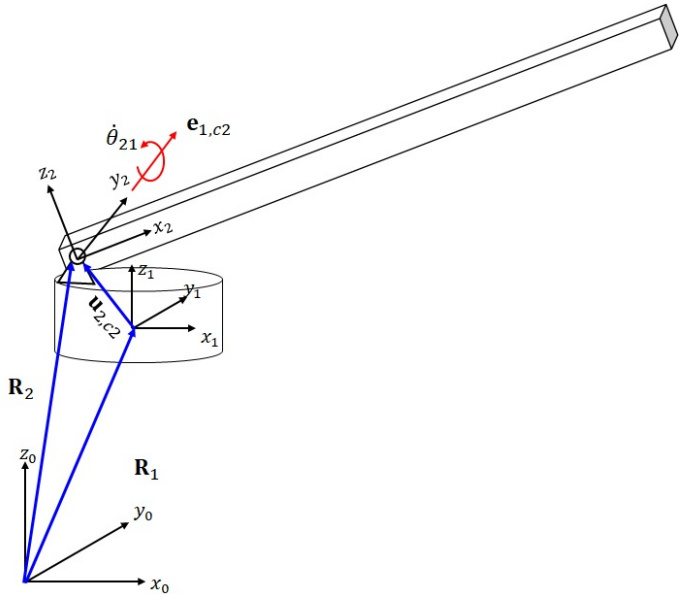

Fig. C.3: The slewing platform and boom constraint

In this model, the independent coordinates were the generalized coordinates of the boom, the angle of the hoisted load, slewing angle and the lifting angle. The acceleration constraint equations were used to map the body's generalized coordinates into the independent coordinates. Firstly, the constraint acceleration of the revolute joint between the slewing platform and ground was rewritten as follows;

$$\begin{bmatrix} \ddot{\mathbf{R}}_1 \\ \dot{\boldsymbol{\omega}}_1 \\ \ddot{\mathbf{q}}_{2,f} \\ \ddot{\mathbf{q}}_{32} \end{bmatrix} = \begin{bmatrix} \mathbf{0} & \mathbf{0} \\ \mathbf{0} & \mathbf{0} \\ \mathbf{I} & \mathbf{0} \\ \mathbf{0} & \mathbf{I} \end{bmatrix} \begin{bmatrix} \ddot{\mathbf{q}}_{2,f} \\ \ddot{\mathbf{q}}_{32} \end{bmatrix} + \begin{bmatrix} \mathbf{0} & \mathbf{0} \\ \mathbf{e}_{1,c1} & \mathbf{0} \\ \mathbf{0} & \mathbf{0} \\ \mathbf{0} & \mathbf{0} \end{bmatrix} \begin{bmatrix} \ddot{\bar{\psi}}_{10} \\ \ddot{\theta}_{21} \end{bmatrix} \tag{C.8}$$
$$\dot{\mathbf{V}}_1 = \mathbf{P}_{10}\ddot{\mathbf{q}} + \mathbf{H}_{10}\ddot{\mathbf{q}}_r$$

Then, the acceleration constraint at the revolute joint between the slewing platform and the flexible boom was rewritten as

$$\begin{bmatrix} \ddot{\mathbf{R}}_2 \\ \dot{\boldsymbol{\omega}}_2 \\ \ddot{\mathbf{q}}_{2,f} \\ \ddot{\mathbf{q}}_{32} \end{bmatrix} = \begin{bmatrix} \mathbf{I} & -\tilde{\mathbf{u}}_{1,c2} & \mathbf{0} & \mathbf{0} \\ \mathbf{0} & \mathbf{I} & \mathbf{0} & \mathbf{0} \\ \mathbf{0} & \mathbf{0} & \mathbf{I} & \mathbf{0} \\ \mathbf{0} & \mathbf{0} & \mathbf{0} & \mathbf{I} \end{bmatrix} \begin{bmatrix} \ddot{\mathbf{R}}_1 \\ \dot{\boldsymbol{\omega}}_1 \\ \ddot{\mathbf{q}}_{2,f} \\ \ddot{\mathbf{q}}_{32} \end{bmatrix} + \begin{bmatrix} \mathbf{0} & \mathbf{0} \\ \mathbf{0} & \mathbf{e}_{1,c2} \\ \mathbf{0} & \mathbf{0} \\ \mathbf{0} & \mathbf{0} \end{bmatrix} \begin{bmatrix} \ddot{\bar{\psi}}_{10} \\ \ddot{\theta}_{21} \end{bmatrix} + \begin{bmatrix} (\tilde{\boldsymbol{\omega}}_1)^2\mathbf{u}_{1,c2} \\ \dot{\theta}_{21}\tilde{\boldsymbol{\omega}}_1\mathbf{e}_{1,c2} \\ \mathbf{0} \\ \mathbf{0} \end{bmatrix}. \tag{C.9}$$
$$\dot{\mathbf{V}}_2 = \mathbf{P}_{21}\dot{\mathbf{V}}_1 + \mathbf{H}_{21}\ddot{\mathbf{q}}_r + \mathbf{N}_{21}$$

Eq. (C.8) was, then, substituted into Eq. (C.9) and resulted in

$$\begin{aligned} \dot{\mathbf{V}}_2 =& \mathbf{P}_{21}\left(\mathbf{P}_{10}\ddot{\mathbf{q}} + \mathbf{H}_{10}\ddot{\mathbf{q}}_r\right) + \mathbf{H}_{21}\ddot{\mathbf{q}}_r + \mathbf{N}_{21}, \\ =& \mathbf{P}_{21}\mathbf{P}_{10}\ddot{\mathbf{q}} + \left(\mathbf{P}_{21}\mathbf{H}_{10} + \mathbf{H}_{21}\right)\ddot{\mathbf{q}}_r + \mathbf{N}_{21}, \\ =& \mathbf{P}_{20}\ddot{\mathbf{q}} + \mathbf{H}_{20}\ddot{\mathbf{q}}_r + \mathbf{N}_{21}. \end{aligned} \tag{C.10}$$

The equation of motion of each body were

$$\mathbf{M}_1\dot{\mathbf{V}}_1 = \mathbf{Q}_{1,g} + \mathbf{Q}_{1,v} + \mathbf{Q}_{1,c1}, \tag{C.11}$$

$$\mathbf{M}_{2-3}\dot{\mathbf{V}}_2 = \mathbf{Q}_{2,k} + \mathbf{Q}_{2,g} + \mathbf{Q}_{2,v} + \mathbf{Q}_{2,c1}. \tag{C.12}$$

By substituted Eqs. (C.8) and (C.9) into Eqs. (C.11) and (C.12), then multiplied $\mathbf{P}_{10}^T$ to the left-side of Eq. (C.11) and $\mathbf{P}_{20}^T$ to the left-side of Eq. (C.12), the equation of motions were rewritten into form of the independent relative coordinates as

$$\mathbf{M}_{1,0}\ddot{\mathbf{q}} + \mathbf{M}_{1,r}\ddot{\mathbf{q}}_r + \mathbf{\Gamma}_{10} = \mathbf{Q}_{1,g,r} + \mathbf{Q}_{1,v,r} + \mathbf{P}_{10}^T\mathbf{Q}_{1,c1}, \tag{C.13}$$

$$\mathbf{M}_{2-3,0}\ddot{\mathbf{q}} + \mathbf{M}_{2,r}\ddot{\mathbf{q}}_r + \mathbf{\Gamma}_{20} = \mathbf{Q}_{2,k,r} + \mathbf{Q}_{2,g,r} + \mathbf{Q}_{2,v,r} + \mathbf{P}_{20}^T\mathbf{Q}_{2,c1}. \tag{C.14}$$

Since $\mathbf{P}_{10}^T\mathbf{Q}_{1,c1} = -\mathbf{P}_{20}^T\mathbf{Q}_{2,c1}$ was the joint reaction force at body-1 and 2, Eqs. (C.13) and (C.14) could be combined and resulted in the finalized equation of motion of the flexible rotary crane systems as

$$\mathbf{M}_{sys,0}\ddot{\mathbf{q}} + \mathbf{M}_{sys,r}\ddot{\mathbf{q}}_r + \mathbf{\Gamma}_{sys} = \mathbf{Q}_{g,r} + \mathbf{Q}_{v,r} + \mathbf{Q}_{k,r} \tag{C.15}$$

Appendix D

Dynamic model for laboratory-size crane

This appendix explains the formulation of the dynamic model of the laboratory size crane that was used in Chapter 3. The schematic of the nonlinear dynamics model of the laboratory-scale flexible crane is shown in Fig. D.1.

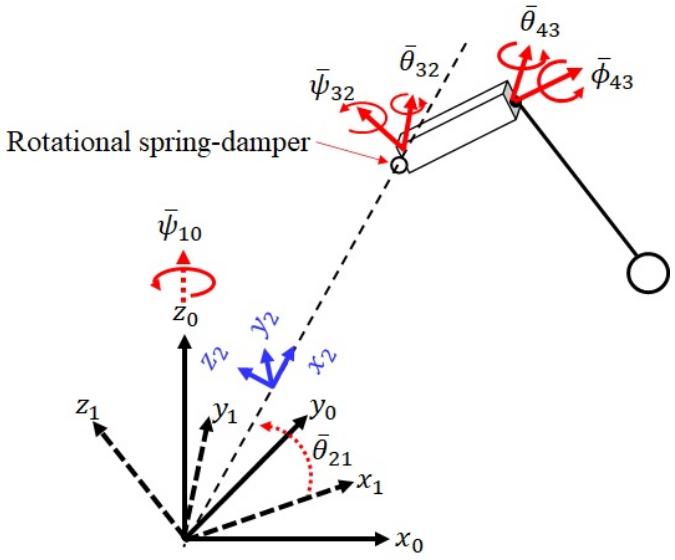

Fig. D.1: The schematic of the dynamics model of the laboratory-scale flexible crane

The boom was modeled as two rigid beams that were connected through the flexible universal joint. The hoisted load was considered as an additional particle that extended from the top boom as explained in Chapter 2. The top boom and the hoisted load model are shown in Fig. D.2. The rope vector $\bar{\mathbf{d}}_{rope}$ was calculated with Eq. (D.1).

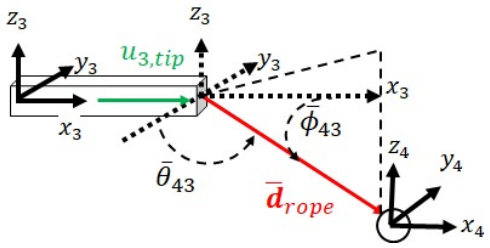

Fig. D.2: The schematic for the hoisted load on the top boom of the laboratory-size crane

.

$$\bar{\mathbf{d}}_{rope} = \begin{bmatrix} -\ell \cos\bar{\phi}_{43} \sin\bar{\theta}_{43} \\ \ell \sin\bar{\phi}_{43} \\ -\ell \cos\bar{\phi}_{43} \cos\bar{\theta}_{43} \end{bmatrix} \tag{D.1}$$

The position vector from (x_0, y_0, z_0) to an arbitrary point on body-3 and 4, $\mathbf{X}$, was calculated as

$$\mathbf{X} = \begin{cases} \mathbf{R}_3 + \mathbf{A}_3\bar{\mathbf{u}}_{3,X} & \text{if } \bar{x}_3 \le L_{top} \\ \mathbf{R}_3 + \mathbf{A}_3(\bar{\mathbf{u}}_{3,tip} + \bar{\mathbf{d}}_{rope}) \text{ or } \mathbf{R}_4 & \text{if } \bar{x}_3 > L_{top} \end{cases}, \tag{D.2}$$

where ℓ is the length of rope. $\bar{\mathbf{u}}_{3,X}$ and $\bar{\mathbf{u}}_{3,tip}$ are position vectors from body-3 origin to an arbitrary point X and boom tip, respectively. $\bar{\mathbf{u}}_{3,X}$ and $\bar{\mathbf{u}}_{3,tip}$ were described on body-3 coordinates systems.

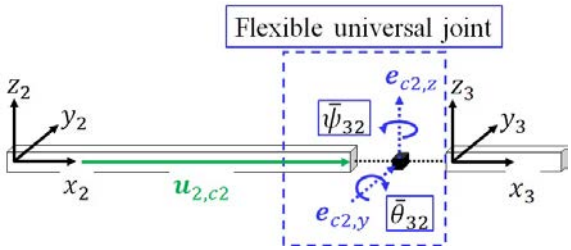

Fig. D.3: The schematic for base boom and top boom of the laboratory size crane

Figure D.3 shows that the base boom and the top boom were constrained by the flexible universal joint. The constraints position was the tip of the base boom and the origin of the top boom coordinates system. The acceleration constraint from body-2 to 4 was calculated as follows:

$$\begin{bmatrix} \ddot{\mathbf{R}}_3 \\ \dot{\boldsymbol{\omega}}_3 \\ \ddot{\mathbf{q}}_{43} \end{bmatrix} = \begin{bmatrix} \mathbf{I}_{3\times3} & -\tilde{\mathbf{u}}_{2,c2} \\ \mathbf{0}_{3\times3} & \mathbf{I}_{3\times3} \\ \mathbf{0}_{2\times3} & \mathbf{0}_{2\times3} \end{bmatrix} \begin{bmatrix} \ddot{\mathbf{R}}_2 \\ \dot{\boldsymbol{\omega}}_2 \end{bmatrix} + \begin{bmatrix} \mathbf{0}_{3\times1} & \mathbf{0}_{3\times1} & \mathbf{0}_{3\times2} \\ \mathbf{e}_{c2,y} & \mathbf{e}_{c2,z} & \mathbf{0}_{3\times2} \\ \mathbf{0}_{2\times1} & \mathbf{0}_{2\times1} & \mathbf{I}_{2\times2} \end{bmatrix} \begin{bmatrix} \ddot{\bar{\theta}}_{32} \\ \ddot{\bar{\psi}}_{32} \\ \ddot{\mathbf{q}}_{43} \end{bmatrix} + \begin{bmatrix} (\tilde{\boldsymbol{\omega}}_2)^2\mathbf{u}_{2,c2} \\ \dot{\bar{\theta}}_{32}\tilde{\boldsymbol{\omega}}_2\mathbf{e}_{c2,y} + \dot{\bar{\psi}}_{32}\left(\tilde{\boldsymbol{\omega}}_2\mathbf{e}_{c2,z} + \dot{\bar{\theta}}_{32}\tilde{\mathbf{e}}_{c2,y}\mathbf{e}_{c2,z}\right) \\ \mathbf{0}_{2\times1} \end{bmatrix},$$

$$\dot{\mathbf{V}}_3 = \mathbf{D}_{32}\dot{\mathbf{V}}_2 + \mathbf{H}_{32}\ddot{\mathbf{q}}_r + \mathbf{N}_{32},$$

(D.3)

where $\bar{\mathbf{q}}_{43} = \begin{bmatrix}\bar{\phi}_{43} & \bar{\theta}_{43}\end{bmatrix}^T$ is the vector of the hoisted load's generalized coordinates. $\mathbf{u}_{2,c2} = \mathbf{A}_2\bar{\mathbf{u}}_{2,c2}$, $\mathbf{e}_{c2,y} = \mathbf{A}_2\bar{\mathbf{e}}_y$, and $\mathbf{e}_{c2,z} = \mathbf{A}_2\mathbf{A}_{32,y}\bar{\mathbf{e}}_z$. Thus, $\mathbf{A}_3 = \mathbf{A}_2\mathbf{A}_{32,z}\mathbf{A}_{32,y}$.

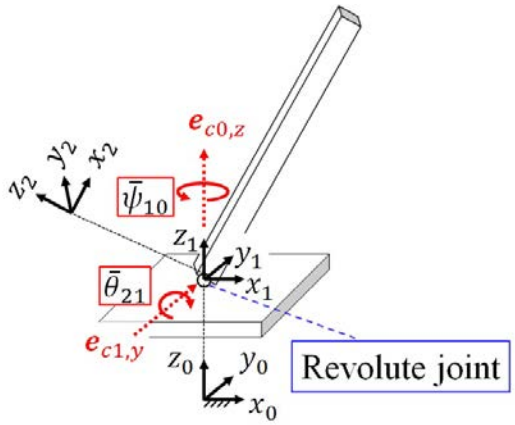

Fig. D.4: The schematic for slewing platform and base boom of the laboratory size crane on the ground

.

Figure D.4 illustrates the schematic of the slewing platform and the base boom on the global coordinates systems, (x_0, y_0, z_0), or ground model. The origin of the base boom was constrained on the center of the slewing platform with revolute joint and rotated around y_1 axis. The acceleration constraint of this model was written as follows:

$$\begin{aligned}\begin{bmatrix}\ddot{\mathbf{R}}_2\\ \dot{\boldsymbol{\omega}}_2\end{bmatrix} &= \begin{bmatrix}\mathbf{I}_{3\times3} & -\tilde{\mathbf{u}}_{1,c1}\\ \mathbf{0}_{3\times3} & \mathbf{I}_{3\times3}\end{bmatrix}\begin{bmatrix}\ddot{\mathbf{R}}_1\\ \dot{\boldsymbol{\omega}}_1\end{bmatrix} + \begin{bmatrix}\mathbf{0}_{3\times1}\\ \mathbf{e}_{c1,y}\end{bmatrix}\ddot{\bar{\theta}}_{21} + \begin{bmatrix}(\tilde{\boldsymbol{\omega}}_1)^2\mathbf{u}_{1,c1}\\ \dot{\bar{\theta}}_{21}\tilde{\boldsymbol{\omega}}_1\mathbf{e}_{c1,y}\end{bmatrix},\\ \dot{\mathbf{V}}_2 &= \mathbf{D}_{21}\dot{\mathbf{V}}_1 + \mathbf{H}_{21}\ddot{\bar{\theta}}_{21} + \mathbf{N}_{21},\end{aligned} \tag{D.4}$$

where $\mathbf{u}_{1,c1} = \mathbf{A}_1\bar{\mathbf{u}}_{1,c1}$ and $\mathbf{e}_{c1,y} = \mathbf{A}_1\bar{\mathbf{e}}_y$. Thus, $\mathbf{A}_2 = \mathbf{A}_1\mathbf{A}_{21,y}$.

The slewing platform was constrained on the origin of the global coordinates system (x_0, y_0, z_0) with a revolute joint that was rotated around z_0 axis. The origin of (x_0, y_0, z_0) was assumed to be at the center of the slewing platform as well. The acceleration the constraint of the slewing platform was calculated as

$$\begin{aligned}\begin{bmatrix}\ddot{\mathbf{R}}_1,\\ \dot{\boldsymbol{\omega}}_1\end{bmatrix} &= \begin{bmatrix}\mathbf{0}_{3\times1}\\ \mathbf{e}_{c0,z}\end{bmatrix}\ddot{\bar{\psi}}_{10}\\ \dot{\mathbf{V}}_1 &= \mathbf{H}_{10}\ddot{\bar{\psi}}_{10}.\end{aligned} \tag{D.5}$$

where $\mathbf{e}_{c0,z} = \bar{\mathbf{e}}_z$.

In this model, only the coordinates of the top boom and the hoisted load was considered because the slewing platform and the base boom were rigid bodies, and their motion was controlled by input slewing angle $\bar{\psi}_{10}$ and lifting angle $\bar{\theta}_{21}$. By substituting Eqs. (D.4) and (D.5) into Eq. (D.3), the vector of generalized acceleration of body-3 was rewritten as follows:

$$\dot{\mathbf{V}}_3 = \mathbf{H}_{32}\ddot{\bar{\mathbf{q}}}_r + \mathbf{H}_{30}\ddot{\bar{\psi}}_{10} + \mathbf{H}_{31}\ddot{\bar{\theta}}_{21} + \mathbf{N}_{31} + \mathbf{N}_{32}, \tag{D.6}$$

where $\mathbf{H}_{30} = \mathbf{D}_{32}\mathbf{D}_{21}\mathbf{H}_{10}$, $\mathbf{H}_{31} = \mathbf{D}_{32}\mathbf{H}_{21}$, and $\mathbf{N}_{31} = \mathbf{D}_{32}\mathbf{N}_{21}$. The equation of motion of the top boom and the hoisted load was calculated via virtual work in Eq. (D.7) and resulted in Eq. (D.8).

$$\delta W = \int_{V_3} \delta \mathbf{X}^T \left(\rho_3 \ddot{\mathbf{X}} - \mathbf{f}_3 \right) \mathrm{d}V_3 + m_4 \delta \mathbf{R}_4^T \left(\ddot{\mathbf{R}}_4 - \mathbf{f}_4 \right), \tag{D.7}$$

$$\mathbf{M}_3 \dot{\mathbf{V}}_3 = \mathbf{Q}_{3,g} + \mathbf{Q}_{3,v} + \mathbf{Q}_{3,k} + \mathbf{Q}_{3,c}, \tag{D.8}$$

where ρ_3 and V_3 are density and volume of the top boom. $\mathbf{f}_i$ is the external force vector, $\mathbf{M}_3$ is the mass-inertia matrix of the top boom and the hoisted load (because the hoisted load was model as one part of the top boom), $\mathbf{Q}_{3,g}$, $\mathbf{Q}_{3,v}$, $\mathbf{Q}_{3,k}$ and $\mathbf{Q}_{3,c}$ are vectors of generalized gravity force, quadratic velocities vector, stiffness-damping force, and joint reaction force. By substituting Eq. (D.6) into (D.8) and left-multiply with $\mathbf{H}_{32}^T$, Eq. (D.8) was rewritten in form of independent relative coordinates as follows:

$$\begin{aligned} \mathbf{M}_r \ddot{\mathbf{q}}_r &= \mathbf{Q}_{r,g} + \mathbf{Q}_{r,v} + \mathbf{Q}_{r,k} - \mathbf{M}_{in}\ddot{\mathbf{q}}_{in} - \mathbf{\Gamma}_r, \\ \mathbf{M}_r \ddot{\mathbf{q}}_r &= \mathbf{Q}_{r,total} - \mathbf{M}_{in}\ddot{\mathbf{q}}_{in} - \mathbf{\Gamma}_r, \end{aligned} \tag{D.9}$$

where $\mathbf{q}_r = \begin{bmatrix} \bar{\theta}_{32} & \bar{\psi}_{32} & \bar{\phi}_{43} & \bar{\theta}_{43} \end{bmatrix}^T$ $\mathbf{q}_{in} = \begin{bmatrix} \bar{\psi}_{10} & \bar{\theta}_{21} \end{bmatrix}^T$, $\mathbf{M}_r = \mathbf{H}_{32}^T \mathbf{M}_3 \mathbf{H}_{32}$, $\mathbf{M}_{in} = \mathbf{H}_{32}^T \mathbf{M}_3 \begin{bmatrix} \mathbf{H}_{30} & \mathbf{H}_{31} \end{bmatrix}$, $\mathbf{\Gamma}_r = \mathbf{H}_{32}^T \mathbf{M}_3 (\mathbf{N}_{31} + \mathbf{N}_{32})$, and $\mathbf{Q}_{r,n} = \mathbf{H}_{32}^T \mathbf{Q}_{3,n}$ while $\mathbf{H}_{32}^T \mathbf{Q}_{3,c} = 0$. The generalized flexible forces, $\mathbf{Q}_{r,k}$, was calculated as

$$\mathbf{Q}_{r,k} = \begin{bmatrix} k_\theta \bar{\theta}_{32,f} + d_\theta \dot{\bar{\theta}}_{32,f} \\ k_\psi \bar{\psi}_{32} + d_\psi \dot{\bar{\psi}}_{32} \\ 0 \\ 0 \end{bmatrix}, \tag{D.10}$$

where k_n and d_n are rotational stiffness and damping coefficient in n-direction. As illustrated in Eq. (D.10), the flexibility of the silicone joint was assumed to be linear and only vibrated in two directions.

In this model, $\bar{\theta}_{32} = \bar{\theta}_{32,o} + \bar{\theta}_{32,f}$. $\bar{\theta}_{32,o}$ was the assumed offset angle of $\bar{\theta}_{32}$ whereas, $\bar{\theta}_{32,f}$ was its relative deformed angle. This was because the silicone joint was deformed with large bending under static force. Because of its nonlinear material property, the vibration occurs around this offset angle. $\bar{\theta}_{32,o}$ was designed by trial and error. Furthermore, the designated boom's angle θ_{in} also had to include this offset, therefore,

$$\bar{\theta}_{in} = \bar{\theta}_{lift} - \bar{\theta}_{32,0} \tag{D.11}$$

where $\bar{\theta}_{lift}$ is the original designated lifting angle. It was important to note that this was the specific condition that happen in our laboratory-scale crane setting. It was not the general design of a rotary crane.

The input trajectory that was calculated with a simplified dynamic model had to be recalculated into rotational trajectory as

$$\bar{\theta}_{21} = -\cos^{-1}\left(\frac{R_o - L_{top}\cos\bar{\theta}_{in}}{L_{base}} \right), \tag{D.12}$$

$$\dot{\bar{\psi}}_{10} = \frac{\dot{u}_{in}}{R_o}. \tag{D.13}$$

The equivalent stiffness and mass for designing the optimal trajectory in laboratory size crane were as follows:

$$k_{e,y} = \frac{k_\psi}{L_{top}^2}, \tag{D.14}$$

$$k_{e,r} = \frac{k_\theta}{(L_{top} \sin \bar{\theta}_{in})^2}. \tag{D.15}$$

Since the natural frequency of the top boom in rotational direction and its respective linear direction were the same, the equivalent masses are calculated as,

$$m_{e,y} = k_{e,y} \frac{J_3}{k_\psi}, \tag{D.16}$$

$$m_{e,r} = k_{e,r} \frac{J_3}{k_\theta}. \tag{D.17}$$

This dynamic model was verified by calculating the simulated motion, and comparing the motion of the boom tip and the hoisted load from simulated results to experimental results. The input motion was calculated with the reference approach [35] with the minimized jerk trajectory. The control period of $T_c = 0.5T_n$ was used, and the control velocity, V_c was 0.19[m/s]. The duration of the constant period, T_{const}, was 1.89[s]. The numerical simulation was calculated, and the experiment was conducted using the input motion in Fig. D.5. Then their trajectory of the boom tip and the hoisted load were compared.

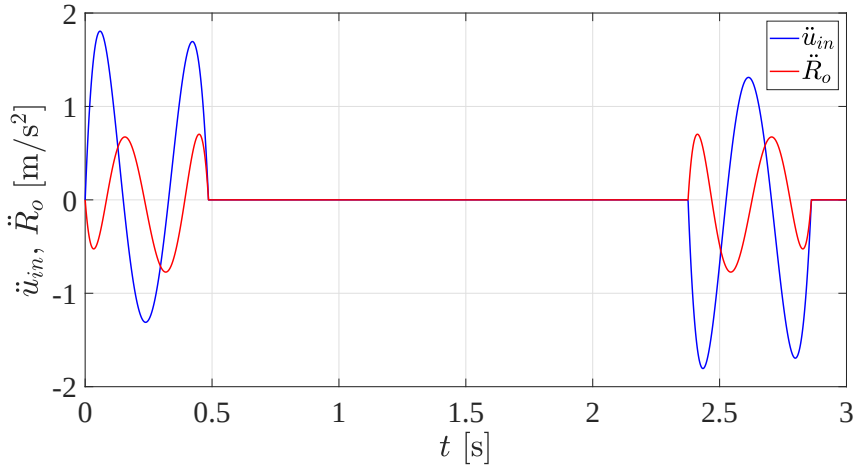

Fig. D.5: The input acceleration calculated with the reference model. The input motion was calculated at control period of $T_c = 0.5T_n$ and the control velocity of $V_c = 0.19$[m/s]. The duration of the constant velocity period was $T_{const} = 1.89$[s]

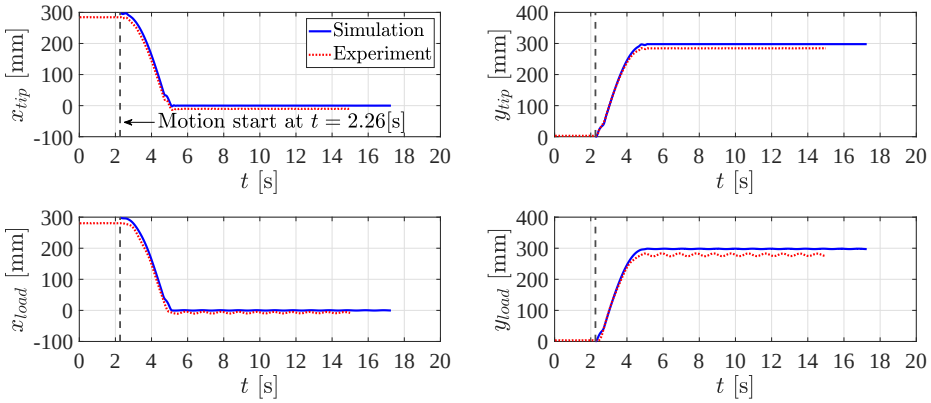

(a) Full motion

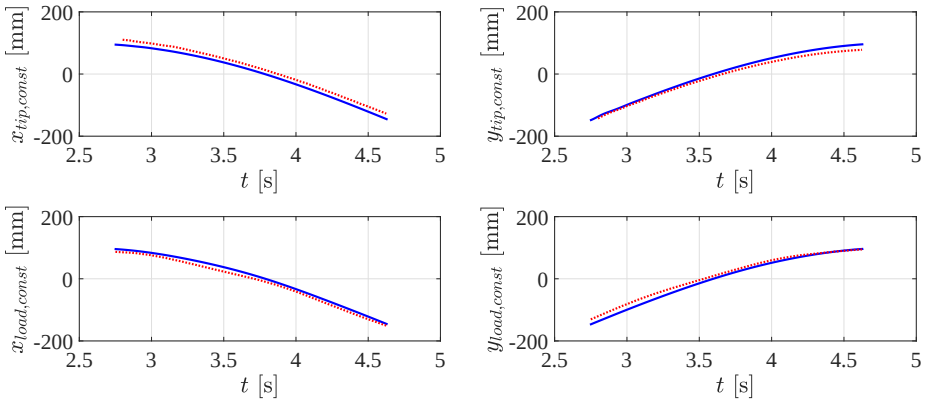

(b) Constant velocity period

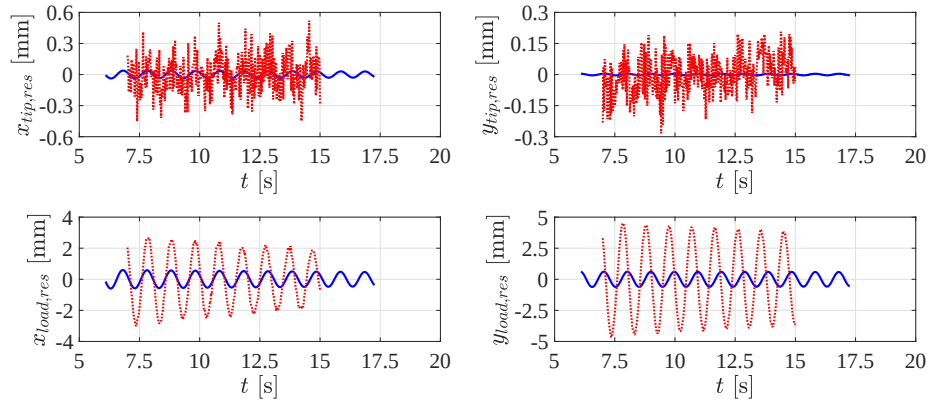

(c) Residual vibration

Fig. D.6: The comparison between the simulated motion (blue line) and experimental motion (red dot-line) under the controlled trajectory from Fig. D.5.

Figure D.5 illustrates the good agreement between the simulated motion and the captured motion from the experiment. The overall trajectory of the boom tip and the hoisted load from both results were similar. During the residual period, Fig. D.5(c), the simulated model had smaller amplitudes than the captured motion. However, the similar frequencies were achieved. Although there were the differences between the simulated results and experimental results, the accuracy of

the dynamics model was sufficient for this study.

The comparison between the simplified dynamic model of flexible crane in Section 3.1 and the nonlinear equation of motion in Appendix D was considered. The unit impulse response of the simplified dynamic model and the nonlinear model in Eq. (D.9) was calculated. However, the damping force in Eq. (D.10) was neglected, and its impulse responses in the slewing and the lifting direction were calculated separately. All models were calculated with the fourth order Runge-Kutta's integration. Figure D.7 shows the unit impulse response of the nonlinear model and the simplified model. Table D.1 shows the natural angular frequencies of the nonlinear model and simplified model.

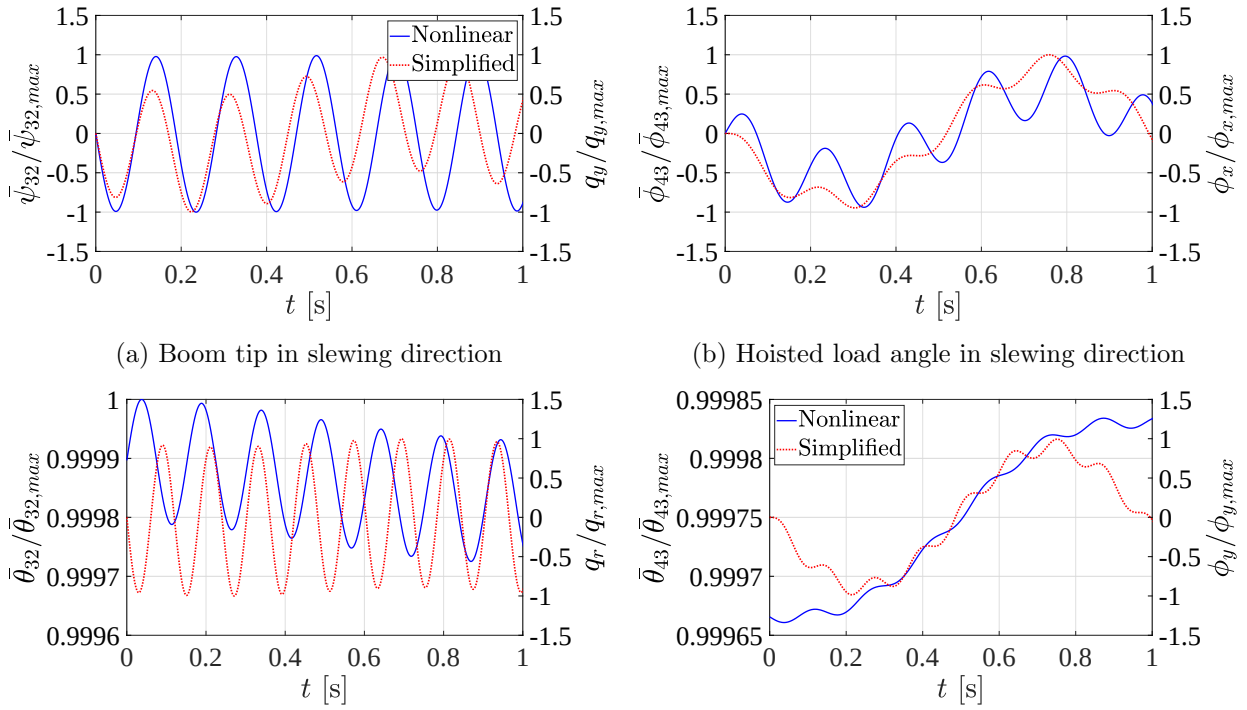

(a) Boom tip in slewing direction

(b) Hoisted load angle in slewing direction

(c) Boom tip in radial direction

(d) Hoistwed load angle in radial direction

Fig. D.7: The normalized unit impulse responses of the generalized coordinates of the simplified dynamics model and the nonlinear dynamics model.

Table D.1: The natural angular frequencies of the simplified model and the noninear model ([rad/s])

Direction	Simplified model	Nonlinear model	Difference
Slewing	6.27	6.12	2.45%
	35.2	33	6.66%
Lifting	6.43	6.17	4.21%
	52.1	50.9	2.35%

Figure D.7 shows the good correspondence between the simplified models and the nonlinear model. The change of the equilibrium point in Figs. D.7(c) and D.7(d) of the nonlinear model's coordinates $\bar{\theta}_{32}$ and $\bar{\theta}_{43}$ were caused by the change of the generalized gravity force in this direction. Table D.1 shows the small differences between the natural angular frequencies from the simplified model and the nonlinear model, where the differences were around 2.3% to 6.6%.

Appendix E

Cost function of vibration control model

This appendix shows the cost function of the vibrationless trajectory from Chapter 3. The cost function under the slewing and lifting control were calculated at variated T_c and a_c. The comparison between the cost from the reference control model[35] and the proposed control model was shown in this appendix. Only the trajectory from the minimized acceleration was considered.

E.1 Cost function of the crane model which mimicking the real size crane

The cost function of the vibrationless trajectory that was designed based on the crane model in Section 3.3.1 were shown in Fig. E.1.

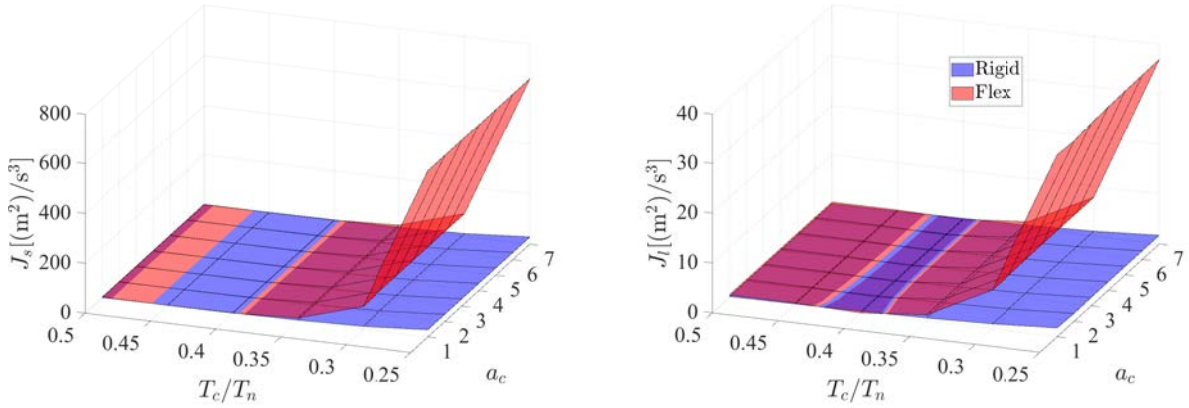

(a) Slewing control

(b) Lifting control

Fig. E.1: Cost function of the vibrationless trajectory calculated for the model in Section 3.3.1 under minimized acceleration

Figure E.1 shows that the cost of the vibrationless trajectory from the proposed control was larger than the reference control that did not consider the boom's flexibility. The cost increased as the control period decreased.

E.2 Cost function of the laboratory size crane

Next, the cost function of the vibrationless trajectory for the laboratory size crane model in Section 3.3.2 were shown in Fig. E.2.

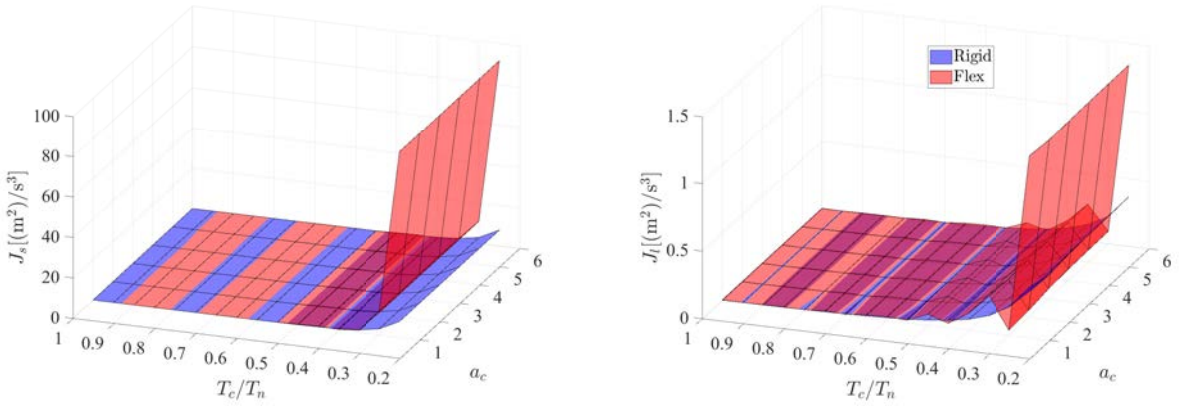

(a) Slewing control (b) Lifting control

Fig. E.2: Cost function of the vibrationless trajectory calculated for the model in Section 3.2.2 under minimized acceleration

Figure E.2 shows the same results as Fig. E.1 as the proposed control model that considered the flexibility of the boom required higher cost than the rigid boom control. The cost drastically increased at $T_c = 0.25T_n$.

E.3 Discussion

The cost function of the vibrationless trajectory from the flexible boom control model was larger than the rigid boom control. It was understandable since the flexible control model needed to suppress both the boom tip and the hoisted load. When the control period became shorter, the acceleration became higher, thus, the flexible crane subjected to higher forces and led to larger deformation. Therefore, the cost was drastically increased due to the system required higher energy to suppress the deformation.